AGING OF

POLYETHYLENE/POLYPROPYLENE

(PE/PP) DUAL LAYER PRESSURE PIPE

BY OUTDOOR EXPOSURE

JIAN HUANG

SUBMITTED IN PARTIAL FULFILLMENT OF THE REQUIREMNTS FOR THE AWARD OF DOCTOR OF PHILOSOPHY OF LOUGHBOROUGH UNIVERSITY

JULY 2010

DEPARTMENT OF MATERIALS

SUPERVISOR: PROFESSOR M. GILBERT

DIRECTOR: DR. N. THOMAS

SPONSOR: RADIUS-SYSTEMS LTD.

ACKNOWLEDGEMENT

I would like express my highest gratitude to Professor Marianne Gilbert for her guidance and encouragement from the beginning to the end of this project. I am deeply inspired by her expertise, diligence and effectiveness even after her retirement near the end of this project. I also thank the people in our department who help me with my experiments, lab demonstrations and many other works. Thanks to Ray for his strict but helpful suggestions. Thank Keith for the discussion of the contact angle results. I appreciate Pat, Sue and Jade for their cooperation with the coursework collection. I also cherish the friendship with Abdul, Xiaoran, Qingting, Feng and many others I met but could not name. Thank you all to give me enjoyable and unforgettable time during my PhD study.

I really appreciate the funding from Radius-Systems Ltd and EPSRC, without which this project will not be possible.

Thanks to Dr. Jeremy Bowman from Radius-Systems Ltd for the insight and enlightening discussion with this project and giving me the opportunities to earn experience in the industry and even in the business of the company. My appreciation also goes to Dave, Paul, Tim, Andy et al in the company who help me with my practical work.

Last but not the least, I am deeply grateful to my parents for their understanding, financial and psychological supports and kind suggestions on my study, research and life. Thanks to Ding for her company.

ABSTRACT

This project investigated the effect of PP skin on the PE core pipe in a PP/PE dual layer pipe during production and outdoor exposure under various radiation dosages by comparing the results with the corresponding uncoated pipe using different characterization techniques.

It was found for unaged samples that after extrusion the adhesion reducer present in the PP skin migrated to the PE core pipe outer surface but had little effect on the electrofusion (EF) joint quality. The PP skin prevents the PE core pipe from quenching therefore more perfect PE crystal is formed as shown by a higher crystallinity and the residual stress is reduced as shown by a slit ring method. Due to the reduced residual stress, the skinned pipe had higher long term hydrostatic strength (LTHS) than the uncoated pipe.

After outdoor weathering, photo-oxidation products were evident at the solar irradiated PP outer surface after 3 GJ/m^2 weathering and the whole PP outer surface was oxidized after 10 GJ/m^2 weathering. By deconvoluting the IR peaks, ketones, carboxylic acid and esters were found the main products. Although only slight photo-oxidation was identified after 10 GJ/m^2 aging on the uncoated PE pipe outer surface, oxidation induction time (OIT) results indicated that the solar irradiated side of the surface lost most of its antioxidants after only 1 GJ/m^2 weathering which led to production of weak layer in the EF joint. In the middle pipe wall and at the inner surface, a more gradual decrease of antioxidant was found. The skinned pipe showed better resistance to antioxidant loss than the uncoated pipe and still had adequate antioxidant for EF. The thermal effect of solar irradiation was thought to cause secondary crystallization of the uncoated pipe at the irradiated side and release of residual stress of both uncoated and skinned pipes after aging. The residual stress release rate was found to decline with weathering. As the pipe with thicker skin always had a lower residual stress, it can be inferred that the skinned pipe still had a higher LTHS value than the uncoated pipe even after aging.

Keywords: PE/PP, dual layer pressure pipe, outdoor aging, antioxidant, OIT, LTHS.

TABLE OF CONTENT

LIST OF FIGURES

LIST OF TABLES

Chapter 1 INTRODUCTION

1.1 Background- ElectoFusion and ProFuse

Thermoplastic polyethylene (PE) pipes are extensively used in new gas and water distribution systems as well as rehabilitations of traditional metal pipe systems at present. Electrofusion is a common technique in plastic pipe industry and it is essential to the integrity of the pipe system.

General electrofusion includes butt fusion, tapping T (saddle coupler) fusion and socket fusion. All these fusion procedures require melting surfaces which are clean and freshly made so that no dirt is present to form weak site within the joint. The stabilisers within the polymer must be adequate during the fusion period. The butt fusion process uses a rotor blade to scrape pipe ends, a hot plate as heat source and a standard clamp to press the pipe ends together. All of these processes are already mechanized and their aspects will not be developed here. In the case of tapping T and socket fusion, laborious and time consuming scraping is needed for conventional solid wall pipe to attain a clean pipe surface.

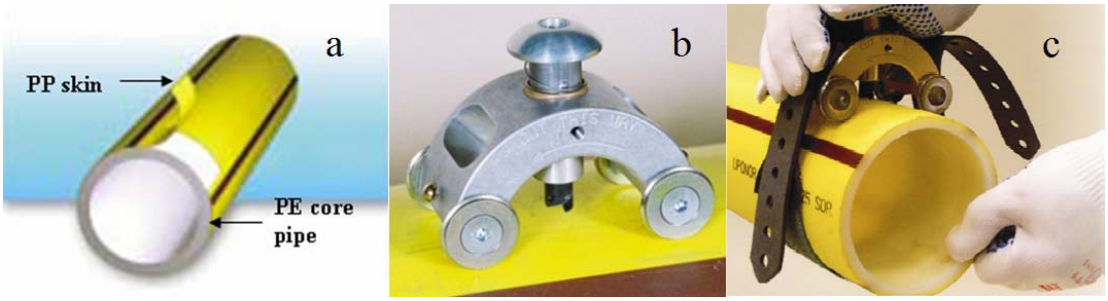

Figure 1-1 ProFuse and its exposure tool [1-3]

In order to save time and labour, a PE pipe designed with a polypropylene (PP) skin has been developed by Radius Systems to facilitate tapping T and socket fusion. As shown in Figure 1-1 a, clean surface can be prepared by just peeling off the skin. An exposure tool (Figure 1-1 b and c [2]) has been invented to assist this procedure and to avoid damage to the PE core pipe. The literature also shows that the peeled pipe provides a consistent gap between the fittings and PE core pipe wall as well, ensuring the optimum EF spacing to achieve high joint strength [4]. The skin can also act as a

physical protection layer to the PE core pipe surface in many cases such as transportation, pulling through the directional drilled path or damaged old pipe path where sharp obstacles might be present. Due to the benefits of further protection and the ease of electrofusion, the company gave it a trade name ProFuse which is a combination of these two benefits.

The inner core pipe of ProFuse is made of conventional bimodal grade PE. It is thermally and UV stabilised without pigments and extruded using a conventional single screw extruder. The PP skin (normally 0.8~1mm thick) material, pigmented in the required colour, is formulated by the company with a nucleating agent and an adhesion-reducer to control melt adhesion strength between the skin and core pipe. The skin is coextruded on to the core pipe within the extruder head by another single screw extruder. Detailed information of the product is described in patent WO2006/092567 [5].

1.2 Aging of ProFuse

ProFuse has been extensively used for new gas and water pipe systems in the UK in the recent decade. Being a leading product in the market, attentions has been drawn to the long term performance of the product (normal lifetime requirement of PE pipe is 50 years). In contrast, few similar previous studies have been done on such composite pipes. Therefore, a study of the aging of ProFuse is necessary and this project is initiated to see whether the skin retards the process of aging or, if the aging behaviour is not affected.

The literature survey is focused on several topics including development of PE pipe, aging mechanisms, stabilizers, solid PE pipe studied with or without aging effects, and various characterisation techniques suitable for the aging study. By reviewing the literature, it is found that unlike metal materials, where aging studies began early and the knowledge is more thorough, polymer aging is an ongoing research. The complexity of the environment and the intrinsic viscous-elastic nature of a polymer make the research even more difficult. At present, the relationship between artificial aging and natural aging has not been established.

Due to the complexity of polymer aging, natural aging was performed on ProFuse in a desert area for this project, on one hand accelerating the aging process, and on the other hand making the process close to the genuine aging process on site (e.g. storage in a stock yard).

1.3 Aims and objectives of the project

As mentioned above, natural aging was carried out in order to meet the genuine aging process on site. The project will not focus on the deviation between accelerated aging and natural aging which is an important issue in polymer aging. The aim of this project will focus on the effect of skin on the core pipe before and after natural aging. The objectives are specified as follows:

- To characterize unaged sample properties (both plain solid wall pipe and ProFuse) such as molecular weight, molecular weight distribution, crystallinity, surface free energy, thermal resistance, residual stress and long term hydrostatic strength (LTHS).
- To understand the effect of PP skin on the pipe properties during processing according to the results from the unaged samples.
- To characterize the outdoor aged samples (both plain solid wall pipe and ProFuse) at different aging periods with respect to the same properties that were measured for the unaged samples.
- To analyse the solid wall pipe aging procedure according to the change between different aging periods with reference to the aging mechanism.
- To understand the effect of PP skin on the properties during outdoor aging and develop a method to evaluate stabilizer profile across the pipe wall and along the pipe circumferential direction.
- To compare the consequences of outdoor aging on electrofusion joint quality.

Chapter 2 LITERATURE REVIEW

2.1 PE pipe

2.1.1 Generations of PE pipe materials

PE was first produced as an industrial product in the 1930s by ICI using a high pressure high temperature method (normally 15000~22500 psi, 180~200 ^{o}C) [6, 7], and which was classified as low density polyethylene (LDPE) with long and short side branches and low crystallinity. The strength of LDPE does not meet the strength requirements as a pressure pipe material and so it is used as film, container and cable, etc. Not until the late 1950s with the invention of Ziegler-Natta catalysts [8] that are typically based on titanium compounds and organo-metallic aluminium compounds, could PE be produced at lower pressure (300 psi, 30~100 ^{o}C) [7]. This would give a polymer with higher molecular weight, shorter branch length, and much less branch density and therefore higher crystallinity. This PE is classified as high density polyethylene (HDPE). In 1959, HDPE was introduced as a pressure pipe material in Germany as the first generation of PE pipe material.

Although the first generation PE pipe material met the short term static strength requirement, it was found that these pipes had short comings for long term applications. A case in point is their poor environmental stress cracking resistance. Later research found that short chain branching is essential to the long term performance with regard to slow crack growth. Especially, short chain branching (SCB) on the longest chain gave distinct increase of slow crack resistance due to the formation of tie-molecules among lamellas [9]. Therefore, alpha olefins such as hexene were copolymerised with ethylene in order to introduce short chain branching on the PE backbone using Ziegler-Natta catalyst system which is titanium based or Philips catalyst system which is chromium based. The pipes made from this new PE material classified as PE80 material passed the minimum strength requirement test [10] with a statistical extrapolated 50-year hydrostatic strength higher than 80 bars at

20 ^{o}C. The PE80 material has increased static strength and slow crack growth resistance, therefore it is categorized as the second generation of PE pipe material.

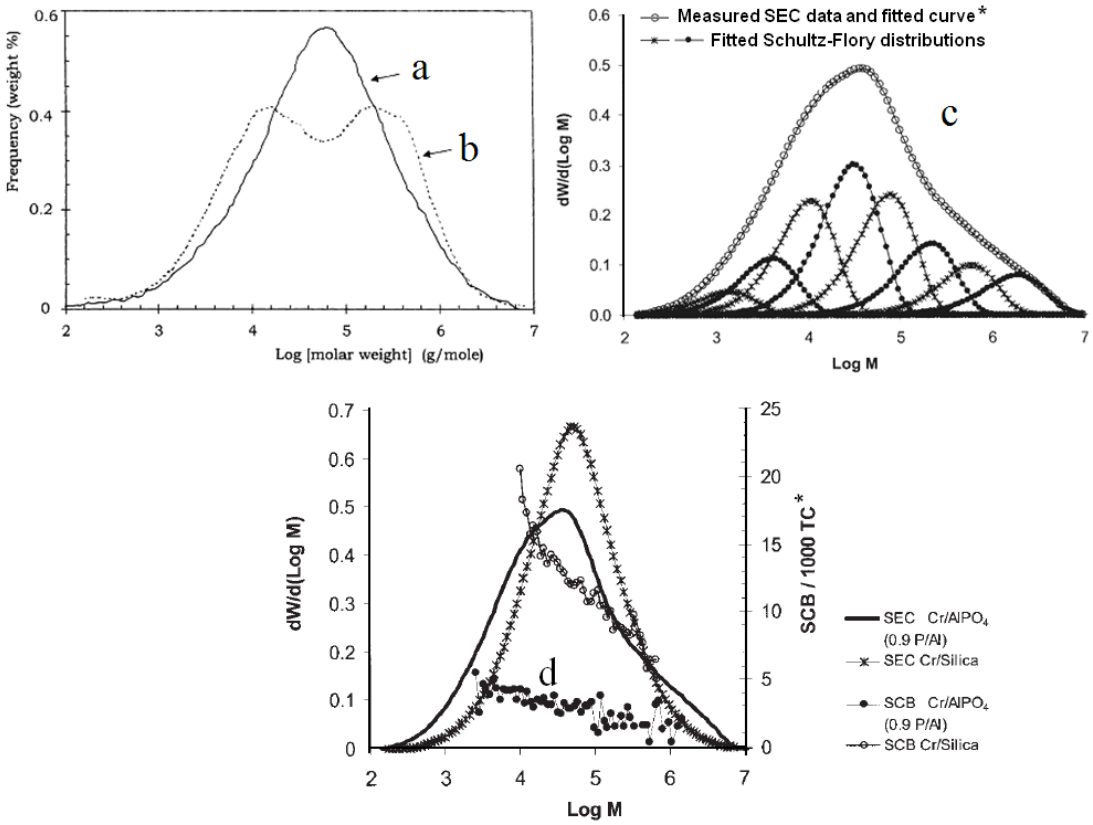

Figure 2-1 MWD of unimodal (a), bimodal (b), multimodal HDPE (c) and SCB distributions of unimodal and multimodal Philips type HDPE (d) [9, 11]

***SEC: Size Exclusion Chromatography, SCB: Short Chain Branching**

Further research aimed to produce a stronger material, PE100, by following the ideas from the first and second generation PE materials which are to increase the molecular weight and to modify the molecular structure. Materials with high molecular weight that meet the requirement of PE100 were developed in a laboratory, but researchers encountered problems with the poor processabilty of the high molecular weight material in a conventional pipe extruder, limiting its industrial application. The problems stem from the high viscosity of the material which will cause serious wear and generate excessive heat that leads to material degradation. Research on the relationship between molecular weight distribution (MWD) and material properties shown that the high MW component determines the material strength (both melt elasticity and mechanical strength in the solid state [11]), and the low MW component acts as a lubricant and lowers the melt viscosity. The MWD of the first and second

generation PE materials are both unimodal (Figure 2-1 a). Studies were then focused on increasing both low and high MW components of the of the unimodal PE material (Figure 2-1 b) by developing new catalysts and polymerization technologies without interfering with or even better manipulation of the SCB density which is essential to the slow crack growth resistance. In the 1980s, PE80 rated bimodal PE first appeared in the PE pipe market and gradually became a dominant PE pipe material owing to its versatile processabilty and excellent performance. In the 1990s, the bimodal PE was developed and it is strong enough for a PE100 rated material. This bimodal PE is now extensively used in the pipe industry and is classified as the third generation PE pipe material. Due to the importance of the PE100 material, an association named PE100+ was established in 1999 to promote consistent quality at the highest level in the production and the use of polyethylene for PE100 pipes in the industry.

At present, the most popular bimodal PE polymerization technique in the industry runs catalysts (either Ziegler-Natta or Philips type) in dual gas or slurry reactors in series. There are other methods to produce bimodal PE by melt mixing the two polymer components into a uniform blend or by using multi-catalysts that are capable to polymerize the low and high MW components in a single reactor, but there are limitations. For the former method, the uniformity of low and high MW components produced by melt mixing is still far lower than those produced by reactors. For the latter method, it is difficult to control the reaction conditions independently for the multi-catalysts in a single reactor to produce consistent bimodal PE continuously. The development on catalysts and their supporting compounds make tailoring of MWD possible without comprise of MW. Single catalyst, single reactor under simple reaction conditions became the development trend of PE pipe material production. A recently example is a PE100 rated multimodal PE (Figure 2-1 c) with high MW (Mw > 400kg/mol), broad MWD (Mw/Mn > 50) and uniform SCB density (Figure 2-1 d) produced by a single catalyst of chromium on modified aluminophosphate in a single reactor [9]. With a number of producers well established in the PE100 category, PE pressure pipe producers are now pursuing the next pressure rating standard of PE125 and the fourth generation of PE pipe material is emerging on the horizon.

It should be noted that the PE material being introduced here is thermoplastic PE. There is another PE type that is crosslinked (thermoset material). The crosslinked PE

has a higher application temperature (for example, hot water distribution) and normally used for pipes with smaller dimensions than thermoplastic PE, but it is not the major concern in this project.

2.1.2 Development of PE pipe structure

The development of PE pipe structure goes along side with the evolution of the materials.

At present, a corrugated structure has been developed for PE pipe in sewage pipe systems. The corrugated structure increases the flexibility of the pipe during lining and retains its strength.

Like conventional composite products, virgin PE is compounded with fibre segments or nano-clays to produce PE composite materials for pipes. The PE composite materials had shown better strength than the virgin PE material. In other cases, continuous fibres (including stretched PE fibre [12]) are laminated within the material during processing [13] to form multi-layer composite pipe also attaining higher strength. Pipes are also laminated with other materials such as metal and other polymers to act as a diffusion barrier or scratch resistance layer, functionizing the PE pipes.

The dimensions of PE pipe are growing to a larger and longer scale. Recently, a thick wall PE100 pipe with wall thickness of 109.1 mm and standard dimension ratio (SDR) of 11 was produced and laid on the seabed of the Bosporus channel for water transportation. This was claimed to be the thickest PE100 pipe in the world [14]. PE100 water pipe segments with lengths of 500 metre are also produced concurrently on the coast in Istanbul and towed off shore for water supply in Libya [14].

These new pipe structure designs indicate the growing application areas of PE pipes. ProFuse composite pipe being a part of these innovations is attracting research interest.

2.1.3 Processing of PE pipe

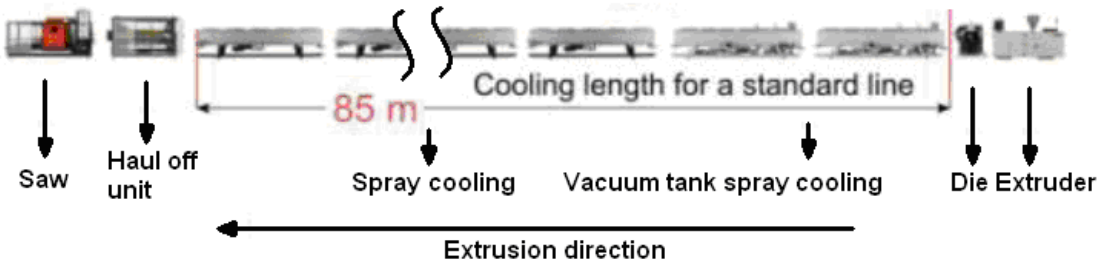

Figure 2-2 Schematic of a pipe extrusion line [15]

Most PE pipe is manufactured using single screw extruders. This is because firstly, the PE melt viscosity is low enough to be extruded. Secondly, the melt can maintain enough melt elasticity for some time after extrusion. And thirdly, extrusion meets the pipe manufacturing requirement of continuousness and uniform profile. Figure 2-2 shows the composition of a standard PE pipe extrusion line. It consists of the extruder, die, vacuum spray cooling chamber, cooling chamber, haul off unit and rotational blade saw. These units will be introduced below in detail.

The structure of a typical extruder is illustrated in Figure 2-3. Dried polymer pellets are fed through the hopper and enter the feeding zone, where they are solid and loose. Then they are pushed along the screw channel to a compression zone, where the screw channel depth decreases. At the mean time, the material is gradually heated to a homogeneous melt by combination of mechanical shear heating and barrel heaters. The decreasing screw channel space compresses the melt and expels air out of the melt. Finally, the homogeneous melt goes through a metering zone as a steady flow and is propelled to the extruder die by the screw to form desired shape. Figure 2-4 shows a general structure of an extruder die. The PE melt goes through the mandrel which is supported by the spider to form an annulus shape melt flow while exiting the die. The PP skin of ProFuse is coextruded through several channels in the same extruder die after the main spider. For some newly developed die heads, cooling air or nitrogen can be pumped in the pipe bore to shorten the cooling time and reduce the length of the production line [15, 16].

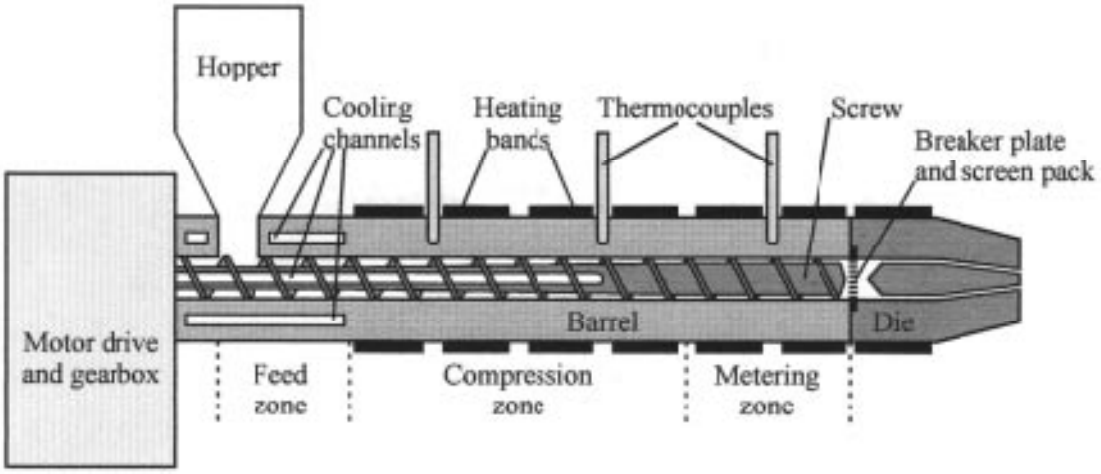

Figure 2-3 General structure of a single screw extruder [7]

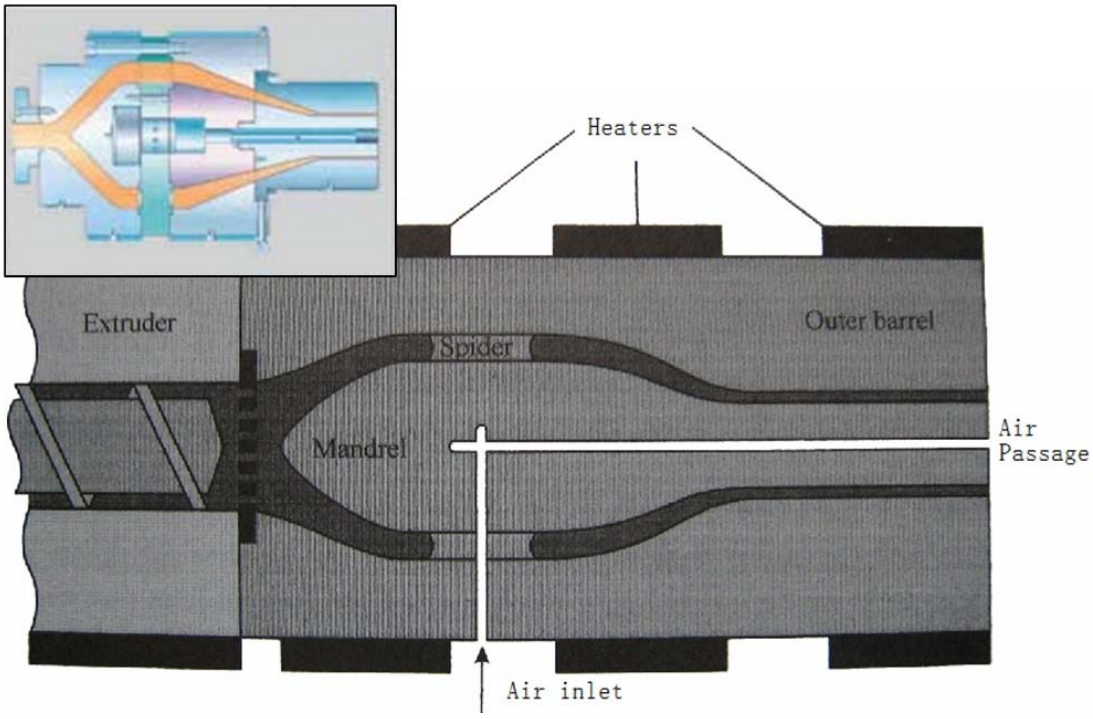

Figure 2-4 General structure of a single screw extruder die [7]

Figure 2-5 Vacuum cooling chambers

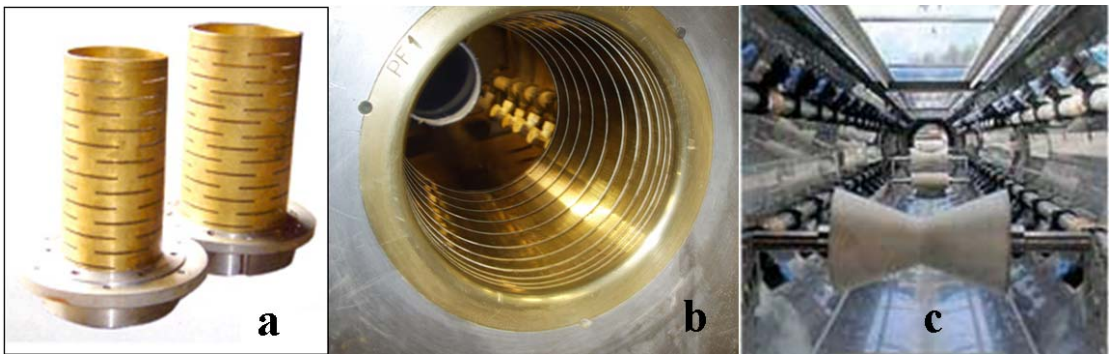

Figure 2-6 Sizing sockets and cooling water sprays

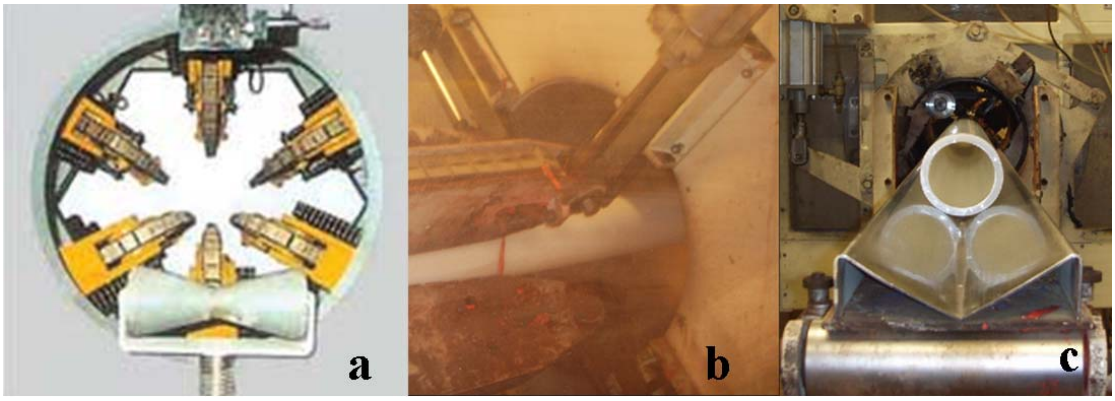

Figure 2-7 Haul off unit

The extrudate is pulled through a series of water spray cooling chambers (Figure 2-5) which are normally 80-90 metre long by haul off unit caterpillar belts that are situated at the end of the production line. The first one or two spray cooling chambers are vacuum controlled. The outer profile of the extrudate is calibrated by a sizing socket (Figure 2-6 a, b) at the entrance of each chamber with the aid of the vacuum to reach the desired outer diameter and circularity. Meanwhile, it is cooled down by water sprays (Figure 2-6 c) within the chamber and solidified.

At the final stage of pipe production, the caterpillar belt of the haul off unit (Figure 2-7 a, b) clamps the pipe and pulls it through the chambers. The haul-off speed and output rate of the extruder determine the pipe thickness. Pipes are cut off by rotational blades (Figure 2-7 c) and packed or for small diameter pipes, coiled into loops for transportation.

2.2 Polymer Aging

Polymer aging is a process in which the material properties change over a period of time. The process has drawn much interest from researchers because it may lead to ultimate failure that determines the lifetime of the materials. Polymer aging can be classified as physical aging and chemical aging with regard to the nature of aging process. For physical aging, there are not many agreements in the literature at present. On the other hand, chemical aging has received much more interest and abundant literature can be found on this subject. The following sections will review these two aspects of aging in detail and special attention is paid to PE and PP related literatures.

2.2.1 Physical aging

Physical aging commonly happens in thermoplastic polymers. Most thermoplastic polymers are shaped in the melt state during all processing methods. After shaping, the polymer normally undergoes a rapid cooling procedure. Take amorphous polymer for example. When the temperature rapidly drops below the glass transition temperature (Tg), the chain segments are frozen spontaneously and they are too slow to keep pace with the change that is required to form a thermodynamic equilibrium state. As a result, the molecules reach a thermal equilibrium state with the surrounding, but not a thermodynamic equilibrium state. Cooling is an entropy decreasing procedure and the system tends to form a more ordered molecule arrangement, i.e. thermodynamic equilibrium state, and chain segment rearrangement happens. An effect of this change is the density. The density of the material will increase consequently due to more compact alignments of chain segments and the material will undergo volumetric relaxation. The physical aging phenomenon was proven in many experiments [17], but the physical principles behind it are not yet been well understood.

Without clear understanding of the principles behind physical aging, the relaxation behaviour of physical aging can only be expressed empirically. Mathematical methods have been applied and some models give an excellent fit to the experiment data. These models include the Kohlrausch-Williams-Watts's stretched exponential

function (KWW function), continuous distribution of relaxation time function [18] and sum of exponentials or power law function [19]. The parameters of these functions were determined by experiments on specific polymers. If the aging process needs to be analysed, empirical models should be applied with caution.

Much of the research on physical aging has been focused on amorphous polymers rather than semi-crystalline polymer. It is because firstly, the understanding of physical aging phenomena is challenging, and requires focussed research. Secondly, research on amorphous polymers can help the understanding of the physical aging of the amorphous phase in semi-crystalline polymers to some extent. For semi-crystalline polymers, because the amorphous phase is restricted by the crystalline phase and the crystalline phase has different physical aging behaviour (e.g. secondary crystallisation), the physical aging of a semi-crystalline polymer is even more complex than an amorphous polymer. Therefore, the physical aging of an amorphous polymer has been put as a priority.

In this project, physical aging is not a main concern and it is thought to be less obvious than the chemical aging, so it will not be discussed any further here. However, this type of aging process should always be borne in mind because of its wide existence.

2.2.2 Chemical degradation

The nature of polymer degradation is breakage of molecular chains. Therefore, polymer degradation behaviour is inherently determined by their molecular structures. For example, the benzene ring network structure (interlocked regular hexagonal pattern) of carbon fibre endows the material with high temperature resistance and high strength/weight ratio. PVC is very susceptive to thermal decomposition of processing because the side hydrogen and chlorine atoms are labile to dehydrochlorination and the accumulation of resultant, hydrochloride will in turn catalyze the decomposition reaction. Although PE and PP are resistant to many aggressive acid and alkaline environments, they tend to be oxidized at a speed that can largely shorten their useful life. PP has a less stable structure than PE due to the existence of tertiary hydrogen in

the polymer chain repeating unit. In order to overcome the molecular structural weakness of some polymers, it is common that stabilisers are added to the polymers like PE and PP to prevent unexpected degradation.

Chemical degradation involves reactions that cause alterations to the molecular chain such as chain breakage or crosslinking, leading to embrittlement or hardening, and finally material failure. According to the source of chemical degradation, the general degradation can be classified into thermal-oxidative degradation and photo-oxidative degradation. Both degradations are chain reactions that include initiation, propagation and termination. The general affecting factors, mechanisms, reactions and effects on material structure and properties of the chemical degradation will be reviewed in detail in this section. Other research on degradation in specific environments such stress aided chemical degradation and aggressive chemical induced degradation will also be introduced.

2.2.2.1 Thermal degradation

The thermal degradation behaviour is well studied because it is the first destructive reaction in the product and has an important effect on the polyolefin's lifetime [19]. According to the temperature range and time span, thermal degradation can be divided into thermal degradation during material processing and thermal degradation during material service.

Polymer processes involved in the industry are milling, calendaring, injection moulding and extrusion etc. During processing, the material is kept in the molten state at elevated temperature to form the desired shape. Meanwhile, the polymer undergoes decomposition when the temperature reaches the critical reaction temperature of the degradation reactions. The mechanical force that is applied in the processing procedure will generate heat, and assist the degradation reactions.

It is well known that extrusion is one of the severe forms of processing that thermoplastic polymers undergo [21]. Extrusion involves factors such as high temperature, high mechanical stress and shear rate, and they will be introduced below.

Among factors affecting thermal degradation, temperature is the dominant one. Physically, temperature controls the rate of oxygen and stabilizer diffusion as well as the mobility of polymer chain segments, governing the possibility of chemical reactions. Chemically, thermal degradation at different temperatures will lead to different chemical reactions and consequences. It was proposed by Amin and his co-workers that LDPE at 160^{o}C produces hydroperoxides that have a photo-initiating effect, resulting in rapid material failure. But those produced by thermal oxidation in the range 85 ^{o}C~95 ^{o}C do not have photo-initiating effect [22]. This is because many degradation reactions are activated at high temperature. And more long lasting free radicals can be produced at high temperature while at low temperature these reactions less likely to happen in PE and PP. Temperature also determined whether chain scission or crosslinking dominates in the polymer matrix.

The shear rate also affects the thermal degradation but has a less obvious influence on molecular degradation than temperature. Billiani et al [23] used the weight average molecular weight to assess molecular degradation during injection moulding of PP and found that degradation was more sensitive to increase in processing temperature than increase in shear rate. Further conclusion is also given in research on PVC. Reports showed that introducing lubricant to lower the shear rate has little reduction of the susceptibility of PVC to future oxidation [24]. But at the same temperature, shear rate can be the dominant factor to thermal degradation. A recent study of processing different metallocene PEs by Hoàng et al [25] showed that the PE with broader molecular weight distribution and higher portion of low molecular weight component has higher oxidation stability in an open mixer at 225^{o}C. They concluded that shear rate is lowered by the low molecular weight component of the material and shear is the major source for initiation of free radicals formed through homolytic fission caused by mechanical cleavage of polymer chains.

Thermal degradation during material service alone is much slower than thermal degradation during processing due to the relatively low temperature. The radicals formed only from thermal degradation at low temperature will not obviously affect future degradation as mentioned in [26]. But thermal degradation during material service is usually accompanied by photo-oxidation which gives additional destructive effects on the polymer and this will be discussed in the photo-degradation sections.

2.2.2.2 Consequences of thermal degradation – chain scission and crosslinking

Research on thermal degradation of PE and PP has been carried out to estimate the thermal processing effect on the molecular weight. It is found that chain scission and crosslinking reactions are competing reactions during thermal degradation. For PE, the reactions after chain cleavage are shown in Figure 2-8.

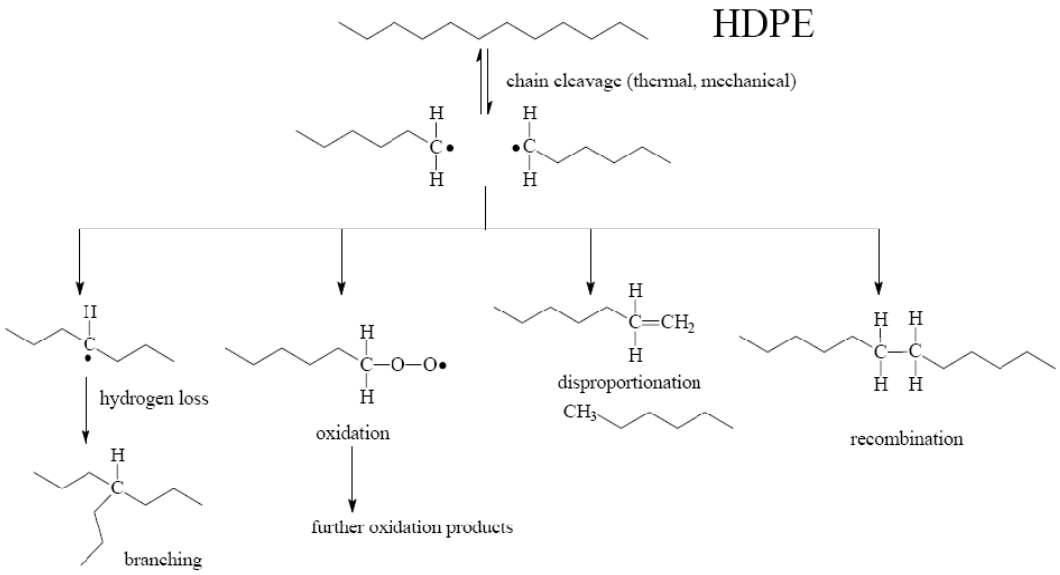

Figure 2-8 Reactions after thermal processing of polyethylene [27]

Among these reactions in PE, the branching reaction can lead to crosslinking in the polymer matrix. The oxidation will lead to formation of more stable alkoxyl radicals which will be active in photo-oxidation and chain scission reactions. The disproportionation results in the formation of an alpha double bond which is a potential source of an alkyl radical that can also cause further chain scission. Both the oxidation and disproportionation of free radicals result in chain scission. Recombination is a reverse reaction of chain cleavage. Whether crosslinking or chain scission dominates as a result of these reactions depends on many factors and include the type of polymerisation catalyst, stabilizer content, and temperature etc. A report [28] showed that unstabilized Philips type (chromium catalyst based) PE gave an increase in average molecular weight upon repeated extrusion, independent of temperature range between 240°C~260°C, whilst the Ziegler type (titanium based) polymer showed a converse effect. These results imply that in the former system

crosslinking predominates over chain scission, which leads to an increase in molecular weight. On the other hand, chain scission predominates in Ziegler type PE under the same conditions. Further research by Hoàng and Allen showed that the new metallocene PE (titanium and zirconium based) has better thermal oxidation resistance than Philips type PE because of the catalyst systems and the intrinsic polymer chain structures [29]. Taking stabilizer content into account, reactions will be retarded or inhibited to different extents, and the dominant reaction may alter. Temperature appeared to be an independent variable in a certain range in the report but it is well known that temperature will also affect the reaction rates of these competing reactions, making the analysis more complex.

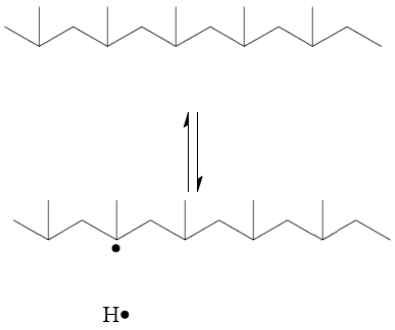

Figure 2-9 Radical formation of polypropylene [27]

Few publications that discussed the effect of polymerisation catalyst systems and temperature on chain scission and crosslinking of PP were found. This may because there are more reactive tertiary carbons in PP as shown in Figure 2-9, and in most cases chain scission is predominant. According to Gugumus' experiment [30], a sequence of hydroperoxide groups are much easier to form along a polymer chain of PP than PE and chain scission is preferable in PP rather than crosslinking. Tertiary ketone is the main chemical group formed as a consequence of thermal oxidation for PP [31].

2.2.2.3 General reaction scheme of thermal oxidation

Thermal oxidation is the main reaction that leads to thermal degradation. Thermal oxidation is a chain reaction that is composed of initiation, propagation and termination.

The initiation process can be completed through various ways because of the wide range of reactants. But anyhow, the general process of initiation is a converting small amount of polymer chains, PH, into free radicals, P•, as expressed in equation (2-1).

Initiation-

$$R\bullet + PH \rightarrow RH + P\bullet \quad (2\text{-}1)$$

Once the reaction is initiated, free radicals can grow to an appreciable amount. This is because of the propagation and branching reactions that follow the initiation as shown below.

Propagation-

$$P\bullet + O_2 \rightarrow POO\bullet \quad (2\text{-}2)$$

$$POO\bullet + P'H \rightarrow POOH + P'\bullet \quad (2\text{-}3)$$

Branching-

$$POOH \rightarrow PO\bullet + \bullet OH \quad (2\text{-}4)$$

$$2POOH \rightarrow POO\bullet + PO\bullet + H_2O \quad (2\text{-}5)$$

$$PO\bullet + PH \rightarrow POH + P\bullet \quad (2\text{-}6)$$

$$PH + \bullet OH \rightarrow P\bullet + H_2O \quad (2\text{-}7)$$

The key reaction in the propagation reaction is the absorption of oxygen (2-2), converting alkyl radicals into peroxy-radicals (POO•). The next step of the propagation is the abstraction of hydrogen from another polymer chain (P'H) by the polymer peroxy-radical to generate polymer hydroperoxide (POOH) and a new polymer radical (P'•).

Hydrogen atom abstractions in reaction (2-3), (2-6) and (2-7) are critical in chain propagation because far more new alkyl free radicals are produced through this process. The possibility of hydrogen atom abstraction reaction depends on the association energy of C-H bond and the surrounding chemical environment. The dissociation energy is listed in Table 2-1.

Table 2-1 Dissociate energies of carbon hydrogen bonds [32]

R—H	D_{R-H}, kJ/mol	Bond type
CH_2=$CHCH_2$—H	356	Allylic
$(CH_3)_3$C—H	381	Tertiary
$(CH_3)_2$CH—H	395	Secondary

PP has more tertiary C-H bonds than PE, i.e. more possible propagation sites for the oxidation reaction, therefore PP is more labile in oxidation than PE. It is generally found that secondary radicals exist mainly in PE and tertiary radicals mainly exist in PP [33]. Experiments have further proved that PP is much more sensitive to oxidation than PE [34].

The surrounding chemical environments, both intra- and inter- molecular, are factors that influence the possibility of hydrogen atom abstraction. For PP, Gugumus re-examined the hydrogen atom abstraction during a hydroperoxide thermal oxidation decomposition based on model compounds such as 2, 4, 6-trimethylheptane. It was proposed that the PP molecular chain restricted the hydrogen atom abstraction to the hydrogen atoms from neighbouring polymer chains [30]. Furthermore, it was inferred that intramolecular hydrogen atom abstractions took up 90% and more of all the hydrogen atom abstraction in PP. His further paper [35] analysed the intramolecular hydrogen atom abstraction of PE. The results indicated that in PE, there seemed to be an upper limit of intramolecular hydrogen atom abstraction which is approximately 30%. Among radicals that involved in hydrogen atom abstraction, alkyl radicals in both PE and PP had low reaction activity, while alkoxyl radicals were the most active.

The branching reactions are independent from initiation reactions and produce much more free radicals therefore, they accelerate the oxidation process. Hydroperoxide decomposition reactions (2-4) and (2-5) are the main reactions in branching. The behaviour of hydroperoxide decomposition depends on the polymer composition as well as its state. Gugumus re-examined solvent based hydroperoxide decomposition experiments and proposed a more reasonable hydroperoxide decomposition mechanism that was based on the polymer matrix [30]. Both melted state and solid state PE were considered. Among all decomposition reactions, the bimolecular decomposition reaction (2-5) is the most likely to happen in PP and PE. The alkoxyl

radicals produced after the decomposition will abstract a surrounding hydrogen atom along the polymer chain, producing alkyl radicals for further oxidation. Or in an other case, the alkoxyl radical will be further decomposed through β-scission reaction. After chain decomposition and oxidation, sequences of more than three hydroperoxide groups along the polymer chain are usually formed through reaction (2-2), (2-3) and chain scission will most likely happen.

Among reactions (2-1) to (2-7), there is no termination of free radicals (i.e. kinetic chain propagation of oxidation is continuous). Once the oxidation is initiated, the procedure is self-accelerated and continues automatically, forming auto-oxidation cycles. The overall thermal oxidation cycles can be expressed more comprehensively in Figure 2-10.

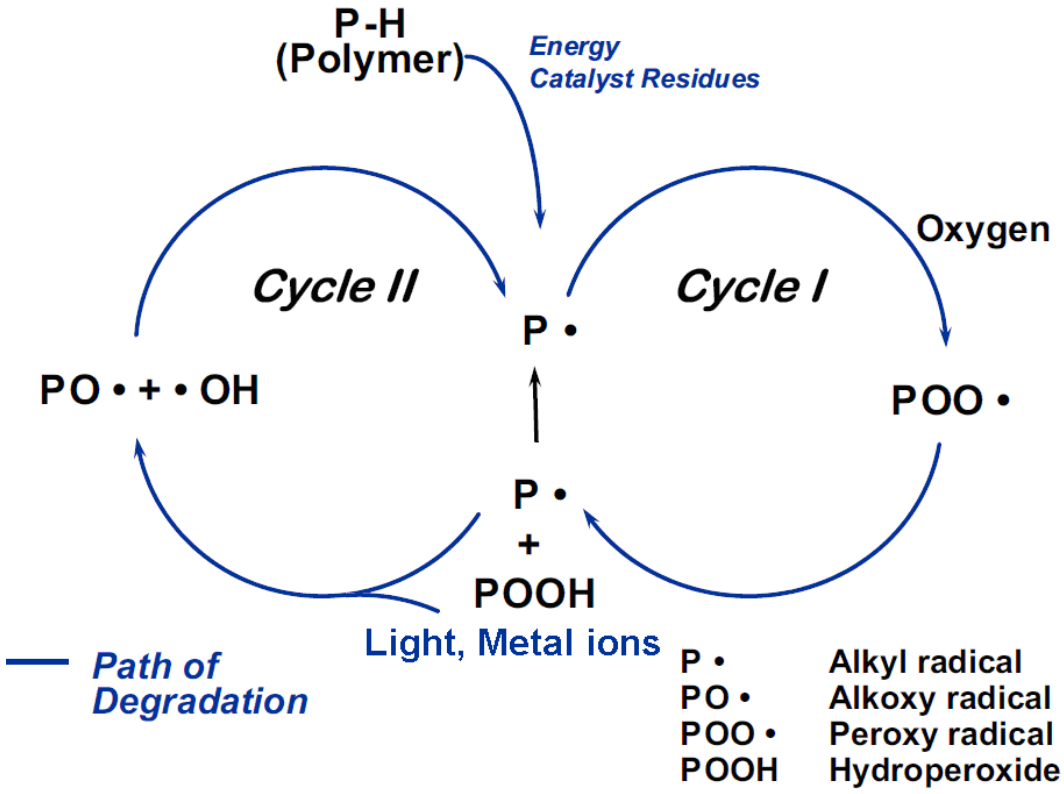

Figure 2-10 Polymer auto-oxidation cycles [36]

Terminations are normally through recombination of pairs of free radicals as shown in (2-8).

Termination-

$$\left.\begin{array}{l} P\bullet + P\bullet \\ P\bullet + PO\bullet \\ P\bullet + POO\bullet \\ POO\bullet + POO\bullet \end{array}\right\} \rightarrow \text{inactive products} \qquad (2\text{-}8)$$

These recombination reactions are influenced by cage effects, steric control effect, mutual diffusion of reacting radicals and parameters of the polymer matrix. Termination can cause cross-linking and hardens the polymer. For PE the termination reaction is also affected by temperature [35], resulting in different inactive termination products. For PP, the termination follows the formation of 1, 2-dioxetane and its decomposition [30]. Ketones are the most common product after termination for PP. Other groups include ester, per-ester, alcohol, acid, hydroperoxide, and alpha-lactone.

2.2.2.4 Further consideration about chain scission

During the thermal oxidation process, the polymer will not degrade if there is no chain scission reaction. The chain scission reaction happens only in the case that molecules such as PO, POOH and free radicals such as P•, PO•, and POO• are unstable. In the case of POH, it is less likely to be active because of the high dissociation energy of PO-H bond (437 kJ/mol [38]). Others molecules or radicals that are unstable will have breakage of C-C bonds in the back bone, leading to decrease in the average molecular weight.

The β-scission reaction (2-9) was proposed to explain the alkoxyl radical decomposition.

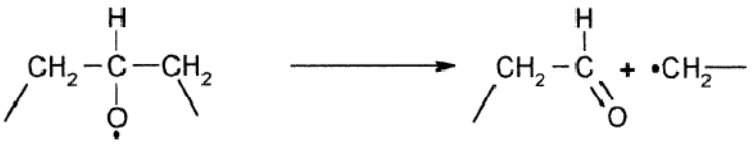

(2-9)

Although the β-scission reaction, which results in formation of aldehyde, end carbonyl group and end polymer alkyl radicals, can explain some oxidation products

and reduction in molecular weight in some polymers, it cannot give a satisfying explanation of high chemiluminescence observed in PP and chain scission in PE. Gugumus proposed that the role of β-scission of alkoxy radical in auto-oxidation in PP is over estimated [30]. This has been proved by investigation of thermal decomposition products of the PP model compound. He concluded some preference for hydrogen atom abstraction by alkoxy radicals in reaction (2-6) as shown in Figure 2-11 and Table 2-2. Various alternate possibilities were also proposed to explain the results.

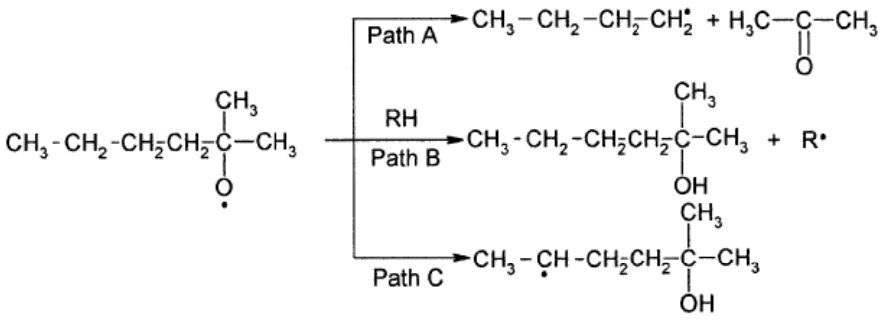

Figure 2-11 Reactions of alkoxy radicals with long side chain [30]

Table 2-2 Composition of alkoxy radials decomposition in various solvents [30]

	% reaction at 0°C according to path		
Solvent	A	B	C
CCl_4	13	3	80
Cyclohexane	2	8	81

Because alkoxyl radicals are products of hydroperoxide decomposition, hydroperoxide decomposition reactions are also considered in Gugumus' research [30]. In PP the reaction involves intermolecular as well as intramolecular decomposition of hydroperoxide sequences. The intramolecular decompositions of hydroperoxide sequences are demonstrated on Figure 2-12. The intermolecular decomposition is similar to intramolecular decompositions. The closeness of the radicals formed leads to proximity reactions favouring further reactions. One of the main reactions is 1, 2-dioxetane formation out of sequences of hydroperoxides in the polymer chain. The decomposition of 1, 2-dioxetane can easily explain the chain scission and the strong chemiluminescence observed in PP.

For PE, there is a controversy about the chain scission mechanism. It is mentioned earlier in this section that there seemed to be an upper limit of 30% for intramolecular hydrogen atom abstraction in PE at 150°C [35]. The products from hydrogen atom abstraction reactions are responsible for some specific reactions. But reasonable degradation reactions have not yet been agreed. It is noteworthy to mention that hydroperoxide decomposition in PE shows specific features such as pseudo-monomolecular hydroperoxide decomposition, bimolecular decomposition and free-radical induced hydroperoxide decomposition. Bimolecular decomposition explains why decomposition of PE produces essentially ketone and no alcohols and the reactions concerned are shown in Figure 2-13.

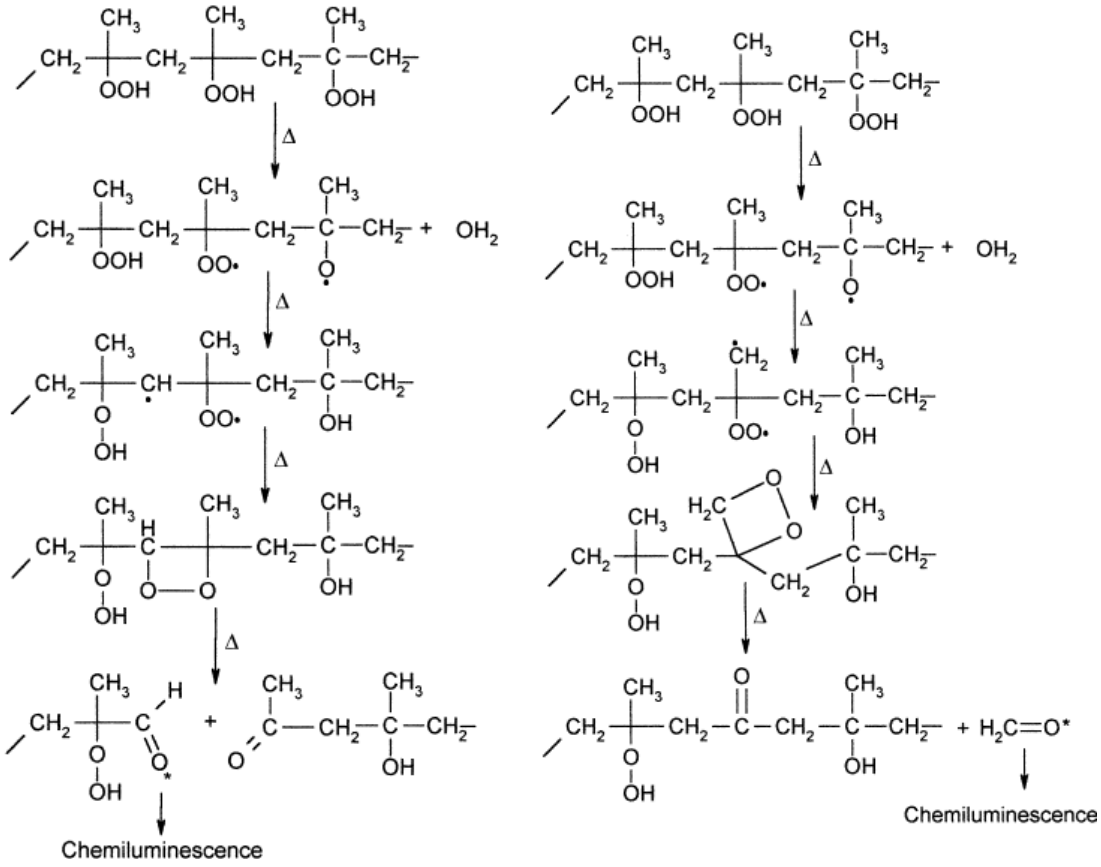

Figure 2-12 Major (left) and minor (right) path of Interaction of intramolecular alkoxy and peroxy radicals. [30]

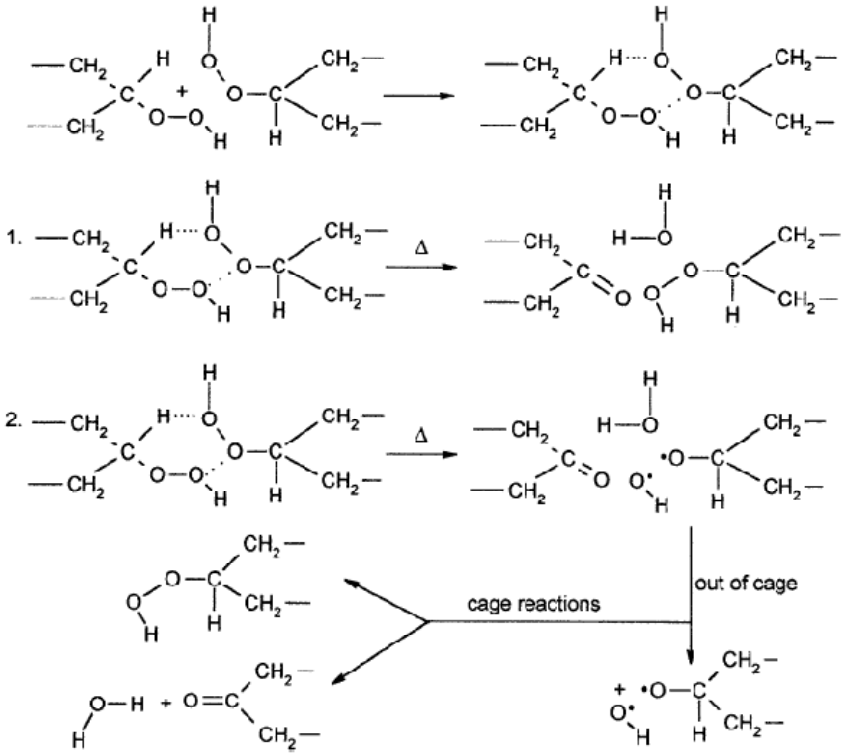

Figure 2-13 Bimolecular hydroperoxide decomposition in PE [35]

After thermal oxidation, residue radicals and even micro-crazes are introduced to the polymer, leading to consequent deterioration of the material. The general mechanism of photo-oxidation is identical to thermal degradation and it will be discussed in the following section.

2.2.2.5 Photo-oxidation degradation

Photo-oxidation degradation is the main chemical degradation process in long term outdoor aging of polymers. Photo-degradation is affected by many internal and external factors as illustrated on Figure 2-14. Significant research has been conducted in this area in the past few decades. Rånby and Rabek et al published textbooks [39-41] based on their fundamental research on photo-oxidation and its stabilization with respect to the basic photo-chemistry, dealing with both synthetic and natural polymers. McKellar and Allen [42] also published text books that treated more general photochemical reactions of man-made polymers

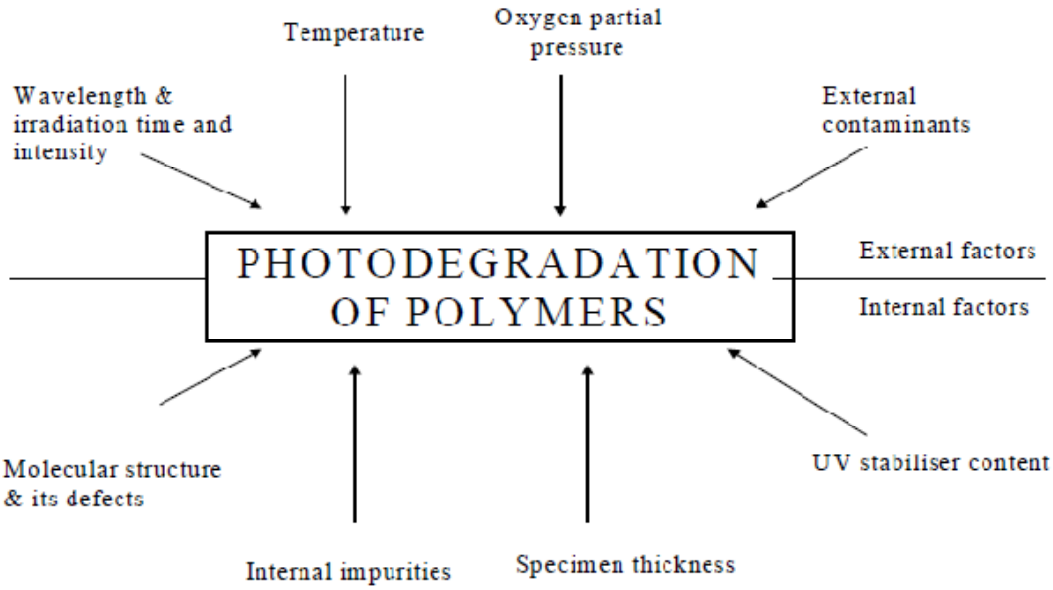

Figure 2-14 Factors affecting the photo-oxidative degradation of polymers [27]

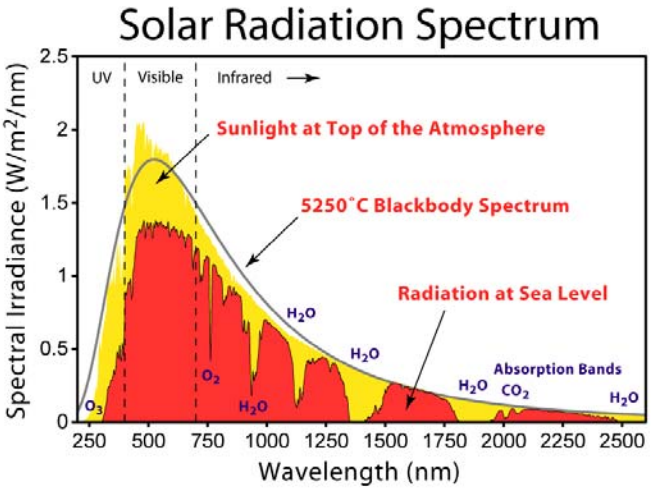

Figure 2-15 Solar radiation spectrum

Polymer chains are commonly composed of C-C, C=C, C≡C, C-H, C-O, C=O, C-N and C-Cl bonds. Among these bonds, single bonds do not absorb radiation of wavelength longer than 190 nm [40]. The sunlight spectrum ranges between 250 nm to 2500 nm (Figure 2-15). Therefore, most polymers such as PE and PP with only single bond backbone cannot be activated by natural radiation. The fact that polymers absorb radiation stems from the presence of chromophores. The chromophores come from impurities introduce in the polymerization and processing procedure such as trace metal and metal salts, catalyst residues, hydroperoxides, carbonyl groups, unsaturated bonds and additives such as stabilizers, pigments and dyes. The

chromophores absorb radiation to form free radicals, and initiate the photo-oxidative reaction.

According to the reaction conditions, the photo-oxidation is restricted to a certain depth from the polymer surface. The depth of the photo-oxidation depends on the radiation as well as the diffusion of oxygen. Generally for polymer, the depth for PE and PP can be from several micrometres to millimetre scale depending on the irradiation time [43, 44]. After photo degradation, a brittle layer with similar thickness will form at the surface.

Photo-oxidation reactions are chain reactions and most of the reaction scheme is similar to thermal oxidation. But the initiation reactions photo-oxidation is activated by absorbing the energy of photons rather than raising temperature. The difference of the energy source results in some different responses of the molecular structure. For example, generally the aromatic polymers have a higher temperature oxidation resistance than aliphatic polymers, but their conjugate ring structure inherently absorbs UV light, therefore they are photodegradable when exposed to sunlight. If the aromatic ring is connected with ester groups in the polymer backbone (i.e. aromatic polyester), the degraded structures react with oxygen to form semiquinone and quinone groups on the polymer surfaces. The semiquinone and quinone structure at the surface act as a photo stabilizing protection layer for the bulk polymer [45]. For PE and PP, the backbone is saturated C-C bond and the photo-oxidation is largely dependent on chromophores.

In pure photo-oxidation, the differences in the method of photo-initiation does not have much influence on the rate and extent of photo-oxidation for a certain polymer [41]. In practice, the thermal oxidation that is prior to the photo-oxidation will strongly affect the lifetime of the polymer. For example, the consumption of antioxidant during processing partly lowers the effectiveness of antioxidants. The impurities and hydroperoxides that are introduced during processing will also initiate photo-oxidation. [20, 46, 47, 48, 49] For PE and PP, the hydroperoxide is a key compound in photo-oxidation.

A research by Amin et al [46] on the mechanisms of the photo-initiation process in LDPE, using an open mixing at 165 °C to simulate processing procedure, shows that there is a growth and decay process of hydroperoxide during processing as illustrated in Figure 2-16. The hydroperoxide content, which is determined by a ferrous iron titration technique, can be related to vinylidene and carbonyl groups when the material is processed. The destruction rate of vinylidene can be related to the hydroperoxide concentration. Carbonyl concentration increases in an auto-accelerating mode follows the formation and decay of hydroperoxide. [46]

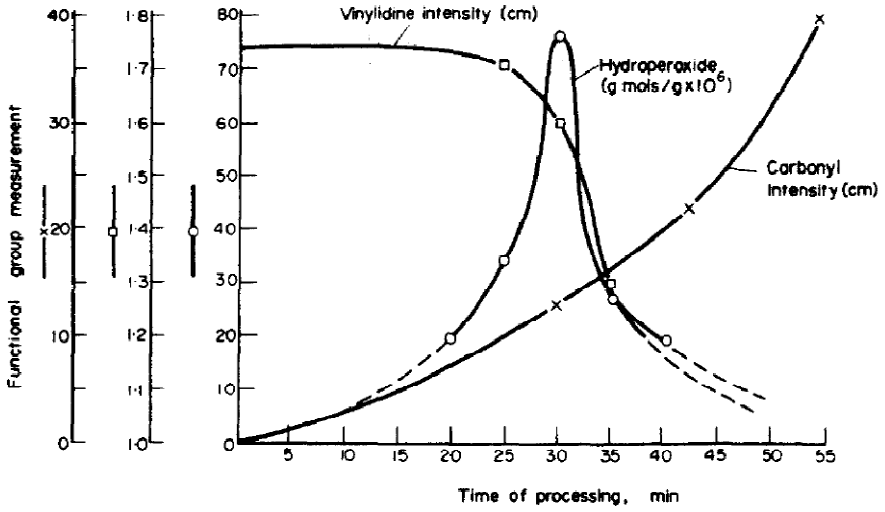

Figure 2-16 change in concentration of functional groups in LDPE after processing [46]

The samples after mixing at different mixing times were immediately compression moulded into film then irradiated under artificial UV light source and the chemical groups were analysed at various irradiation times. The investigation showed that the reaction occurs in two distinct stages. Each stage will have different photo-oxidation behaviour and produce different chemical species.

$$\text{}\left[\text{CH}_2\text{–CH}_2\text{–}\overset{\overset{\text{O}}{\|}}{\text{C}}\text{–CH}_2\text{–CH}_2\right]_n \rightarrow \text{–CH}_2\text{–CH}_2\text{–}\overset{\overset{\text{O}}{\|}}{\text{C}}\cdot + \cdot\text{CH}_2\text{CH}_2\text{–} \quad \text{(Norrish I)} \quad (2\text{-}10)$$

$$\left[\text{CH}_2\text{–}\overset{\overset{\text{O}}{\|}}{\text{C}}\text{–CH}_2\text{–CH}_2\text{–CH}_2\right]_n \rightarrow \text{–CH}_2\text{–}\overset{\overset{\text{O}}{\|}}{\text{C}}\text{–CH}_3 + \text{CH}_2\text{=CH–} \quad \text{(Norrish II)} \quad (2\text{-}11)$$

Before discussion of the two stages, a generally agreed photolysis reaction should be introduced here. At the beginning of irradiation of a polymer, chain scission may happen which is caused by decomposition of ketones, known as Norrish type I and II photolysis as shown in (2-10) and (2-11), and generate free radicals that are photo-initiative.

Both reactions result in chain cleavage. From Norrish reaction I, two free radicals are produced from one polymer chain. The radicals can further initiate oxidation reactions and finally be oxidized to aldehyde and carboxylic acid in the polymer. The Norrish reaction II is a non-radical reaction which results in chain scission by way of a six-member ring transition state yielding a methyl ketone and vinyl unsaturation. PE under UV radiation will undergo both Norrish I and II reactions at different stages of photo-oxidation. [37, 46, 47, 48]

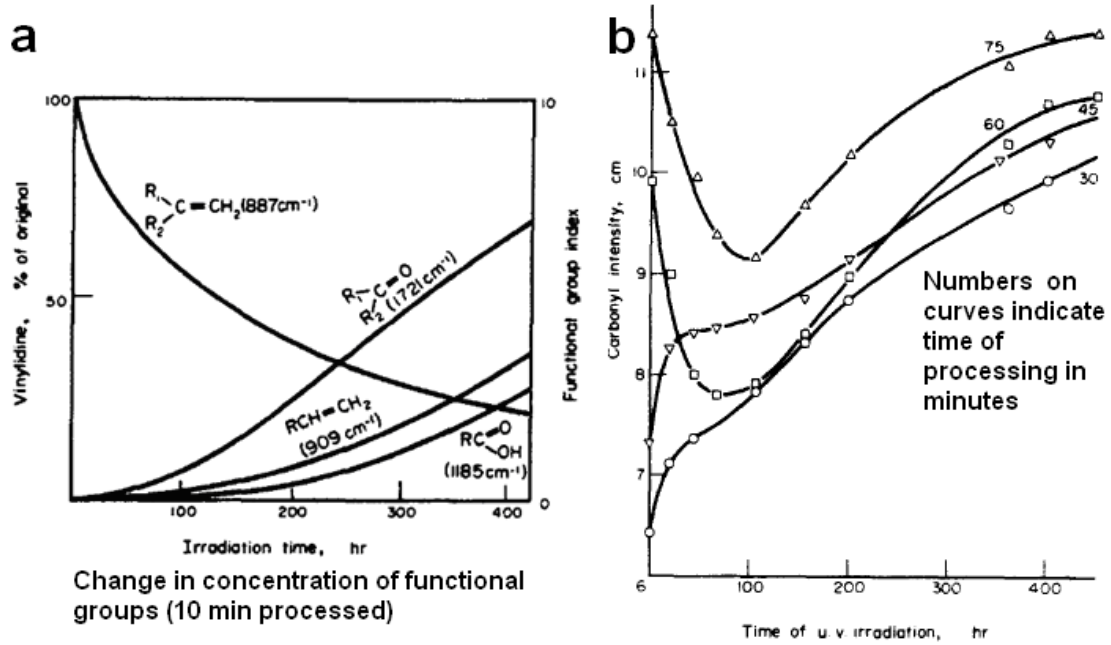

Figure 2-17 Effect of UV irradiation on the change in concentration of functional groups in LDPE processed for a) 10min and b) 30, 45, 60 and 75 min.[46]

In the two stages of the photo-oxidation in the LDPE processed by the open mixer, it is shown that during the first stage, the photo-initiator appears to be hydroperoxide formed during thermal processing of the polymer and the rate of carbonyl (ketone) formation is initially directly proportional to the hydroperoxide concentration [49].

In the mildly processed (10 min mixing time) LDPE, vinylidene initially present in the sample decays rapidly on UV irradiation and this precedes the formation of significant amounts of carbonyl groups as shown in Figure 2-17 a, suggesting that certain products from the vinylidene decay must be in some way associated with the photo-initiation step [46]. The vinyl and carbonyl groups increase proportionally which is believed to be a consequence of the Norrish II photolysis of ketone.
At the end of this stage, the rate of carbonyl formation auto-retards to give a plateau or if the concentration of thermally formed ketone is high, the carbonyl formation may actually decrease into vinyl and methyl ketone by Norrish II photolysis as shown on Figure 2-17 b.

During the second stage, the hydroperoxide concentration drops to a very low value and the rate of carbonyl formation becomes self-accelerating. The Norrish I photolysis of carbonyl which give rise to the ultimate product such as carboxylic acids appears to be much more important. [46]

The continued investigation [47] of photo-oxidation mechanism of PE showed that in both LDPE and HDPE, when the thermally formed hydroperoxides are photo-decomposed and produced substantial ketone groups, it is possible for Norrish I photolysis to occur. For a later stage of photo-oxidation, Norrish I produce final products of photo-oxidation such as carboxylic acids. The two polymers differ in that cross-linking occurs initially in LDPE with reduction in vinylidene unsaturation whereas chain scission dominates in HDPE. [47]

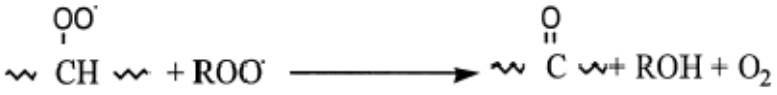

(2-12)

Tidjani and his colleagues [48] compared the oxidation products from linear low density polyethylene (LLDPE) after both natural and artificial weathering. It is concluded that whatever the mode of irradiation, carboxylic acid, secondary-alcohol and ester species are produced to a closely related extent. The evolutions of sec-hydroperoxides, vinyls and, to a less extent, ketones were very sensitive to the mode of UV irradiation. After analysing the oxidation products, they proposed a scheme of

hydroperoxide decomposition [48] as shown in Figure 2-18, giving more details of photo-oxidation. They also considered an alternative pathway as shown in reaction (2-12) for the formation of ketone and alcohol from the well-known Russel mechanism for bimolecular reaction of secondary peroxy radicals [50, 51].

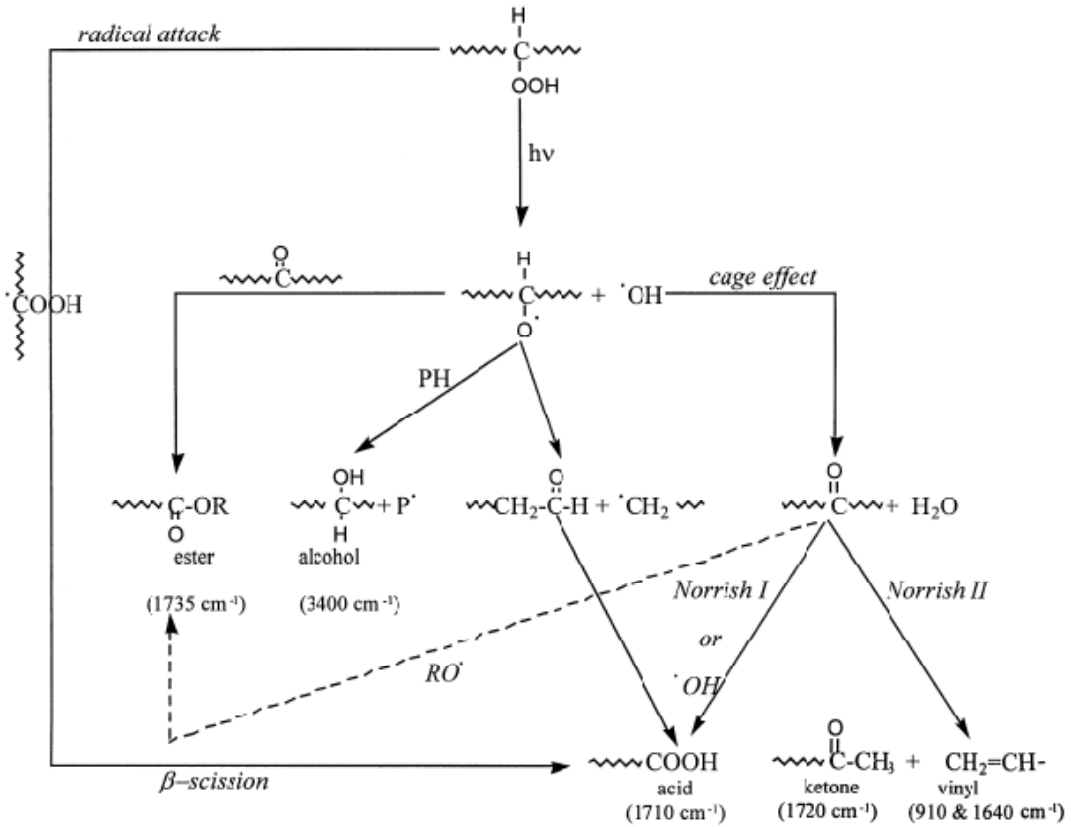

Figure 2-18 Scheme of hydroperoxide decomposition in LLDPE [48]

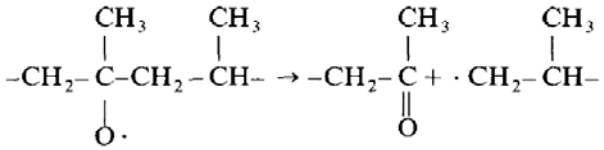

(2-13)

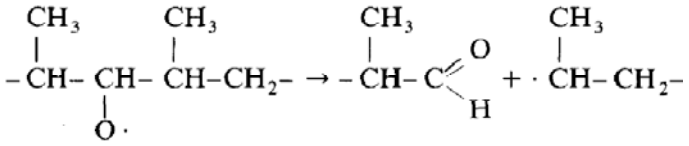

(2-14)

In photo-oxidation, PO• (alkoxyl radicals) may cause chain degradation by the β-scission reaction as mentioned in reaction (2-9). Earlier, it has been suggested that

decomposition of alkoxy radicals PO• is probably the principal mode of chain scission in the photo-oxidation degradation of PP [52]. The oxidized PP will undergo β-scission through reactions (2-13) and (2-14). But the detailed reactions were not proposed. The decomposition of photo-initiated radicals is more difficult to monitor than those in thermal-initiated radicals due to the solid phase of the materials and low concentration of the radicals. More research is required to be carried out in this area to reveal the general mechanism of polymer photo-oxidation.

2.2.2.6 Consequences of photo-degradation – chain scission and crosslinking

Chain scission and crosslinking are competing reactions in photo-degradation. An example of this is the further photo-initiative reaction of alkoxy radicals as shown in Figure 2-19.

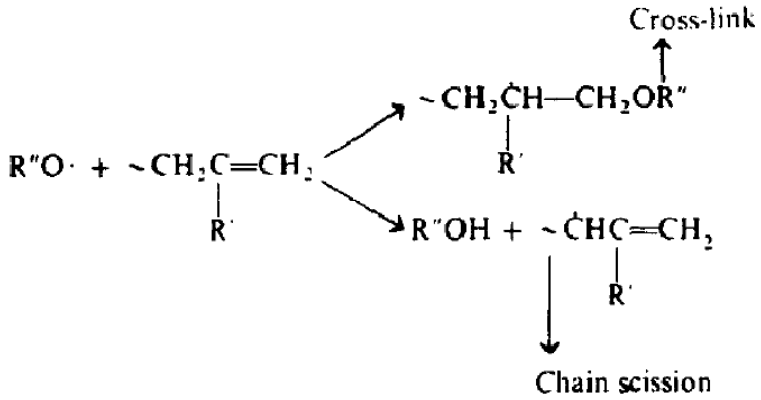

Figure 2-19 Reactions of alkoxy radicals that account for chain scission and crosslinking [46]

Shyichuk and White have carried out substantial work on chain scission and crosslinking rates in polymer photo-oxidation. They proposed a method called Molecular Weight Distribution Computer Analysis (MWDCA) which can derive chain scission and crosslinking rates from molecular mass distributions obtained from gel permeation chromatography (GPC) results [53].

Their recent research [53] on HDPE, LDPE, LLDPE, polypropylene homopolymer (PPHO) and polypropylene copolymer (PPCO) showed that as the oxidation progressed, the scission rate for HDPE, LLDPE, PPHO and PPCO increased near to the exposed surface whereas for LDPE the rate remained almost unchanged. The crosslinking rate fell near to the surface with HDPE and LDPE but increased with

PPHO and PPCO. Both scission and crosslinking reaction rates are low at a depth of 1.5mm or deeper from the surface due to the absence of oxygen that causes fast oxidation near the surface. The UV-degradation depth-profiles in polyethylene, polypropylene and an ethylene–propylene copolymer were also visualized [43]. Preceding these researches, the effects of stabilizers [54, 55], pigments [55] and tensile stress [56] on the chain scission and crosslinking reaction rates of PE and PP were investigated. For the effect of stabilizer, it was found that at the interior of the sample after prolonged exposure, the stabilized PP had a higher scission/crosslinking ratio than unstabilized PP [54], possibly due to different oxygen diffusion behaviour. Pigment (rutile TiO_2 made by the chloride process and provided with an alumina and organic coating) showed better stabilization behaviour than the stabilizer packages [55]. There was very little advantage to be gained by combining with both pigment and stabilizer package into the polymer. It was generally found that at high photo-oxidation reaction rates, chain scission was more likely to happen while lower reaction rates resulted in a higher relative crosslinking concentration [54, 55]. For the effect of tensile stress, PP samples exposed to UV while loaded in uniaxial tension (10 MN/m^2) showed markedly increased chain scission but little change in the crosslinking rate [56]. It should be noticed that most of their research is based on artificial weathering and some of the materials were free of stabilizers for the sake of highlighting the effect of photo-oxidation. Research carried out at a longer time span under natural weathering is needed for a more accurate prediction of practical application lifetime of polymers.

2.2.2.7 Chemical degradation of stressed polymers

It was just mentioned in section 2.2.2.6 that tensile stress affects the chain scission and crosslinking rate in the PP samples. In practice, a large number of polymer products are used in load-bearing environments like hydraulic pressure, compressive stress, tensile stress, torsional stress or even cyclic forms of them, etc. The failure behaviour and lifetime of products are affected because of the stresses that are suffered by the material. The relationship between applied stress and oxidation rate is still under discussion.

In 1970s to 1980s, the relationship between change of degradation rate and stress was studied quantitatively by Zhurkov and Bueche et al [57-60]. An Arrhenius-type expression was given in their research as follows:

$$r = A \exp\left(\frac{\Delta G - B\sigma}{RT}\right) \tag{2-15}$$

Where r is the rate of degradation; ΔG is energy barrier term; σ is applied stress; A and B are constants, A is a frequency factor and B has the dimension of volume; R is gas constant and T is absolute temperature. The term ($\Delta G - B\sigma$) is the apparent activation free energy. Compressive stress gives a positive value of stress and yields a lower absolute value of the apparent activation energy, therefore retarding oxidation reaction. Tensile stress gives a negative value therefore accelerating the reaction. Internal (residual stress) and external stress are both applicable to the equation. It is found that compressive residual stress formed at the surface of polycarbonate and polystyrene by rapid cooling improved the resistance to pollutant gas [61].

However, Popov et al in the 80s state that stress does not necessarily increase reactivity but may leave it unaffected or even inhibit it [62]. Scott [63] and Billingham et al [64] also stated their different views on the expression of relationships between applied stress and oxidation rate proposed by Zhurkov. Lemaire and his co-workers go even further and conclude that the chemical reactions during photo-chemical, thermal and hydrolytic aging do not depend on mechanical stress. Internal stress or external stress only modifies the physical consequences of the chemical reactions, not the kinetics [65]. All these disagreements suggest that the formula (2-15) is much more like an empirical formula rather than a fundamemtal one.

But, interestingly, the above findings are not valid in other research. Recently, the work of Jacobson et al showed that there is scattered relationship between the degradation rate and the applied stress [66], creating more discussion on this topic. In his experiment, the oxidation of stressed polymer samples (compression moulded PA6 strips, injection moulded PP, HDPE and PA6 Samples) was studied by in situ chemiluminescence with loads from 0% to 100% of load at yield. The stress induced

chemiluminescence results showed no obvious change in oxidation with load but fairly large data scattering, especially for PP samples [66].

The different conclusions result from different test methods, environments and are mostly based on different materials. Inter-laboratory test analyse is needed to normalized the test methods and summarize the results found by the researchers from different laboratories.

As stressed testing conditions are mentioned, it should be noted that stress and orientation are different concepts. Stress is a mechanical phenomenon and orientation is an alignment of the polymer chain in a preferred direction. Highly oriented polymers generally have improved degradation resistance because the preferred alignment of the polymer chain lowers the diffusion rate of oxygen, similar to the protective effect of compressive stress on pollutant gas. But in some situations, the diffusion rate of the antioxidant is also decreased due to the orientation. Therefore, whether orientation benefits or is detrimental depends on the exact mechanism of degradation and stabilisation in operation.

2.2.2.8 Other degradation reactions

Polymer degradation usually happens in air or oxygen environments. The same material in other environments such as water and aggressive chemicals may have different degradation mechanisms.

Hydrolysis attack can cause chain scission in some polymers such as polycarbonate. The hydrolysis will become fatally destructive to the material at elevated temperature. Disc-shaped defects will be formed and act as stress concentrating flaws causing serious material failure. Some polymers such as polyamides absorb water. The water can plasticize the material therefore decrease the modulus. PP and PE have strong resistance against hydrolysis and other aggressive chemicals and oxidation is the main degradative reaction within these two materials. With regard to PP and PE, other degradation reactions will not be discussed here.

2.2.3 Mechanical degradation

Breaking a polymer chain bond within the polymer matrix solely by stress is difficult. For a polymer chain bond to be broken, the segment in which it is contained must not be able to uncoil nor slip. Such constraints may be present in a crosslinked polymer, highly oriented polymer or at the tip of a growing crack. Mechanical degradation can be regarded as final degradation before the material is fractured. The molecular fracture can be observed by electron spin resonance because free radicals are produced when chain scission occurs. Fracture study is a subject of engineering and it will be reviewed in the later characterization sections.

2.3 Stabilization and stabilizers

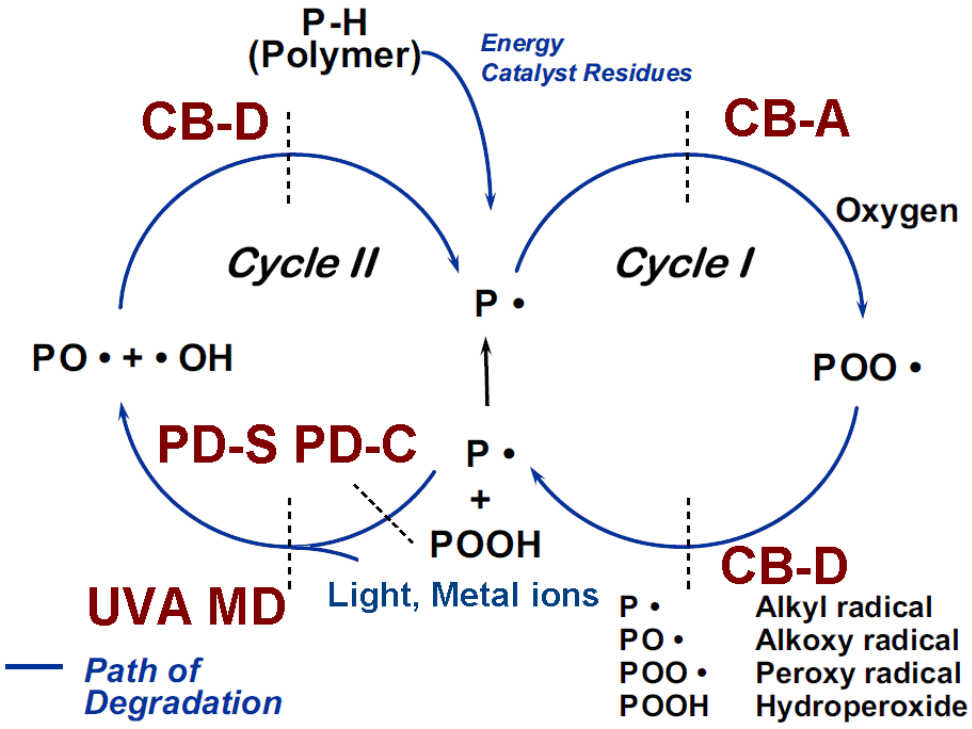

Figure 2-20 Mechanism of polymer stabilization

The research on degradation helps to find ways for material stabilization. Stabilization mechanisms are summarized for the auto-oxidation cycles in Figure 2-20. Measures include application of chain-breaking acceptors (CB-A), chain-breaking donors (CB-D), stoichiometric peroxide decomposers (PD-S), catalytic peroxide decomposers (PD-C), UV absorbers (UVA) and metal deactivators (MD) applied at each cycle

branch to retard the auto-oxidation procedures. The inclusion of the stabilizers can produce an enormous improvement in the life time of a polymer. Stabilizers have become essential additives in a commercial polymer even at the stage of polymerization. The following sections will have a review on thermal stabilization, photo stabilization and the relevant stabilizers.

2.3.1 Thermal stabilizers

Stabilizers are effective in temperature ranges from 0 ^{o}C to 300 ^{o}C as shown in the following figure. Phosphites, hydroxylamines and lactones are most effective thermal stabilizers during processing, either through mechanisms of free-radical scavenging or hydroperoxide decomposition. They are not as effective as long term thermal stabilizers but these stabilizers can also help with long-term thermal stability. By sacrificing themselves during melt processing, they lessen the consumption of the phenolic, which is a primary stabilizer, allowing more to remain effective for long-term thermal stabilization. The main thermal stabilizers and their behaviour will be introduced in the following sections.

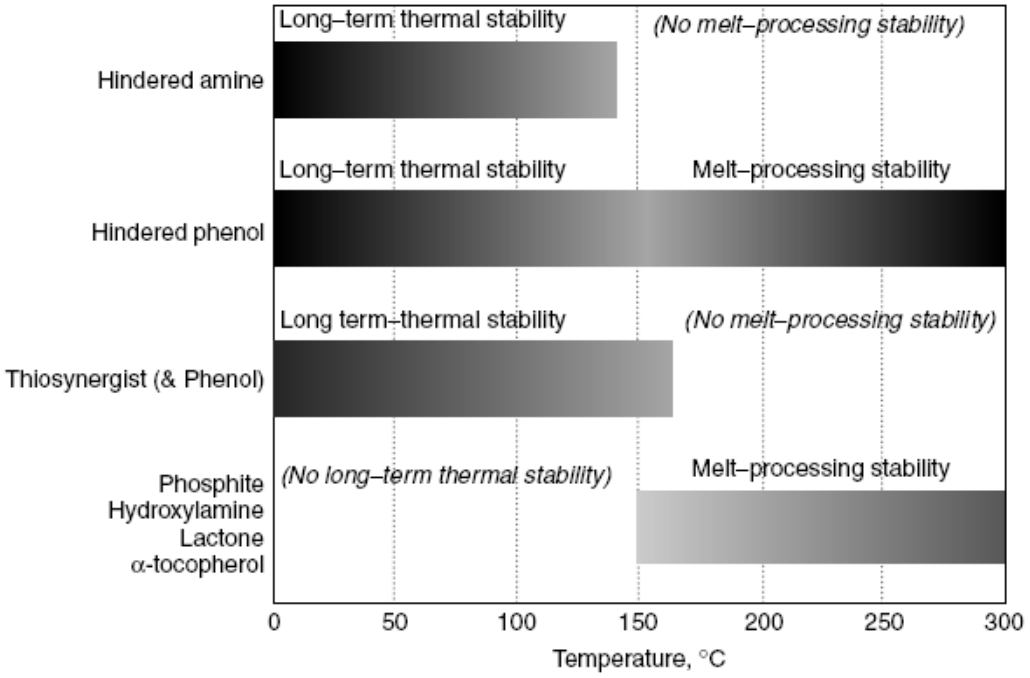

Figure 2-21 General representation of effective temperature ranges for common stabilizers [67]

2.3.1.1 Hindered Phenol

Generally, chain-breaking donor (CB-D) stabilizers form the basis of heat-stabilizing systems for polyolefins. The 'chain' mentioned here refers to kinetic chain of the propagation reaction of oxidation. The hindered phenols are widely used as hydrogen atom donating stabilizers. The general structure of hindered phenol stabilizers is shown in Figure 2-22.

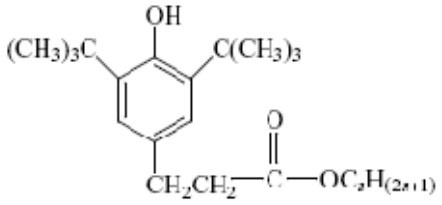

Figure 2-22 General structure of hindered phenol stabilizers

where n=18 gives the well known commercial stabilizer Irganox 1076.
The reaction of the hindered phenol and its competing reaction are as follows:

$$ROO\cdot + AH \xrightarrow{k_a} ROOH + A\cdot \qquad (2\text{-}16)$$

$$ROO\cdot + RH \xrightarrow{k_p} ROOH + R\cdot \qquad (2\text{-}17)$$

Where *AH* and *RH* represent a hindered phenol stabilizer molecule and polymer molecule relatively. Because the value of k_a is much larger than k_p, hydroperoxide free radicals react with hindered phenols more effectively than polymer chains.

Hydrogen atom donating stabilizers can be used at low concentration, usually 0.01-0.05% by weight. The steric hindrance decreases the ability of a phenoxyl radical to abstract a hydrogen atom from the polymer chain, therefore retarding the degradation procedure. Disadvantages of hindered phenol stabilizers are that they may form coupled products which will lead to discoloration, they can also react with titanium dioxide or carbon black and their stabilization effectiveness is reduced [68].

2.3.1.2 Trivalent Phosphorus Compound

The most important preventive mechanism is hydroperoxide decomposition (PD). Antioxidants acting on the Cycle II are preventive because they interfere with the generation of free radicals that feed back to Cycle I. There are two classes of peroxidolytic antioxidants: Stoichiometric peroxide decomposers (PD-S) and catalytic peroxide decomposers (PD-C).

Phosphite esters are typical PD-S stabilizers. The phosphite stabilizers are trivalent phosphorus compounds that can decompose hydroperoxides to alcohol (2-18), preventing hydroperoxide decomposing to free radicals following reactions (2-4), (2-5) and therefore stabilizing the system.

$$ROOH + PR'_3 \rightarrow ROH + O{=}PR'_3 \qquad (2\text{-}18)$$

Phosphites generally used are phosphite esters derived from hindered phenols, as shown in the following figure.

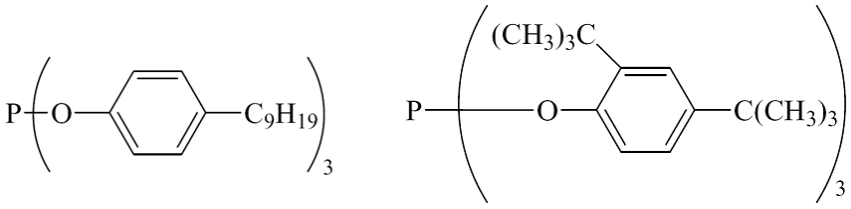

Figure 2-23 General phosphites stabilizers [67]

2.3.1.3 Divalent Sulfur Derivatives

A variety of sulphur compounds can act as PD-C stabilizers. For example, di-alkyl ester of thiodipropionic acid is capable of decomposing at least 20 mol of hydroperoxide into alcohol [69], as shown in reaction (2-19). The sulphide group is oxidized to protonic and Lewis acid by a series of reactions. The acid products are capable of catalyzing the decomposition of hydroperoxides to non-radical species.

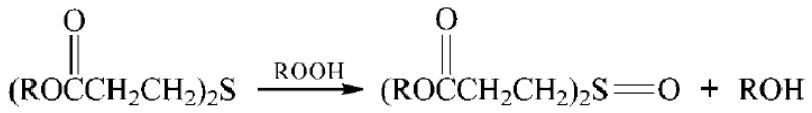

(2-19)

A thio-synergist in combination with a hindered phenol is highly effective in stabilization during the melt processing in extreme cases where peroxides have built up in the polymer. However this is not usual, so this type of melt-processing effect has been left out of Figure 2-21.

2.3.1.4 Hydroxylamines

Hydroxylamines are relatively new thermal stabilizers. They were first introduced as commercial stabilizers in 1996. They are more effective than conventional phenolic and phosphite thermal stabilizers because they can serve as both hydrogen-atom donor and free radical scavenger. Detailed chemical reactions are listed in reference [70].

2.3.2 Photo stabilisation and stabilizers

The mechanisms that can offer protection against photo-oxidation are classified as UV screening, UV absorption, excited state deactivation, free radical scavenging and hydroperoxide decomposition. Some of the protection mechanisms are similar to thermal stabilization methods such as free radical scavenging and hydroperoxide decomposition. The stabilizers based on these mechanisms are introduced in this section.

2.3.2.1 UV screening

Pigments and reflective coating can shield polymer surfaces against UV radiation. Such protection is called screening. Carbon black can be a very effective UV screening stabilizer with a very low level amount of application (0.05% by weight). It is also compatible with many outdoor grade stabilizers. But the compounds containing carbon black are themselves black, limiting the application of these products into mainly the construction industry. Other screening stabilizers are chemically inert pigments such as chalk, talc and short glass fibres. These stabilizers also change the appearance of the final product which is not welcome. It is worth noting that some pigments can also act as screening stabilizers, for example a coated rutile titanium dioxide (TiO_2) which was mentioned in section 2.2.2.6 shows a much better

stabilizing effect than phenolic stabilizers [55]. But this is not necessarily the case for other TiO_2 compounds with different crystal structure (anatase type or mixture of anatase and rutile type) without coating. A report has shown that in PP, these titanium dioxides are photo-catalytic to chemical reaction and produce CO_2 and CO which can form micro voids of size ~1000nm and weaken the material. [71]

2.3.2.2 UV absorption

This stabilization requires stabilizers to absorb all the UV wave length range (<400nm), and to dissipate the absorbed energy without damaging the polymer. In order not to affect the appearance of the product, they are also required to be totally transparent to visible light. There are several chemical compounds that meet these requirements. The most commonly used are 2-hydroxybenzophenones (I), the 2-hydroxyphenylbenzotriazoles (II), the 2-hydroxyphenyl-sym-triazines (III) and derivatives of phenyl salicylates (IV) [72], which are shown in Figure 2-24.

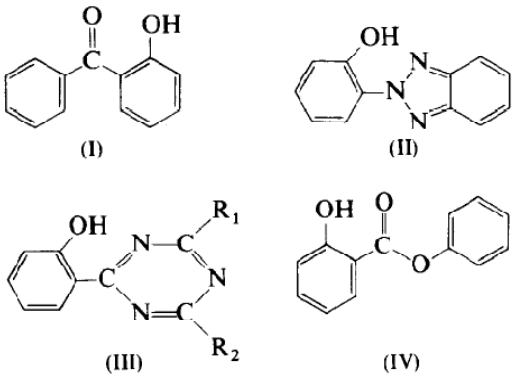

Figure 2-24 Structure of common UV absorbers [72]

The general mechanism of these stabilizers is by absorbing radiation energy to activate the stabilizer and form a hydrogen bonded ring system. Allen and his co-workers have given detailed photo-stabilization mechanisms of these stabilizers.

2.3.2.3 Excited state deactivation

Stabilizers acting through this mechanism do not require absorbance in the wavelength range covering the UV spectrum. The stabilizers, for example, transition metal chelates, deactivate excited groups (e.g. active ketone groups) from a high

energy state to lower ones and transfer energy to the stabilizer to achieve a quenching effect. A typical chelate is shown in Figure 2-25. By uniformly distributing these stabilizers, the effective amount of them can be no more than 0.1% by weight. But it is believed that photo-decomposition of peroxide and hydroperoxide happens instantaneously upon absorption of UV photon rather than being deactivated. Therefore, the deactivation of these groups is less important than that of carbonyl groups [72].

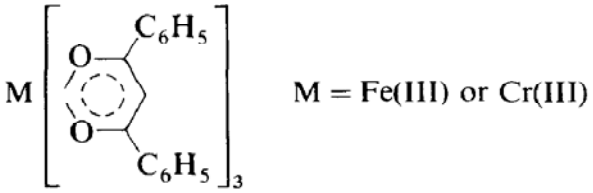

Figure 2-25 Example of reactive quencher [72]

2.3.2.4 Radical scavengers

It is common that radical scavengers act as both thermal stabilizers and photo stabilizers, because radicals are key factors in both thermal-oxidation and photo-oxidation cycles. According to their different scavenging mechanisms, the radical scavengers can be divided into two groups, chain breaking donor (CB-D) and chain breaking acceptor (CB-A) which is identical to the types mentioned previously in thermal stabilizer section.

For the chain breaking donor, a hydrogen atom of the stabilizer is donated to an alkylperoxyl radical to form a hydroperoxide. The donor itself becomes a less reactive free radical, therefore retarding the oxidation chain reaction. The less reactive products react to produce further products that may still have pro-oxidant or antioxidant activity. Hindered phenol is a common CB-D and it has been reviewed in section 2.3.1.1. Aromatic amines (Figure 2-26) are used in rubber and elastomers. Due to the intense staining effect of their oxidised products, they are not widely used in plastics [67].

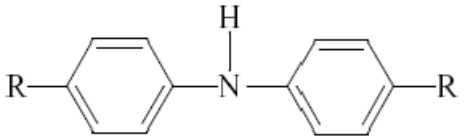

Figure 2-26 Alkylated diphenolamine [67]

In the chain breaking acceptor mechanism, alkyl radicals (P•) are the target. By stabilizing alkyl radicals which are the first radicals produced in the auto-oxidation cycles, the polymer decomposition can be prevented. Compounds with free radicals that are relatively stable, do not initiate reactions with the undamaged polymer chain and react with alkyl radicals can be used as CB-A. Generally, these compounds include nitroxyls, phenoxyls and quinones. The CB-A mechanism of quinone is shown in Figure 2-27.

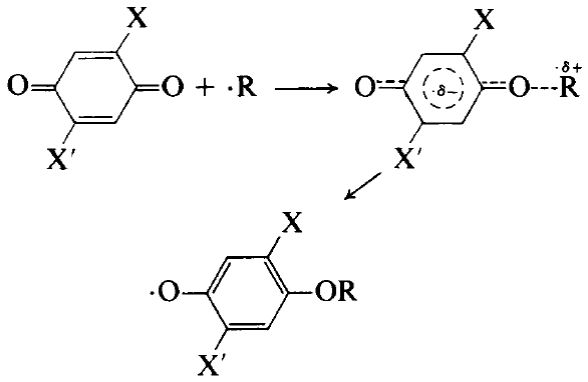

Figure 2-27 Schematic of Chain breaking mechanism of quinone [72]

It should be note that CB-D stabilizers are most efficient in an excess oxygen environment whereas CB-A stabilizers function best in oxygen deficient enviroment. Molecules which can provide both characteristics are much more efficient in different environments [72].

2.3.2.5 Hindered Amine Light Stabilizers (HALS)

Hindered amines are discovered in the late 1960s. They are extremely effective light stabilizers in polyolefins. Most of the commercial hindered amines are derivatives of 2, 2, 6, 6-tetramethylpyperidine, as shown in Figure 2-28 left.

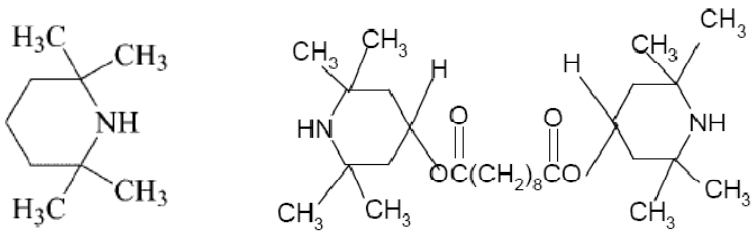

Figure 2-28 General structure of a HALS stabilizer (left) and Tinuvin 770 (right) [67]

The exact stabilization mechanism of HALS is still under discussion and a review is available in [73]. However, a general process which is known as Denisov cycle is proposed to explain the high efficiency and longevity of HALS and a simplified cycle is shown in Figure 2-29. The primary stabilizing mechanism of HALS involves reaction of nitroxyl radicals with polymer alkyl radicals to give alkoxyl hindered amine derivatives which react with alkyl peroxy radicals to regenerate nitroxyls.

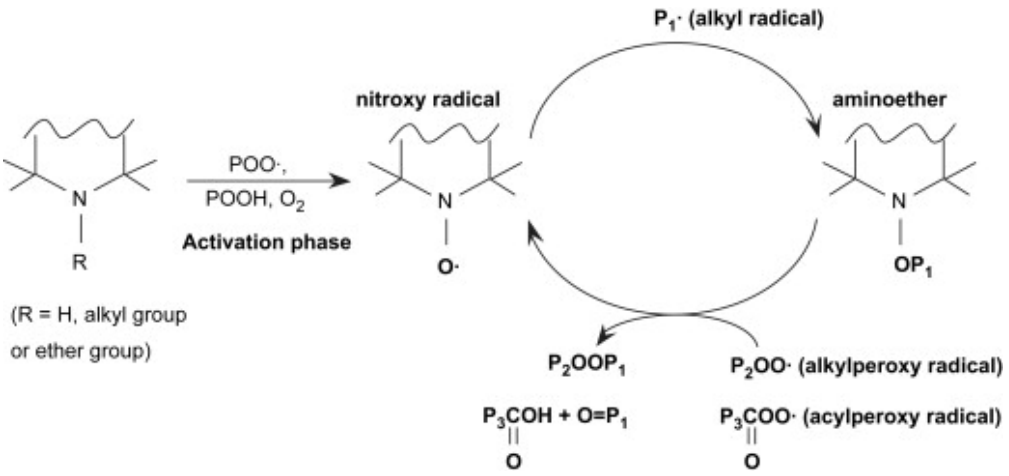

Figure 2-29 Simplified action mechanism of HALS antioxidants [74]

From these reactions it can be found that O_2, alkyl radicals and hydroperoxide radicals are all incorporated in the stabilization reactions where, nitroxyl radicals are regenerated. These characteristics endow the HALS high effectiveness and longevity in photo-stabilisation. There are other possible reaction pathways presented by Klemchuk and Kurumada et al [75, 76], but these will not be detailed here.

HALS can also inhibit the catalytic action of metal impurities within the plastic by forming complexes with them. Kurumada [76] proposed that the HALS form complexes with transition metal ions such as titanium from the polymerisation

catalyst residues, to prevent the formation of metal ion-hydroperoxide complexes which will initiate auto-oxidation.

The excellent efficiency of HALS will be significantly reduced in the presence of protonic acids such as H_2SO_4, HNO_3 and HCl, because they react with HALS to form salts which offer no stabilisation effect. HALS offers little protection against thermal oxidation [77]. Low molecular weight HALS will be lost during processing by volatilisation.

2.3.3 Combinations of stabilizers

In order to prevent polymer degradation in different environments, different stabilizers are combined together. For example, phosphites and divalent sulphur compounds are used for thermal stabilisation during processing. In the same material, hindered phenols are incorporated as long term stabilizers, and HALS are also used as photo stabilizers. The most common combination of stabilizers used for polyolefins are blends of a phenolic antioxidant and a phosphite melt-processing stabilizer. Another common combination is a blend of a phenolic antioxidant and a thioester, especially for applications that require long term thermal stability.

Experiments showed that a mixture of stabilizers that function by different mechanisms might be synergistic and provide a higher degree of protection than the sum of the stabilizing activities of each component. On the other hand, mixtures of stabilizers can also work against each other, i.e. are antagonistic. These interactions are also significantly influenced by the concentration of additives [78] as well as the polymer types and manufacturing history [79].

2.3.3.1 Synergistic combinations

Synergistic combinations are achieved through different ways. For example, one stabilizer helps to regenerate the other to reduce the consumption of the latter. Hindered phenols are often used in combination with phosphites. This combination results in improvement in the resistance to degradation during processing. The role of phosphites is believed to be primarily to react with hydroperoxides which are formed

by reaction of the hindered phenols with peroxy radicals, reducing them to alcohols. Regeneration of the hindered phenol is believed to occur during these reactions [80]. Synergism can also be attributed to the protection that each stabilizer gives in different environments. For example, a divalent sulphur compound acting as a hydroperoxide decomposer to protect a UV absorber against thermal degradation during processing. In turn, the UV absorber protects the divalent sulphur compound from photolytic destruction by quenching during photo oxidation [81].

2.3.3.2 Antagonistic combinations

Antagonistic combinations alone are less likely to happen in comparison with synergistic combinations. The mechanisms of antagonistic reactions are also different. For example, when a phenolic antioxidant and a divalent sulphur compound is used for thermal stabilisation and a hindered amine is incorporated for photo stabilisation, the oxidation product of the divalent sulphur compound can be quite acidic and can complex the hindered amine as a salt, preventing the hindered amine from entering into its free-radical scavenging cycle, as mentioned in section 2.3.2.5.

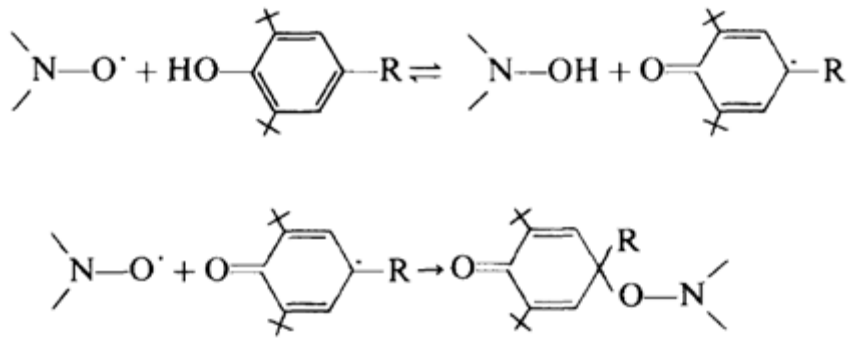

Figure 2-30 Antagonist reaction between hindered phenol and HALS [82]

The phenolic antioxidant will inhibit the activity of the hindered amine through several mechanisms proposed by Allen et al [82]. The first is associated with acid-basic properties of the two types of additives. The second is associated with inhibition of hydroperoxide formation by the phenolic antioxidant thus preventing the oxidation of the parent amine to nitroxyl radical as indicated in Figure 2-29. The third is that oxidation of the phenolic antioxidant to an active quinone by the nitroxyl radical and the active quinone can react again with the nitroxyl radical to form a stable product as

shown in Figure 2-30, which would effectively remove active nitroxyl radicals from the cyclic mechanism of hindered amine stabilization.

2.3.3.3 Inter-tranform of synergistic and antagonistic reactions

In some situations, synergistic and antagonistic reactions both exist in a polymer system. Sometimes they even inter-transform to each other by slightly changing the system. From example, the peroxide decomposing stabilizers and chain breaking donors have a synergistic effect during the thermal oxidation of LDPE. Antagonistic reactions are found when the oxidation products of phenolic stabilizer prevent the decomposition activity of the peroxide decomposing stabilizers [83]. Another example is that synergistic effects have been observed in both oven-aging and UV exposure of Ziegler-Natta type PE. But under the same conditions, antagonism was found when a Philips type PE was tested [78]. In other cases, some observations are even difficult to explain. Gugumus reported that a mixture of low molecular weight HALS and high molecular weight HALS gave a strong synergism in some PP when subject to UV exposure in film form. But in other situation, he found that a combination of low and high molecular weight HALS is not always beneficial [84]. More examples were given in which low molecular weight HALS performed best but others showed high molecular weight HALS gave the best results. It is also found that synergistic and antagonistic reactions can occur between stabilizers and pigments in thermal and photochemical degradation [85].

2.4 Techniques for aging study

Because of the wide range of factors relating to polymer aging, techniques used for aging study are also cover a large range of methods. Generally, these techniques can be divided into three groups according to their test purpose: weathering methods, characterization methods and lifetime prediction methods. Some of these techniques are most frequently used for simple polymer stabilization analysis in the industry such as quality control, screening of stabilizer systems, etc. More specialised techniques are used for scientific research such as characterizing various aging behaviours within the polymer, investigating the mechanisms of the stabilization of a specific stabilizer

system and predicting the lifetime of a specific product etc. The general methods will be discussed with relation to PE, PP and PE pressure pipe in the following sections.

2.4.1 Weathering methods

Weathering provides aged samples for characterisation and lifetime prediction. Because the lifetime of stabilized polymer covers a long time span (normally several decades) in natural aging, weathering factors are usually amplified to shorten aging time and highlight the aging effects. According to different weathering time and aging conditions, there are two main weathering methods: natural weathering and accelerated weathering.

2.4.1.1 Natural weathering

Natural weathering is a method to weather samples in extreme climates. The 'natural' does not refer to the actual service conditions of products but a more severe environment that can shorten the aging time to an acceptable range and also preserve the natural conditions. Weathering under actual service conditions are not applicable because a long lifetime (50 years) for the PE pressure pipes is usually demanded.

The test sites for natural weathering are all located in hot climate areas with high UV levels. Arizona is popular for studies using a hot dry climate and Florida for a hot damp climate. There are many reports in which the natural weathering was conducted in other parts of the world such as South France, Australia, Israel and Saudi Arabia.

Normally in the natural weathering test, samples are mounted on an open frame without any shade from trees or buildings. Frames are placed facing south and the angle of exposure is often recommended in standards as 45^{o} to the horizontal. There are several standards published by British Standards Institution (BSI) and International Standard Organisation (ISO), giving details of natural weathering tests [86-88]. The results from natural weathering can be related to degradation under actual service environment to predict the products lifetime. Research has been carried out based on natural weathering and some of the results showed good agreement with

the actual results [89]. Further accelerations can be achieved by using mirrors to concentrate the solar radiation on test samples, arranging the exposure frame to track the sun, or tilting the sample from the horizontal by an angle equal to the latitude of the location.

It is generally believed that solar radiation (mostly due to the ultra violet light portion) is mainly responsible for the degradation of polymers as mentioned in previous sections concerned with about photo-oxidation [90]. But, the aging factors such as the solar radiation, temperature and humidity in natural aging are not constant and they vary according to latitude, season, time of day, cloud coverage etc. Therefore, samples of the same polymer batch will most likely have different degrees of photo-oxidation if they are studied at different latitudes or during different seasons. Research had shown that PE samples degraded faster in the summer months due to more intense solar radiation, shorter wavelengths of light penetrating the atmosphere and a higher temperature compared with other seasons [91]. Furthermore, Satoto and his co-workers found that for white coloured HDPE materials, the main factor affecting degradation is the ambient temperature of the polymer sample being studied [92]. They concluded that variation of carbonyl group growth was apparently correlated with variation of temperature, but not directly with variation of solar radiation dose at sample sites of different latitudes [92]. This implies that the solar radiation induces the photo-degradation process, but after the formation of hydroperoxide species, the temperature actually controls further degradation. This is because firstly, temperature controls the diffusion of oxygen and stabilizer onto the polymer surface, which affects the incorporation of oxygen and efficiency of the stabilizers in photo-oxidation propagation. Secondly, radical transformation rate depends on temperature, affecting the production of effective oxidation radicals. And thirdly, temperature affects mobility of polymer chain at the surface which further affects on degradation behaviour. But this does not necessarily mean that temperature is the only factor affecting degradation, further correlation between radiation and degradation needs closer investigation [27].

2.4.1.2 Artificial weathering

In order to shorten the aging time, accelerated tests are designed for weathering. These tests simulate the weathering factors in natural aging using devices available in the laboratories. By comparison to natural aging, the accelerated tests are also known as artificial weathering.

One way of accelerating the deterioration is to use a high intensity of UV irradiation [67]. But care must be taken in choosing the intensity level because high level intensity will largely increase the sample temperature and some reactions take place at higher temperatures which will not occur during natural aging, producing large deviation to the experimental results. Another way of providing acceleration is to maintain illumination at the chosen peak level for 24 hour each day instead of simulating day and night [67]. This method is probably the most acceptable method of acceleration. But the limitation of this acceleration method is that it may change the distribution of oxygen, stabilizers and other reactants within the polymer compared with natural aging, because diffusion of stabilizers will continue in dark periods in natural aging, and replenish the surface that are main sites for oxidation degradation, but depletion of stabilizers on the surface will occur in this accelerated method [93].

There are two types of radiation source can be used in accelerated tests, one is a Xenon arc and the other is a fluorescent tube. Both of them are commercially available. A Xenotest 1200 weathering chamber uses a xenon lamp as light source, offers water spray and humidity control and it is widely accepted by the industry at present known as a weather-o-meter. A Xenon light source has its limitations in that it emits a high intensity of infrared radiation. Application of a filter can overcome this drawback. The QUV weathering chamber produced by Q-panel Co. uses fluorescent tubes as the UV light source and does not produce unwanted radiation, especially, type UVA-340 provides radiation very close to solar radiation. However, it has been shown that simply matching the UV spectrum of the artificial source to the solar spectrum is not enough to obtain a good correlation with outdoor performance [68, 94].

In artificial weathering, attention should also be paid to applied oxygen pressure and pollutant. The rate of the oxidation process involved in weathering is sensitive to the partial pressure of oxygen at the gas-solid surface [93], and some acceleration of it can be achieved by increasing the partial pressure of oxygen within the conditioning chamber above ambient. The influence of oxygen pressure and temperature on oxygen uptake in artificial and outdoor weathering has been studied by Gijsman and Sampers [95, 96]. Their research indicated that the increase was enhanced only at higher temperatures of 40–50ºC. They concluded that the degradation chemistry in an accelerated weathering test by increasing oxygen pressure differed from the natural outdoor degradation chemistry and the artificial weathering method did not simulate outdoor weathering very well.

The introduction of pollutants is difficult in an accelerated weathering chamber because the level of knowledge is not adequate. But pollutants in natural weathering may have large effects on polymer degradation. Indirectly, for example, pollutants can lower the concentration of ozone in the upper atmosphere, affecting the intensity of the radiation to which the samples are exposed. Directly, for example, sulphur dioxide, oxides of nitrogen and carbon can be active in photo-oxidation accelerating degradation occurs in polymer. There is research on LDPE film which screened the sample from exposure to rain and wind, whilst allowing all other weathering factors to influence the sample. It showed that the sheltered sample have lifetimes much longer than those that are measured in direct weathering [97].

2.4.1.3 Correlations between the effects of natural and artificial weathering

Artificial weathering is useful to illustrate some similar trends to natural weathering as mentioned in reference [33]. However, it is generally agreed that there are few correlations between natural weathering and artificial weathering, and this view is even expressed in some Standards [98]. This means that results from these two weathering methods are not comparable. Some results from accelerated testing and natural weathering even showed contradictory information on polyolefins [102]. Gugumus discussed examples showing good and bad correlations and suggested that a good correlation may result from a restricted amount of data or from data generated with closely related compositions or stabilization systems, because the factors in

natural aging are much greater than those in accelerated weathering. It was also suggested by Tidjani [33] that to minimize errors in the prediction of polymer life service, natural aging is necessary even if it is time consuming.

2.4.2 Surface characterization

It is well documented that much of polymer degradation is limited to several micrometers from the surface [44]. Therefore, surface characterization techniques are crucial in aging studies. General surface characterization techniques will be discussed as follows.

2.4.2.1 Contact angle measurement

The shape of a liquid bead on a flat solid surface is determined by the surface free energy of gas, liquid and solid. A contact angle is defined to quantify the shape of the liquid in such a case. The contact angle is the angle made by the intersection of the liquid/solid interface and the liquid/air interface as shown in Figure 2-31. Normally, the surface tension of gas is small (except the case of vapour adsorption) and can be neglected and gives $\gamma_{LG}=\gamma_L$ and $\gamma_{SG}=\gamma_S$.

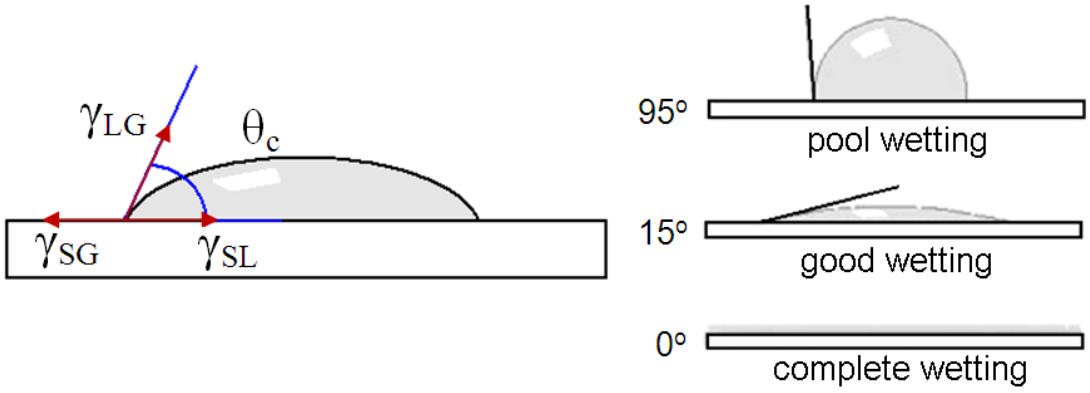

Figure 2-31 Contact angle and wettability of a surface (γ_{SG}, γ_{LG} and γ_{SL} are surface tension of solid, liquid and solid-liquid interface respectively)

Analysis of the surface tensions as shown by the red arrows in Figure 2-31 gives the Young's equation:

$$\gamma_S = \gamma_{SL} + \gamma_L \cos(\theta)$$

The term γ_L and contact angle θ are readily measurable. In order to obtain the surface tension of the solid (γ_S), another equation in the form of γ_S=f (γ_{SL}) is needed. Such relations of γ_S, γ_{SL} can be acquired empirically by building up an equation of state using extensive contact angle data. At present, various theories of the relationship γ_{SL}= g(γ_S, γ_L) are available, but have different application ranges on different solid surfaces. The Owens, Wendt, Rabel and Kaelble theory (OWRK theory) [99, 100] is widely used for polymer surfaces. Their theory suggested that the surface tension of each phase can be divided into a dispersive and a polar component. The dispersive component (γ^d) is due to the London dispersion forces between the molecules while the polar component (γ^p) is due to the rest of the intermolecular forces which originate from polar interactions between molecules. It is also assumed that the simple sum of these fractions is the surface tension ($\gamma = \gamma^d + \gamma^p$). The relationship γ_{SL}= g(γ_S, γ_L) in this theory is as the follows:

$$\gamma_{SL} = \gamma_S + \gamma_L - 2(\sqrt{\gamma_S^d \gamma_L^d} + \sqrt{\gamma_S^p \gamma_L^p})$$

Substituting this equation into the Young's equation and transposing gives an equation in the form of y = mx + b as follows:

$$\frac{(1 + cos\theta)\gamma_L}{2\sqrt{\gamma_L^d}} = \sqrt{\gamma_S^p}\sqrt{\frac{\gamma_L^p}{\gamma_L^d}} + \sqrt{\gamma_S^d}$$

$$\underbrace{\quad}_{y} \quad = \quad \underbrace{\quad\quad}_{m\ x} \quad + \quad \underbrace{\quad}_{b}$$

As shown on Figure 2-32, by using different reference liquids of known γ_L^d and γ_L^p, various x and y values can obtained and a linear regression curve can be drawn. The values γ_S^p and γ_S^d are the square of the slope m and the coordinate intercept b.

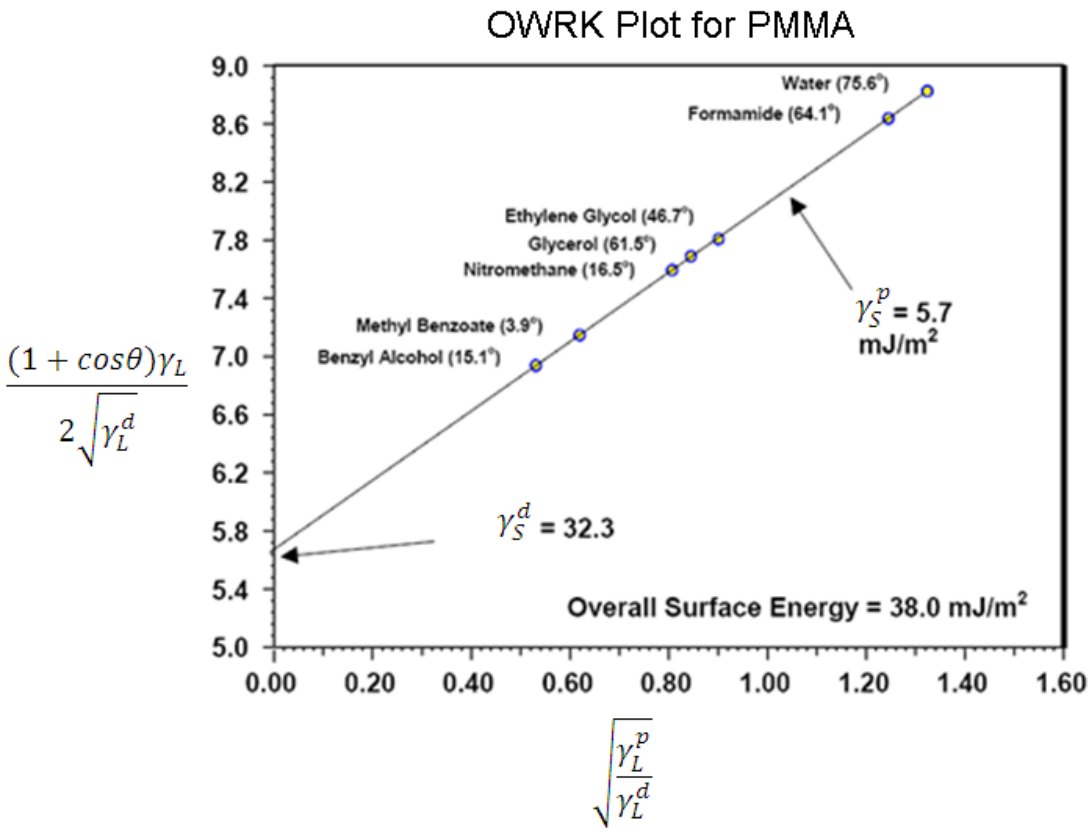

Figure 2-32 Owens/Wendt Plot for PMMA [101]

2.4.2.2 Scanning Electron Microscopy (SEM)

SEM is a type of electron microscope that creates various images by focusing a high energy beam of electrons onto the surface of a sample and detecting signals from the interaction of the incident electrons with the sample surface. The interaction of incident electrons and sample surface produces secondary electrons, X-rays and background scattering electrons. Secondary electrons that are emitted from the electron shells of the sample surface atoms after impingement of incident electrons contain information about the material surface topography and they are monitored to form the image. X-rays are emitted when an inner shell electron is ejected after impingement, containing information about elemental composition. The X-ray signals are detected by an energy dispersive spectroscopy device (EDS) which is linked to the SEM. Background scattering electrons also indicate the elemental composition on the surface. Combining background scattering electrons with X-ray information can give atomic number contrast information of the elemental composition of the sample.

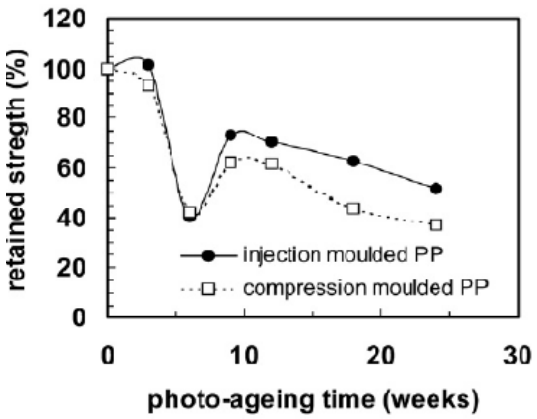

Figure 2-33 Retained strength versus photo-aging time showing recovery behavior [18]

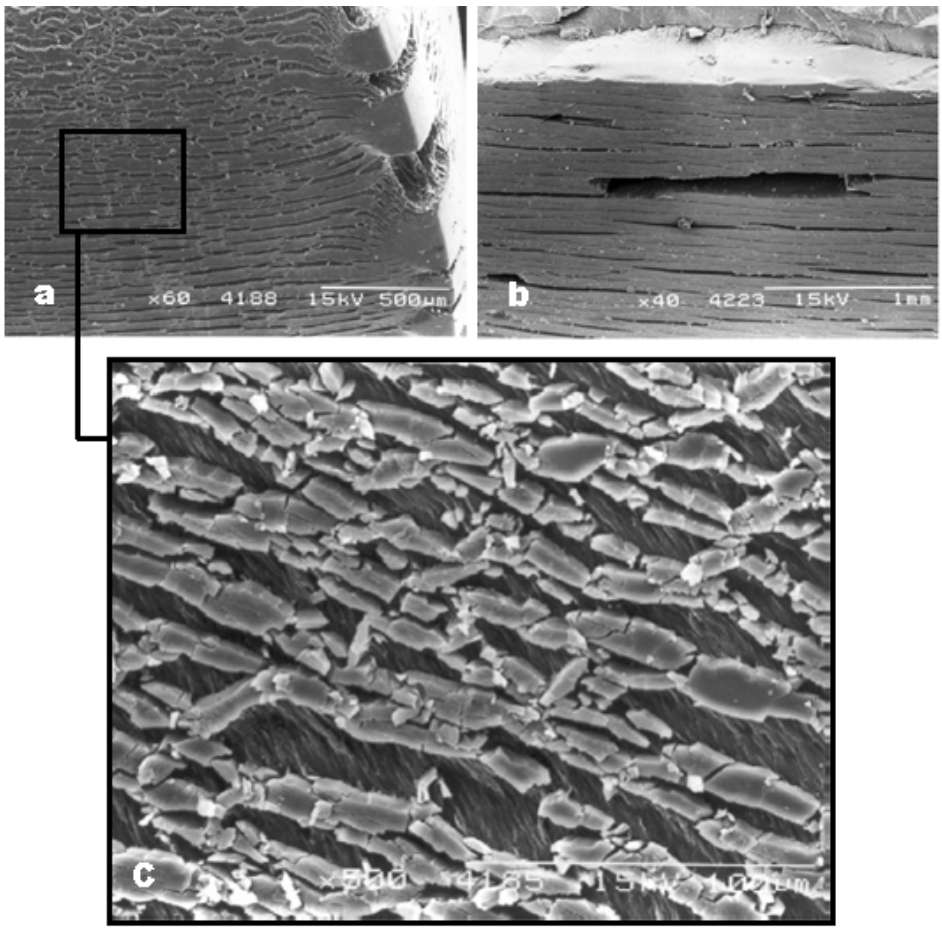

Figure 2-34 Brittle layer on moulded PP surface a) c) 4 weeks aging, b) 12 weeks aging [18]

SEM is widely used to observe the aging destruction of samples to illuminate the effects of aging [103]. For example, White [18] used SEM to investigate the moulded surface of a PP bar after photo-aging. From comparison of the tensile strength with different aging times, they observed recovery of mechanical strength with increasing aging time, as shown on Figure 2-33. After SEM analysis on the aged sample surface,

it was proposed that the recovery of strength was due to the loss of a brittle layer as shown on Figure 2-34. The sharp decrease of strength at short aging times is because the brittle layer and the interior undegraded material still retain integrity, as shown on Figure 2-34 a) and c). Cracks formed in the brittle layer can transmit stresses to the ductile interior undegraded material and grow within it followed by rapid fracture. As aging time increases, the thickness of the brittle layer increases as well. The degraded layer is so fragile that it became poorly adhered to the material in the interior and fell off, as shown on Figure 2-34 b). Cracks can no longer transmit to the interior so the strength is retained.

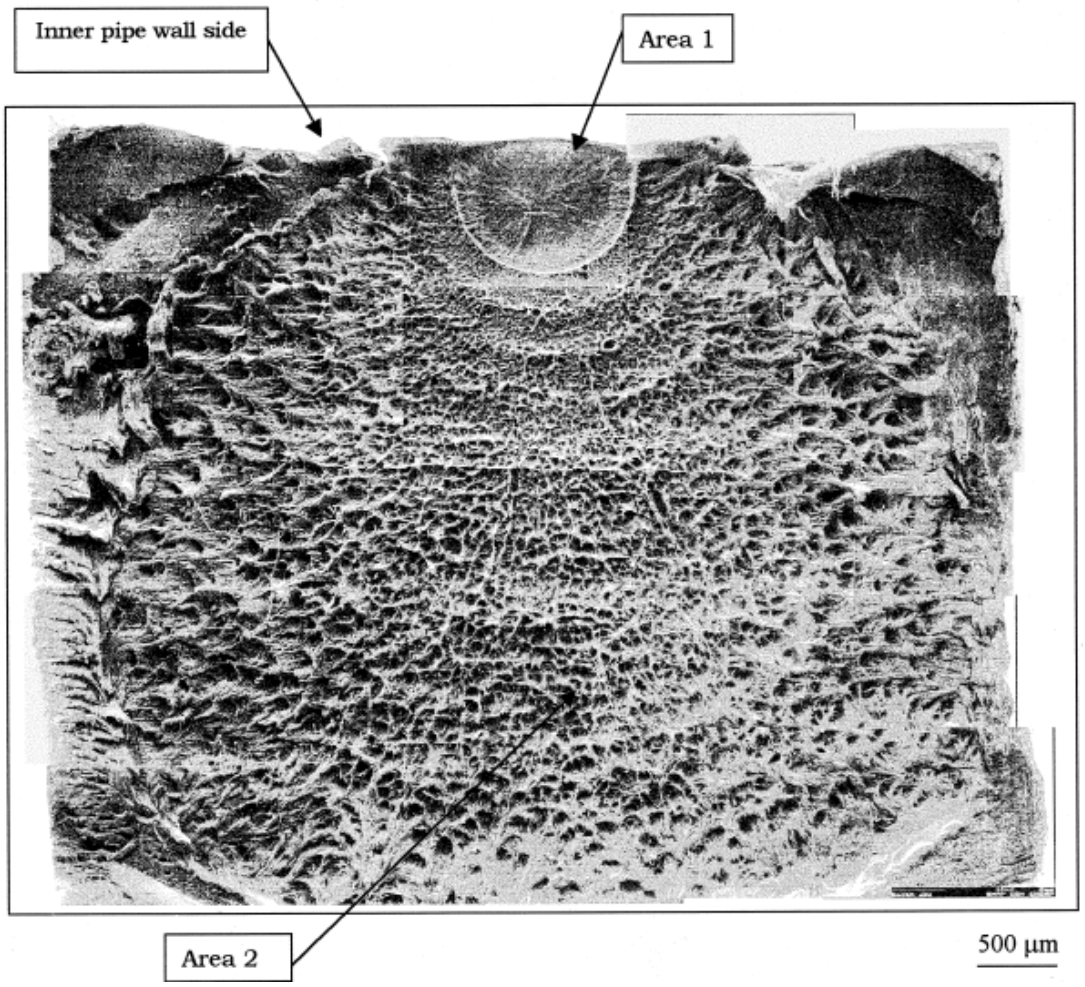

Figure 2-35 Brittle fracture surface: gas pipe creep failure (9.6 bar) at 80°C [104]

SEM was also used to investigate failure of PE pressure pipe. Hamouda used SEM to investigate the failure of PE gas pipe and explained the reasons of failure in service [104]. It was found that the brittle failure of slow crack growth (SCG) was initiated at the inner pipe wall as indicated in Figure 2-35. The fracture surface can be divided

into two areas, mirror zone (Area 1) and discontinuous bands (Area 2). The mirror zone contains the initiating source of failure. Surrounding the mirror zone is propagation of the initial crack with an increasing roughness showing discontinuous bands.

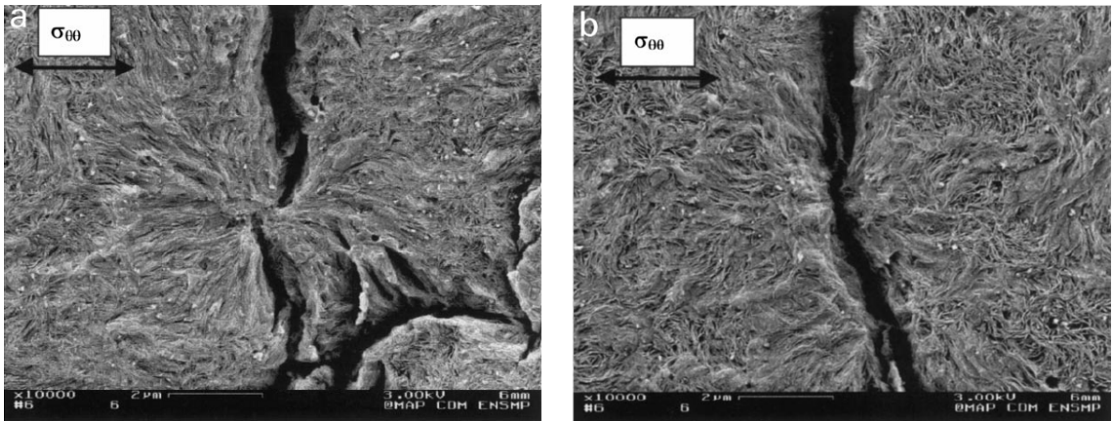

Figure 2-36 Inter-lamellar propagation of creep micro-cracks in a transverse cross-section of a pipe [104]

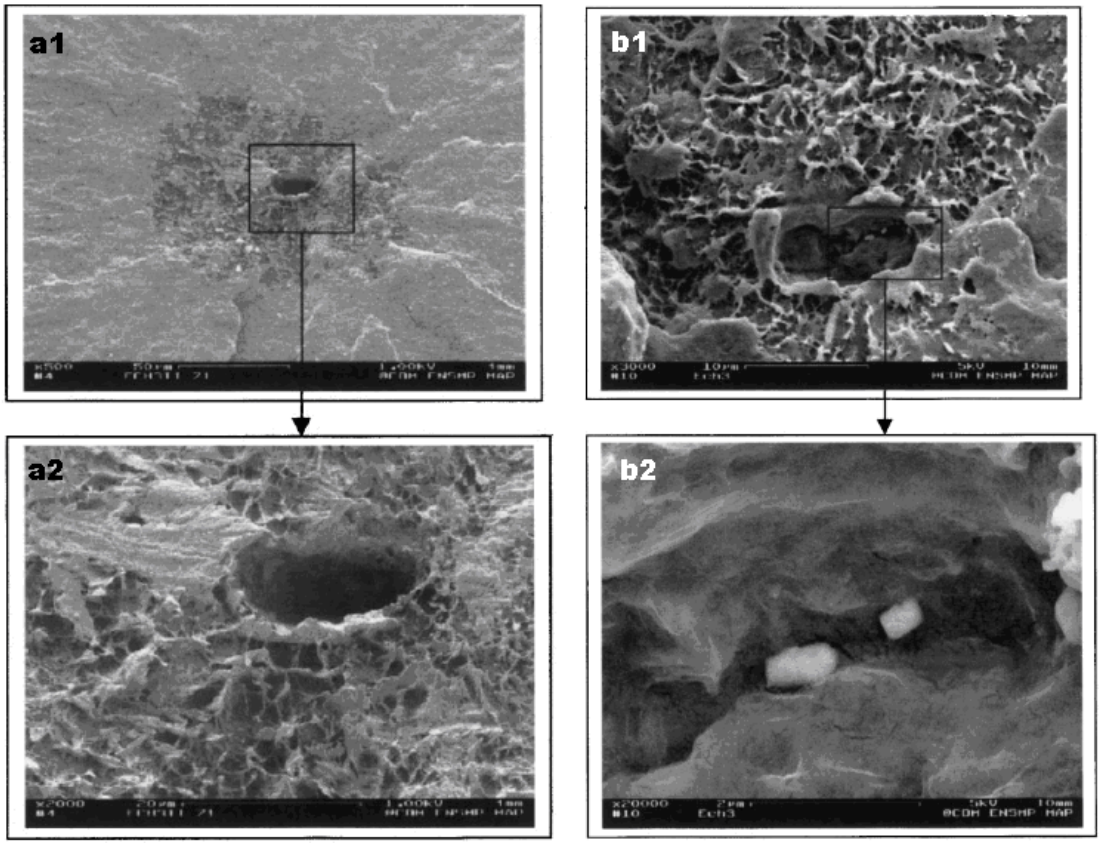

Figure 2-37 a1) and a2) central fibrillated zone and around cavity; b1) and b2) catalytic residue particles inside the creep cavity [104]

By focusing on to these two areas, it was found that creep damage is inter-lamellar and the disentanglement of tie molecules through the spherulites produces the mirror like fracture surface (Area 1), as shown in Figure 2-36. Soon after Area 1, cracks propagate by discontinuous bands and create a fibrillated fracture surface (Area 2), causing catastrophic destruction. Catalytic residues were identified by EDS, situated in a central fibrillated zone cavity within the mirror zone and believed to be the initiating factors of the creep damage (shown in Figure 2-37). From the SEM results, it was suggested that micro-cracks initiate in the zone where a catalytic residue is embedded in the spherulites and then propagate until they reach the spherulites centre point where they can be deviated. When many spherulites are creep damaged, cracks may coalesce [104].

2.4.2.3 Fourier-Transformed Infra-Red (FTIR) Spectroscopy

Attenuated total reflectance mode FTIR (ATR-FTIR) can be used to characterize the surface chemical composition by Infra-Red radiation absorption spectra of the sample surface. It is a fast method and the sample is easy to prepare. General ATR-FTIR techniques can detect absorption of chemical groups and bonds within a depth of several micrometres from the surface.

A recently developed method takes advantage of the variations of the IR absorption at different depths to measure the oxidation profile of the surface [105]. The different depth of IR absorption is achieved by varying the angle of incidence of IR light. Detection of the variations in composition of distinct layers from the surface can be down to a depth of 1.2 micrometres. Absorption value at a certain depth is calculated through mathematical manipulation. Deeper layers were reached by microtoming the samples. Samples from PE cable aged in an accelerated weathering chamber were tested and the results are shown in Figure 2-38. The WOM is a weathering chamber equipped with a xenon lamp and QUV is another with a fluorescent bulb as described previously (sections 2.4.1.2). From the results, it can be seen that severe oxidation is limited to 2-6 micrometre deep from the surface for WOM weathered samples. Micro-domain analysis is made possible by using an ATR microprobe based on a silver halide fibre of circular cross-section with an outer diameter of 700 micrometres [103].

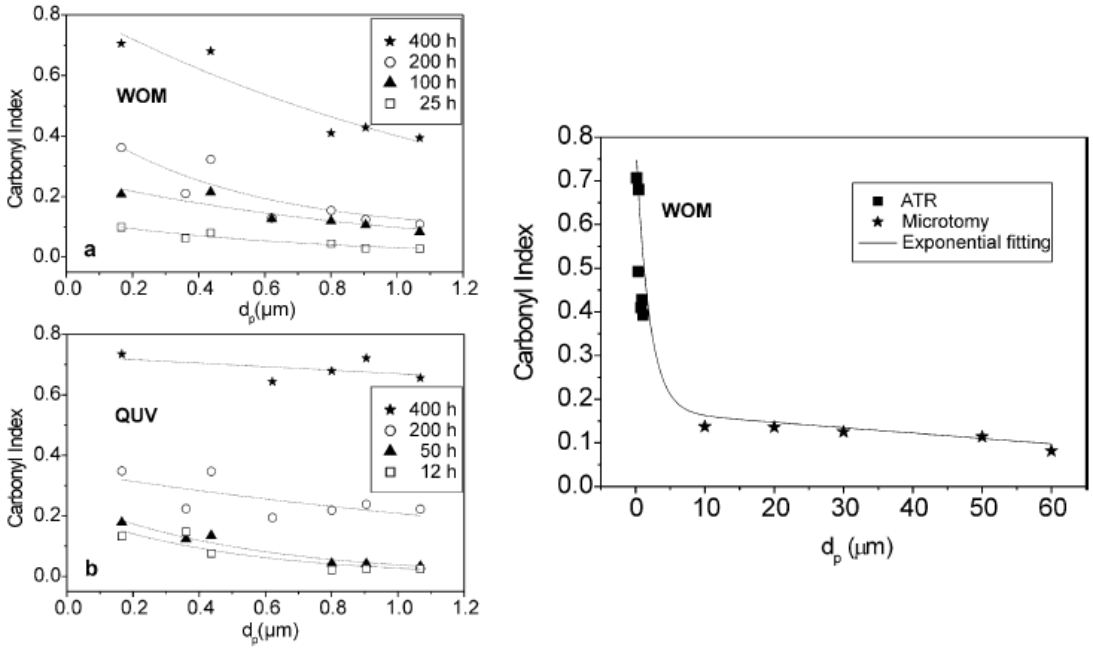

Figure 2-38 Oxidation profiles of PE cable with different depth [105]

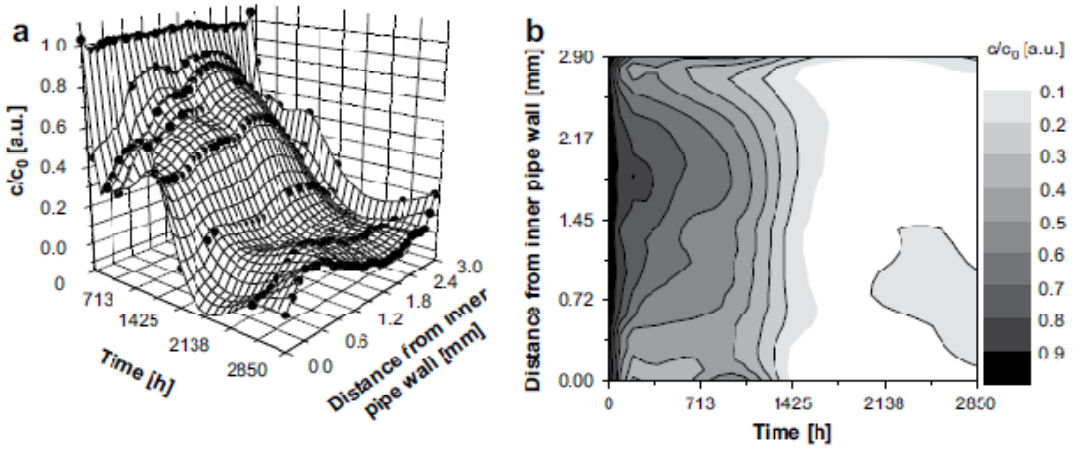

Figure 2-39 a) Relief and b) colour coded contour plot for the radial distribution of Irganox 1010 [106]

By using microtoming, an IR microscope and transmittance mode FTIR, the depth profile of antioxidant (Irganox 1010) content was also determined and visualised in recent research on stabilizer diffusion in PP pressure pipe as a function of aging time [106]. The result from the IR microscopy is in line with those from high performance liquid chromatography (HPLC) and oxidation induction time (OIT) on the same sample batch. FTIR is an informative characterization technique and its application in polymer degradation research is too numerous to mention one by one here.

2.4.2.4 Other surface characterization techniques

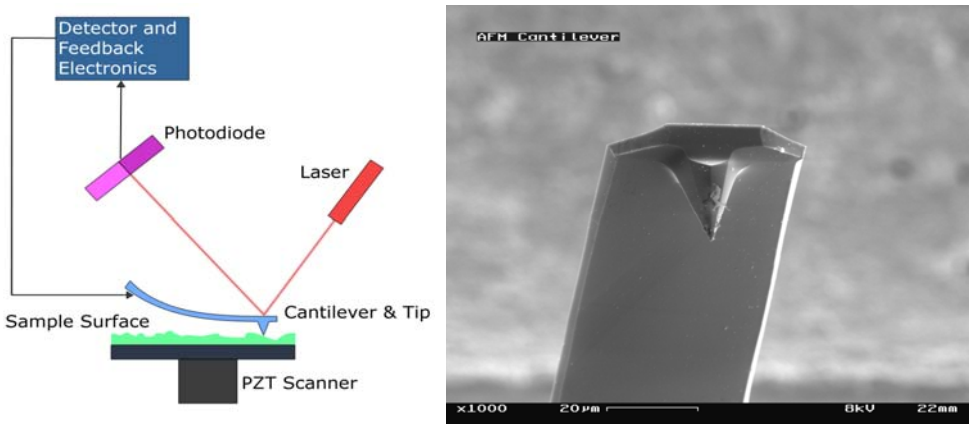

Figure 2-40 Schematic of AFM and SEM image of scanning cantilever and tip

AFM is a very high resolution scanning probe microscope. It uses a micro-scale cantilever as a probe to scan height of the sample surface to form a true three dimensional surface profile, as shown in Figure 2-40. The precise scanning movement is controlled by a piezoelectronic tube (PZT) on which the sample is mounted. Compared to SEM, AFM has a higher resolution, and samples viewed by AFM need no special treatments (such as metal coating) that would irreversibly change or damage the sample surface. It can work in ambient air or even a liquid environment while SEM needs to perform at ultra high vacuum. But there are also some disadvantages of AFM. The depth of field and scanning area are smaller for AFM than SEM. The scanning time for AFM takes several minutes while SEM can do a real time image to observe the change of sample surface in nano-scale. The scanning probe is limited by its shape and cantilever and may give an erroneous image of very sharp or very steep surfaces.

X-ray photoelectron spectroscopy (XPS) is a quantitative spectroscopic technique that measures the elemental composition, empirical formula, chemical state and electronic state of elements that exist within a material. XPS spectra are obtained by irradiating the material surface with X-rays and detecting the escaped electrons activated by the X-ray radiation (photoelectron) as shown on Figure 2-41. The binding energy of the photoelectron can be measured and it can be used to identify the element that exits on or in the material surface. The number of electrons can also be measured and indicate the amount correlated binding energy. XPS can measure the surface element

composition with a depth of 10-12 nm. Although X-rays can penetrate 1-5 micrometre of the sample surface, the electrons which escape below 10-12 nm depth cannot detected by the analyzer because they are recaptured or trapped in various excited states within the material. Small amount of elements can also be measured by XPS. The ultimate detection limit for most elements is approximately 100 ppm. XPS takes a longer time than ATR-FTIR, SEM and AFM. For trace elements, the test may be run overnight. The measurable area for XPS is larger than SEM and AFM and can be as large as 30x30 cm. For polymers, X-ray radiation is destructive and causes degradation.

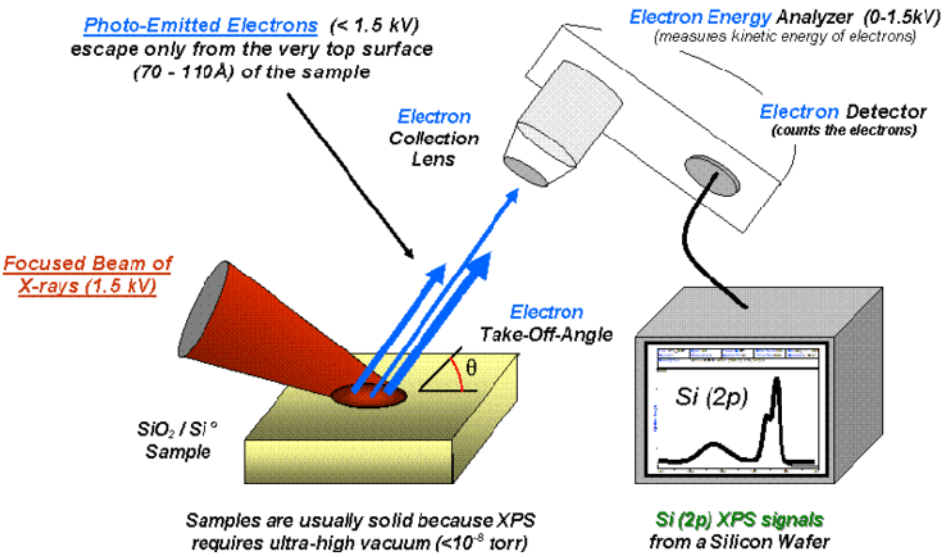

Figure 2-41 Schematic of XPS imaging mechanism

2.4.3 Thermal analysis techniques

Thermal analysis (TA) techniques are most frequently used to characterize the thermal properties of polymer during aging because thermal and photo-oxidation generally alter the thermal properties of the material. The most commonly thermal analysis device applied to polymer aging is differential scanning calorimetry (DSC). DSC can be used to measure various thermal properties as well as to perform thermal assessments on the samples. The following section describes these techniques with examples.

2.4.3.1 Differential Scanning Calorimetry (DSC)

DSC is now a very popular thermal analysis technique, because it can be used to investigate several important phase transition temperatures and the enthalpy changes involved in these phase transition procedures such as glass-rubbery state transition, crystallization and melting. Further analysis of the enthalpy can give more meaningful results, for example, melting enthalpy of a crystalline polymer can be used to calculate crystallinity. The mechanism of DSC is measuring the enthalpy difference between sample and the reference as a function of temperature. There are two modes of measuring: a) during the measurement, the temperatures of the sample and the reference are kept the same; b) temperature difference is measured and converted to heat flow (this method is used in the experimental in this project). A typical DSC trace is plotted as heat flow difference against temperature.

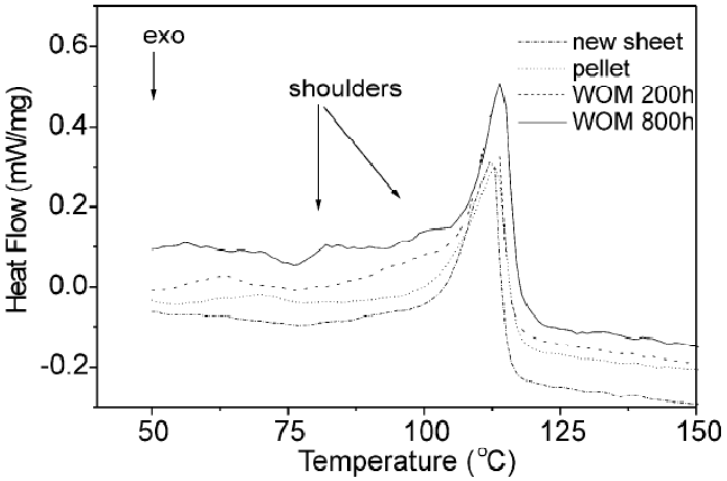

Figure 2-42 DSC traces for virgin and weathered PE [105]

DSC can be used to measure many important properties in polymers. A series of standards have been published to normalize DSC measurements [108-110]. DSC can be used to investigate several aspects during or after polymer aging.

For example, it can be used to identify the change of overall crystalline phase in the sample. It was found that an MDPE plaque aged in 105°C pressurized water can lead to increase of melting temperature and narrowing of the melting peak [111]. Similar trends were found from another study [105] in which accelerated weathering methods are applied producing DSC traces as shown in Figure 2-42.

Another example of DSC application is the evaluation of polymer degradation. Oxidation induction time (OIT) test is developed based on DSC for this purpose. The OIT test is easy to perform and it is widely accepted as indicator of quality of stabilized polymer in industry. The standards also normalized the OIT test, for example, in part 6 of reference [108]. It is also indicated that OIT values can also used to determine activation energy of decomposition [128] and predict life time [112]. Whether these approaches are applicable to PE and PP still need further investigation. The detailed procedure of OIT test will be introduced in the experimental part.

There are some limitations of OIT test. Firstly it is a destructive test, secondly there is a hysteretic response of oxidation due to heat conduction, and thirdly the result has poor repeatability and reproducibility if the OIT value is less than 30 minutes [113]. These limitations are not critical to the assessment of materials therefore DSC is still widely accepted in the industry. But in scientific research, new techniques are developed to meet specific demands. For example, oxidation onset temperature (OOT) test which is still based on DSC has been suggested [113] as an alternative to overcome the poor repeatability and reproducibility with a low OIT value, and it was found that this method of evaluation is also suitable to replace an OIT test on samples with long OIT value to save testing time. A chemiluminescence test was also developed to measure OIT and overcame disadvantages such as the hysteresis effect and poor repeatability and reproducibility, but it is too lengthy to be expanded here.

2.4.4 Mechanical test methods on pipes

In practice, mechanical properties are the most important properties that are concerned. Therefore, mechanical tests are carried out to evaluate the effect of degradation on the ultimate material properties in service. The principle of a mechanical test is simulating the loading or impact situation and monitoring the procedure during loading and the consequences after loading. There are various specialized mechanical tests for materials in specific applications. This section will discuss the mechanical tests that are used for PE pressure pipes.

2.4.4.1 Long term hydrostatic strength test

A long term hydrostatic strength test (LTHS, also known as creep rupture test and internal pressure test) is the traditional way to determine the long term performance of PE pressure pipes. This test was performed as early 1956 when the first generation of HDPE pipes was about to be introduced to the market and it is still being used to predict service lifetime of plastic pipes. Standards giving general details of the test are described in ISO 9080:2003 [10]. The tests are carried out on pipes under internal pressure to take into account the effect of the multi-axial strain (hoop, radial and pipe axial) occurring in practice. The pipes are filled with water and suspended in a temperature-controlled water bath. When a leakage happens through the pipe wall, the pressure and failure time is recorded. Hoop stresses are plotted against failure time on a log-log graph to obtain a regression line.

It is known that ductile failure and brittle failure may happen on pipes depending on applied pressure and temperature. A typical creep and rupture curve is shown in Figure 2-43.

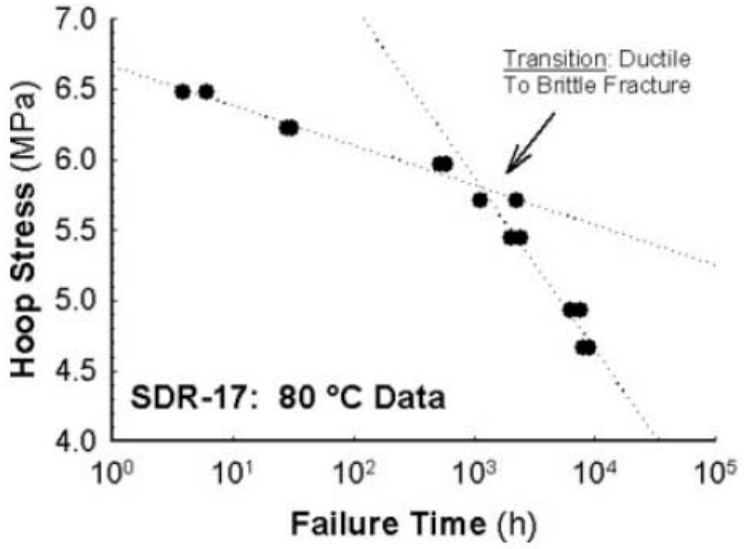

Figure 2-43 Typical creep rupture test curve [114]

In industry, prediction of failure of more than 50 years is required. Extrapolation methods are applied for the prediction. A standard extrapolation method (SEM) is adopted in ISO 9080:2003 and is widely used in plastic pipe industry. The strength of prediction after 50 years at 20 ^{o}C is used to classify pipe material, and is known as

minimum required strength (MRS). LTHS is normally time consuming and expensive. A more economic alternative approach based on a shorter-term test (named 'ramp test' in the study) has been described for the evaluation of creep rupture resistance of PE water pipe [115]. It was proposed that the ductile-brittle transition hoop stress obtained from the approach is compatible with those obtained from LTHS and can be used with LTHS ductile failure results to predict the lifetime of the pipe. However, this economic approach has not been widely accepted by the industry.

2.4.4.2 Fully notched creep test (FNCT)

The FNCT can be described as a constant load tensile test, measuring the failure time of notched specimens at elevated temperature in an active environment as shown in Figure 2-44. ISO 16770: 2004 described the details of FNCT. FNCT is used to characterise the environmental stress cracking (ESC) resistance of the material. Whether the material is ductile or brittle can be classified by this method [104].

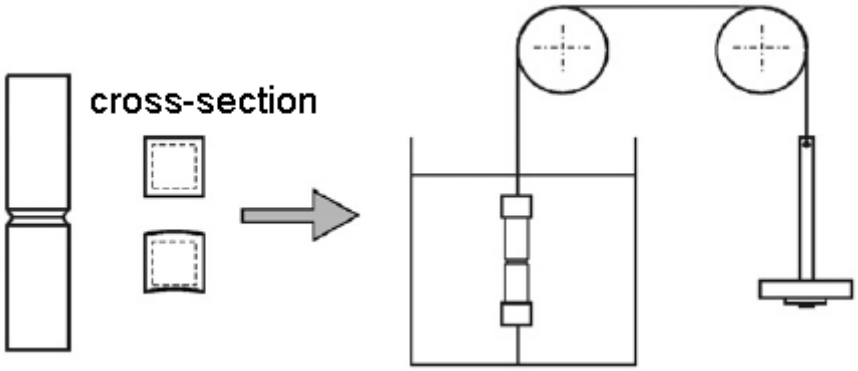

Figure 2-44 Schematic of FNCT [116]

An amended version of FNCT is used to evaluate the long-term performance of PE [116], as shown on Figure 2-45. A notched round bar specimen is used instead of a notched cubic specimen. Cyclic load is applied instead of a static load. Fatigue crack growth behaviour (FCG) is characterised in this method. FCG experiments were performed on five commercially available PE pipe materials and the results were comparable with the FNCT results. The same ranking of materials was found with both methods [116], but it was obvious that FCG experiments were faster by up to two orders of magnitude, especially suitable for characterizing modern bimodal type PE which has a better slow crack resistance and requires longer testing time.

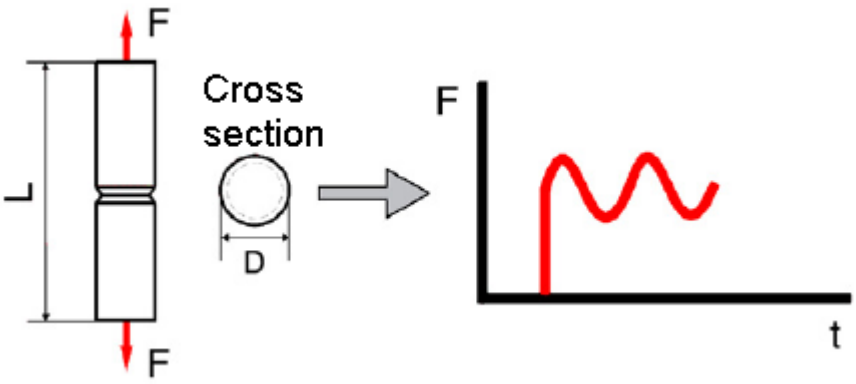

Figure 2-45 Schematic of FCG test [116]

2.4.4.3 Other mechanical test methods on pipes

Other mechanical testing methods applied on PE pipes include tensile testing, falling weight impact testing and peel testing. Tensile bars can be machined from the pipe along the extrusion direction. Falling weight impact testing can be performed on notched or un-notched pipe rings. Peel testing can be performed on electro-fusion joints to assess the joint integrity. These tests are all used to quantify the properties of the raw materials or final products. Some of them will be introduce later in the Experimental Section.

2.4.5 Other characterization techniques

There are other characterization techniques that are useful to characterize the change during and after aging, such as hardness testing, gloss and color assessment, density measurement, gel permeation chromatography (GPC), gas chromatography-mass spectroscopy (GC-MS), electron spinning resonance (ESR) and nuclear magnetic resonance (NMR).

Hardness, gloss and color are other indicators of surface oxidation and they can be use to compare the degree of oxidation. But these assessments are less widely used in aging study of PE.

Density gradient columns can measure density with excellent accuracy. Samples can be cut along thickness and be tested in the column to get density profiles. Crystallinity

can be calculated from the density results and crystallinity changes during aging can be obtained at different depths.

GPC is a widely used technique for molecular weight distribution (MWD) measurement. The principle of GPC is separating molecule of different sizes in flowing solution by size exclusion phenomenon in porous filler in the column. A recent photo-aging study [27] shown that MWD of PP changed at different depths after UV radiation (Figure 2-46). Compared with the raw material, the MWD of PP shifted to the left with another lower and broader peak when samples were taken closer to the outer surface. This was because there are more degraded short chain molecules present and the average molecule weight was reduced at the outer surface. As the degree of degradation becomes higher at the outer layer, fewer long chain molecules remain. A highly degraded material with depth of 0.1mm showed a narrow distribution of low molecular weight material.

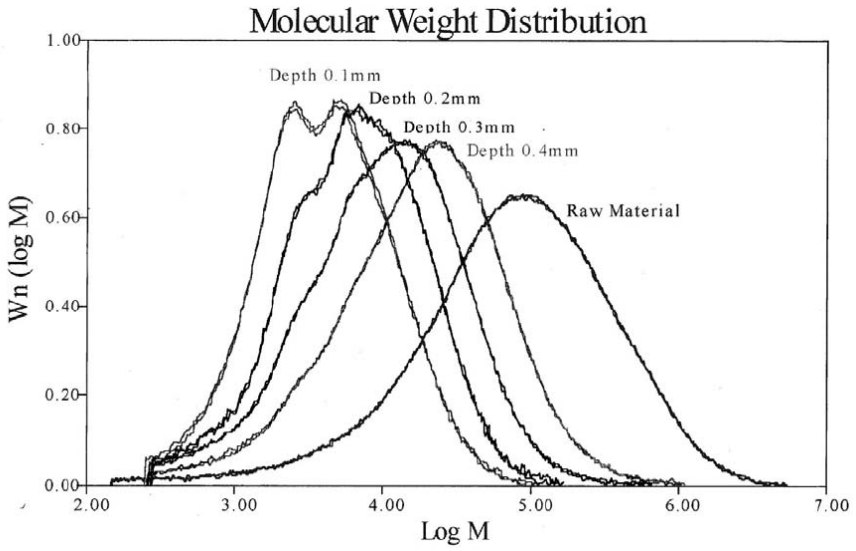

Figure 2-46 Different MW distributions at various depths of aged PP [27]

Gas chromatography – mass spectroscopy (GC-MS) can be used to detect the amount of residual antioxidant in the polymer. These techniques can also be applied to evaluate consumption of antioxidants and used as a mean of degradation assessment. Various degradation degree assessments such as OIT, carbonyl index, concentration change of hydroperoxides were compared and evaluated in a recent study [117] but it was based on ABS rather than PE or PP.

Conventional nuclear magnetic resonance (NMR) spectroscopy is less frequently used in the industry because of the cost. NMR can be used in scientific research for purposes such as identification of degradation products and investigation of reaction mechanism. In an NMR study on PE pipe [118], ^{1}H NMR imaging techniques were used to image the extrusion aid (EA) at the cross section of PE pipe material. It was found that there was migration of EA to the pipe wall surface within degraded pipe samples. Recently, a mobile NMR device has become available for non-destructive analysis of plastic pipe properties such as deformation and change of morphology [119]. But this technique is not widely used yet.

Electron spin resonance (ESR) is a similar technique to NMR, except that in ESR free electrons rather than nuclei are observed as in NMR. Therefore, only free radicals can be detected by ESR. Because thermal and photo-oxidation and their stabilization process involve various free radicals, ESR is an essential technique to investigate the specific degradation of stabilization reactions. Recently, some new applications were developed on ESR. For example, polymer morphology can be investigated by monitoring free radicals know as “spin probe” that was used to dope in the material. Nitroxide radicals derived from oxidized HALS can be used as a “spin probe” and can be doped in the polymers such as PE and PP. The signals detected from the “probe” by ESR can give an indication to the morphology of the amorphous phase of the materials [120].

Chapter 3 EXPERIMENTAL

3.1 Sample preparation

3.1.1 Material Specifications

The core pipe material supplied by Borealis is a free flowing bimodal grade PE designed for pipe extrusion and meets the PE100 requirements according to ISO 12162 (1995) [121] . The virgin material is thermally and UV stabilized for processing and outdoor weathering without pigments, and the specifications are listed in Table 3-1.

Table 3-1 Specifications of the core pipe material [122]

Property	Test method	Unit	Limits	Aim
Melt Flow Rate(190^{o}C, 5.0kg)	ISO 1133	g/10 min	0.24-0.36	0.3
Compound density	ISO 1872/2, ISO 1183	kg/m^3	947-955	951
Moisture content	BTM 14571 [1)]	ppm	max 300	-
Oxidation induction time	EN 728 [2)]	minutes	min 15	-

1) Karl Fischer titration

2) Aluminum pan, O2, 210 Deg C (BTM 14352 used by Borealis, conforms to EN 728)

Both the skin and brown stripes are pigmented isotactic PP, compounded with nucleating agent, adhesion reducer and other additives by Radius-systems [5].

3.1.2 Extrusion of pipes

The main procedure for pipe sample extrusion is identical to standard PE pipe extrusion (Figure 2-2) and was introduced in section 2.1.3. This section will introduce the specific extrusion procedure in this project.

All pipe samples are produced with the same core PE pipe dimensions. The standard dimension ratio (SDR) of the core pipe is 11 and Outside diameter (OD) is 110mm. The standard dimension ratio is defined in equation (3-1).

$$SDR = \frac{AverageOD}{MinimumThickness} \quad (3\text{-}1)$$

Pipes without skin and with 0.4, 0.8 and 1.5 mm skin were extruded using the bimodal PE100 rated PE. Another set of standard blue pigmented PE100 water pipes (without skin) were produced for comparison with the skin pipes. The dimensions of these five types of pipes are listed below:

Table 3-2 Target dimensions of the pipes

	BPP	NSPF	0.4SPF	0.8SPF	1.5SPF[1)]
SDR	11	11	11	11	11
Thickness/mm	10	10	10	10	10
Skin Thickness /mm	0	0	0.4	0.8	1.5

1) Full names: BPP (Blue Plain Pipe); NSPF (No Skin ProFuse); 0.4SPF (0.4mm Skin ProFuse); 0.8SPF (0.8mm Skin ProFuse); 1.5SPF (1.5mm Skin ProFuse).

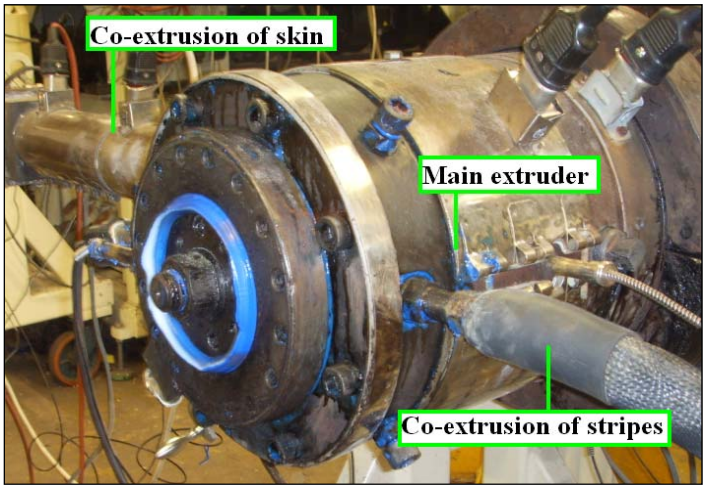

Figure 3-1 Extruder head showing co-extrusion of blue skin and brown stripes

The PE core pipe was extruded through a single screw main extruder made by Krauss-Maffei Ltd as shown in Figure 3-1. The blue PP skin and four evenly distributed PP stripes were co-extruded on the PE core pipe in the same extruder head supplied by two other separate singe screw extruders. The blue color and brown stripes on the pipe indicate that it is for drinking water distribution and it is a multilayer pipe respectively. The temperature set for extrusion of core pipe in the main extruder barrel was 200±5 °C. For PP skin and stripes, the temperature was 230±5 °C. The general pipe diameter and thickness were determined by the main extruder die. The minor change of pipe thickness was controlled by the extruder output rate and haul-off speed.

When the pipe thickness was stabilized in an acceptable error range, the skin extruder output rate was adjusted to produce the desired skin thickness.

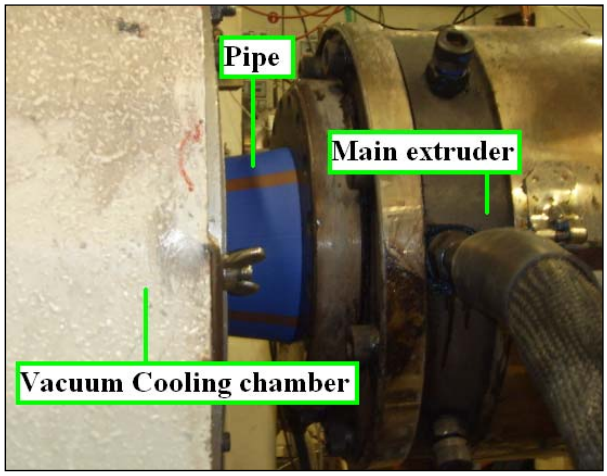

Figure 3-2 pipe extrudate exiting extruder die and entering vacuum cooling chamber

As shown in Figure 3-2, after exiting the main extruder head, the pipe extrudate was pulled through vacuum water cooling chambers with a sizing socket at the entrance (Figure 2-6) where the outer diameter of the pipe was gradually solidified to the final desired pipe diameter. The vacuum value applied was between -0.15 to -0.35 bar. After the outer pipe was solidified, cooling water continued to spray on the pipe without vacuum until the pipe was fully cooled down across the thickness. The layout of water sprays are shown in Figure 3-3.

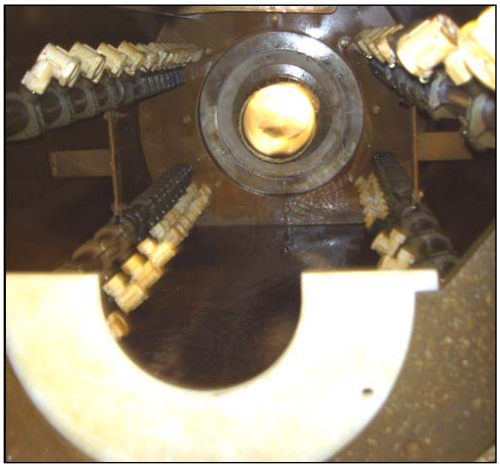

Figure 3-3 Layouts of water spray heads in the cooling chamber

The pipe was pulled through several cooling chambers by the haul off unit, printed with batch numbers and then cut into 1 meter then 1.2 meter long sections by

rotational blades. The pipe sections were packed as shown in Figure 3-4 and then stored in a cool and shaded area.

Figure 3-4 Pipes packed for storage

3.2 Weathering

The outdoor weathering was carried out by Atlas Material Testing Ltd. The weathering site is situated in an unpolluted desert, approximately 50 km to the north of Phoenix city center, Arizona in the US. The desert environment provides a high level of natural radiation, temperature and low humidity without pollutants that could directly or indirectly lead to unknown reactions as mentioned in [97]. Specifications of the environment are listed in the Table 3-3.

Table 3-3 Specifications of weathering environment

Latitude	Longitude	Elevation	Annual Average Temp	Annual Average Relative Humidity	Annual Total Rain	Annual Total Radiant Exposure
33°29' North	112°08' West	610 m	22 °C	37%	255 mm	8004 MJ/m^2

The radiation energy was recorded by the testing company. The radiation dosages applied were 1 GJ/m^2, 3 GJ/m^2 and 10 GJ/m^2. The time for radiation of 1GJ/m^2 is roughly 30-40 days in the summer. The whole natural weathering experiment lasted for more than one year.

10 x 1.2 m pipe sections of the same pipe type, totally 5 batches of each pipe type, began to be weathered at the same time under the 3 radiation dosages. The skin pipes were weathered with skin on.

All the samples were mounted on racks parallel to the ground without rotation. When the pipe is manufactured, the top of the pipe is called the top-dead-centre (TDC). On three of the samples from the 10, the TDC faced the sun. On another three, the TDC was 120 degree from the direction of the sun. For the last four samples from the 10, the TDC will be 240 degree from the direction of the sun.

3.3 Characterizations

In this section, the characterization methods applied in this project are divided into physical and chemical assessments to be introduced.

3.3.1 Physical Characterization

3.3.1.1 Density measurement

A Davenport density measuring apparatus DMA 718/175 as shown in Figure 3-6 left was used for the density measurement following standard BS 2782 Part 6: Method 620D [123].

25 ± 2 mm wide pipe rings were cut off from the middle of each pipe perpendicular to the pipe axis as shown in Figure 3-5. Then, a 10mm wide, dice shaped piece randomly selected around the ring was cut off along the pipe axial direction from the ring using a band saw. The dice was marked with lines with gaps of 1mm parallel to the pipe outer surface. 1± 0.3mm thick films were slowly sliced along the marked line from the outside to inside surface with a scalpel. The edge of each film was trimmed to obtain a uniform shape and to avoid the heating effect during cutting by the band saw. 11 pieces of film can be obtained for each pipe. The films were numbered with alcohol resistant marker pen.

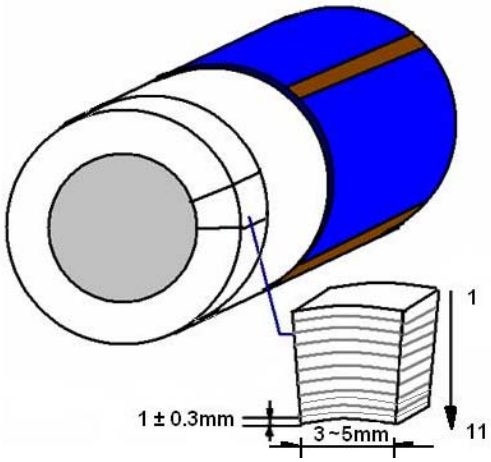

Figure 3-5 Schematic of sampling for density measurement

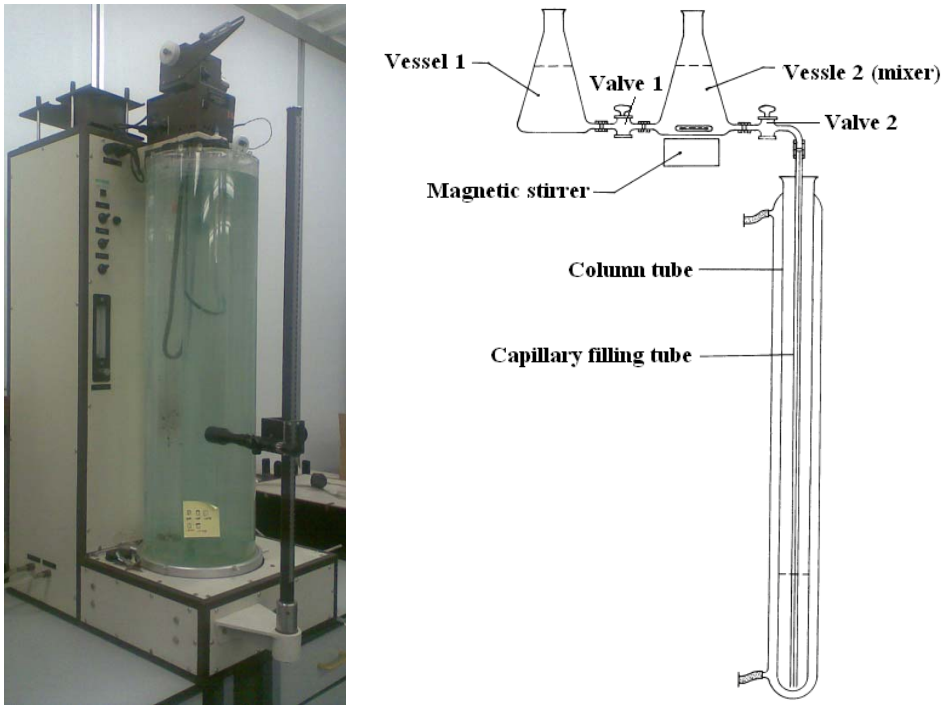

Figure 3-6 Schematic of density gradient column and filling device [123]

A schematic of the gradient filling device is shown in Figure 3-6 right. The column tube was thermally controlled in a water bath at temperature 23 ± 0.1 ^{o}C. Five glass floats of known density to the accuracy of 0.0001 g/ml were purchased from H&D Fitzgerald Ltd. The density of the glass floats were evenly distributed at the range of 0.9425~0.9550 g/ml, covering the density range of the samples. Analytical grade isopropanol and deionized water, which were fully miscible to each other, were used as column filling liquids. The light liquid was prepared 0.01 g/ml lighter than the least dense glass float and the heavy liquid was prepared 0.005 g/ml heavier than the most

dense glass float by mixing the two pure column filling liquids and using hydrometers to check. When the two liquids were prepared, the heavy liquid was contained in vessel 1 and gradually mixed into vessel 2 by opening valve 1, in which the light liquid was contained, with assistance of a stirrer. At the meantime, the mixed liquid was slowly filled in the column tube at a speed of ~10mm/min by controlling valve 2. The column was stabilized for 24~48 hours after filling was finished. Then, the glass floats were put in a basket connected to a slow speed motor with a fine wire and lowered down in the column at a speed of 5~10 mm/min without disturbing the density gradient. When the floats were settled in the tube, the height of each tube was measured by a travelling microscope vertically mounted on a gauge rod. The heights were plotted against the known densities of the glass floats to obtain a calibration line. If the density gradient was formed successfully, the calibration line is a continuous, monotonic linear line without more than one data point that is deviated from the calibration line and a linear equation of the line can also be obtained.

Before placing the sample in the tube, samples were soaked in the light liquid for around 1 hour in order to wet the sample surface and avoid adhesion of air bubbles during measurement. After soaking, samples were gently placed into the tube one by one. The height of each sample was measured when the samples were settled down in the tube. The density of each sample was calculated from the calibration line equation. After measurement, samples can be swept from the column by lifting up the basket at the same speed as it was lowered down.

3.3.1.2 Melting temperature and enthalpy of fusion measurements

A differential scanning calorimeter (DSC) model 2010 made by TA instruments was used for melting temperature and enthalpy of fusion measurement of the pipe samples.

The sample films were cut from the outer surface, middle part and internal surface of the PE core pipe as shown in Figure 3-7 a by a scalpel in the same way as the sample prepared for the density measurement. The slices were cut to ~0.3mm thick and punched into round disks which just fitted in the DSC aluminium pan. The sample

weight was controlled to around 10 mg. Then samples were placed in the DSC aluminium pan and sealed with lids with the sample surface side faced upward.

The sealed sample was tested under pure nitrogen environment with a gas flow rate of 50 ± 5 ml/min. The temperature was raised from room temperature to 200°C at a speed of 20°C/min and the heat flow of the sample was recorded. The melting temperature was identified as the peak of melting curve and the enthalpy of fusion was integrated from the area within the melting curve and a base line drawn from two flat ends of the curve as shown in Figure 3-7 b.

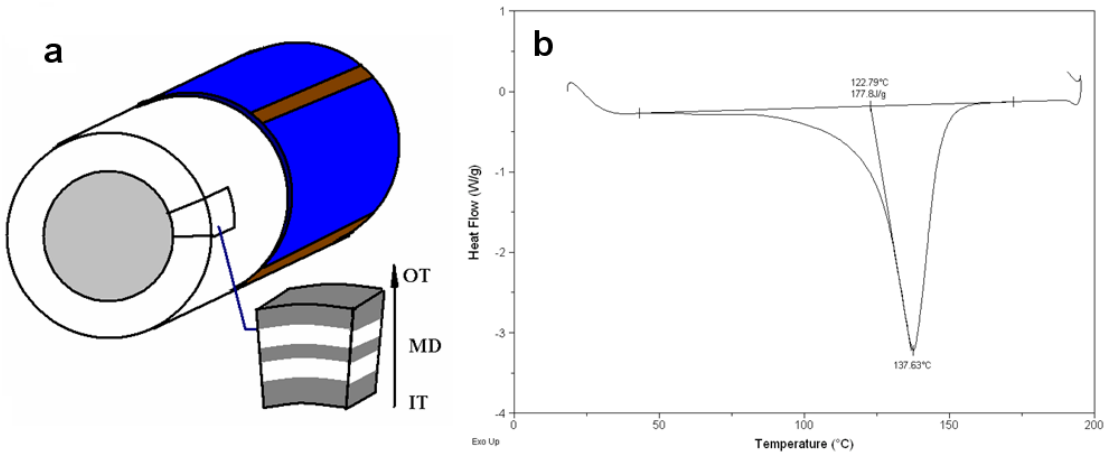

Figure 3-7 Schematic of sampling for DSC measurements and a melting curve

3.3.1.3 Electro-fusion (EF) peel testing

The general procedure of electro-fusion was mentioned in section 1.1. Both aged and unaged Profuse pipes with (0.4mm skin) and without skin were electro-fused with couplers made of PE according to industrial standard procedure. The skinned pipe electro-fusion surface was prepared by peeling off the skin. The uncoated pipe electro-fusion surface was prepared by cleaning the outer surface with an alcohol wipe then dry. The electro-fused pipes were conditioned at room temperature for more than 24 hours indoor.

After conditioning, each pipe cross section was marked into equal 12 sectors as shown in Figure 3-8 top left, making sector number 2 where the print-line of unaged pipes or the bottom-line of aged pipes during aging was. The pipe was cut parallel to the pipe axial into 12 strips according to the marking by a band saw. Only the 6 highlighted

and numbered strips were further machined to 25±2 mm wide for the EF peel testing. The average width was measured by a vernier calliper for each sample. Holes were drilled through the width as indicated in Figure 3-8 bottom right, then fitted with metal rods and mounted on tensile machine jigs. Peel forces were applied at a peeling speed of 25mm/min until total failure happened at the electro-fusion joint surface. The peeling force and peeling displacement were recorded by the tensile machine. The electro-fusion joint quality was assessed by analysing the portion of ductile or brittle failure area on the peeled surface.

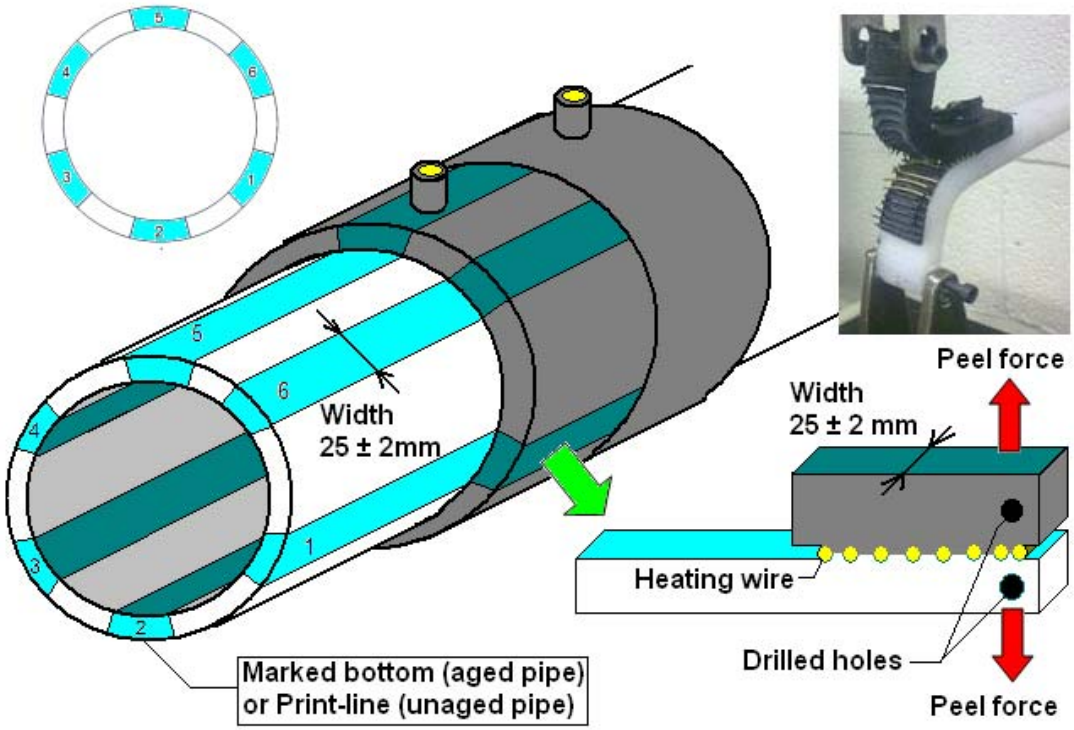

Figure 3-8 Schematic of EF peel test sample preparation and testing

3.3.1.4 Long term hydrostatic strength (LTHS) measurement

12 x 1.2 mm long NSPF and 12 x 1.2mm long 1.5SPF pipe samples were selected for the LTHS testing. Sample thicknesses and diameters were measured for hoop stress analysis. Samples were then electro-fused with couplers that fitted with end caps at both ends; one end was drilled and further fitted with a metal connector as a pressurized water inlet. 1.5SPF pipes were tested with skin on; only skin at the two ends was peeled off for electro-fusion.

The LTHS test was performed by Bodycote Materials Testing AB in Sweden. The pipe samples were filled with water and hydrostatic pressure was maintained within the pipe. Various designated pressure values were applied to different pipes until the pipe failed (identified by rapid drop of pressure). All the pipes were kept in isothermal water bath at 20 °C during the test. Hydrostatic pressure and failure time were recorded after the test.

3.3.1.5 Residual stress assessment

The residual stress assessment was carried out to analyse the skin effect on residual stress along the hoop direction of PE pipe before and after natural aging. 25±2mm pipe rings were cut following the same way as the skin peel testing from pipes NSPF and 1.5SPF. Pipes aged at 3 radiation levels and unaged pipes were assessed.

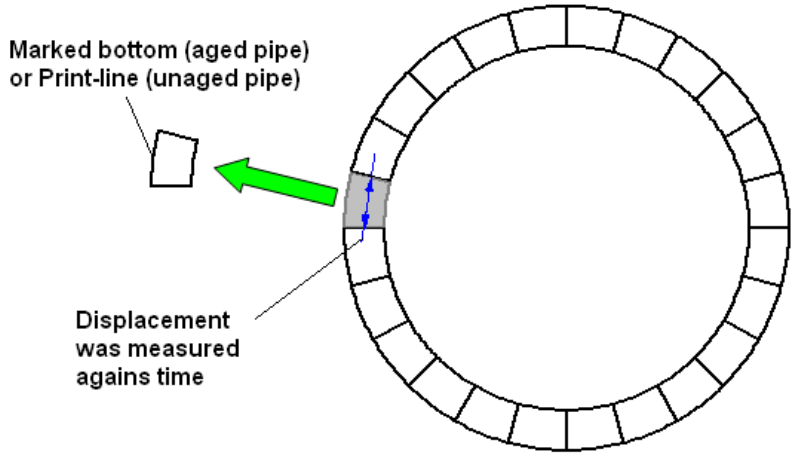

Figure 3-9 Schematic of residual stress assessment

A sector block marked with bottom-line (aged pipe) or print-line (unaged pipe) which is 1/24 of the pipe ring as indicated by the shadowgraph in Figure 3-9 was slowly cut off parallel to the pipe axis, and left on the original place for the assessment.

The pipe ring with the sector block (the shadowgraph) was placed on a horizontal stage of a profile projector with scale. The gap length of the slit at the middle of two ring ends as indicated in Figure 3-9 by the blue arrows was measured by the projector.

The block was quickly removed and the gap length and removal time of the block were recorded.

3.3.2 Chemical Characterization

3.3.2.1 Oxidation induction time (OIT) measurement

The DSC device used for melting temperature and enthalpy of fusion measurements was also used for the OIT measurement. Samples were cut in the same way as for the former melting heat and enthalpy of fusion measurements as indicated in Figure 3-7 . The material at the outer surface, middle part and inner surface were cut from the pipe.

In order to check the reproducibility of the test, the OIT measurement were carried out on the DSC (model DSC2010 made by TA instruments) in Loughborough University and the DSC (model 823e made by Mettler-Toledo) in Radius-Systems Ltd. Different type of DSC aluminium pan were used. The samples that were tested in Loughborough University were fitted into an open aluminium pan rather than a sealed one, leaving the surface side at the top and then tested in the DSC chamber. The samples that were tested in Radius-Systems were fitted in aluminium pans then sealed with aluminium lids and each lid was punched with three holes with needle as inlets for oxygen.

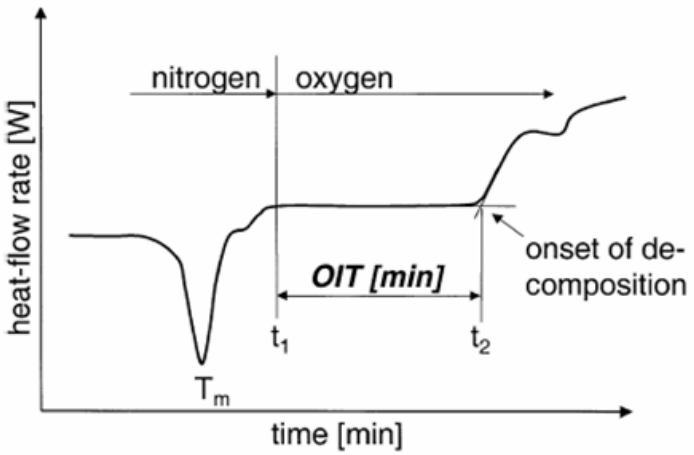

Figure 3-10 Schematic of OIT curve [113]

During the test, the temperature of the sample was increased from room temperature to 210°C at a heating rate of 20°C/min then held isothermally at this temperature in nitrogen atmosphere at a gas flow rate of 50 ± 5 ml/min and. Pure oxygen was introduced exactly 3 minutes after the sample reached 210°C, also at a gas flow rate of 50 ± 5 ml/min. The test was stopped when a complete oxidation exothermic peak appeared as shown in Figure 3-10. The OIT value't' was the time from the gas switchover to oxygen (t_1) to the time corresponding to the intercept of the extended baseline and the extended tangent drawn to the exotherm at the point of maximum slope (t_2).

3.3.2.2 Attenuated Total Reflectance (ATR)-FTIR measurement

ATR-FTIR was used to analyse the chemical changes on both PP skin surfaces and PE pipe surfaces (i.e. for uncoated pipe, inner and outer surfaces and for skinned pipe, core pipe outer and inner surface were examined). All the PE surfaces from the pipe were sliced to films of roughly 5 x 5 mm large and 0.2-0.5 mm thick.

A SHIMADZU FTIR-8400S instrument and a Specac Golden Gate single reflectance ATR attachment with a diamond prism (2 x 2 mm surface area), ZeSn lenses and sample pressure control unit were used in the measurement. The measurement was carried out in the air at ambient temperature and each spectrum was measured using the following the parameters: 600 to 4000 cm^{-1}, 64 scans and a resolution of 2 cm^{-1}. Background spectrum were taken after 2~3 measurements to avoid interference of CO_2 and H_2O absorption on the results. All spectra obtained had taken ATR corrections (due to the differences in penetration depth of infrared light with different wavelength) by the software.

3.3.2.3 Surface free energy measurement

Contact angle technique was applied for the surface free energy measurement using OCA20 made by DataPhysics instrument Ltd. Pipe rings were cut by band saw using the same technique as the skin peeling test. To investigate the chemical changes along the circumferential direction, the pipe rings were marked into equal 48 sectors and each sector was numbered, making the bottom-line (aged pipe) or print-line (unaged

pipe) in-between number 24 and 25. Then the pipe ring was cut into 48 numbered pieces.

Pure deionized water, diidomethane, and ethylene glycol were used as reference liquids for the surface free energy measurement. As the outer surface of the core pipe is hydrophobic, deionized water cannot wet the surface. Therefore, only the other two reference liquids were applied on this surface. During the measurement, reference liquids were dropped on the outer and internal surface individually to measure the contact angle value. At least 5 drops of each reference liquid were applied and the contact angle values were collected by the instrument software. Contact angle values within standard deviation of 5 degree were accepted. Otherwise, the measurement was repeated on fresh sample at the same location. After contact angles were collected, the surface free energies of each sample surface were obtained by Owen-Wendt-Kaeble method [99, 100]. The standard surface free energies of the reference liquids measured by Ström were selected for the surface free energy calculation from the software.

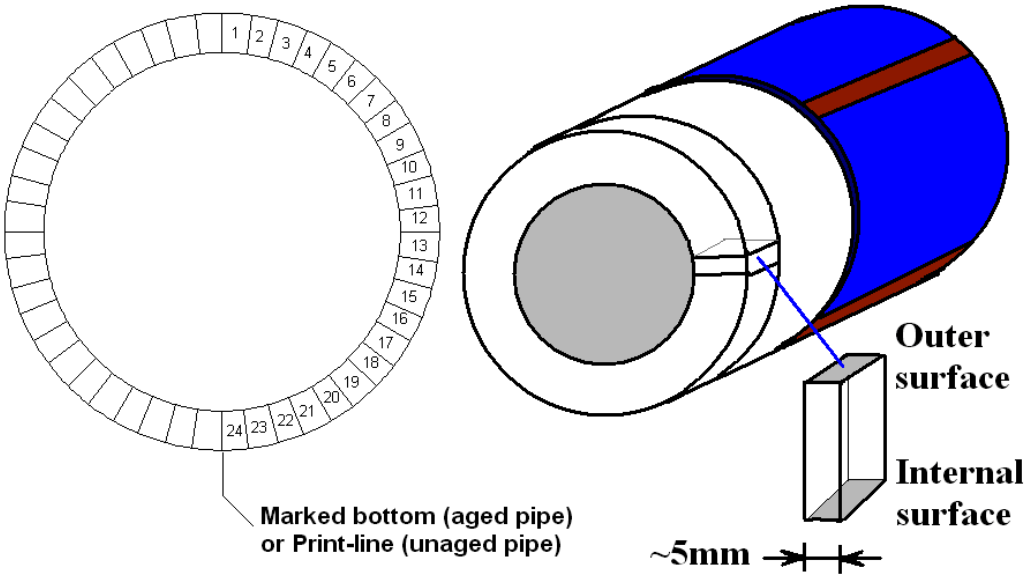

Figure 3-11 Schematic of contact angle sample preparation

3.3.2.4 X-ray Photon-electron Spectroscopy (XPS) measurement

Due to the high sensitivity on trace chemicals, XPS was used to investigate the surface oxidation on the 10GJ aged BPP, NSPF and 0.4SPF PE core pipe outer

surfaces. An unaged NSPF pipe outer surface was also tested as a control to the aged samples.

Samples were cut from the pipes into blocks with outer surface area of 10 x 10 mm. Loughborough Material Characterization Center (LMCC) carried out the XPS characterization using an ESCALAB Mk I instrument made by VG Scientific Ltd.

3.3.2.5 Gel Permeation Chromatography (GPC) measurement

Conventional high temperature GPC was used to characterize the molecular weight and its distribution of the PE pipe material at the outer pipe surface before and after aging.

Unaged and aged NSPF, BPP and 1.5SPF PE core pipe outer surface were scraped into 3~5mm wide, 0.2~0.3mm thick film strips by an industrial pipe scraping tool used for bare pipe socket electro-fusion preparation. The strips located at the top and bottom of the pipe during aging were selected for the measurement carried out by Rapra Technology Ltd.

1, 2, 4-trichlorobenzene (TCB) with antioxidant was used as GPC solvent. A single solution of each sample was prepared by adding 15ml solvent to 10~ 15 mg samples and heating at 190^{o}C for 20 minutes with shaking to dissolve. The solutions were filtered through a 1.0 μm glass-fiber filter and the filtered solutions were then transferred to glass sample vials. Injection of the solutions was carried out automatically after the solutions were thermally equilibrated in a heated sample compartment for 30 minutes. A Polymer Laboratories GPC220 with 2 x 300 mm long PLgel Olexis guard plus columns packed with 13μm particles was used for the measurement. The solvent flow rate was 1.0 mL/min at a temperature of 160^{o}C. The reflective index (concentration) of the eluted solvent was detected and the data were processed and analyzed using Polymer Laboratories software Cirrus 3.0.

Chapter 4 RESULTS AND DISCUSSIONS ON UNAGED SAMPLES

4.1 PP skin effect on pipe surfaces

Because the pipe surfaces were characterized and evaluated, the PE pipe surface quality is crucial for the electrofusion joining process.

Three letters and numbers were used for sample nomenclature in this project. For example, the label in Figure 4-1 right, the first letter "U" means the sample is unaged. For aged samples, numbers "1", "3", and "10" mean weathering radiation dosages are 1, 3 and 10 GJ/m^2 respectively. The second number or letter means the pipe type, "B" is BPP, "N" is NSPF and "0.4", "0.8" and "1.5" are ProFuse pipe with 0.4, 0.8 and 1.5 mm skin. An "S" following the figure means it is a PP skin rather than a PE pipe. The third number or letter relates to the location of the sample on the pipe. Letters "O", "M" and "I" mean outer surface, middle part and inner surface. If it is a number, it means the location across the pipe thickness or around the pipe circumference which will be explained in relevant sections.

4.1.1 Surface Free Energy

The surface free energy obtained from contact angle measurement gave general estimations of the samples' outermost surface properties. The surface free energies for unaged pipe surfaces are summarized in Table 4-1. The surface free energy values presented in bold type can be divided into its following dispersive component (D) and polar component (P). Columns "Pipe I" and "Pipe O" represented PE pipe internal surface and PE pipe outer surface. Columns "Skin I" and "Skin O" represented PP skin internal surface and PP skin outer surface. The data in the table can be divided into three groups.

Table 4-1 Surface free energies for unaged pipe surfaces (unit: mN/m)

Samples	**Pipe I**	D	P	**Pipe O****	D	P	**Skin I****	D	P	**Skin O**	D	P
BPP	**38.0**	37.9	0.2	**31.8**	29.8	2.0	**-**	-	-	**-**	-	-
NSPF	**33.3**	30.2	3.1	**36.8**	34.8	2.0	**-**	-	-	**-**	-	-
0.4SPF	**38.4**	33.4	5.0	**15.7**	12.9	2.8	**12.2**	8.3	3.9	**28.5**	24.1	4.4
0.8SPF	**36.0**	30.5	5.4	**15.0**	13.6	1.4	**9.8**	8.3	1.4	**31.3**	24.0	7.3
1.5SPF	**33.4**	33.0	0.4	**15.0**	11.4	3.5	**11.4**	8.6	2.8	**29.4**	25.2	4.1

*I: inner surface; O: outer surface; D: dispersive components; P: polar components. **PP/PE interface for skinned pipes

The first group of data (in blue) are the values in the column of "Pipe I" and the values from sample BPP and NSPF in the column "Pipe O". These values are from the five PE pipe inner surfaces and the two uncoated PE pipe outer surfaces. These values range from 31.8 to 38.4 mN/m. The typical surface free energy of unmodified PE is 33 mN/m [124]. The measured values in this group represented the surface free energy of PE.

The second group of data (in orange) are the values in the column "Skin O". These values are from the PP skin outer surface which is exposed to the environment. These values are in the range from 28.5 to 31.3 mN/m. The typical surface free energy of PP is 30 mN/m in [125]. The measured values in this group represent the surface free energy of PP.

The screening of contact angle data with a standard deviation ≤ 5 degree minimized the error of the surface free energy values which is derived from the former. But the surface free energies value measured here still maintained errors that deviated from standard values. This is because the sample surfaces may be contaminated, for example by dust or even grease from hands, although the sample was stored in a shaded area, packed with black plastic films during transportation and handled with care.

The third group of data (in green) are the values in the columns "Pipe O" and "Skin I" for the skin pipes (0.4SPF, 0.8SPF and 1.5SPF). These values are from the PE/PP interface. Among these values, the value in column "Pipe O" are from the PE side and

value in column "Skin I" are from the PP side. These values showed more than a 50% decreased surface free energy compared to the typical values of PE and PP. By comparison of the dispersive and polar components of the data from the PE side in the first group of data and those from the PP side in the second group of data, it can be found that the polar component did not change much and the decrease of free surface energies is due to the decrease of dispersive components.

The decrease of dispersive component of the surface free energy may due to migration of non-polar additives with low dispersive component of surface free energy into the PE/PP interface. A typical additive is possibly the adhesion reducer in the PP which is mentioned in the patent file of the product [5]. If so, the skin outer surface (i.e. the second group of data) should also show low surface free energy similar to the third group of data. But because of the PP skin was subject to water spray during cooling, the additive at the outermost surface may be washed out by the spray. For the purpose of confirmation of the above assumption, ATR-FTIR was applied.

4.1.2 ATR-FTIR

The ATR-FTIR technique can reveal the chemical compositions of sample surfaces with a penetration depth of several micro-meters [126]. The PE core pipe outer and inner surfaces and the PP skin outer and inner surface were characterized.

The results for PE core pipe outer and inner surface are normalized by vertical shifting as shown in Figure 4-1. Groups A and B are for samples BPP and NSPF respectively. The two spectra of each group are overlaid. Hence, the chemical composition of the outer and inner surface can be regarded as similar. For groups C, D and E, which belong to skinned pipes, two distinct peaks can be found at 1559 cm^{-1} and 1637 cm^{-1}. Another distinct peak can also be found at 3298 cm^{-1}. After referencing to standard FTIR charts [127], these peaks are attributed to secondary amide group absorption in the solid state which shows complicated vibration modes. In order to clarify the amide band assignment, the absorptions that are characteristic

for amide group were numbered with Roman numbers. These numbers are simply names without other meanings.

The band with peak at 1637cm^{-1} belongs to amide C=O stretching, as the 'amide I' band of secondary amides in solid state falls between 1680 and 1630 cm^{-1}[127]. The band with peak at 1559 cm^{-1} belongs to the interaction of secondary amide C-N stretching and C-N-H deformation vibration, as the 'amide II' band of secondary amides in solid state falls in the range of 1515-1570 cm^{-1} [127]. The 'amide III' to 'amide VI' bands overlap with PE peaks and they are difficult to be distinguished. The single peak at 3298 cm^{-1} that is attributed to N-H stretching vibration further confirmed this group is a secondary amide, since two bands are observed for primary amides and no band is for tertiary amides [127].

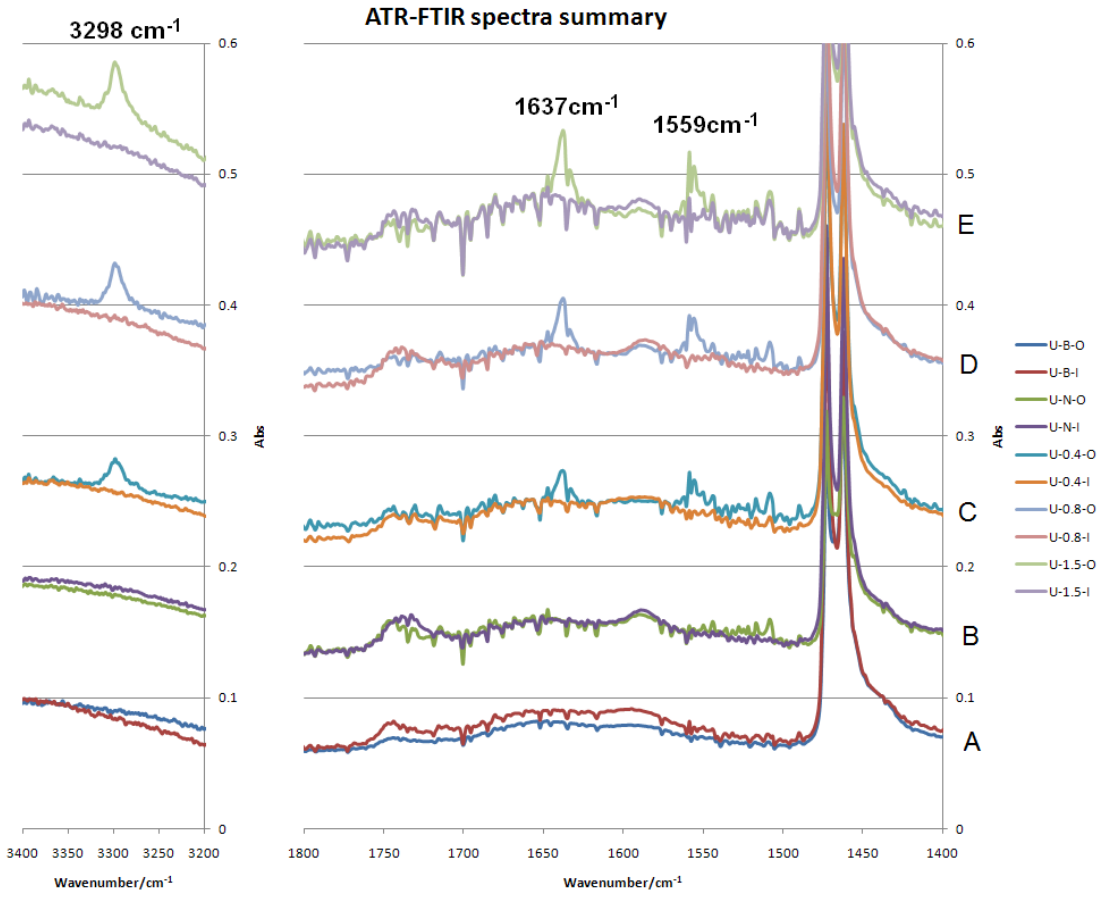

Figure 4-1 ATR-FTIR spectra summary on unaged PE pipe surfaces

The PP skin outer and inner surfaces were also characterized and the spectra are summarized in Figure 4-2. The spectra are classified into group F, G and H which

belong to 0.4SPF, 0.8SPF and 1.5SPF relatively. The same amide peaks that were found in Figure 4-1 can also be found on all PP skin outer and inner surfaces in Figure 4-2. For the same group of spectra (i.e. the same pipe type), the amide peak intensity from the outer surface is lower than the peaks from the inner surface.

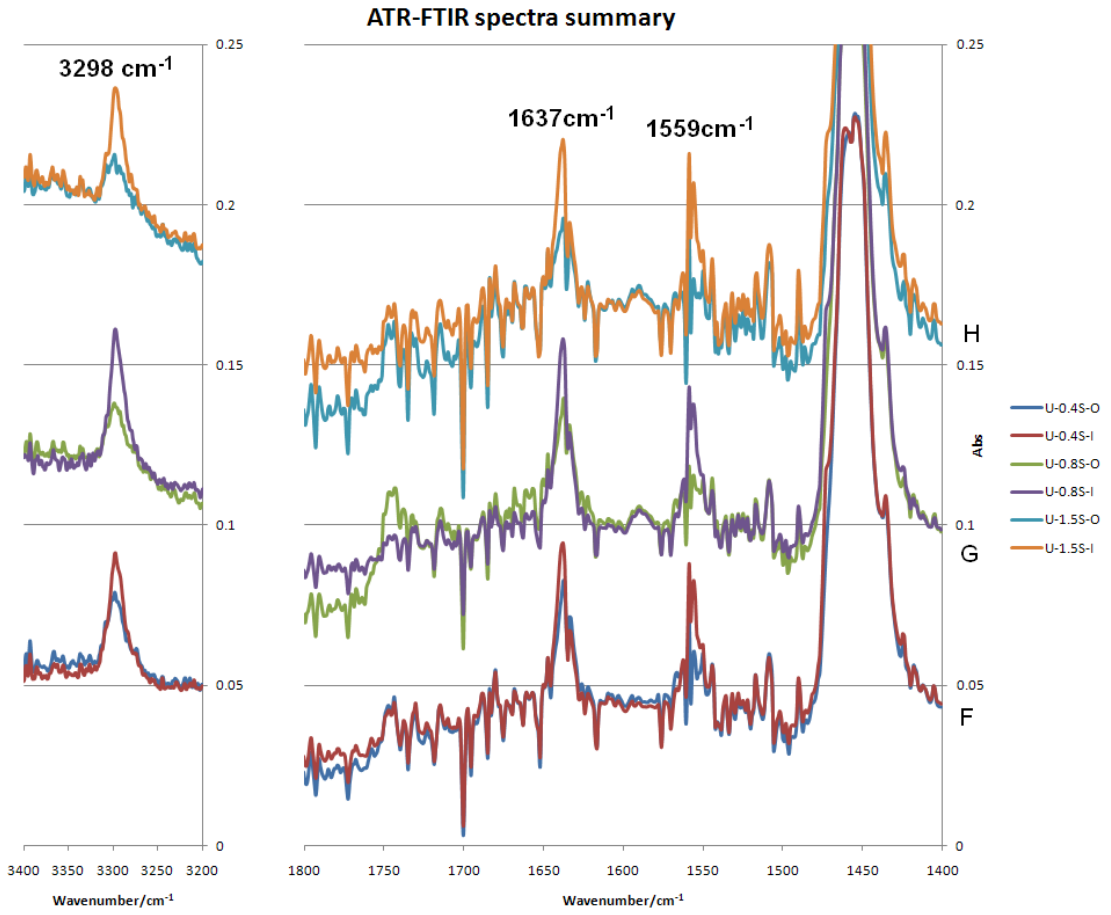

Figure 4-2 ATR-FTIR spectra summary on unaged PP skin surfaces

The patent associated with this skinned pipe [5] indicates that a fatty acid amide is incorporated into the PP skin to reduce melt adhesion between PE and PP. Combined with the analysis of surface free energy results and the infrared spectra, it can be concluded that the additive which migrated to the PP/PE interface is the designated fatty acid amide from the PP skin.

On the PP outer surface, the surface free energy value was close to standard value and no significant reduction was found. But the infrared spectra of these surfaces showed distinct amide peaks with a lower intensity than those found on the PE/PP interface. This is because of the different measuring depth of these two techniques. Contact

angle measured the outermost surface and the ATR-FTIR technique will penetrate several micro-meters deep from the outermost surface (depend on prism type and incident light angle [126]). The amide additive at the outermost surface is washed away by the water spray during cooling but at the depth of several micro-meters, the amide group is still detectable to the ATR-FTIR technique, which showed a lower intensity of the amide peaks than those peaks from PE/PP interface.

From the spectra, it can also be found that the amide absorption peaks intensity increases with skin thickness. This may because that a thicker skin can maintain a high temperature in the water spray vacuum chamber for a longer time than a thinner one, therefore allowing a longer time for the migration of the amide additive and increasing its concentration on the outer surface. In order to quantitatively analyse the fatty acid amide concentration at the outer surface, an amide index was calculated. The 'amide I' absorption value at 1637 cm^{-1} (attributes to interaction of secondary amide C=O stretching vibration) were subtracted by the absorption at 1617 cm^{-1} (baseline) the carbon backbone C-H deformation absorption values, for PE at 1473 cm^{-1} and for PP at 1452 cm^{-1} were subtracted by absorption at 1487 cm^{-1} (baseline) The subtracted 'amide I' absorption is divided by the subtracted C-H deformation absorption and produces the amide index. The amide indices are calculated and summarized in Figure 4-3 for both PP and PE surfaces.

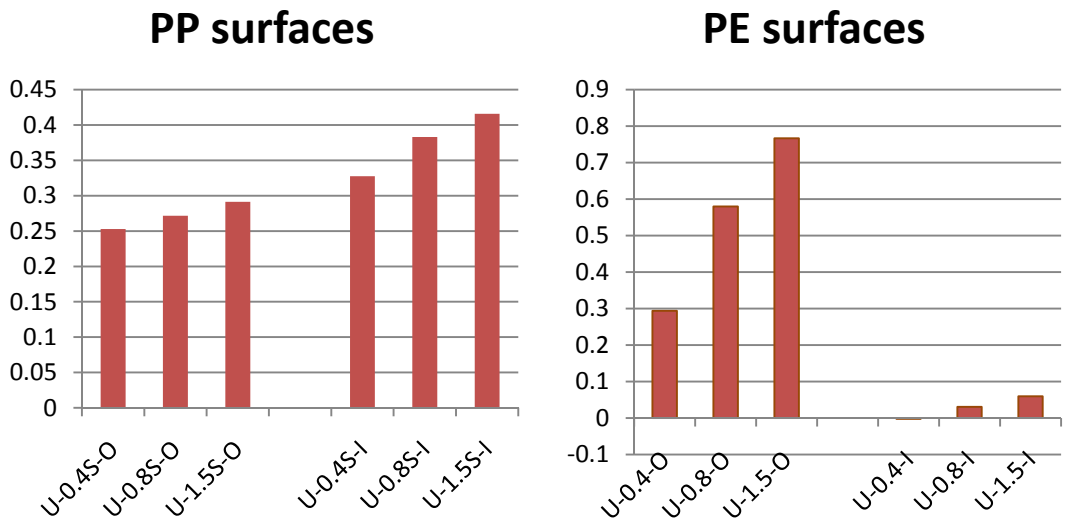

Figure 4-3 Summary of amide index from unaged PP and PE surfaces

From Figure 4-3, it can be seen that the index increase with the skin thickness, reconfirming the findings in Figure 4-1 and Figure 4-2.

From the surface characterization results, it can be concluded that the fatty acid amide which acts as adhesion reducer to control the PP/PE melt adhesion is migrated to the PP/PE interface. After peeling the PP skin off, the additive still resides at the PE pipe surface. The consequences of the additive to the electro-fusion joint quality will be evaluated in the section concerned with pipe performance.

4.2 PP skin effect across pipe wall

4.2.1 Oxidation induction time (OIT)

It is well documented [128] that OIT value is proportional to the phenolic antioxidant content. Therefore, the OIT value can be used to evaluate the level of the phenolic or phenolic/phosphite antioxidant content in the polymer. The virgin PE pellets, unaged NSPF and 1.5SPF samples were selected for the OIT test. The material located at the outer surface, middle part and inner surface were sliced and punched into a disk shape as described in section 3.3.1.2.

The OIT values of the virgin PE pellets, U-N and U-1.5 are summarized in Figure 4-4. The latter two OIT value were averaged from the three locations across the pipe wall as indicated above.

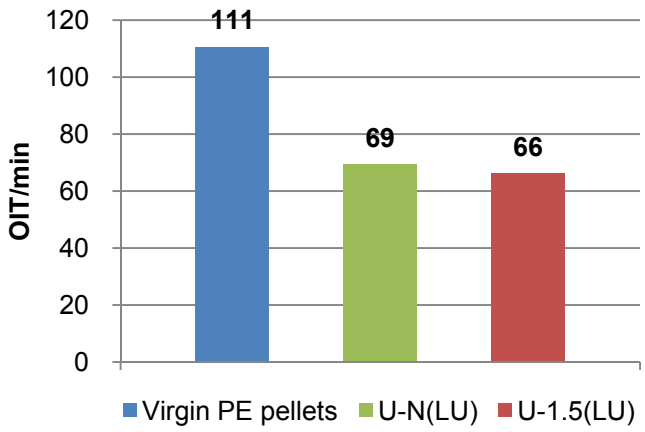

Figure 4-4 OIT value of PE before and after extrusion

From Figure 4-4 it can be seen that after extrusion, some oxidation had been consumed. The antioxidant consumed is probably the secondary thermal stabilizer in the polymer mentioned in section 2.3. Because these stabilizers are not as effective as long term thermal stabilizers but they can sacrifice themselves during melt processing and lessen the consumption of the phenolic antioxidant, which is the primary stabilizer. Therefore, the virgin pellets showed a higher OIT value. After extrusion, both uncoated and coated pipe have similar OIT value. The addition of PP skin does not affect the overall antioxidant content across the pipe wall.

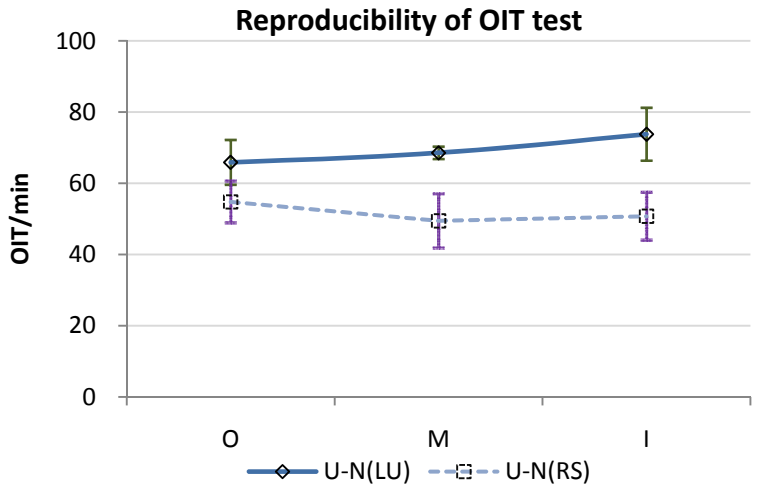

Figure 4-5 Reproducibility of OIT test

Figure 4-5 summarizes the OIT value obtained from two different DSC devices and aluminium sample pans to see the repeatability and reproducibility of the OIT test. The samples were sliced from the same pipe at the same locations and experiment programs were also set the same. The sample U-N (LU) was tested in Loughborough University and U-N (RS) was in Radius-Systems Ltd by author.

It can be seen from the error bars that the repeatability of both measurements are similar except those middle part measured at LU showed a better repeatability. This indicates that the results obtained from both devices were reliable.

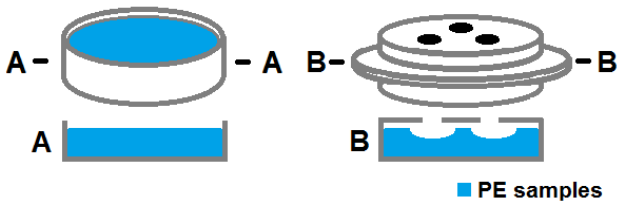

Figure 4-6 Schematic of aluminium pans from TA instruments and Mettler-Toledo

For the OIT values, the results obtained at LU were all higher than those obtained at RS. This may because of the differences of the aluminium pan as shown on Figure 4-6.

In pan B (measured in RS), oxygen blew through holes on the lid and the melt surface was interrupted. Concave surfaces that blew down by the oxygen below the holes can be evident by the tested samples within pan B. The PE melt surface in the pan A is relatively flatter because it subject to more even flow of oxygen. PE sample in pan B has more contact area with oxygen than those in pan A. Therefore it consumes antioxidant faster than PE sample in pan A and resulted in a lower OIT value. Such difference in the results indicates poor reproducibility of the OIT test carried out using different type of aluminium pans and attentions shall be paid to them. In this project, most OIT measurements were carried out in LU. Those carried out in RS will be identified.

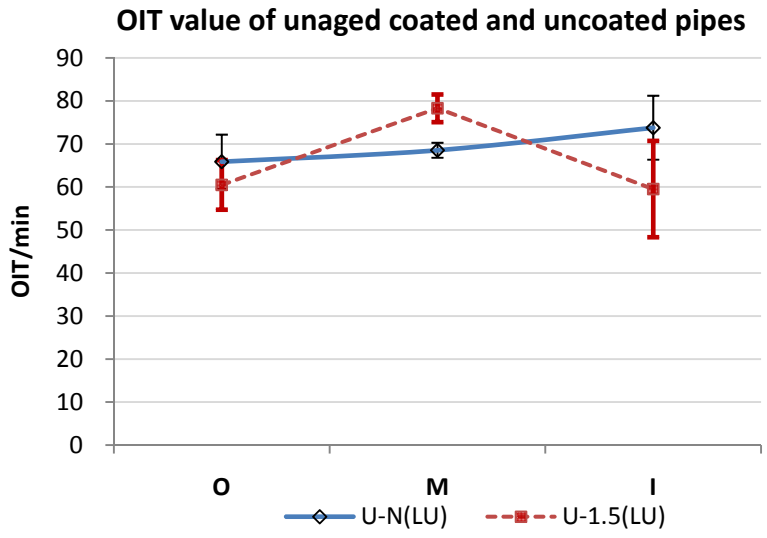

Figure 4-7 OIT value of unaged coated and uncoated pipes

Figure 4-7 summarized the OIT value of unaged U-N and U-1.5 samples across the pipe wall. The two curves showed that by the addition of PP skin, the overall

antioxidant content was not affected. However, the distribution of antioxidant was affected. The bare pipe retained a more evenly distributed antioxidant while the 1.5mm skin pipe has a higher concentration of antioxidant at the middle of the pipe wall. These may due to the different cooling rate of the pipes. The bare pipe retained the distribution of the antioxidant as melt state while the 1.5mm skin pipe was cooled down more slowly and it was possible for the antioxidant to redistribute when the pipe remain at melt state. The analysis of antioxidant migration needs to take the concentration of antioxidant, the polymer viscosity and the solubility of the antioxidant in the polymer into account. The last two factors were controlled by temperature. Since most interests of this project are on aging rather than processing, less effort has been made on the analysis of the pipe cooling procedure during processing and the information of the temperature change across pipe wall is not measured, limiting the discussion of the antioxidant distribution across the pipe wall.

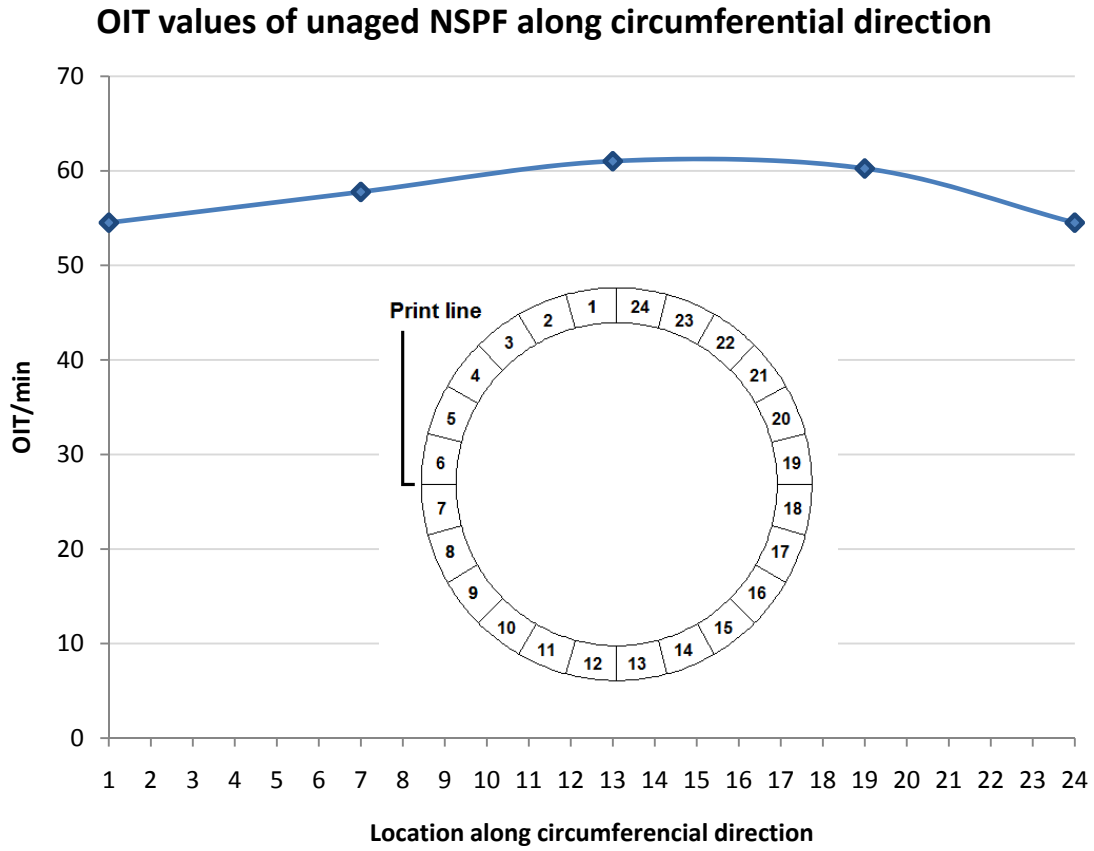

Figure 4-8 OIT values of unaged NSPF along circumferential direction

Because the bare pipe outer surface is directly subject to the environment and solar irradiation during natural aging, the OIT values along unaged bare ProFuse pipe outer surface were measured. These results were measured in RS and are shown in Figure 4-8.

Since all the values were within the error range indicated as error bars on Figure 4-5 which was calculated from duplicated run of data, the variation of the OIT value along circumferential direction can be regarded as system error and the phenolic antioxidant can be regarded to be evenly distributed on the pipe outer surface.

4.2.2 Density

The density across the pipe thickness was measured to investigate the effect of PP skin on the crystallization behaviour during processing.

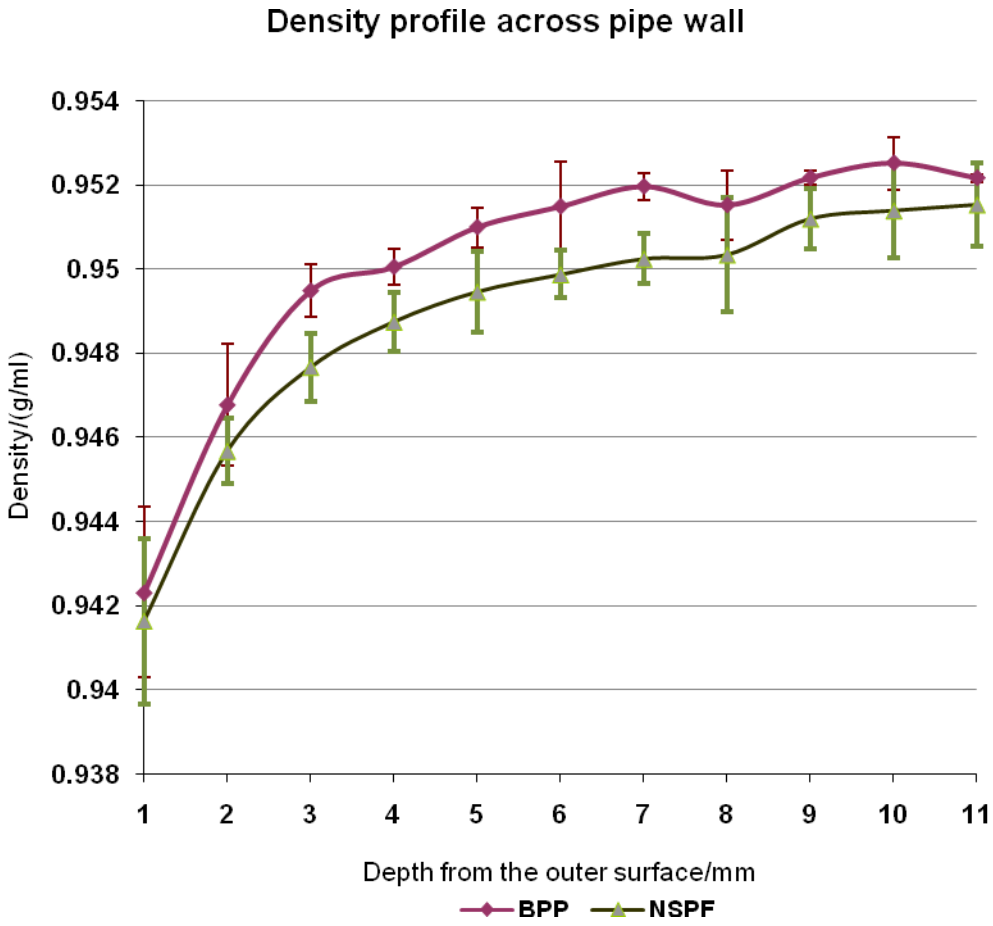

Figure 4-9 Density profile of unaged bare pipes across pipe wall

The measured density values were plotted against depths from the PE pipe outer surface and the results are summarized in Figure 4-9 and Figure 4-10. During the pipe cooling procedure, water at a temperature of 10-15 °C was continuously sprayed onto the pipe outer surface. The temperature of the outer surface was rapidly quenched from 180-200 °C to lower temperatures. Within the pipe bore, a layer of air on the pipe internal surface was heated by the extrudate, acting as a heat insulator so that a higher temperature close to the extrudate is maintained at the internal surface.

From Figure 4-9, it can be seen that due to the quenching effect the uncoated pipe density at the outer surface is much lower than the inner surface. This has been observed previously for HDPE pipe cooled by water at its outer surface in other research [129].

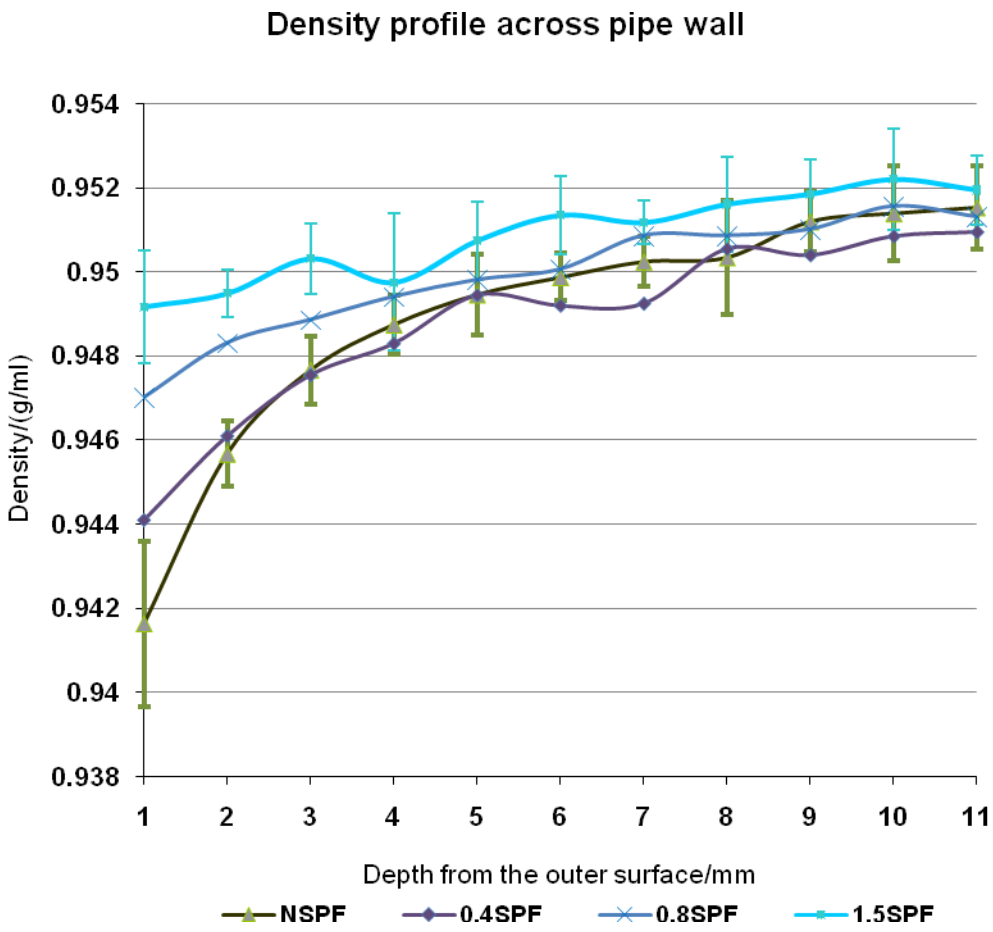

Figure 4-10 Density of unaged ProFuse pipes with different skin thicknesses across pipe wall

From Figure 4-10, it can be seen that with the addition of PP skin, the outer surface of the PE pipe is cooled down more slowly than the uncoated pipe because the skin has a similar heat insulation effect to the air layer at the internal surface. The density values of sample from pipe with 0.4mm, 0.8mm and 1.5mm skin at the depth of 1mm equal the density of sample from bare profuse pipe (NSPF) at the depths of 2mm, 3mm and 5mm respectively. This means that the thermal conductivity of the 0.4mm, 0.8mm and 1.5mm PP skin roughly equal to 2mm, 3mm and 4mm thick PE. This is because at the same temperature, the thermal conductivity of PP is roughly half to one third that of HDPE [130], according to the Fourier's law for thermal conduction as shown in equation (4-1).

$$\frac{\Delta Q}{\Delta t} = -kA\left(\frac{\Delta T}{\Delta x}\right) \qquad (4\text{-}1)$$

Where $\Delta Q/\Delta t$ is the heat flow rate, k is the thermal conductivity, A is the cross-sectional surface area, ΔT is the temperature difference between the ends and Δx is the distance between the ends.

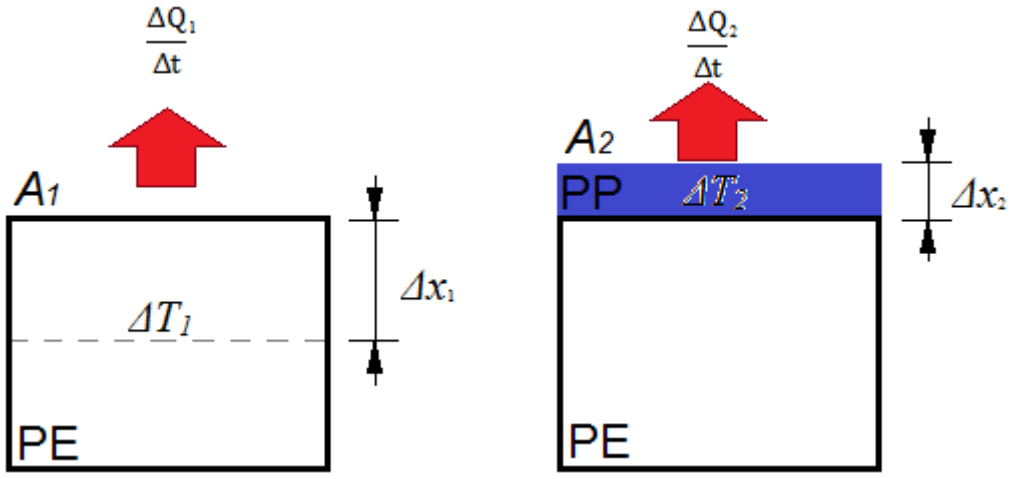

Figure 4-11 Analysis of bare pipe and skin pipe cooling

As shown on Figure 4-11, assuming the heat flow rate is the same for both bare pipe and skin pipe cooling ($\Delta Q_1/\Delta t = \Delta Q_2/\Delta t$), and the cross-section surface area is similar ($A_1 = A_2$), then a formula for bare pipe and skin pipe can be made as (4-2) shown.

$$k_{PE}\frac{\Delta T_1}{\Delta x_1} = k_{PP}\frac{\Delta T_2}{\Delta x_2} \qquad (4\text{-}2)$$

For both pipes at points that are cooled down to the same temperature level, $\Delta T_1=\Delta T_2$. Since Δx_2 (PP skin thickness) and assume that k_{PP} and k_{PE} are constants, then Δx_1 (depth from bare pipe outer surface that is equal to the PP skin) can be obtained as following.

$$\Delta x_1 = \Delta x_2 \frac{k_{PE}}{k_{PP}} \tag{4-3}$$

From reference [130], it is known that $k_{PE}/k_{PP} = 2$, therefore $\Delta x_1 = 2\Delta x_2$. The temperatures of 0.4mm 0.8mm and 1.5mm skin pipe at depths of 1mm from the PE outer surface are equal to the temperature of an uncoated pipe at depths of (0.4×2+1) mm, (0.8×2+1) mm and (1.5×2+1) mm. That is 1.8mm, 2.6mm and 4.0 mm, close to the experiment results.

The assumption $\Delta Q_1/\Delta t = \Delta Q_2/\Delta t$ is pessimistic. Within the cooling temperature range, the ratio of heat capacity of PP and PE ($C_{p(PP)}/C_{p(PE)}$) at the same temperature is around 3 [131]. If the sample needs to be cooled down to the same temperature level at the same cooling rate, i.e. $\Delta T_1=\Delta T_2$, the heat flow taken away by water from PP is roughly 3 times larger than those from PE, resulting in Δx_1 equals to roughly 6 times of Δx_2. The thermal conductivity of material changes with temperature. For polymers, it increases with decreasing temperature, especially when the material is solidified. The heat capacities of PE and PP decrease with decreasing temperature. These make the analysis of heat transfer more complex, but it is not the major concern of this project therefore it will not be further discussed here. But from above analysis, it can be generally concluded that the PP skin slowed down the cooling by acting as an insulation layer with a thickness that is roughly equal to a 2~3 times thicker PE layer.

The slow cooling rate of the pipe outer surface may allow more time for crystallization, therefore a higher crystallinity and density are observed. For sample BPP, similar density profile can be found. The pigments within the PE matrix may act as nucleating agents, increasing the crystallization sites and resulting in a higher overall crystallinity. Moreover the PE of BPP is a different grade from those of

ProFuse pipes (NSPF and the skin pipes), and the cooling behaviour was not comparable.

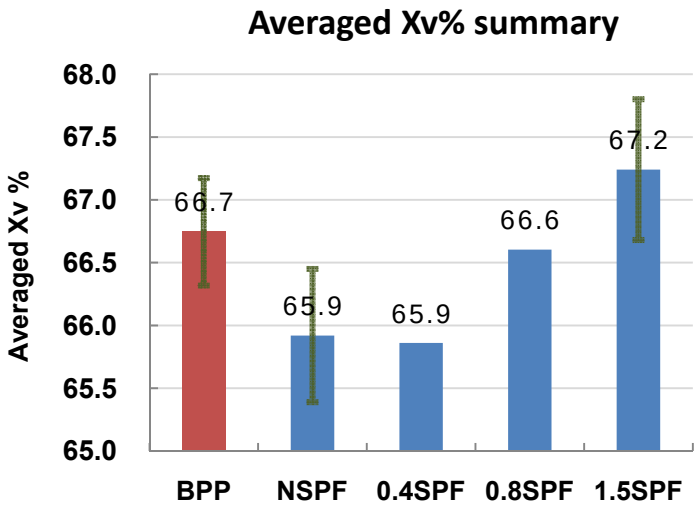

Figure 4-12 Summary of averaged crystallinity by volume

The density is proportional to the crystallinity within the material. The crystallinity by volume (X_v %) of each sample was calculated from equation (4-4).

$$X_v\% = (\rho - \rho_a)/(\rho_c - \rho_a)\ \% \qquad (4\text{-}4)$$

Where ρ is the density of the sample, ρ_a, 0.85 g/ml [132], is the density of the amorphous region of PE, ρ_c, 1.00 g/ml [133], is the density of the crystalline region of PE. All values from the same pipe type were averaged and are summarized in Figure 4-12.

The overall crystallinity of the pipe increased with skin thickness. As the skin thickness increase, density profile will be closer to the bore of the bare pipe and become a flatter line.

4.2.3 Thermal analysis

Thermal analysis was carried out for further investigation about the effect of the PP skin on the crystallization behavior of the PE across the pipe wall. For each DSC

curve, the melting temperature and the enthalpy of fusion were obtained as described in section 3.3.1.2. The melting temperature was summarized in Figure 4-13 and Figure 4-14 and the crystallinity calculated by enthalpy of fusion is summarized on Figure 4-15 and Figure 4-16. On Figure 4-13 and Figure 4-15, the bars in the same colour represent samples at the same location. Standard deviations were calculated and are illustrated as error bars on both figures.

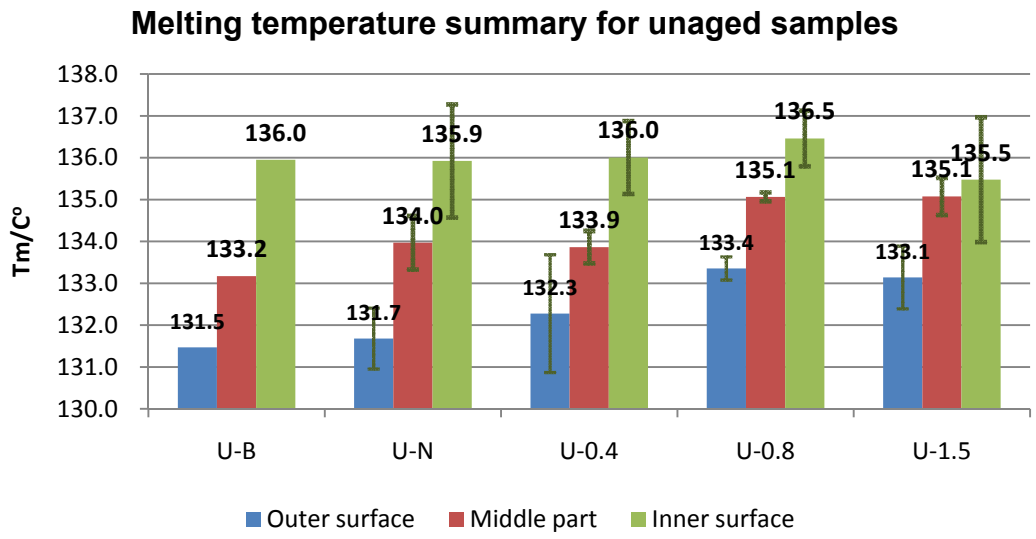

Figure 4-13 Melting temperature summary for unaged samples

The melting temperature is determined by the perfection and size of the crystal in the chain direction [134] (i.e. Tm is related to the properties of the thickest lamellae). In Figure 4-13, the Tm at the PE pipe outer surface increases with the skin thickness indicating that lamellae thickening occurred as the thermal insulation effect of the PP skin became greater. For pipes with thicker skin, more perfect/larger PE crystallites with a higher melting temperature were produced.

The quenching effect was eliminated toward the bore due to low thermal conductivity of PE. Hence, the difference of melting temperature from skin pipes and uncoated pipes at the same depth was reduced. Finally, at the inner surface for both skinned and uncoated pipes (green columns on Figure 4-13), the melting temperatures can be regarded as the same at 136 ± 0.5°C.

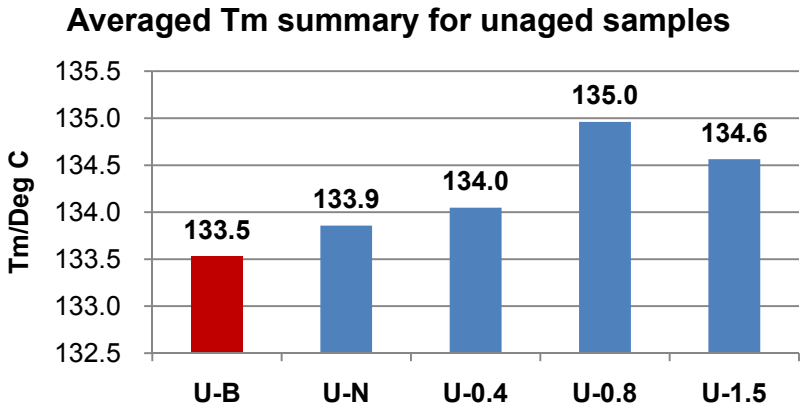

Figure 4-14 Averaged melting temperature summary for unaged samples

The effect of the skin on the overall Tm across the thickness is summarized in Figure 4-14. Generally, by addition of the PP skin the overall Tm increased by 0.1~1.1 ^{o}C depending on the skin thickness. The unexpected decrease at sample U-1.5 is due to the drop of Tm at the inner surface as shown in Figure 4-13. This is because of the larger degree of uncertainty in the Tm value at that location as shown by the longer error bar. Such error may arise from the differences of the sample resulting from the hand slicing procedure. For the samples that were sliced from the inner surface, since the surface area of the samples were the same because they were all shaped by the same puncher, the thinner sample better represented the properties of the inner surface because it was closer to the inner surface while the thicker sample incorporated more polymer within the pipe wall rather than at the inner surface, therefore leading to large level of error. Hence, although the sample weight was controlled, the irregularity of the slicing will result in thickness differences for the same sample and give rise to error.

The crystallinity by weight (X_w %) on Figure 4-15 is calculated from the enthalpy of fusion using equation (4-5).

$$X_w\% = \Delta H_{fs} / \Delta H_{fc} \times 100\% \qquad (4\text{-}5)$$

Where ΔH_{fs} is the enthalpy of fusion of the sample and ΔH_{fc} is the enthalpy of fusion of a 100% crystalline polyethylene, which is 293J/g [135].

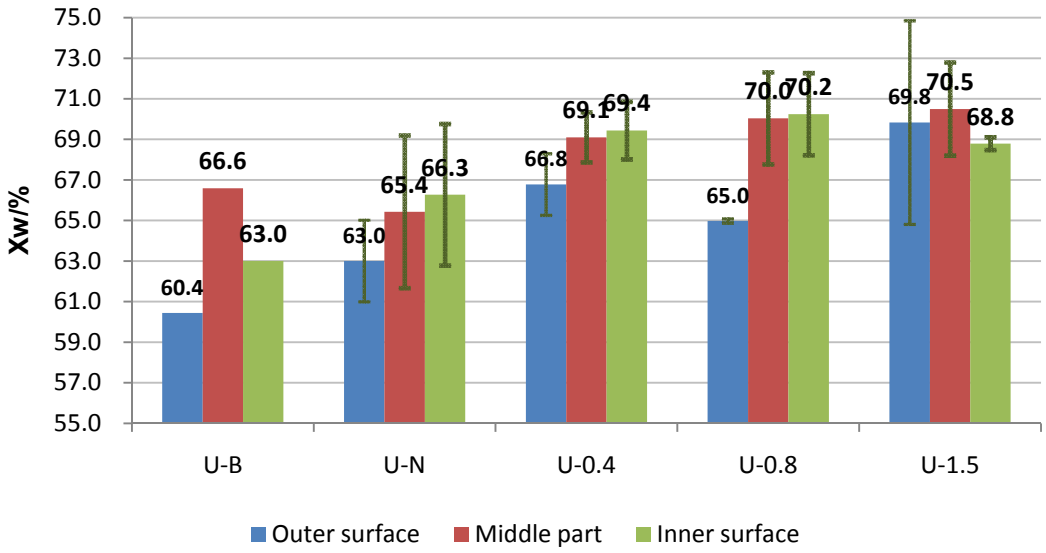

Figure 4-15 Summary of crystallinity by weight for unaged samples

While Tm is related to the crystallite lamellae thickness, crystallinity represents the relative amount of crystals present in the polymer regardless of the crystal size or perfection [136]. Figure 4-15 shows that the crystallinity of most ProFuse pipes increases from outer surface to inner surface, although some data has a larger level of uncertainty. This crystallinity result supports the density profile across the pipe wall that mentioned in section 4.2 and is also identical to similar research on HDPE pipe [137].

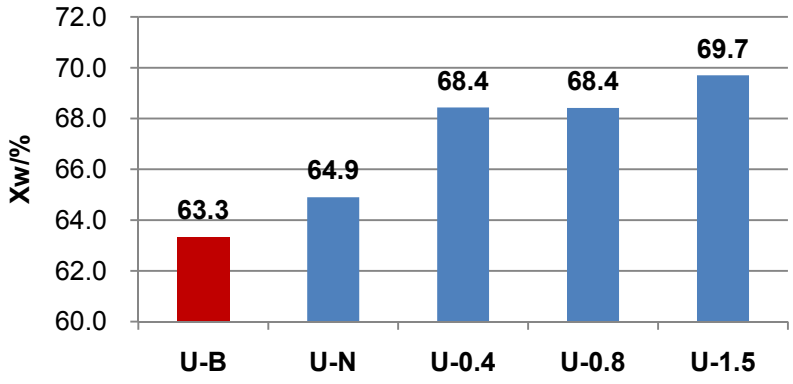

Figure 4-16 Averaged crystallinity by weight summary for unaged samples

The averaged crystallinities by weight measured by DSC are summarized in Figure 4-16. The results obtained from ProFuse pipes which are shown in blue columns are identical to those averaged crystallinity by volume that were measured by density in

Figure 4-12. For the BPP samples that are made from a different PE grade, results are not comparable to those obtained for the ProFuse samples.

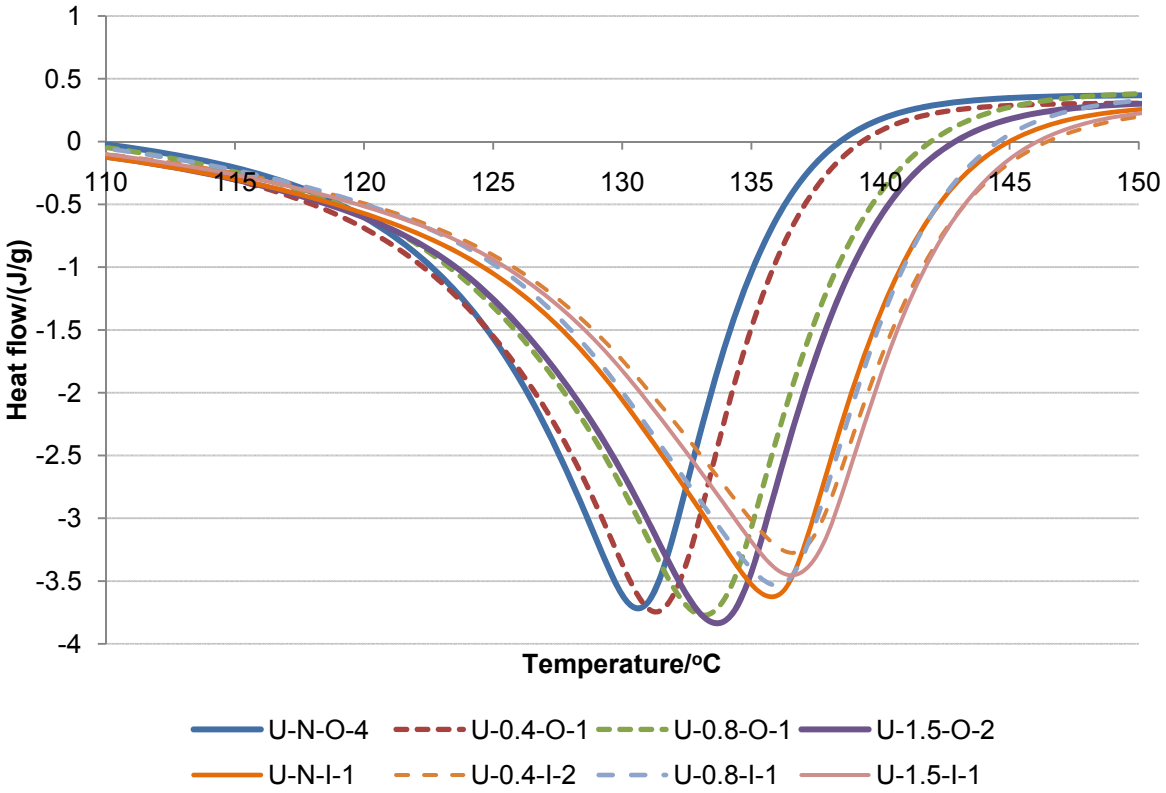

Figure 4-17 Melting curves of ProFuse samples at the outer and inner surfaces

The melting curves of the skin pipe outer and inner surface are normalized and compared in Figure 4-17. This shows the shift in melting temperature of skin pipes to a higher value with increased skin thickness as already summarized in Figure 4-13 and Figure 4-14.

Figure 4-17 also shows that for samples at the pipe outer surface, as the skin thickness increases, the portion of crystallites with higher Tm increased. For samples from the pipe inner surface, the curve shifted to an even higher temperature with more crystallites of higher Tm. Compared with the curves at the outer surface, the shapes at the inner surface of both bare pipes and skin pipes are similar. Overall, the curves from the pipe outer surfaces broadened as the skin thickness increased, the curves from the pipe inner surface are not affected much by the skin.

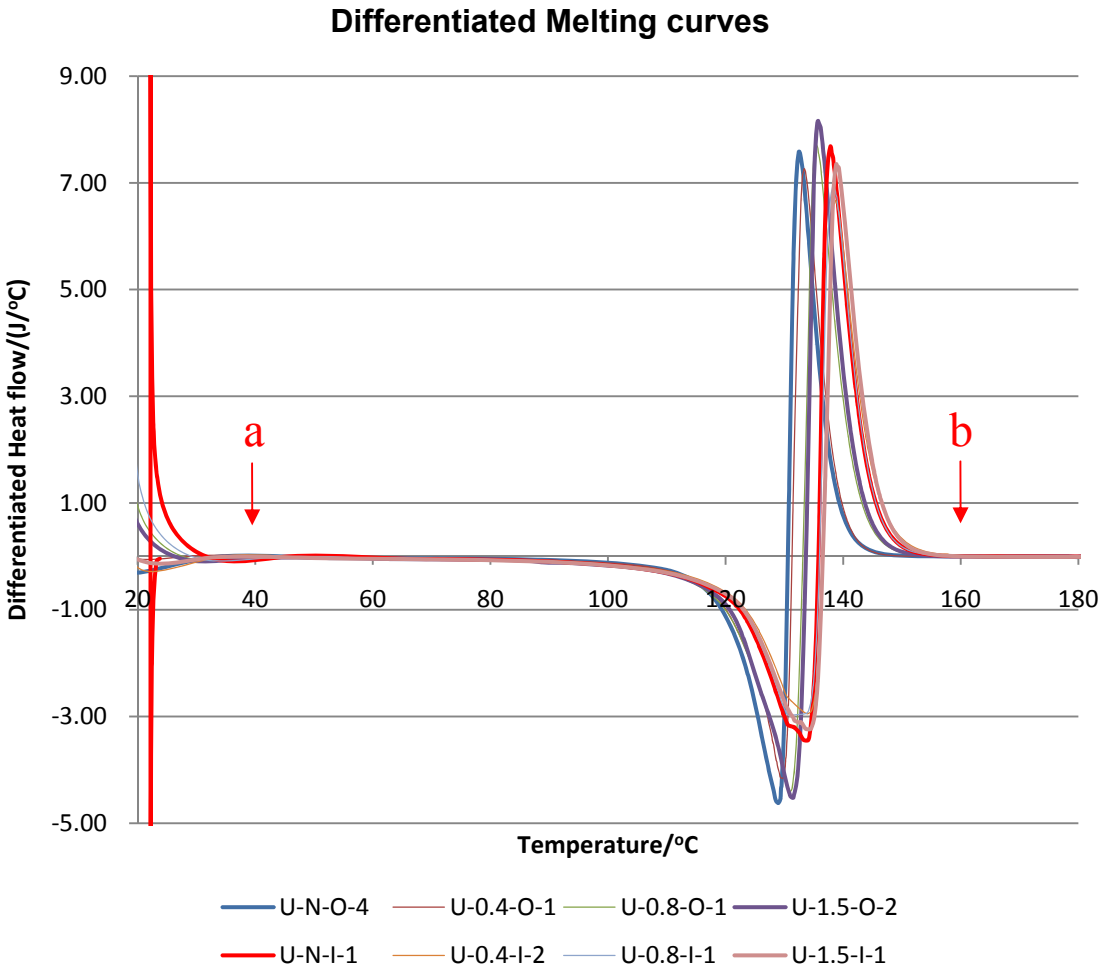

Figure 4-18 Differentiated melting curves

Table 4-2 Summary of start and end points and melting ranges of unaged pipes (values all in °C)

Samples	Outer Surface				Inner Surface			
	Test start temperature	Point a	Point b	Melting range	Test start temperature	Point a	Point b	Melting range
U-N	18	44	157	113	24	55	162	107
U-0.4	7	41	155	114	17	46	164	118
U-0.8	18	28	158	130	19	29	163	134
U-1.5	17	26	159	133	12	19	160	142

The beginning and ending of melting process can be quantified by differentiating the melting curve as showed in Figure 4-18. The melting range is taken between the temperatures at the two ends of the curve where the differentiated values change from zero to zero, as indicated in the figure by 'a' and 'b' respectively. 'Point a' is the last zero value at the beginning of melting (0~100°C) and 'Point b' is the first zero value at the ending of melting (140~180°C). The melting ranges measured from Figure 4-18

are summarized in Table 4-2. The start temperatures of the test are also included for error analysis.

From Table 4-2, it can be seen that for the same pipe type, the PE pipe inner surface has a broader melting range than the PE pipe outer surface. For both PE pipe outer and inner surfaces, the melting range increased as the skin thickness increased, especially when the skin thickness reaches 0.8mm. The change of melting range is because the endotherm of melting start point, 'Point a', shifts to a lower temperature. This means that the PE pipe inner surface starts melting at lower temperature than the outer surface. The skinned pipe outer and inner surfaces with thicker skin start melting at a lower temperature than the corresponding skin pipe outer and inner surfaces with thinner skin or without skin. The result for sample U-N shows an even narrower melting range at the inner surface than the outer surface. This may due to the high test start temperature. At the beginning of the test, the DSC machine needs to adjust the power supply to the test chamber and there will be small variation of heat flow in a range of several ^{o}C just after the test began. Such small variation includes large variation of slope of the curve therefore results in large variation in the differentiated curve as shown on Figure 4-18, and affects the consequential differentiated curve at 'Point a'. Using the differentiated curve to determine the melting range is more objective than manually determining the intersection points of the baseline (which also depends on the operator) and the melting curve.

The broadened shape of the melting curve indicated that the increase of enthalpy of fusion is not only due to the thickening of lamellae which has been confirmed by the shifting of Tm to several degrees higher, but may also due to better-define stacking of the lamellae and larger size of spherulite. Similar research [138] on water cooled commercial HDPE pipe by atomic force microscopy (AFM) showed that the spherulite size increases from outside to inside of the pipe as shown on Figure 4-19, but no clearly defined zone could be distinguished across the pipe wall.

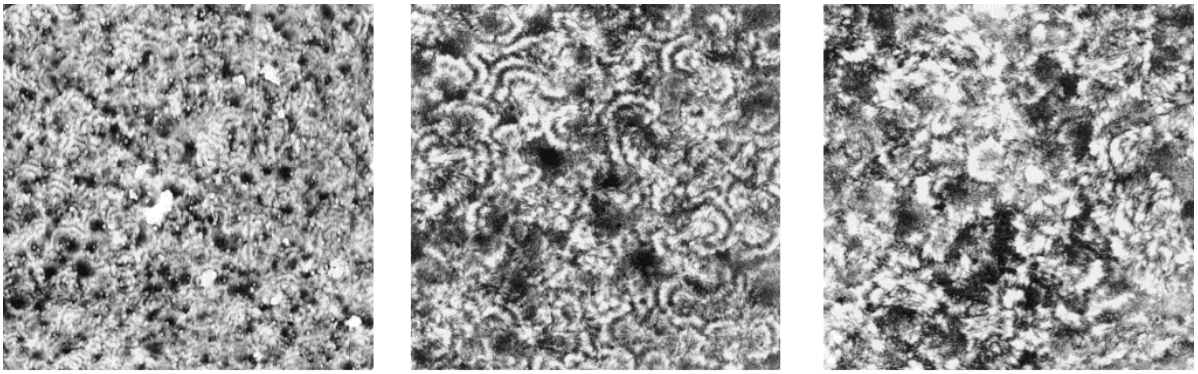

Figure 4-19 AFM height images of the cross section transverse to the extrusion direction: (a) cooled edge; (b) middle; (c) noncooled edge. Scan size: 40x40 µm. Gray scale for the feature heights: black=0.0 nm; white=1.20 µm. [138]

The density measurement and thermal analysis results confirmed that with the addition of the PP skin, thicker and more perfect PE crystals were formed and spherulites grown larger near the PE pipe outer surface. Such morphology change can result in strengthening of the mechanical properties such as stiffness and yield strength at the PE pipe outer surface [139, 140]. The mechanical properties will be discussed after the analysis of the effect of PP skin on the antioxidant and the residual stress in section 4.3.1.

4.2.4 Residual stress assessment

Research showed that by annealing after production, the release of some frozen-in residual stress of PE pipe resulted in a better performance (400% longer failure time) in long term hydrostatic test [141] and slow crack growth measurement (100% longer failure time [142]). The residual stress is an important factor affecting the pipe mechanical performance. Therefore, the residual stress assessment was carried out.

There are several residual stress assessment techniques available and they are summarized in [143]. The Slit Ring Closing Method [144] which is a simple but informative technique was selected for the assessment of effect of PP skin on the residual stress within the PE core pipe.

It is commonly accepted that the conventional water cooled solid PE pipe had a compressive residual stress (in both longitudinal and circumferential directions) near

the pipe outer surface and the stress gradually decreased and changed to a tensile one toward the pipe inner surface [142-145] as shown on Figure 4-20a.

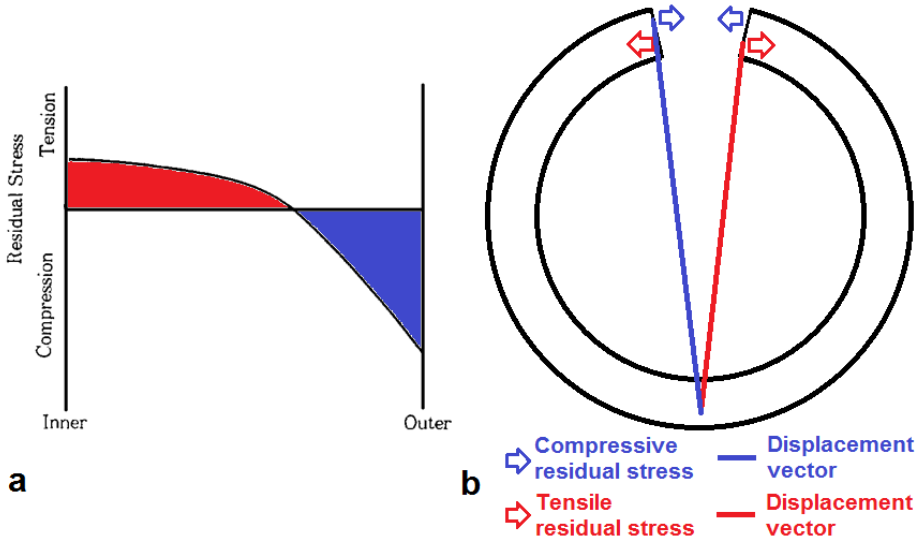

Figure 4-20 a) Possible residual stress through wall thickness of pipes [143], b) schematic of bending moments in a slit pipe ring

The remove of a small sector block of pipe ring sample as shown in Figure 3-9 will release residual stress at the hoop direction. The slit pipe ring ends will tend to close. This is firstly because, due to the fast cooling, the overall compressive stress at the outside surface is larger than the overall tensile stress at the bore as shown previously [144, 145], and secondly, because the compressive residual stress is located near the outer surface, it has a larger displacement vector compared to the tensile residual stress as shown Figure 4-20b. Therefore, the resultant bending moments tend to close the slot along the direction of the compressive stress. It has been demonstrated previously [146] that the slit PE pipe ring deflects in a typical time-dependent viscoelastic fashion. A larger level of residual stress will result in faster creep. Hence, the residual stress can be assessed by comparing the speed of creep procedure for the pipe samples in this project.

The creep behaviour of pipes NSPF, 0.8SPF and 1.5SPF were measured as describes in section 3.3.1.5. The distance between ring ends (D) and the creep time (t_c) were recorded. D was plotted against log t_c (for the convenience of comparison) as shown in Figure 4-21.

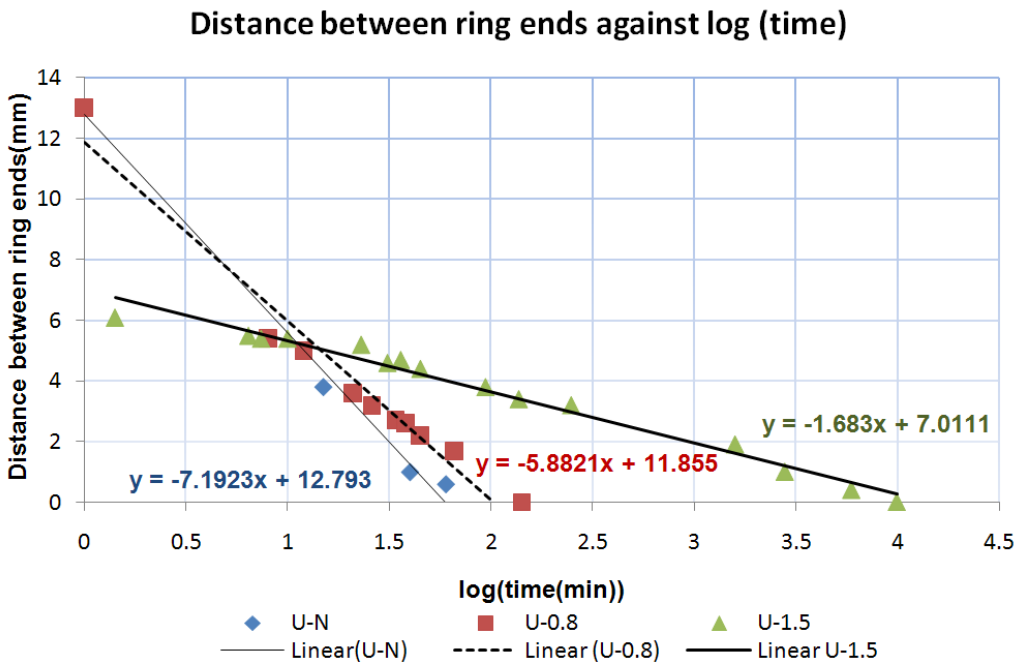

Figure 4-21 Distance between ring ends against logarithm of creep time

From Figure 4-21, it can be seen that a straight line can be fit to each group of data. The absolute value of the slopes of the fit lines decreased as the skin thicknesses increase. The ranking of the slope indicates the speed of the slit ring closure. As the skin thickness increases, the speed decreases which indicated the decrease of residual stress.

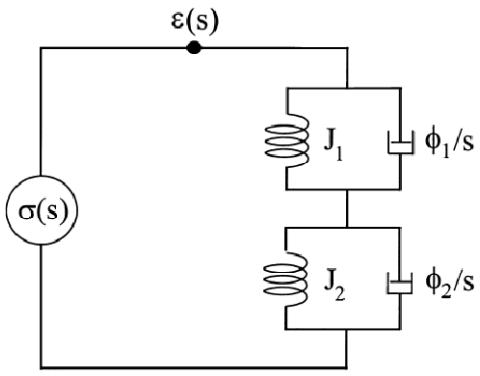

Figure 4-22 Non-standard 4-parameter Voigt model, σ(s) – stress, ε(s) – strain, Φ_i/s – shear fluidity, J_i – shear compliance [144]

To quantify the resultant residual stress, a non-standard 4 parameter Voigt model was used as shown in Figure 4-22 [144] which has been shown to be adequate to use for a number of real plastic materials including PE [147]. The strain can be expressed as a function of creep time in equation (4-6).

$$\varepsilon(t) = \varepsilon_0(1 - \varepsilon_1 \exp(-t/\tau_1) - \varepsilon_2 \exp(-t/\tau_2)) \quad (4\text{-}6)$$

Where t is time; $\varepsilon(t)$ is the strain at time t, defined as the ratio of deflection in the middle of the pipe ring ($\delta_t = D(0) - D(t)$, change in diameter) at time t to the original pipe diameter in the middle of the pipe ring ($D(0)$) (i.e. $\varepsilon(t) = \delta_t/D(0)$) as showed in Figure 4-23. Other variables such as ε_0, ε_1, ε_2, τ_1 and τ_2 are constants.

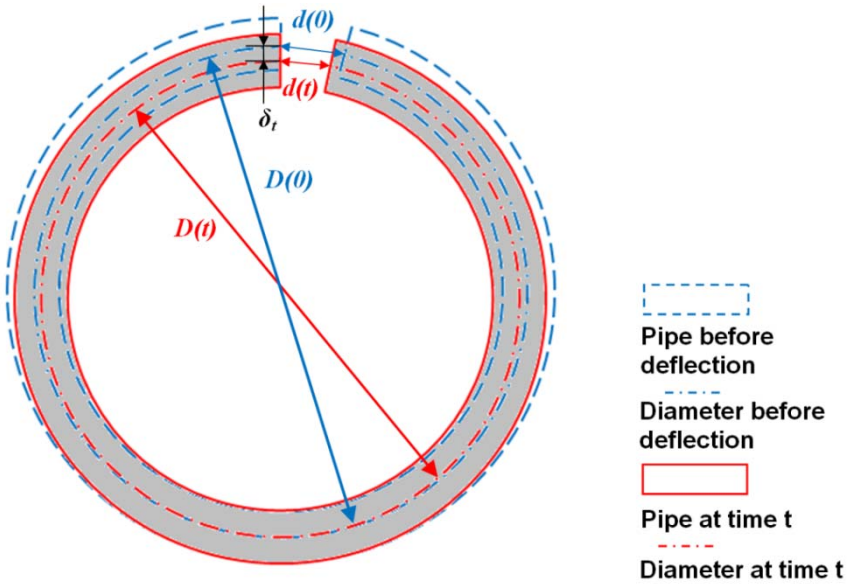

Figure 4-23 Schematic of calculation of strain in a pipe ring

Since the original diameter of the pipe ring $D(0)$, radian of the removed section which is 1/24 of a pipe ring and the distance between two pipe ends, $d(t)$, are known, The circumference of pipe ring at time t can be express as (4-7).

$$\pi D(0) - (\pi D(0)/24 - A(t)\,) = \pi D(t) \quad (4\text{-}7)$$

Since $d(t)$ and $D(t)$ are decreasing, it can be assumed that $d(t)$ is approximately equal to the value of its correspond arc $A(t)$. The strain $\varepsilon(t)$ can be derived from (4-7) as shown in equation (4-8).

$$\varepsilon(t) = 1/24 - \mathrm{d(t)}/(\pi D(0)) \quad (4\text{-}8)$$

Since $\varepsilon(t)$ has a linear relationship with $d(t)$, the plot in Figure 4-21 can be redrawn as strain $\varepsilon(t)$ against time t. By fitting the curve in such a plot, an estimated ε_0 which is the only constant term in equation (4-6) can be obtained. The equation (4-9) was selected as the model equation for curve fitting. The fitted curve is shown on Figure 4-24 and parameters were summarized in Table 4-3.

$$Y = a(1 - exp(-bx)) + c\,(1 - exp(-dx)) \qquad (4\text{-}9)$$

For sample U-N, the ring closure speed is fast and only four data points were recorded. These points were not enough for curve fitting. Only curve for U-0.8 and U-1.5 were processed using software OriginLab.

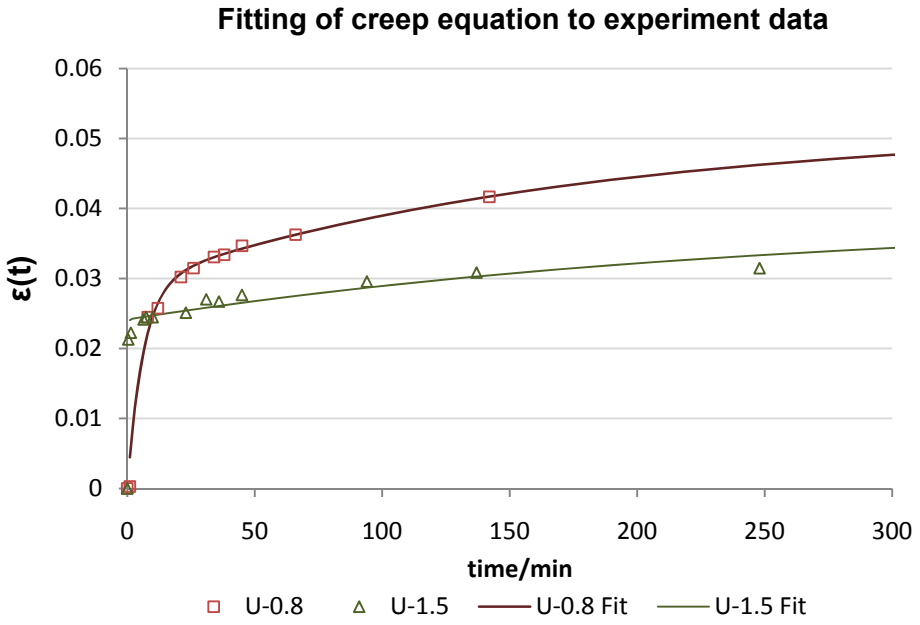

Figure 4-24 the fitting of creep equation to experiment data

Table 4-3 Results of the fitting for residual stress

	U-0.8	U-1.5
a	0.0226	0.0148
b	0.0057	0.0039
c	0.0292	0.0241
d	0.1607	5.0792
$\mathbf{R^2}$	0.987	0.978
$\boldsymbol{\varepsilon_0}^*$	**0.0518**	**0.0390**

$^*\varepsilon_0 = a + c$

From reference, assuming the length of the pipe is unlimited gave an approximated equation (4-10) [144].

$$\sigma_0 = \varepsilon_0 Gh/a \quad (4\text{-}10)$$

where G is the elastic modulus, h is the pipe thickness and a is the original internal diameter of the pipe.

From the approximated equation (4-10), the residual stress σ_0 is proportional to the equilibrium strain ε_0, therefore it can be inferred from Table 4-3 the residual stress level of the pipes. The residual stress of pipe 1.5SPF was ~75% of the 0.8SPF pipe. As the 0.8SPF pipe has a lower residual stress than the uncoated pipe NSPF, it can be inferred that more than 25% of the residual stress of uncoated pipe NSPF was reduced by addition of 1.5 mm PP skin on its outer surface.

Table 4-3 also showed that the coefficient of determination (R^2) which is not high enough (>0.99) for further discussion. These results just showed an approximated comparison of the residual stress level between sample 0.8SPF and 1.5SPF. It is suggested that test time varied from 1250 to 10,000 minutes [144] is required to perform the creep test to acquire fitting results with high R^2 value. For sample NSPF and 0.8SPF, the rings are closed before more data points can be obtained for curve fitting. As shown for sample U-0.8 on Figure 4-24, data points of creep time longer than 150 minutes are unavailable because the ring ends met. A wider ring slit is suggested to be cut from the unaged samples to obtain the required data points for curve fitting.

4.3 PP skin effect on pipe performance

4.3.1 Long term hydrostatic strength (LTHS)

LTHS results on unaged pipes of this project were published in [148]. For solid pipe NSPF, the mean hoop stress can be calculated from Barlow's formula:

$$\sigma_{hoop} = P(D-e)/(2e) \quad (4\text{-}11)$$

where P is the applied hydrostatic pressure, D is the mean outer diameter of the tested pipe and e is the minimum thickness of the tested pipe wall. Barlow's formula has been adapted in an ISO standard for LTHS test and pressure pipe rating [10] and used widely in the pipe industry for quality assurance. It is proved to be accurate enough for stress analysis for thin solid wall pipe.

However, the solid pipe approach is not appropriate for the multi-layered pressure pipe. Because the overall hoop stress applied to total wall thickness breaks down in multi-layered pipes, pipes composed of materials with different mechanical properties will result in different behaviour.

For composite pipe 1.5SPF, an attempt has been made to analyse the stress at different layers. But due to the lack of material properties, especially the long term modulus for both layers, the stress analysis can only be quantitative.

The stress analysis is evaluated using the theory of thick walled composite tubes as described in research on long-term hydrostatic strength of multilayer pipes [148].

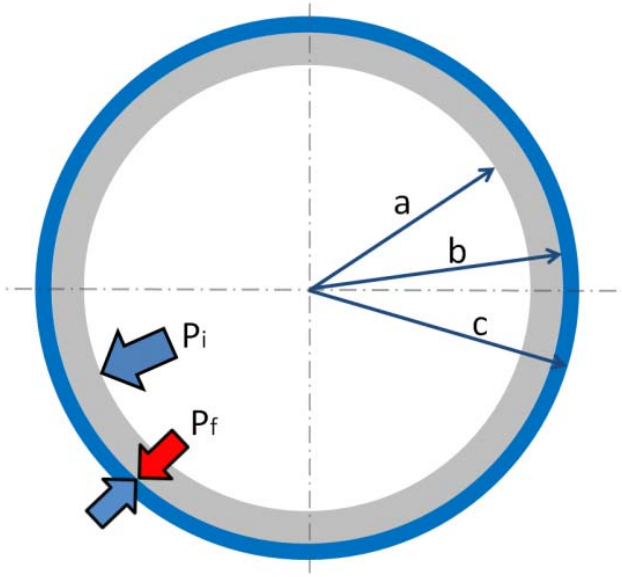

Figure 4-25 Schematic of 1.5SPF pipe structure and interfacial pressure

As show in Figure 4-25, due to the action of internal pressure (P_i), an interfacial pressure (P_f) was produced between the two layers. An assumption was made that both materials are linear elastic in a short term, since creep rupture happens when the pipe failed in a ductile mode, and no obvious creep was identified before pipe failure. The classical elasticity theory of multilayer thick-walled cylinders can be applied for the analysis of P_f using the following equation [148].

$$p_f = \frac{2p_i}{\left\{E_i(R_i^2-1)\left[\frac{1}{E_i}\left(\frac{R_i^2+1}{R_i^2-1}-\nu_i\right)+\frac{1}{E_o}\left(\frac{R_o^2+1}{R_o^2-1}+\nu_o\right)\right]\right\}}$$

where dimension parameter R_i= b/a and R_o=c/b as shown in Figure 4-25 ('b' and 'c' are mean outer diameter measured by pipe tape and 'a' is calculated by subtracting mean PE pipe outer diameter 'b' by the minimum PE pipe wall thickness). The short term elastic moduli of the PE and PP layers, designated to E_i and E_o, are both assumed to be 1000 MPa which falls in the range of typical extrusion grade PP and bimodal grade PE. The poisson ratios of PP and PE layers, designated to ν_i and ν_o, are both assumed to be 0.4 which is typical for polyolefins.

The mean hoop stress at the PE and PP layers (σ_{hi} and σ_{ho}) can be calculated from P_f , P_i using Barlow's formula as shown below.

$$\sigma_{hi} = (P_i - P_f)(b - e_{PE})/(2\, e_{PE})$$

$$\sigma_{ho} = P_f(c - e_{PP})/(2\, e_{PP})$$

According to ISO Standard 9080 [10], the creep rupture time and failure hydrostatic pressure has an Arrhenius relation. Therefore a double logarithm plot of the hoop stress against failure time can be drawn and the strength of the pipe can be predicted at 50-years, as shown in Figure 4-26. A linear regression line can be fitted to the data corresponding to each layer.

The report from the testing company indicates that all tested pipes failed in the ductile mode, which is indicated as 'Stage I' in Figure 4-30. Extensive approval tests in

production for this skinned pipe, made with the same PE resin in a wide range of pipe sizes and SDR values over many years showed that all samples failed in 'Stage I', even using 80°C tests [150]. Therefore, it can be assumed that the extrapolated 50-year strength still failed in 'Stage I' and no knees (change of failure mode due to leaching of antioxidant and brittleness introduced by oxidation) can be identified for any data points.

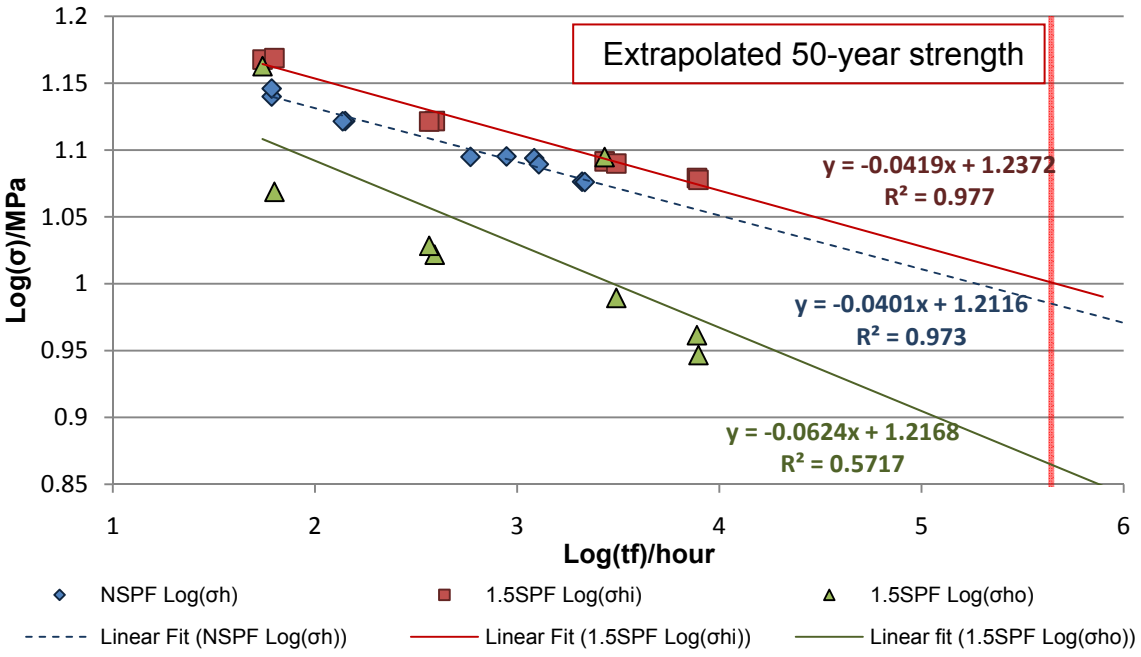

Figure 4-26 creep rupture curve of unaged NSPF and 1.5SPF samples

In Figure 4-26, the data points of NSPF and 1.5SPF PE core pipe fit the regression curve very well ($R^2 > 0.95$). The stress values at the PP skin show relatively scattered data points ($R^2 < 0.95$). This is due to variation of the skin thickness, and the thinner skin has a stress close to the PE core pipe. Overall the low level of stress in the PP skin compared to the core pipe indicates that the PE core pipe failure will immediately be followed by the PP failure because it has a lower level of stress resistance.

From the regression curve, the extrapolated mean hoop stress strength at 50 years can be obtained. Unaged NSPF is 9.67 MPa and that of 1.5SPF core PE pipe is 10.02 MPa. It is assumed that the PP and PE have the same elastic modulus as 1000MPa. In practice, the modulus of PP is normally lower than the pipe grade PE and therefore,

the PE layer will share more pressure than the PP layer and the extrapolated mean hoop stress strength will be greater than the value mentioned above.

To be more pessimistic, lower elastic modulus values of PE are considered from 500 MPa to 1000 MPa while the elastic modulus of PP is assumed to remain at 1000 MPa. Their hoop stresses were recalculated using the same method and plotted in Figure 4-27. Due to the decrease of PE modulus, its calculated 50-year strength decreases. The PP layer shares more pressure than the PE layer and its calculated 50-year strength increases as shown in Figure 4-28.

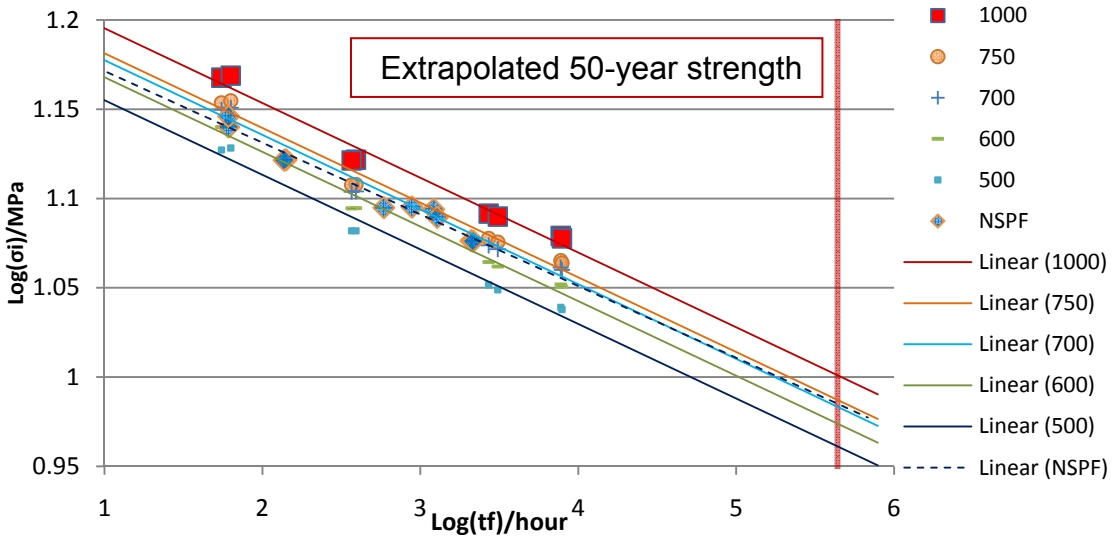

Figure 4-27 Creep rupture curve of unaged NSPF and 1.5SPF PE core pipe with different assumed elastic modulus (The number beside the legend is the assumed elastic modulus of PE, PP fixed at 1000 MPa)

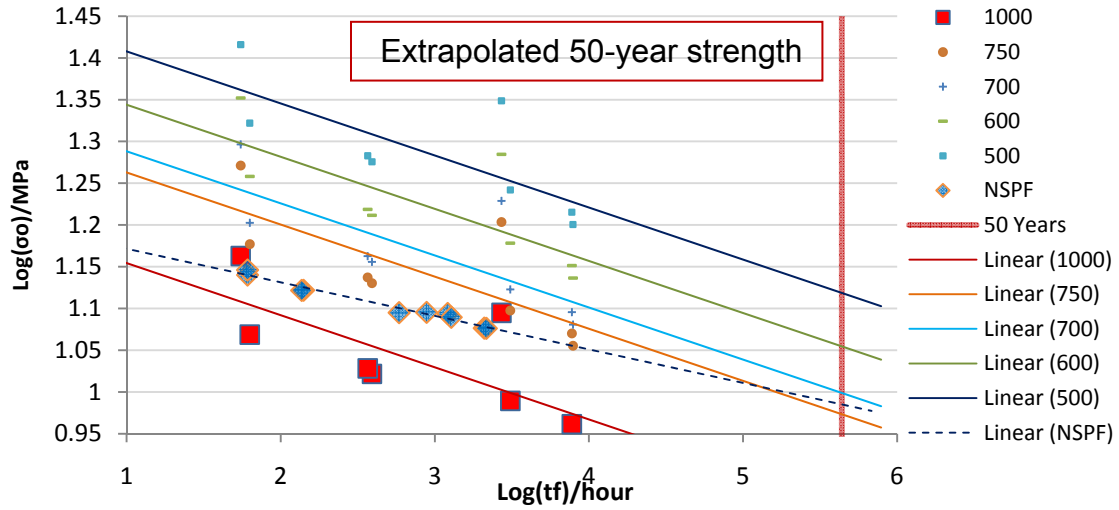

Figure 4-28 Creep rupture curve of unaged NSPF and 1.5SPF PP layer with different assumed elastic modulus (The number beside the legend is the assumed elastic modulus of PE, PP fixed at 1000 MPa)

It can be seen that with an assumed PE modulus as low as 750 MPa, the pipe is still stronger than the unaged NSPF while the PP modulus is fixed at 1000 MPa. This case is not common in practice. Therefore from the view of stress strength, the PP skinned PE pipe is stronger than its corresponding bare PE pipe made from the same grade of the same dimensions.

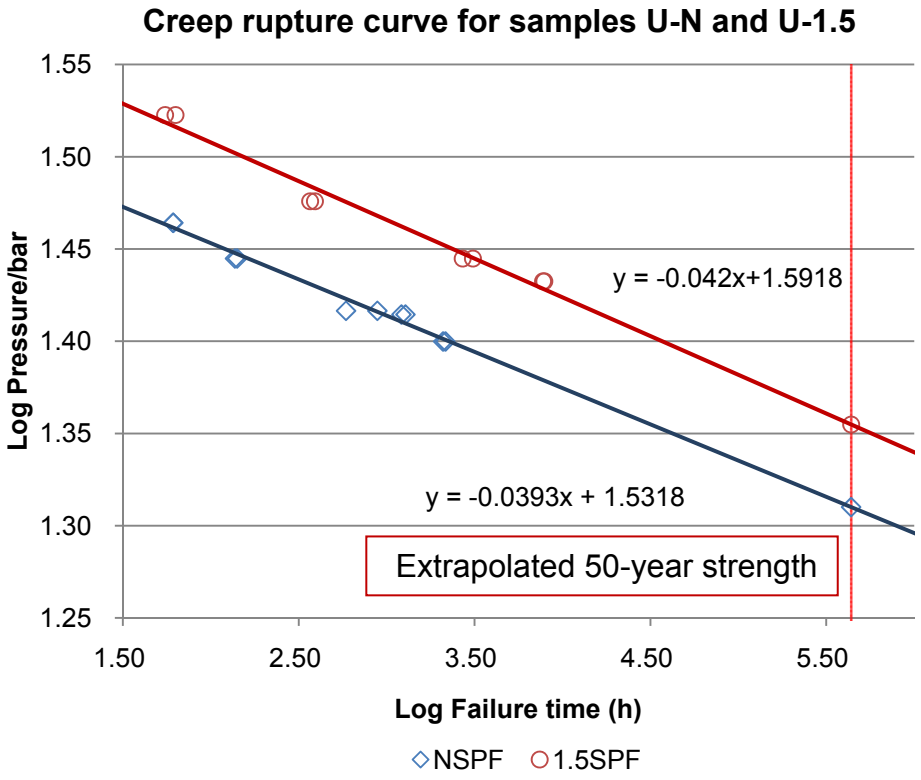

Figure 4-29 Creep rupture curve, log pressure against log failure time

Since in practice the skin pipes and bare pipe are both regarded as pipe of the same dimension (both are regarded as SDR11 pipe of 10mm pipe thickness), the inherent variation due to the differences in wall thickness can be reduced by using imposed pressure as a measure of strength. The results were redrawn using log pressure as vertical axis as shown on Figure 4-30. A linear regression curve can also fit to the two series of data. The extrapolated pressure strength of NSPF is 20.24 bars and 1.5SPF is 22.64 bars. If the same pressure was applied, there is an approximately 10.9% increase in the LTHS strength of the skinned pipe compared with the bare pipe at the 50-year extrapolation.

In the life time prediction standard [10], a lower prediction limit (LPL) of 97.5% was applied to the predicted value to ensure the validity of data. Due to the limited data points in the project, a 95% LPL will applied to the pressure strength. Since the maximum allowed pressure for the SDR 11 pipe in use is 16 bars [148], the safety factor of skin pipe is 22.64 x 95%/16 = 1.34. As the safety factor of conventional PE pipe is 1.25 [148], the safety factor increased by 7.2%

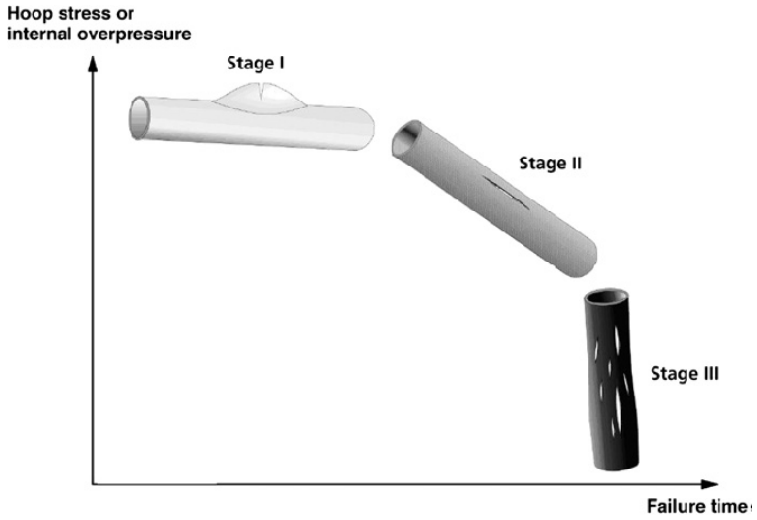

Figure 4-30 full view of a creep rupture curve [152]

Normally a higher temperature LTHS test (40, 60 or 80 ^{o}C) will apply which uses the Larson-Miller relation to shift the failure time to 50 years or longer time at room temperature [151] to get the full view of a pipe life as show on Figure 4-30. All the results obtained here fall in Stage I which is a ductile failure classified by blooming along the longitudinal direction and cracks along the hoop direction. Stage II and Stage III can be classified by crack along longitudinal direction. Failure in Stage III showed independency of stress. Such behaviour is due to brittleness caused by oxidation which is an indication of the depletion of antioxidant. The results from the pressure test has been found to fail in a ductile mode, therefore, it can be inferred that there is still an adequate antioxidant concentration in all failed unaged pipes.

The results from unaged samples showed that the skin pipe has better performance compared with the bare pipe including a higher overall density, reduced residual stress and better creep rupture resistance. In the next chapter, the bare pipe and skin pipe properties after aging will be compared and discussed.

Chapter 5 RESULTS AND DISCUSSIONS ON AGED SAMPLES

5.1 PP skin effect on the pipe surfaces

Oxidation degradation is a common aging effect and it happens at the surfaces in contact with oxygen. Therefore, both aged and unaged pipe surfaces with or without PP skin are examined and their results will be discussed in this section.

5.1.1 Surface free energy

Surface free energies of both aged and unaged samples are summarized in Table 5-1 as an expanded version of Table 4-1 that has been discussed in section 4.1.1. The results give general estimations of the surface property changes after outdoor weathering.

Table 5-1 Surface free energy summary for both unaged and aged pipe surfaces (unit: mN/m)

Samples*		Pipe I**	D***	P***	Pipe O**	D	P	Skin I	D	P	Skin O	D	P
BPP	U	**38.0**	37.9	0.2	**31.8**	29.8	2.0	-	-	-	-	-	-
	1GJ	**35.7**	32.1	3.6	**36.4**	25.0	11.4	-	-	-	-	-	-
	3GJ	**38.8**	31.1	7.6	**36.3**	31.9	4.4	-	-	-	-	-	-
	10GJ	**44.5**	32.8	11.7	**39.3**	30.9	8.3	-	-	-	-	-	-
NSPF	U	**33.3**	30.2	3.1	**36.8**	34.8	2.0	-	-	-	-	-	-
	1GJ	**39.1**	28.5	10.7	**37.1**	30.2	6.8	-	-	-	-	-	-
	3GJ	**41.9**	27.1	14.8	**40.0**	30.3	9.7	-	-	-	-	-	-
	10GJ	**44.2**	31.5	12.7	**37.6**	31.2	6.4	-	-	-	-	-	-
0.4SPF	U	**38.4**	33.4	5.0	**15.7**	12.9	2.8	**12.2**	8.3	3.9	**28.5**	24.1	4.4
	1GJ	**37.2**	31.1	6.1	**18.3**	14.0	4.3	**13.4**	9.7	3.8	**33.9**	23.6	10.3
	3GJ	**44.1**	30.7	13.4	**19.0**	14.9	4.0	**13.7**	9.6	4.2	**33.8**	30.9	2.9
	10GJ	**40.3**	28.5	11.8	**14.0**	12.2	1.8	**11.5**	9.0	2.5	**35.8**	28.1	7.7
0.8SPF	U	**36.0**	30.5	5.4	**15.0**	13.6	1.4	**9.8**	8.3	1.4	**31.3**	24.0	7.3
	1GJ	**36.4**	24.7	11.7	**17.0**	13.9	3.1	**12.3**	10.9	1.4	**33.1**	22.1	10.9
	3GJ	**40.1**	30.2	9.8	**16.2**	13.5	2.7	**10.5**	9.6	1.0	**32.4**	30.5	1.8
	10GJ	**41.0**	31.2	9.8	**13.6**	12.2	1.4	**9.6**	9.1	0.5	**34.7**	31.7	3.0
1.5SPF	U	**33.4**	33.0	0.4	**15.0**	11.4	3.5	**11.3**	8.6	2.8	**29.4**	25.2	4.1
	1GJ	**42.5**	27.7	14.8	**14.6**	10.3	4.3	**10.4**	9.5	0.9	**35.0**	25.4	9.6
	3GJ	**42.1**	32.4	9.7	**14.1**	10.5	3.7	**10.5**	9.7	0.8	**31.6**	29.2	2.4
	10GJ	**43.2**	30.2	13.0	**12.7**	10.9	1.8	**9.6**	8.9	0.6	**34.1**	30.8	3.3

*Aging conditions: U means unaged; 1GJ, 3GJ and 10GJ mean 1, 3 and 10 GJ/m^2 radiation dosages.
**Pipe surfaces: I means inner surface; O means outer surface.
***Surface free energy components: D means dispersive component; P means polar component.

In Table 5-1, data in the same row are from the same pipe type and weathered under the same radiation dosage. The colours pink, orange and red designate the radiation dosage 1, 3, 10 GJ/m^2 respectively. For the convenience of comparison, a bar chart based on Table 5-1 is drawn in Figure 5-1.

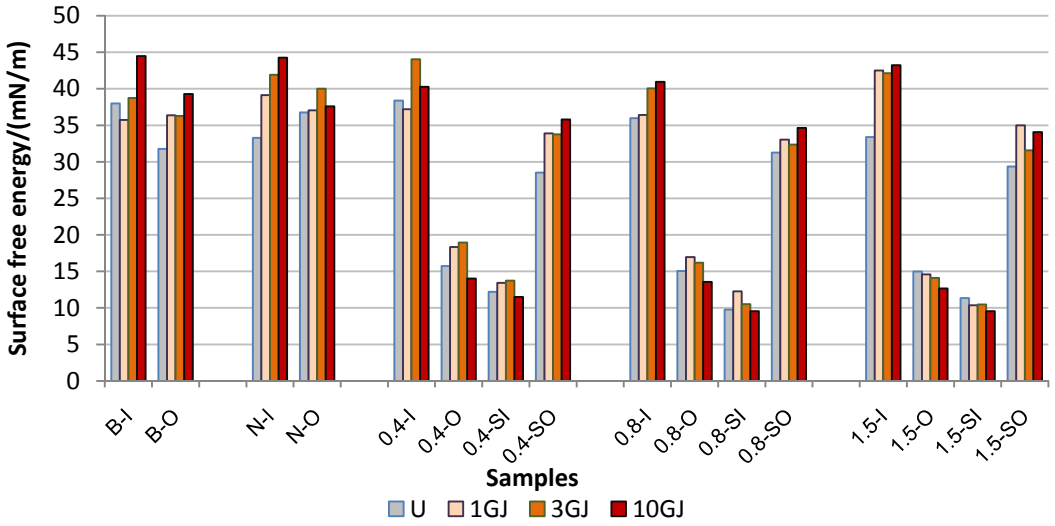

Figure 5-1 Surface free energy summary for both unaged and aged pipe surfaces

The data in the blue boundary in Table 5-1 is for the PE surfaces. Generally, the surface free energy increases as the sample been weathered. Such change is more obvious at the inner surface, which shows the surface free energy as high as 44 Nm after 10 GJ/m^2 outdoor weathering. The increase of the surface free energy is a sum up of its dispersive and polar components. The dispersive component decreases as the weathering proceeds while the polar component increases. Because the decrease amount from the dispersive component is smaller than the increase amount from the polar component, the overall surface free energy increases.

The decrease of the dispersive component may be because the -CH_3 group concentration increases at the outer surface of the sample exposed to air. The standard surface free energy value of a –CH_3 surface is 30 Nm [153] while the standard surface free energy value of a –CH_2- surface is 36 Nm [153]. The increase of -CH_3 group may be due to chain scission which results in more end groups at the PE chain end. The increase of -CH_3 group may also because of the migration of stabilizers. For example, hindered phenols and amines stabilizers normally have two -CH_3 groups next to -OH and >N-H functional groups as mentioned in section 2.3.

The increase of polar component may be because of the appearance of polar groups on the sample surface. It is possible that during aging oxidation produces oxygen atoms on the PE surface as ketones, acids, esters and hydro-peroxides during aging. On the other hand, the polar groups may also come from the stabilizer. For example, the hindered phenols and amines include –OH and >N-H group which are very polar.

The reason whether the change of the dispersive and polar components is due to oxidation or migration of stabilizers needs further investigation.

The data in the green boundary in Table 5-1 is from the PE/PP interface. It has been discussed in section 4.1.1, that due to the migration of adhesion reducer, the surface free energy at the interface decreased to less than half of the standard PE and PP surface free energy values. It can be seen from Figure 5-1 that, generally, there is a further reduction of the surface free energy at these interfaces after natural weathering. Most of the reduction is because both dispersive and polar component decrease to even lower levels.

Because the migrated adhesion reducer has a lower surface free energy, this adhesion reducer may aggregate rather than spread out on both PE and PP surfaces and small part of PE and PP surface still not covered by this additive, on the other hand, there may be vacant regions that the adhesion reducer has not occupied. After natural aging, such occupied area portion may become larger due to more of the adhesion reducer migrated to the pipe surface and shows a lower surface free energy. These surface free energy values at the PE side are higher than the PP side supports such assumption. Because the PP side is the source of the adhesion reducer, it is probable that the PP side contains more of this additive. In order to confirm above assumption, further investigation is required to be carried out.

The data in the brown boundary in Table 5-1 is from the PP skin outer surface. The surface free energy here represents PP since most of the adhesion reducer was washed away by water as discussed in section 4.1.1. Although the adhesion reducer may further migrate to the PP outer surface during natural weathering, it is likely to be

washed away by rain fall as well as by evaporation. Therefore, the surface free energy of this surface after weathering is still representing PP.

The overall surface free energy of the PP outer surface is smaller than that of the PE inner surface because PP has more $–CH_3$ than the PE. After aging, most of the surface energy increases on both surfaces. For the PP outer surface, this may due to the effect of washing away of the adhesion reducer. For the PE inner surface, it may also be because of unknown contaminations during weathering, oxidation, migration of stabilizer and other additives.

The changes of the surface free energy and its components are thought to be due to oxidation and/or migration of stabilizers or other additives, oxidation, etc. These explanations are mostly hypotheses. Further characterization has been carried out to confirm these explanations in the following sections.

5.1.2 ATR-FTIR

FTIR spectra of both PP and PE pipe sample surfaces were measured by the ATR technique as mentioned in section 3.3.2.2. In order to focus on the effect of oxidation after weathering, FTIR spectra in the range of 1850-1650 cm^{-1} and 3000-4000 cm^{-1}, which contain information of C=O and O-H/N-H group absorption bands were analyzed.

Because PP is more labile to oxidation during weathering than PE, the spectra of PP skin inner and outer surface are discussed first. The bare ProFuse pipe NSPF inner and outer surface were analyzed afterwards.

During discussion, peak fitting techniques were applied in the range 1850-1500 cm^{-1} to distinguish peaks of different oxidation products. The peak area was also integrated in the data processing procedure. The results are compared by location along pipe circumferential direction and then by different radiation dosages.

5.1.2.1 PP surfaces after weathering

The spectra of unaged and 1, 3 and 10 GJ/m^2 aged 0.4mm PP inner surface are normalized and summarized in Figure 5-2. The spectra of unaged samples from the PP inner surface were taken quarterly around pipe circumference and it was found that they could be superimposed to each other. One spectrum of each sample was randomly selected and is shown in Figure 5-2. The spectra of aged samples showed in Figure 5-2 were taken from location 1, which was at the top of the pipe during weathering. The normalizing procedure is by vertically shifting the spectra. These spectra, both from unaged and aged samples, are superimposed with each other before normalization. No obvious C=O and –OH group absorption bands can be identified except the amide group absorption peaks which are attributed to the adhesion reducer. A small absorption peak at 1737 cm^{-1} is possibly due to the ester groups in the phenolic antioxidant and hindered amine light stabilizer (HALS).

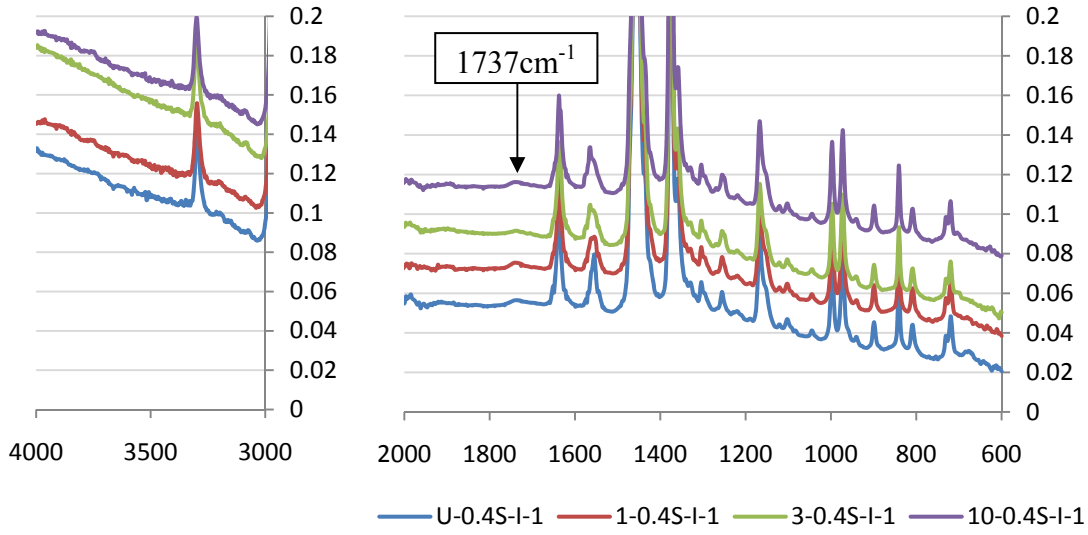

Figure 5-2 Spectra of PP inner surface after aging

There is an increase of baseline 3000 to 4000 cm^{-1} possibly because of over compensation of ATR correction to the baseline of each spectrum by the IR analysis software.

It can be generally concluded that at the PP inner surface before and after outdoor weathering, no obvious oxidation can be identified. The oxidation process during

outdoor weathering did not penetrate through the 0.4mm PP skin. Therefore, for a thicker skin such as the 0.8 and 1.5 mm, the same conclusion can be drawn.

The infra-red spectra of PP outer surface along the pipe circumferential direction after 1GJ/m^2 natural radiation were normalized and summarized in Figure 5-3. It can be seen that carbonyl groups of various chemical species were accumulated at the side facing the sun, while at the side shaded from the sun, the oxidation level is low and close to unaged samples.

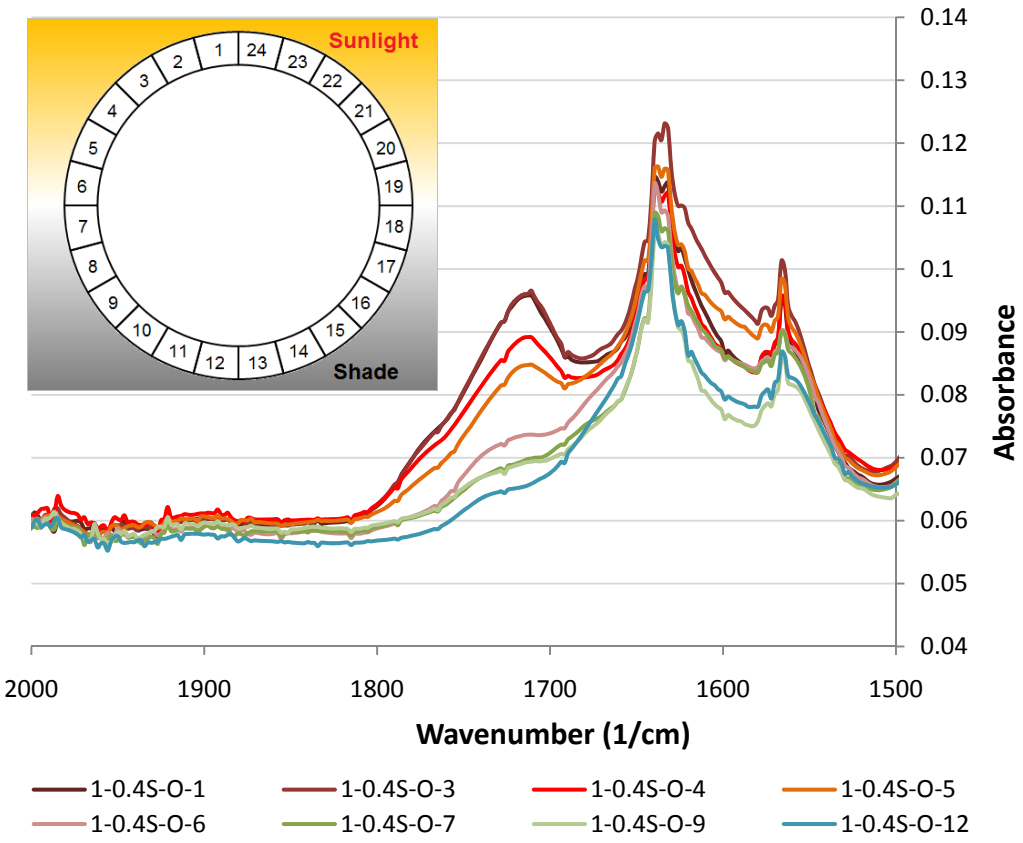

Figure 5-3 Spectra of samples 1-0.4S-O along circumferential direction in C=O stretching region

In order to quantify the various carbonyl groups produced after oxidation, the curves were deconvoluted by mathematical fitting. A Lorentz distribution function has been widely proved to be accurate enough for infra-red fittings [127] and it is adopted for the curve analysis.

The spectrum of the unaged sample (U-0.4S-O) in the range of 1850-1650 cm^{-1} was firstly subtracted from the aged sample spectrum then the baseline was corrected so

that the residual spectra are results from the natural weathering. Peaks of the residual spectra are identified by the second derivative function of the subtracted spectrum, with consideration of common photo-oxidation products of hydrocarbon compound such as ketones, ketoacid, carboxylic acids, esters, peracids and peresters [154, 155]. Lorentz distribution functions are fit at each peak through iteration program provided by the software OriginLab. The cumulated fit functions and the original residual spectra are plotted on the same figure as shown in Figure 5-4.

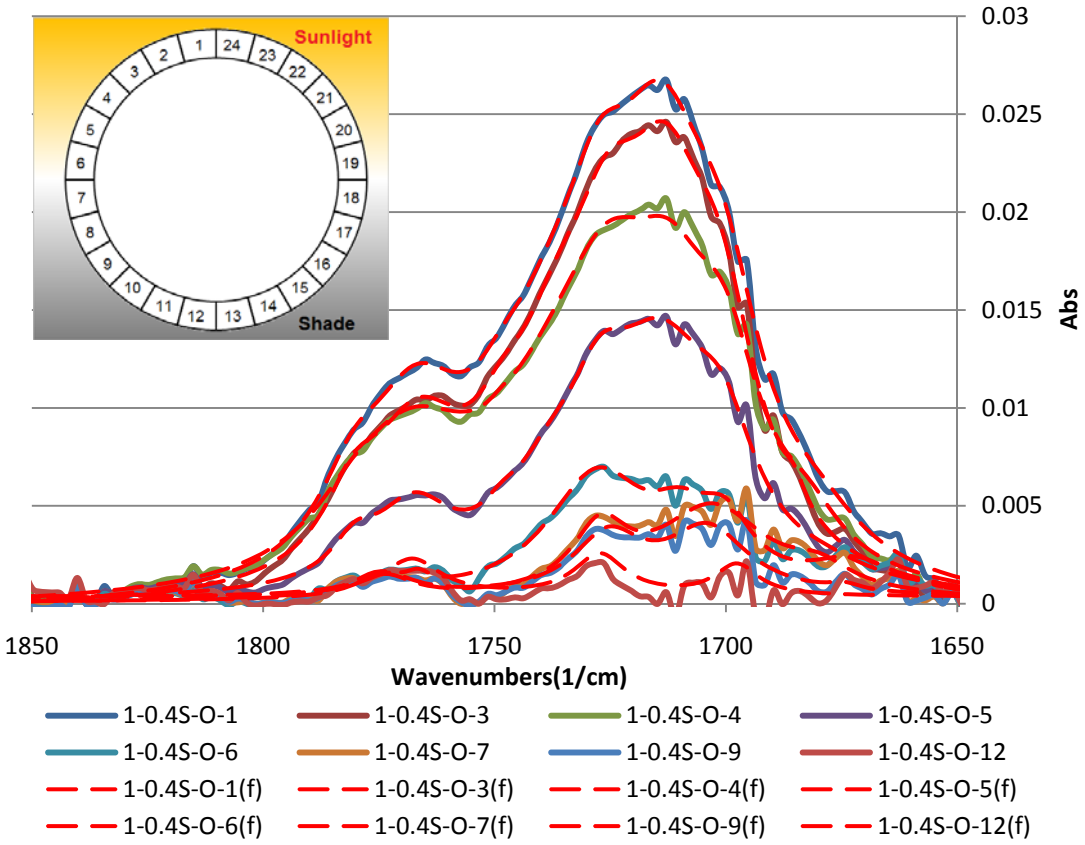

Figure 5-4 Cumulated fitted functions and original target residual spectra

Table 5-2 Quality of the peak fitting by coefficient of determination

Location on pipe	1	3	4	5	6	7	9	12
R^2	0.997	0.997	0.994	0.991	0.960	0.923	0.874	0.554

The quality of the peak fitting is evaluated by coefficient of determination (R^2) as shown in Table 5-2. For a perfect fitting, the R^2 value should be as high as 0.997 [154]. The fitting for the sample at the lower part of the pipe (shaded area) is worse than the oxidized sample. This is because the photo-oxidation products were produced at a low concentration, some did not appear, but the fitting parameters remain the

same for the more oxidized outer surface facing the sun. Also due to the low concentration of oxidation products, the baseline correction will alter these low values to a relatively greater extent. Therefore, the fitting parameter is less suitable for the fitting at these surfaces.

The cumulative area of the fitted Lorentz function as well as the area of its target spectra in the range of 1850-1650cm^{-1} are showed in Figure 5-5.

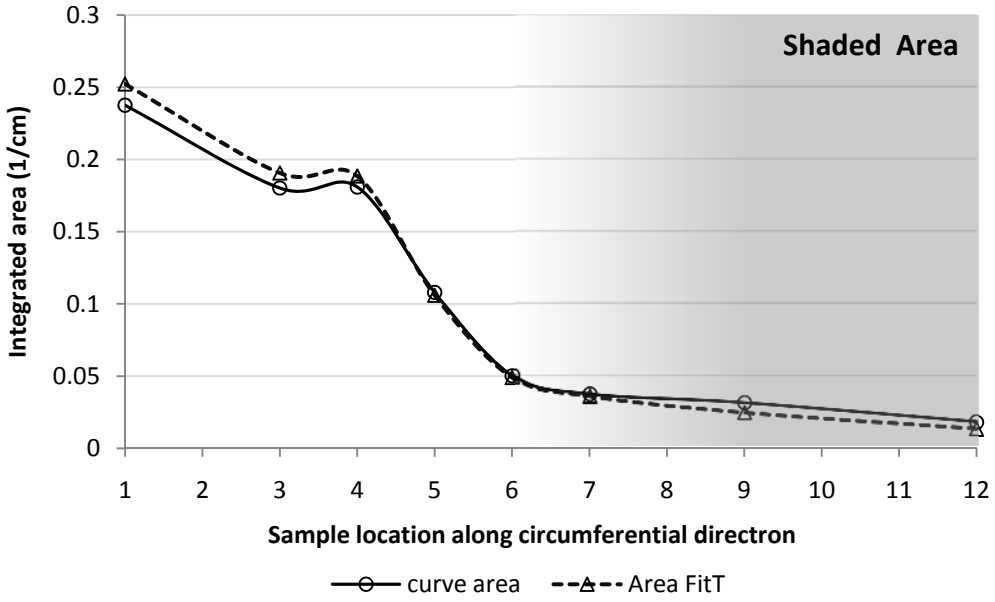

Figure 5-5 Cumulative area of the fitted Lorentz functions and their target spectra

Figure 5-5 reconfirmed the goodness of the curve fitting. It can also be seen that most oxidation occurred at the side facing the sun.

It is lengthy and not necessary to show all the fitting curves here because the same initial parameter was used for the infrared spectrum peak fitting iteration and the location of each fit peak function is similar (± 3 cm^{-1}). An example of the peak fitting result for sample 1-0.4S-O-1 in which oxidation is the most obvious under 1GJ/m^2 radiation is showed in Figure 5-6.

Table 5-3 indicates each fitted peak position and its assignment. The cumulative peak overlaps the spectrum. The coefficient of determination (R^2) calculated from the software for the cumulated peak is 0.997, showing that it is a satisfactory fitting.

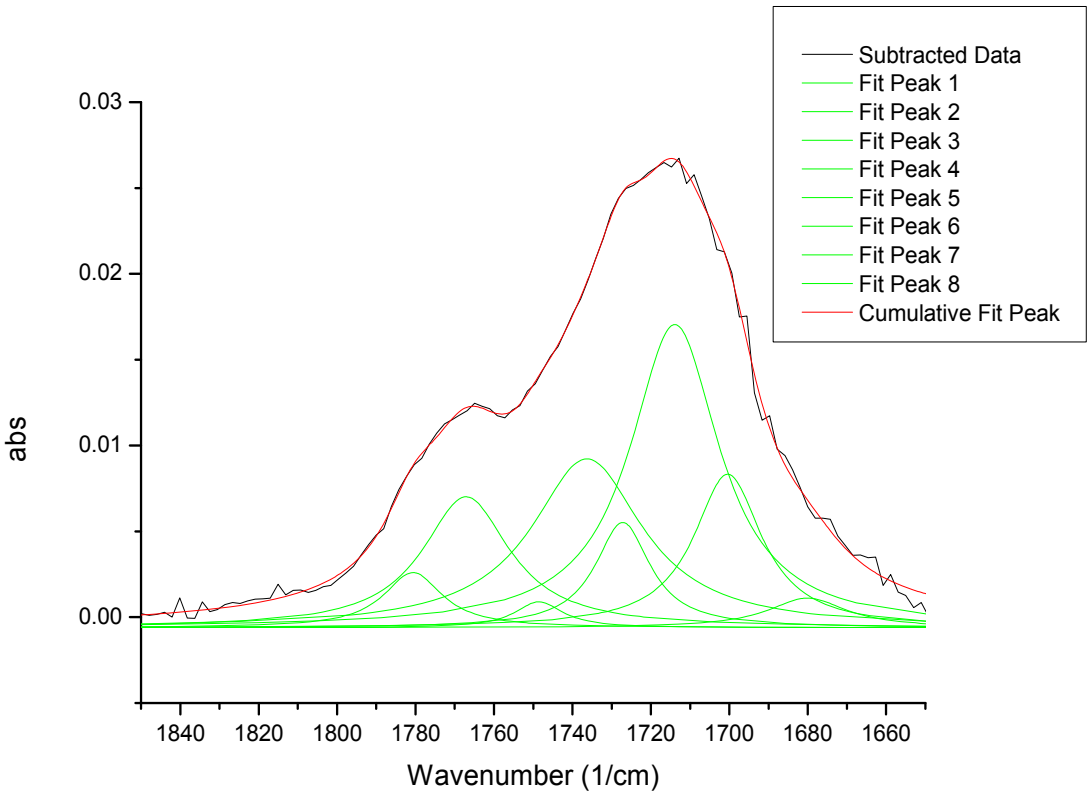

Figure 5-6 Peak fitting results of sample 1-0.4S-O-1

Table 5-3 Curve fitting positions and assignments

Component name	Peak position (1/cm)	Possible Assignment [154, 155]
Fit Peak 1	1684	Ketones, unsaturated α, β acids
Fit Peak 2	1701	Ketoacid (keto group)
Fit Peak 3	1714	Carboxylic acids (associated*)
Fit Peak 4	1727	Ketones
Fit Peak 5	1737	Esters
Fit Peak 6	1748	Peracids
Fit Peak 7	1767	Carboxylic acids (isolated**)
Fit Peak 8	1780	Peresters

*associated by hydrogen bonds **not associated by hydrogen bond

According to the Beer-Lambert law (Equation 5-1), the concentration of the oxidation product can be obtained.

$$C = A/(\varepsilon l) \tag{5-1}$$

where A is the integrated area of absorption band, l is the light path length and ε is the extinction coefficient.

In the case of ATR, the light path length is proportional to the depth of penetration during the total reflectance. The penetration depth was defined by the following equation.

$$d_p = \frac{\lambda}{2\pi n_1 \left(\sin^2\theta_{eff} - n_{21}^2\right)^{1/2}} \quad (5\text{-}2)$$

where d_p is the penetration depth, λ is wavelength, n_1 is the refractive index of the ATR crystal, $n_{21}=n_2/n_1$ is the ratio of the refractive indices of the sample (n_1) and of the crystal (n_2) and θ_{eff} is the effective angle of incidence.

As the sample material and ATR accessory are the same, the denominator of the right hand side equation (5-2) is a constant. A spectrum equivalent to a constant penetration depth was calculated by multiplying the intensity of the spectrum at each wavenumber λ_i by a coefficient λ_{ref}/λ_i, where λ_{ref} is a reference wavenumber. After the calculation, the light path length (l) can be regarded as the same for all the infra-red light with different wavenumbers.

Table 5-4 Summary of extinction coefficient of oxidation products [154]

Component name	Possible Assignment	Extinction coefficient (cm/mmol)	Relative coefficient
Fit Peak 2	Ketoacid (keto group)	6880	1
Fit Peak 3	Carboxylic acids (associated)	16800	2.44
Fit Peak 4	Ketones	6880	1
Fit Peak 5	Esters	10800	1.57
Fit Peak 7	Carboxylic acids (Isolated)	16800	2.44

The extinction coefficients are summarized in Table 5-4 [154]. The absorption value of the Fit Peak 1, 6 and 8 are so small that they are negligible for the qualitative analysis of the photo-oxidation products. For the purpose of comparison, relative coefficient is defined as the ratio of the extinction coefficient of the fitted component and the extinction coefficient of ketones. The relative concentration can be calculated by dividing the area of the fitted component with the relative coefficient and path

length. As the light path of each infrared light in the test is the same, it is taken as unity 1 during the calculation.

Figure 5-7 summarized the relative concentrations of oxidation products. Each peak fitted component was plotted against the location along the pipe circumferential direction. It can be seen that after 1 GJ/m^2 natural weathering from the side facing the sun (location 1 to 6), five possible oxidation products include ketoacid (keto group), carboxylic acids (associated), ketones, esters and carboxylic acids (isolated) were produced to a similar level.

The averaged value at the right hand side of Figure 5-7 indicates that most of these oxidation products are formed at the side facing the sun. At the side shaded from the sun, the oxidation products that can be observed are ketoacid (keto group) and ketones. But due to the relatively poor fitting results at this location, no other oxidation products after the 1GJ/m^2 aging can be further confirmed.

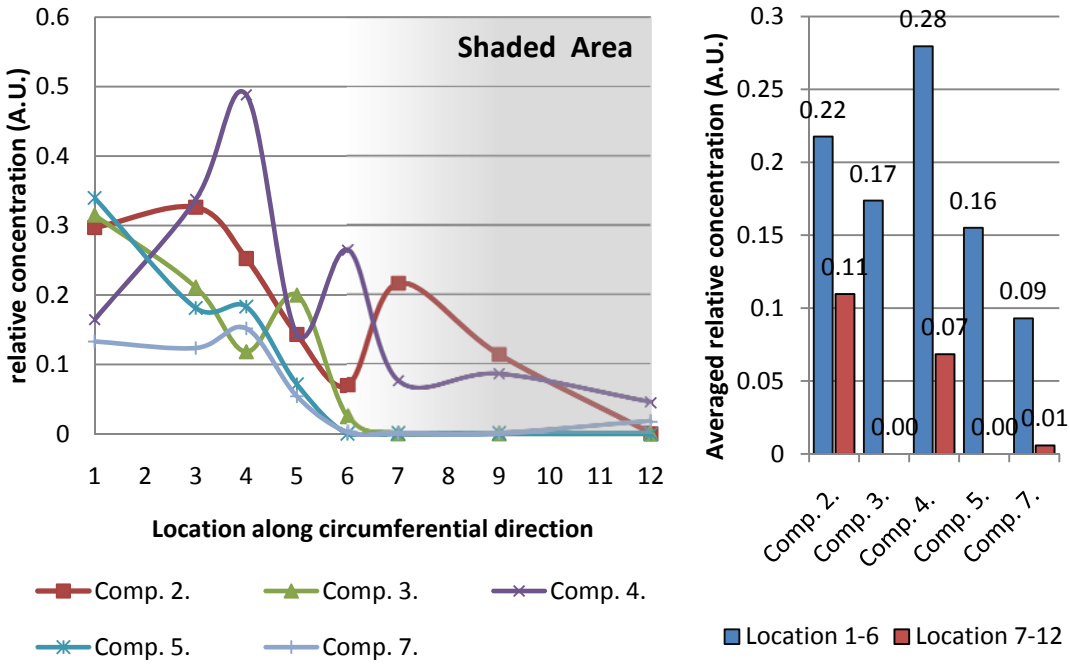

Figure 5-7 Relative concentration of oxidation products

The oxidation products are indications of various photo-oxidation reactions occurred during weathering. By referring to the literature, these reactions are summarized in Figure 5-8.

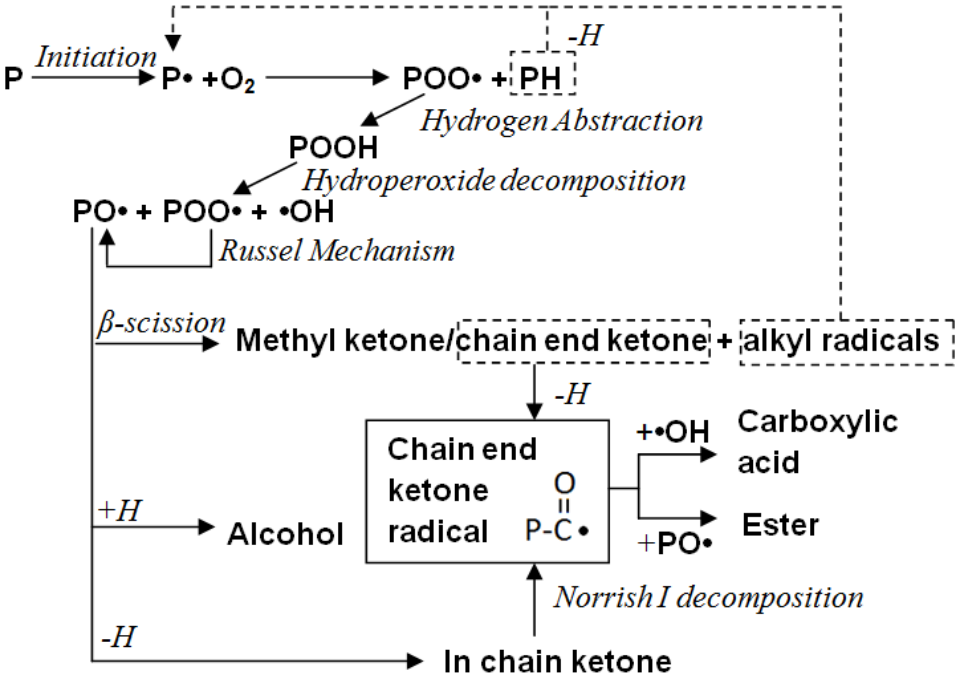

Figure 5-8 Photo-oxidation scheme of the PP skin

It can be inferred that ketones may arise from many sources includes the Russel mechanism, β-scission and Norrish I and II decomposition as reviewed in section 2.2.2.5. Ketones are further reacted to produce carboxylic acids and esters. Carboxylic acids and ester groups may also arise from Norrish I decomposition similar to the scheme of LLDPE showed in Figure 2-18. The associated carboxylic acid may due to the intramolecular decomposition of hydroperoxide sequences along the PP backbone as mentioned in section 2.2.2.4, which is more likely to happen in thermal oxidation. The hydroperoxide sequences will react with surrounding polymers and produce carboxylic acids. As the carboxylic acids are close together, hydrogen bonds are more likely to form between them. The isolated carboxylic group may arise from both inter- and intra- molecular hydroperoxide decomposition which happened more randomly. Keto-acid may come from the combination mechanism of the ketones and carboxylic acids formation. Esters may come from recombination of alkoxyl radicals and keto type radicals.

It should be note that the extinction coefficient in Table 5-4 is based on the possible assignments from reference [154]. It is possible that different group absorption peaks are located close to each other (several wavenumbers) and cannot be distinguished by

the second derivative function of the spectrum using the software. In this case, absorption peaks of the same group located at other wavenumbers should be used for quantitative analysis. Therefore, caution should be made in assigning functional groups to a specific peak. Some chemical groups can be distinguished indirectly by chemical reactions, for example, hydroperoxide groups can be identified by iodometric titration [154], alcohol by NO treatment [155] and carboxylic acid by SF_4 gas [155]. These techniques are time consuming and the accuracy largely depends on the conversion rate and reaction extent, since the effect of aging on the properties of the PP skin is not the major concern in this project, these techniques are not carried out at this stage.

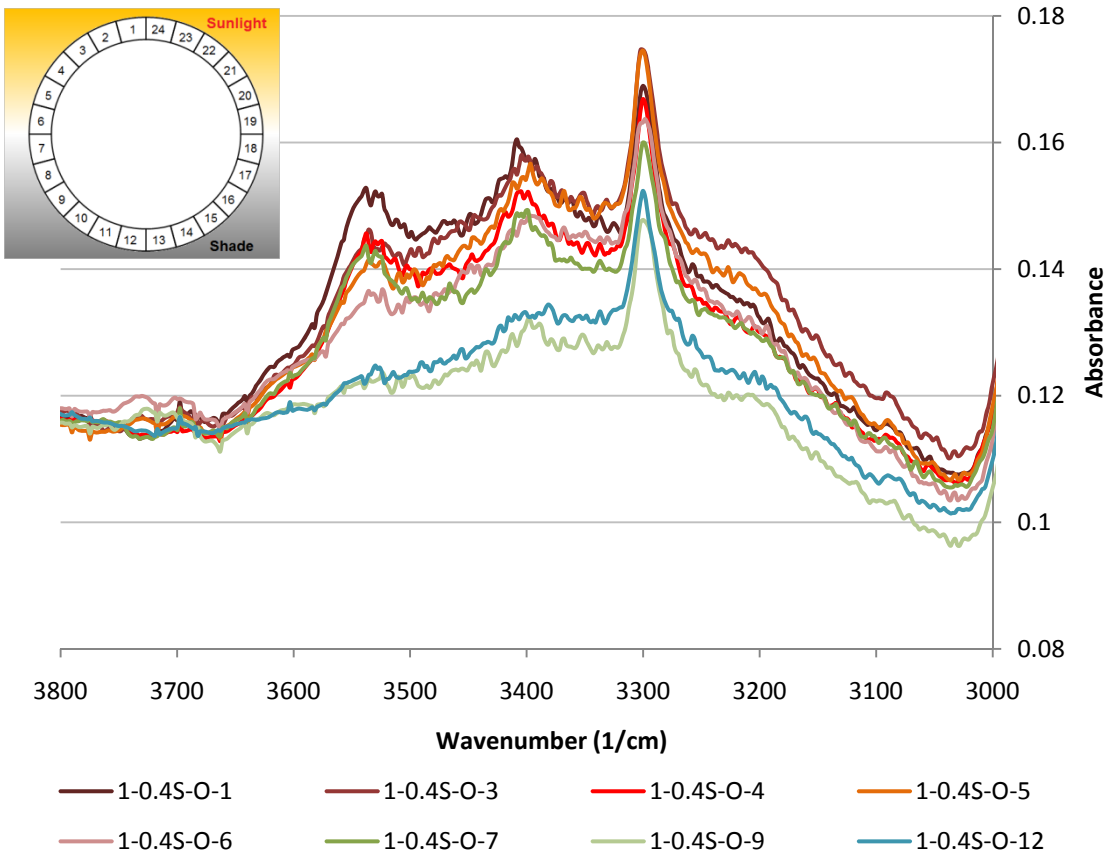

Figure 5-9 Spectra of samples 1-0.4S-O along circumferential direction in -OH vibration region

The analysis of 1GJ aged sample at the range of 1850-1650 cm^{-1} indicated the possible photo-oxidation products containing C=O group at the PP outer surface facing the sun. The following analysis at the range of 4000-3000 cm^{-1} will give complementary information about the photo-oxidation products containing –OH and –NH groups. The –OH vibration absorption band includes information of the possible

oxidation products such as alcohol, carboxylic acid and hydroperoxide groups. The spectra at this region are normalized by vertical shifting and are summarized in Figure 5-9.

A broad absorption peak can be identified in the O-H stretching region. Besides, several obvious peaks can be found at 3300, 3408 and 3538 cm^{-1}. It has been suggested in section 4.1.2 that the peak at 3300 cm^{-1} is assigned to secondary amide N-H group from the fatty acid amide adhesion reducer. The other two peaks at 3408 and 3538 cm^{-1} and the broad hydrogen bonded –OH peak need further analysis.

Before analysis, all the spectra are baseline corrected. The baseline anchor points are set at two ends of the broad –OH band at 3000 and 3670cm^{-1}. The shape of the broad hydrogen bonded –OH band is traced out along its shape from the spectrum by a smooth line. The –OH band is then used as a baseline and subtracted from the spectra again so that the –OH band and the other peaks are separated. The residual spectrum and the –OH band are shown in Figure 5-10 and Figure 5-11. The U-0.4S-O spectrum is incorporated into the 1GJ/m^2 aged spectra as a control and the same treatment is applied.

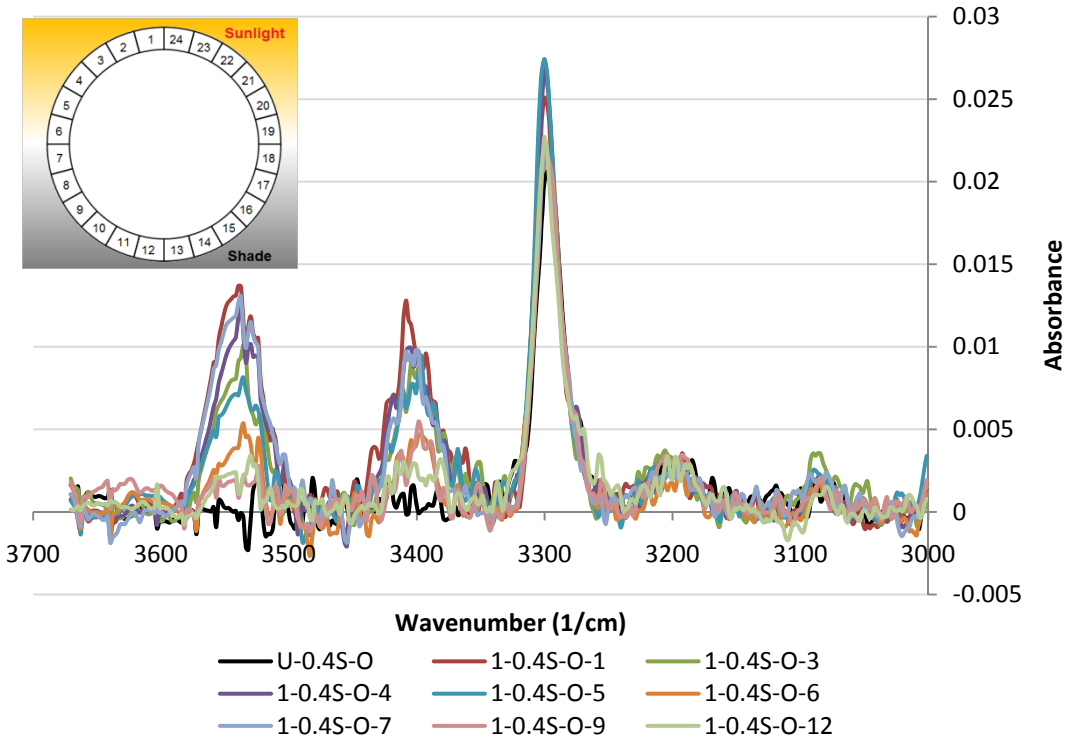

Figure 5-10 spectra at –OH vibration region with broad –OH band subtracted

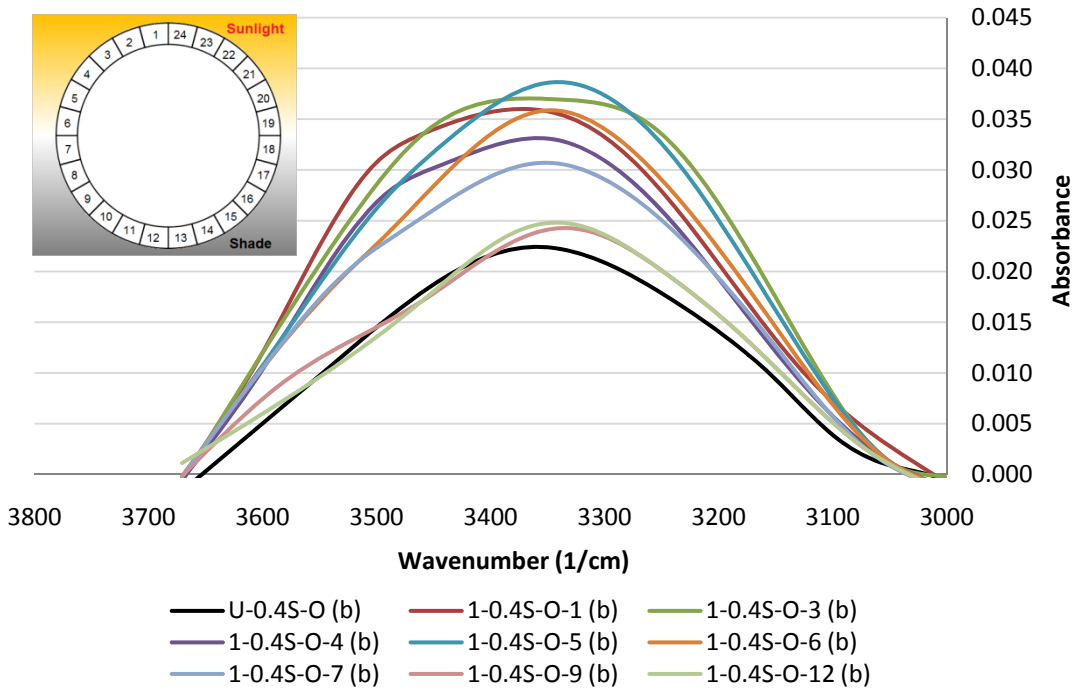

Figure 5-11 the subtracted broad –OH vibration bands

In Figure 5-10 and Figure 5-11, the 1GJ/m^2 aged spectra are further subtracted by the U-0.4S-O spectrum so that the residual spectra are solely the result from weathering. The area of peaks at 3408, 3538 cm^{-1} and the area of the –OH band are integrated and then ratioed to the area from 1309-1510 cm^{-1} which is attributed to the PP backbone absorption band, to produce indices for the peaks 3408, 3538 and associated –OH band. These indices are summarized in Figure 5-12.

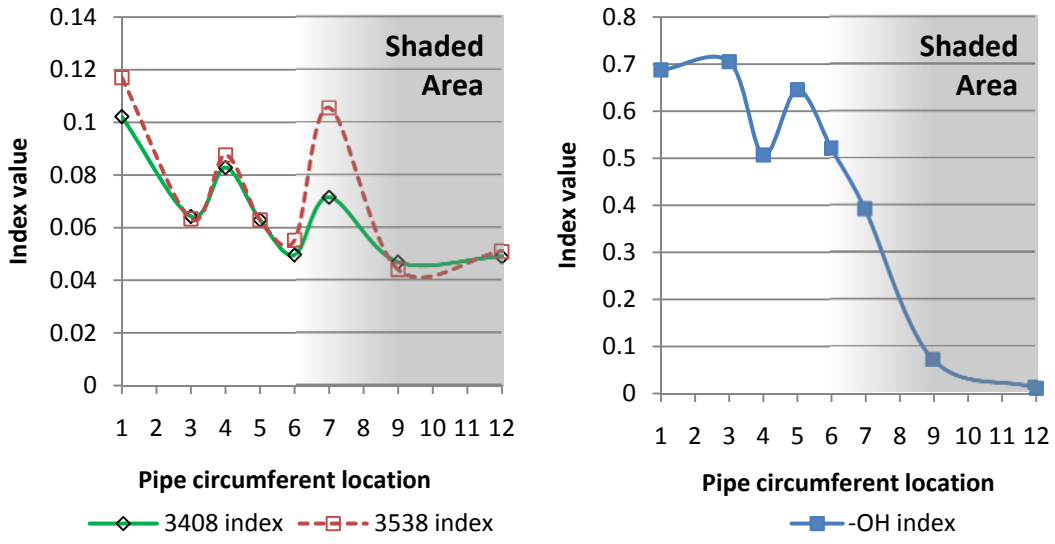

Figure 5-12 indices for the peaks at 3408, 3538 cm^{-1} and the -OH band

The peaks located at 3408 and 3538 cm^{-1} shows irregular distribution along the pipe circumferential direction, but the ratio of the absorptions at 3408 and 3538 cm^{-1} are mostly constant. This indicates that the absorption values of these two bands are attributed to the same functional group and its concentration distribution is not affected much by the different radiation intensity along pipe circumference during weathering. In the later discussion on 3GJ/m^2 and 10 GJ/m^2 aged sample spectra, it is found that these two bands disappeared, indicating that these peaks may not results from the weathering. Due to lack of knowledge of the formulation of the PP skin material, it is difficult to draw any conclusions on this compound. But the functional groups which have vibration absorption bands at such high wavenumber value are rare, limiting the assignment searching range for these bands. After referencing the standard absorption peak, these two bands may be attributed to the primary amide N-H vibration absorption [156, 157].

It has been inferred that the peaks for the primary amide do not result from weathering. Therefore, the primary amide is less likely derived from the secondary amide during the aging process. Figure 5-10 shows that the absorption value of the secondary adhesion reducer peak located at 3300 cm^{-1} is very consistent and not changed along the circumferential direction, indicating that the concentration of the adhesion reducer at the PP outer surface did not change during the weathering and further reducing the likelihood of a link between the secondary amide and the primary amides.

The primary amide may possibly be another additive that has been incorporated in the PP skin. The use of a slip additive (lubricant) in the automotive industry for PP-based interior and exterior parts to enhance the scratch resistance of the materials has been reported [159]. A migratory amide slip additive is typical for this application. Reports showed that this type of additive needs some time (several hours to days [159]) to migrate to sample surface after molding. In the case of pipe, the scratch resistance requirement is lower than for the automotive parts. The migratory slip additive may be incorporated in the PP skin at a lower concentration than those used in the automotive industry. Due to the low concentration, the migration time for such an additive is longer. It is reasonable that after 45 days of 1GJ/m^2 radiation, the additive has migrated onto the pipe surface. But as weathering proceeds, most of the additive

is washed away and is no longer present in the PP skin. Therefore, the primary amide bands cannot be found on the 3 GJ/m^2 and 10 GJ/m^2 aged sample surfaces. The unaged sample is stored in a cool and shaded area, so the additive has probably not migrated onto the surface hence cannot be identified.

The left hand graph of Figure 5-12 shows fluctuation of the indices of 3408 and 3538 indicating irregular concentration distribution of the corresponding groups along the pipe circumference. The effect of weathering on the migration of these compounds is not a major interest in this project hence no further investigation was carried out. On the right hand graph of Figure 5-12, the associated –OH group index along pipe circumference is similar to the C=O group index that showed in Figure 5-5 and Figure 5-7. On the side facing the sun, build up of associated –OH reconfirms that the side subject to direct sunshine undergoes photo-degradation. These –OH group may belong to alcohols and hydroperoxides.

As the radiation dosage increases, the oxidation products increase. The spectra of sample 1, 3 and 10-0.4S-O were baseline corrected then normalized by vertical shifting. These spectra are summarized in Figure 5-13. The spectra of sample U-0.4S-O are also included for comparison.

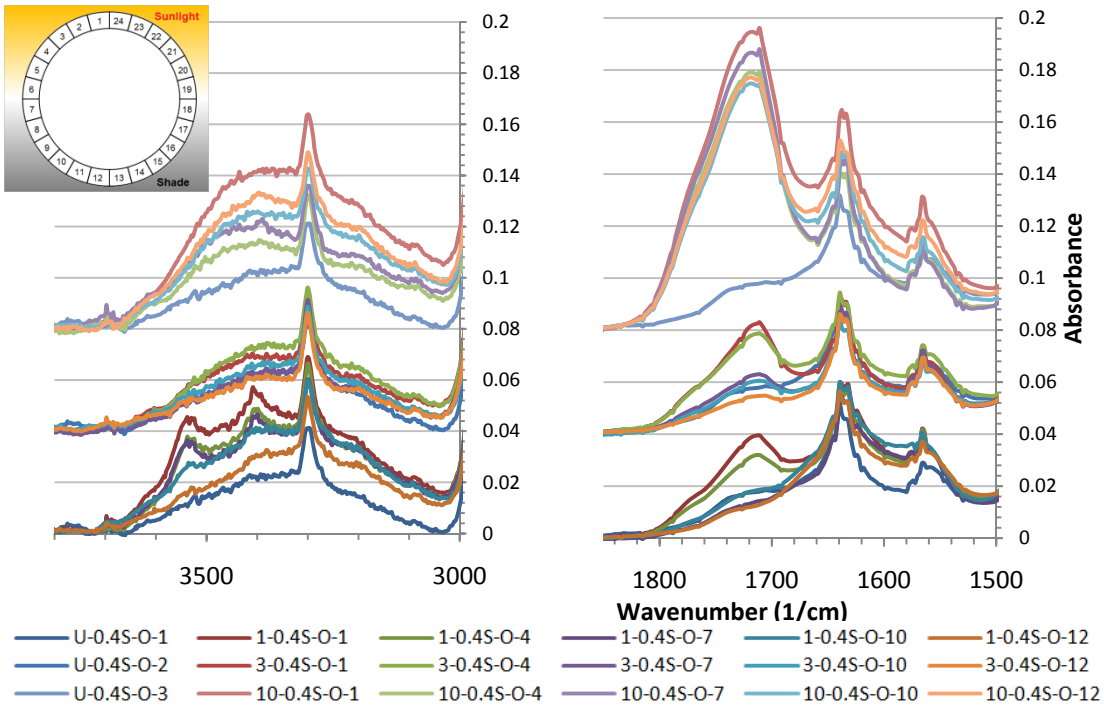

Figure 5-13 Summary of 1, 3 and 10-0.4S-O spectra along pipe circumference

Figure 5-13 showed that in the C=O absorption region that the spectra of 3GJ/m^2 aged samples are similar to 1GJ/m^2 aged samples. All of the spectra of 3GJ/m^2 aged samples still have difference oxidation level between the side facing the sun and the side shaded from the sun. The spectra of the shaded side are close to the unaged spectra while the spectra of the side facing the sun have a similar level of carbonyl type oxidation products. The 10 GJ/m^2 aged samples showed severe oxidation along the whole pipe circumference. In the C=O absorption region, the shape of the 10 GJ/m^2 aged sample spectra in the C=O absorption region is similar to the spectra of 1 and 3 GJ/m^2 aged samples with enhanced intensity.

Although the side of pipe shaded from the sun was not subject to direct solar irradiation, the UV portion of the solar irradiation was reflected or scattered and could also cause severe photo-degradation and produce similar oxidation products to the side facing the sun. This finding shed light on the protection of polymer from photo-oxidation. As the reflected solar irradiation also has a degradative effect to the polymer, the polymer should be shaded in a totally dark area. As the PE core pipe is totally shaded by the PP skin from solar irradiation, the PE core pipe would be free from photo-oxidation. However, the IR portion of the solar irradiation will have heating effect and lead to change of crystal structure and additive distribution within the core PE pipe and these will be discussed later.

For the comfort of comparison, the aged spectra in the C=O absorption region are subtracted by the unaged spectra U-0.4S-O, the residual spectra are baseline corrected and the area are integrated. Carbonyl index is produced by dividing the area of C=O band by the area of C-H band and the results are summarized in Figure 5-14. From the figure, it can be seen that the rate of oxidation during the weathering is not a constant. At the beginning of photo-oxidation of the PP skin between 1 and 3 GJ/m^2 aging, there is a slowdown of oxidation. Later between the aging processes of 3 and 10 GJ/m^2, an auto-acceleration of oxidation occurred.

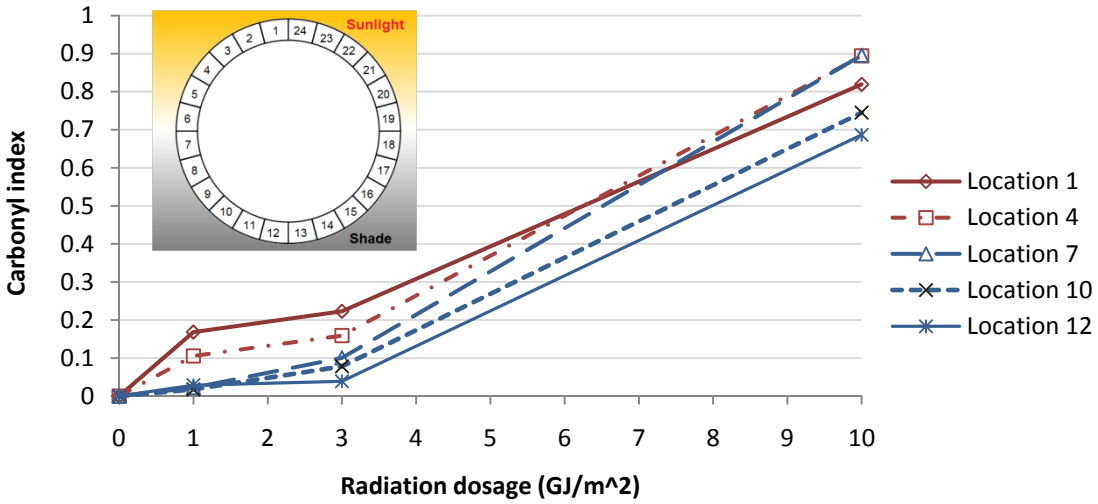

Figure 5-14 Change of carbonyl index with radiation dosage

In order to distinguish different photo-oxidation products, the spectra of the 3 and 10 GJ/m^2 aged samples at location 1 the top facing the sun were peak deconvoluted with the same parameters that have used for the 1GJ/m^2 aged samples. The relative concentrations are calculated from the fitted peak and summarized in Figure 5-15.

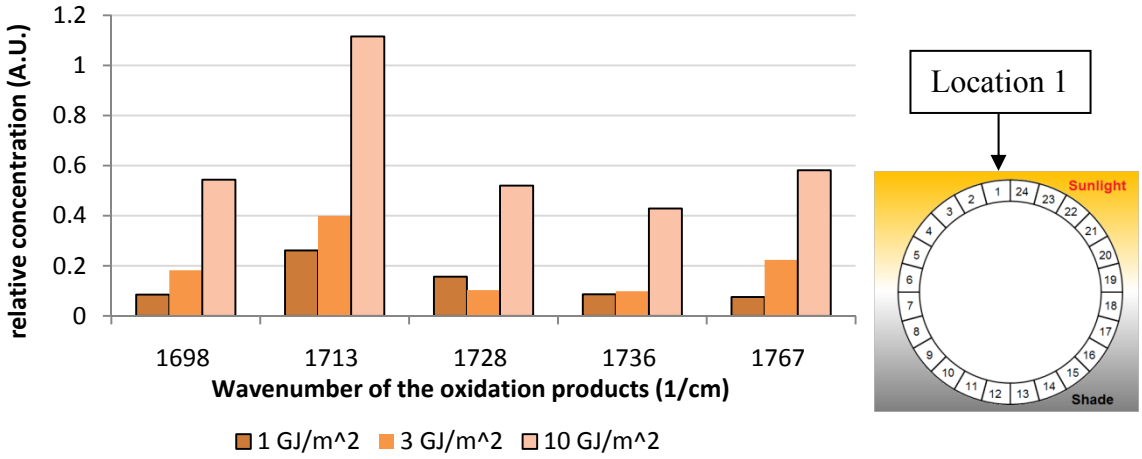

Figure 5-15 Curve fitting results for infrared spectra of all aged samples at location 1 at the top facing the sun in carbonyl region

The assignments of the peaks in Figure 5-15 are summarized in Table 5-3. In each aging condition, the peak at 1713 cm^{-1} which is attributed to hydrogen bond associated carboxylic acid and 1767 cm^{-1} which attributed to isolated carboxylic acid show the highest concentration among the oxidation products containing carbonyl group. This may because carboxylic acid is a more oxidized form than other oxidation products. Further oxidation of other oxidation products may results in production of

carboxylic acid group (esters is also a possible product but at a relatively lower concentration in this case). A drop of 1728 cm^{-1} which attributes to ketones can be found for 3GJ/m^2 aged samples. This may be due to further conversion of chain end ketones into carboxylic acid.

In the –OH/ –NH vibration absorption region, the spectra of 1GJ/m^2 shows obvious primary amide N-H stretching peaks at 3408 and 3538 cm^{-1} while the spectra of 3 and 10 GJ/m^2 aged samples do not. The reason for this difference has been discussed previously. The secondary amide N-H stretching peak at 3300 cm^{-1} did not change over the whole aging process, indicating that adhesion reducer still present on the skin outer surface. The associated O-H peak is traced out and integrated by the same method that was used to treat the spectra of 1 GJ/m^2 aged samples, but the unaged spectra could not be subtracted because some –OH absorption values of the aged samples are below the spectra of the corresponding unaged spectra which will produce a negative absorption value. The integrated area is divided by the area of the C-H absorption peak to produce a hydroxyl index. The indices are summarized in Figure 5-16.

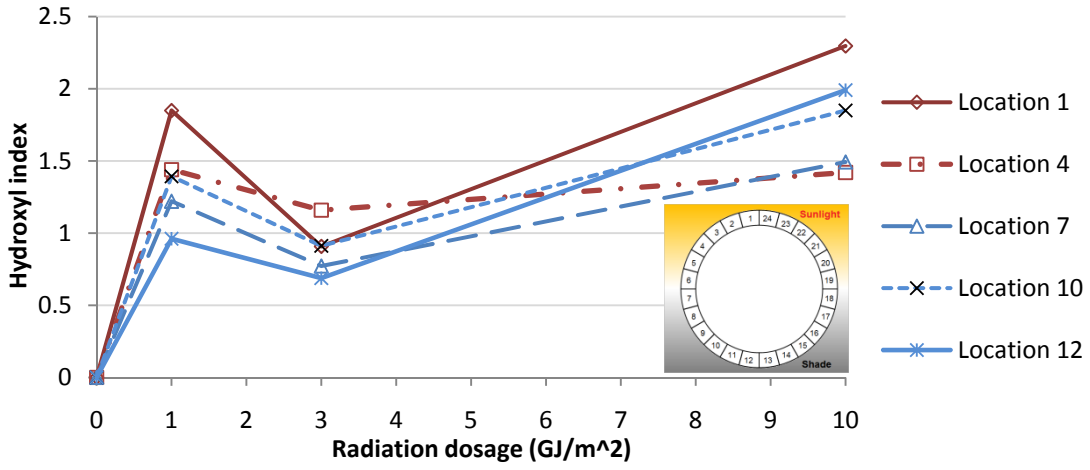

Figure 5-16 Change of hydroxyl index with radiation dosage

From the figure, it can be seen that as solar irradiation proceeds, there is a reduction in the –OH group for samples weathered between 1 and 3 GJ/m^2, indicating transformation of the existing –OH group. This may be due to the consumption of –OH containing species, for example, phenolic antioxidant or oxidation products alcohol and hydroperoxide. There is a further built up of –OH group after 10GJ/m^2

radiation. But this time, it seems that the shaded area shows higher –OH group concentrations than the irradiated side. Since the –OH containing group may be consumed and reproduced and it is associated with several chemical species and the spectrum is broad without any obvious peaks, it is difficult to draw any further conclusions from the spectra in this region.

Figure 5-16 and Figure 5-14 both showed two stages of photo-oxidation during the outdoor weathering process up to10 GJ/m^2 irradiation. The slowdown of the production of photo-oxidation product may due to many reasons. First of all, from the point of view of the polymer itself, it is possible that the built up of a photo-oxidation product would make transformation of such product to other chemical species much easier and therefore, altering the kinetics of the photo-oxidation process as shown by the slow down stage. Secondly, from the point of view of stabilizers (antioxidants), it is widely accepted that there exists a critical concentration of the stabilizers, below which, the oxidation become self-accelerated [158]. As the antioxidants were consumed and below the critical concentration, the photo-oxidation process maybe self-accelerated and the production rate of photo-oxidation products increased as shown by the auto-acceleration stage.

This section discussed ATR-FTIR spectra of the PP skin pipe inner and outer surface before and after aging. For the skin inner surface, no obvious oxidation was identified. For the skin outer surface, different levels of photo-oxidation which were observed in the C=O and –OH absorption regions suggested that at early natural radiation weathering stage with 1 and 3 GJ/m^2 dosage, aging on the pipe side subject to direct solar irradiation began first while the shaded side was still protected by stabilizers. Later with 10GJ/m^2 dosage radiation, the whole skin surface is oxidized to a similar level. Peak fitting techniques showed the relative concentration of five possible oxidation products containing C=O groups during weathering, among which carboxylic acids had the highest concentration after 10 GJ/m^2 aging. There is a slowdown of oxidation between 1 and 3 GJ/m^2 weathering and an auto-acceleration afterwards. The analysis of the-OH/ –NH absorption region shows that another primary amide additive may exist in the PP skin after analysis. Using the -OH group absorption peak to monitor the aging process is difficult due to its broad peak shape and its possible consumption in aging.

5.1.2.2 PE surfaces after weathering

Compared with the spectra of PP skin surfaces, the PE surfaces are supposed to be less labile to oxidation because of the lack of tertiary hydrogen in the repeat unit. The following discussion will focus on the C=O vibration absorption of the PE pipe outer and inner surfaces of both skinned pipe and uncoated pipe between 1850-1500 cm^{-1}.

PE core pipe outer surface of 0.4mm skin pipes (0.4SPF) are analyzed first. The spectra were normalized by vertical shifting and summarized in Figure 5-17.

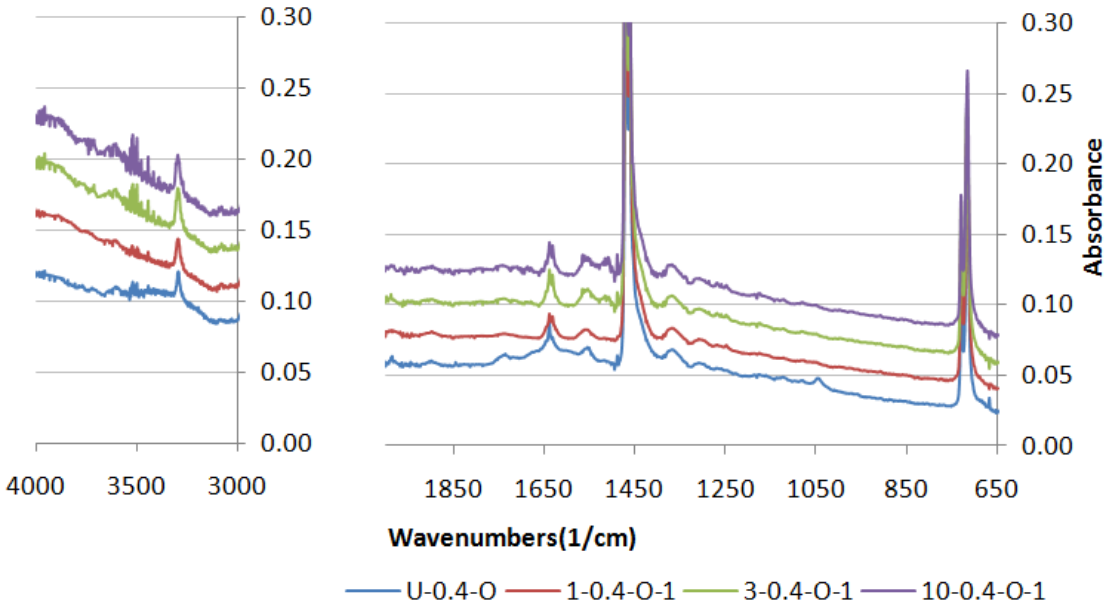

Figure 5-17 IR Spectra of 0.4mm skin PE core pipe outer surface before and after weathering

It has been shown that the PP inner surface remained intact and the oxidation did not penetrate into the inner surface in Figure 5-2. Figure 5-17 shows, as expected, that the PE core pipe outer surface which is contact with the PP inner surface is free from oxidation. No obvious oxidation can be identify either in both –OH or C=O absorption regions. Therefore, it can be concluded that the 0.4mm thick PP skin protects the PE core pipe from oxidation, even after 10 GJ/m^2 natural weathering.

It can be inferred that for thicker skin pipes, the PP skin will still protect the PE core pipe outer surface. Therefore, the PE core pipe outer surfaces of pipes with a thicker skin have not been investigated here.

The variation of location along the pipe circumference created differences in radiation and caused variation in the concentration of oxidation products in the PP skin around the pipe circumference. The following discussions on the uncoated PE pipe outer surface will also take these two factors into consideration to investigate the oxidation effect.

The spectra of sample surfaces at the top facing the sun during weathering (Location 1) under the three radiation levels are summarized in Figure 5-18. An unaged spectrum is also incorporated in the figure as a control.

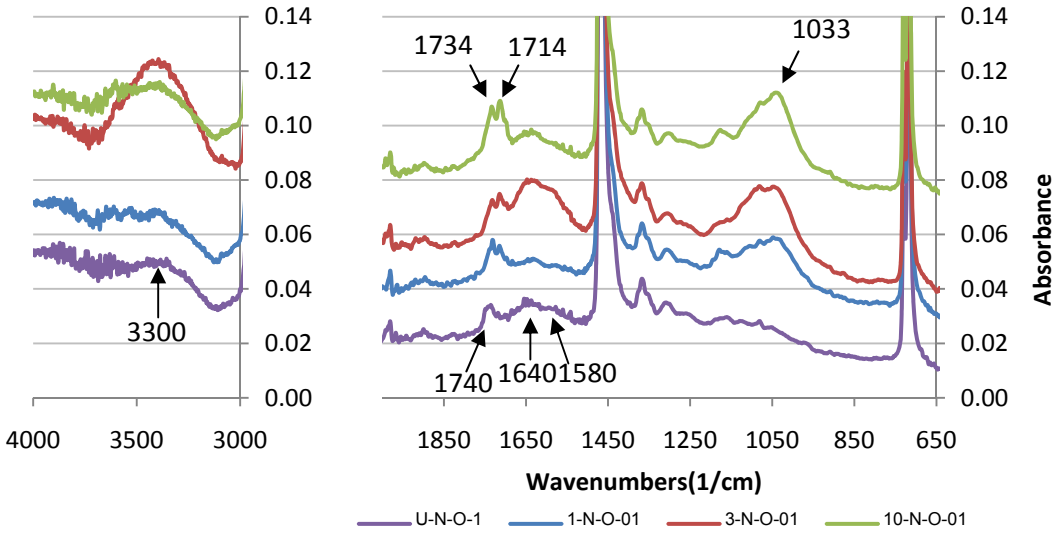

Figure 5-18 IR Spectra of uncoated PE core pipe outer surface at location 1 before and after weathering

There are several changes after weathering. Firstly, there is a gradual increase of the C=O stretching peak located at 1780-1680 cm^{-1}. After 10 GJ/m^2 weathering, the oxidation was still not as obvious as for the PP skin under the same radiation level. However, it is still possible to examine PE oxidation in this region. A smooth base line was taken before integration as shown in Figure 5-19. The area in this region was integrated then divided by the C-H absorption peak between 1390 and 1500 cm^{-1} to produce a carbonyl index (CI). The CI results are summarized in Figure 5-20. For unaged and 10 GJ/m^2 aged samples, the measurement was repeated at least 3 times on different samples and their standard deviation value is incorporated in Figure 5-20 as error bars.

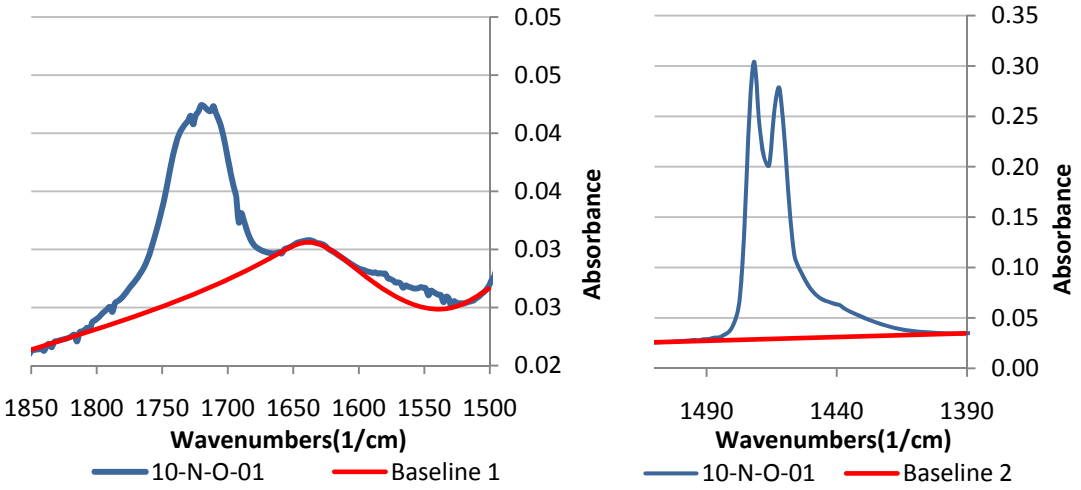

Figure 5-19 Example of baseline taken for peak integration

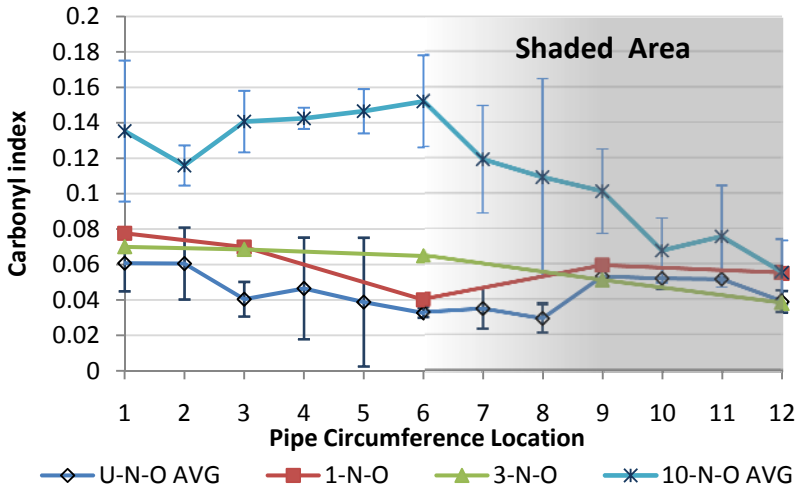

Figure 5-20 Carbonyl index of uncoated PE pipe outer surface along pipe circumference

It can be seen that for 1 and 3 GJ/m^2 aged samples, the CI level is within the variation range of unaged samples. The carbonyl absorption of these three samples is probably due to the ester groups in the antioxidants which have an absorption peak located at 1740 cm^{-1}. Therefore, it can be concluded that there is still no oxidation on the 1 and 3 GJ/m^2 aged uncoated pipe outer surface.

10 GJ/m^2 aged samples show higher CI value at the side facing the sun, indicating oxidation happened at these locations. There is a gradual decrease of CI towards the shaded side, but a large deviation exists for locations 7 to 9, only locations 10 to 12 can be confirmed to have a level of CI that is as low as the unaged samples. At this

point, the oxidation of PE pipe outer surface is confirmed. But the oxidation is to a less obvious level than the PP outer skin even after 10 GJ/m^2 aging.

The second variation in the spectra after weathering is some irregular changes in peaks at 1640, 1580 cm^{-1} and 3300 cm^{-1}. After extensive search, several reports using FTIR to characterize phenol and its radical derivatives has been found useful to explain these peaks [160]. It is assumed that these peaks may be attributed to the phenolic antioxidant and its derivatives. The peak at 1640 cm^{-1} is possibly attributed to C=C bond which is in the 1, 4 cyclohexadiene structure [160] (a meso-structure of phenolic antioxidant). The peak at 1580 cm^{-1} may assign to radical C-O· which is in the phenolic radical structure [160]. However, it is less likely that the radical have such a long time after weathering (at least one month for transportation plus various storage periods) and this assumption needs further characterization such as the ESR to confirm. The production of phenolic radical is also a dehydrogenation process of the phenolic antioxidant and it should be reflected in the –OH peak region. The fluctuation of the broad peak at 3300 cm^{-1} with radiation level may due to transformation of phenolic compound into its corresponding radicals, but it is difficult to draw any conclusions since many hydrogen-bonded –OH groups are also reflected in this region.

Finally, a broad peak at 1033 cm^{-1} is found to increase with radiation level. Because of its broad range, possible absorption peaks include aromatic C-H and C-O in primary alcohols and C=O. It will be shown later that the outer surface may be contaminated by sand dust. The spectrum of the dust, mainly SiO_2 also has a broad absorption peak at this area, making the analysis more complicated.

In order to distinguish the aging effect, the spectra of unaged and 1, 3 and 10 GJ/m^2 aged spectra were normalized and summarized in Figure 5-21. It can be seen that as the aging proceeds, the peak at 1033 cm^{-1} increases. For the 10 GJ/m^2 aged sample at the side shaded from the sun, the peak is most intense. It decreases towards the side facing the sun on which surface oxidation has been observed. Similar but less obvious trends can be found for the peaks 1640 and 1580 cm^{-1}. In contrast a reverse trend can be found in the C=O group absorption region between 1714 to 1680 cm^{-1}, indicating oxidation. It has been mentioned that the peaks at 1640, 1580 cm^{-1} may attributed to

phenolic antioxidant, so taking the trend observed above into consideration, the broad peak at 1033 cm^{-1} may also be attributed to the stabilizers and their derivatives. Besides, the SiO_2 peak has a maximum at 1108 cm^{-1} but there is no obvious peak at this location. Due to lack of information about the stabilizers, the results from the ATR-FTIR technique cannot be interpreted further.

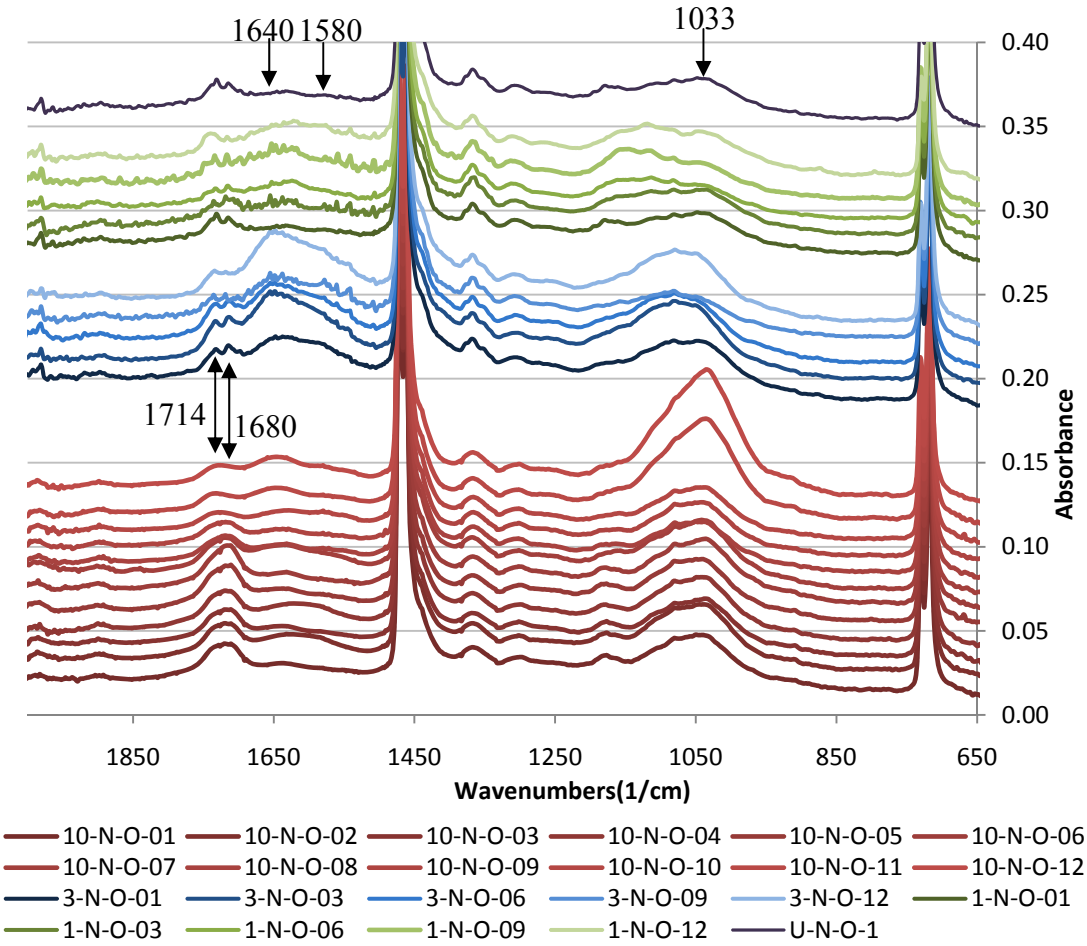

Figure 5-21 IR spectra of uncoated PE pipe outer surface along pipe circumference

From the above analysis, minor oxidation on the 10 GJ/m^2 samples has been observed in the spectra of the uncoated PE pipe outer surface while the 1 and 3 GJ/m^2 aged samples are remain protected by the stabilizers from oxidation. Peaks that may be attributed to stabilizers are also identified.

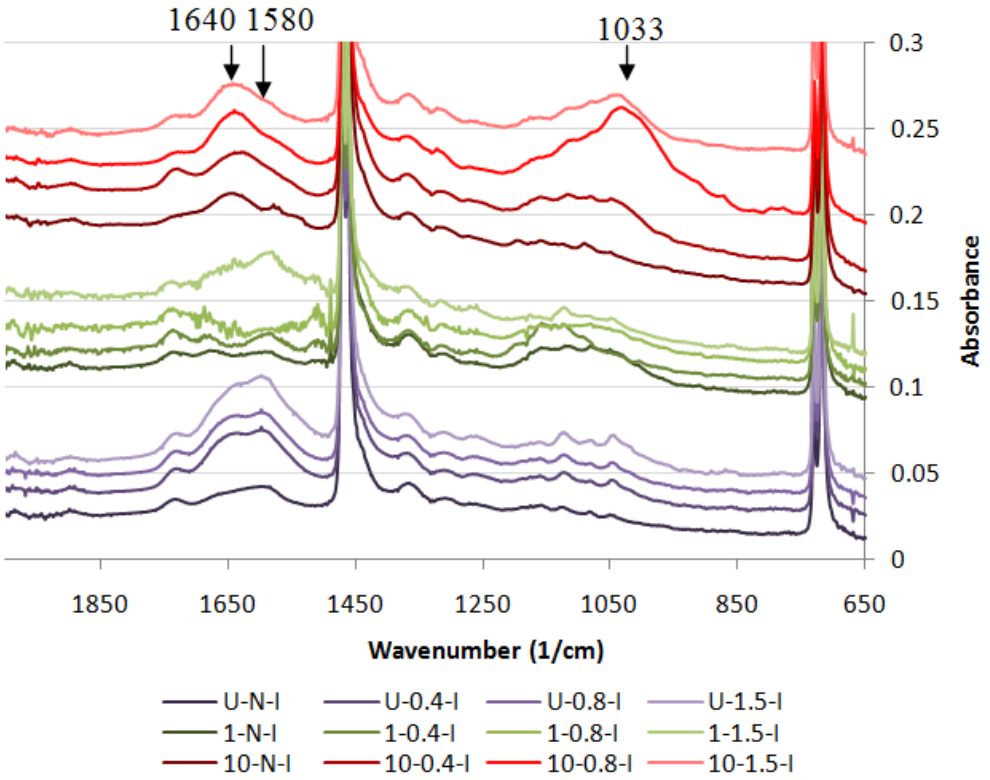

Figure 5-22 IR spectra of pipe inner surface before and after aging

The inner surface of the pipe is in contact with oxygen. Because it is located in the bore of the pipe, the temperature of the inner surface is supposed to be lower than the outer surface and it is supposed free from direct solar irradiation. Hence, thermal- and photo-oxidation is unlikely to happen during the natural weathering at the pipe inner surface. The spectra of the inner surface are summarized in Figure 5-22 for further analysis. In Figure 5-22, the region which was believed to be attributed to stabilizers still shows variations at 1640, 1580 and 1033 cm^{-1} under different weathering conditions.

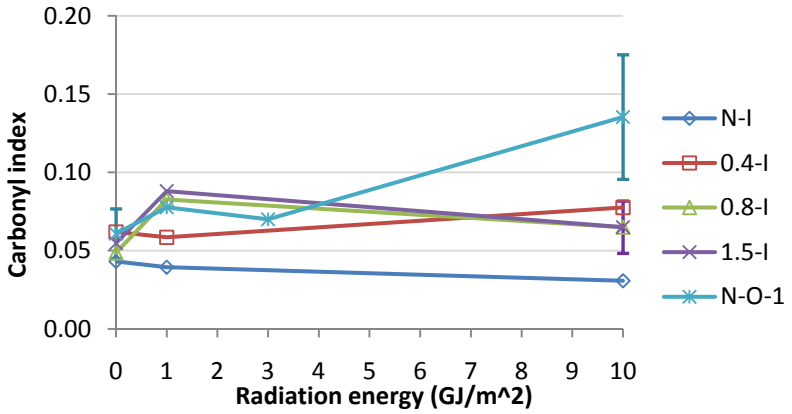

Figure 5-23 Carbonyl index summary for PE core pipe inner surface before and after aging

The C=O absorption peak is integrated as in Figure 5-19 and quantified by carbonyl index. The CI values are summarized in Figure 5-23 as a function of radiation energy. The CI values of the uncoated pipe outer surface at the top facing the sun during weathering are also incorporated in the figure. The figure shows that all the CI values of the inner surface are below the 10 GJ/m^2 oxidized side of sample 'N-O-1'. Therefore, they are still protected by stabilizers and unoxidized. Although the PE pipe inner surface is not oxidized as shown by the ATR-results, the OIT results which will be discussed later suggest that there is antioxidant loss at this surface which leads to oxidation.

This section discussed the IR spectra of the PE inner and outer surfaces. It is showed that the PP skin coated PE outer surface remains intact as virgin material and the uncoated PE outer surface is still protected by the stabilizers during outdoor weathering up to 3 GJ/m^2 radiation. Slight oxidation was observed after 10 GJ/m^2 aging for this surface. During the whole weathering process in this project, the PE inner surface was protected by the stabilizers. The PE surfaces that were subjected to natural weathering have a better overall photo-oxidation resistance than the PP surfaces. The IR spectra also shed light on some information that was possibly attributed to stabilizers. Due to lack of information of the stabilizer package of the material used, it is difficult to discuss it in detail. Hence, the antioxidant content was further analyzed by the OIT test which will be discussed in section 5.2.1.

5.1.3 XPS

In order to further investigate the surface chemical compositions, especially the oxidation state of polymers, XPS was used. The XPS detects signals at atomic level and is therefore more sensitive than FTIR techniques. The 10 GJ/m^2 aged uncoated samples and the sample with 0.4mm skin PE core pipe outer surface at the top are analyzed along with an unaged uncoated PE pipe outer surface as a control. The atom percentage of the samples is summarized in Table 5-5, and the XPS peaks of C1s and O1s are summarized in Figure 5-24.

Table 5-5 Compositions of the PE core pipe outer surfaces before and after aging (atom %)

Sample	C	O	N	Si	Al	Na	Mg	S	Cl
10-0.4-O-2	98.7	0.5	0.8	0.0	0.0	0.0	0.0	0.0	0.0
10-B-O-1	65.3	23.6	0.8	6.1	1.2	0.6	2.4	0.0	0.0
10-N-O-2	81.2	12.7	1.1	3.6	0.7	0.3	0.0	0.0	0.2
U-N-O	87.1	9.6	0.8	1.4	0.0	0.6	0.0	0.3	0.3

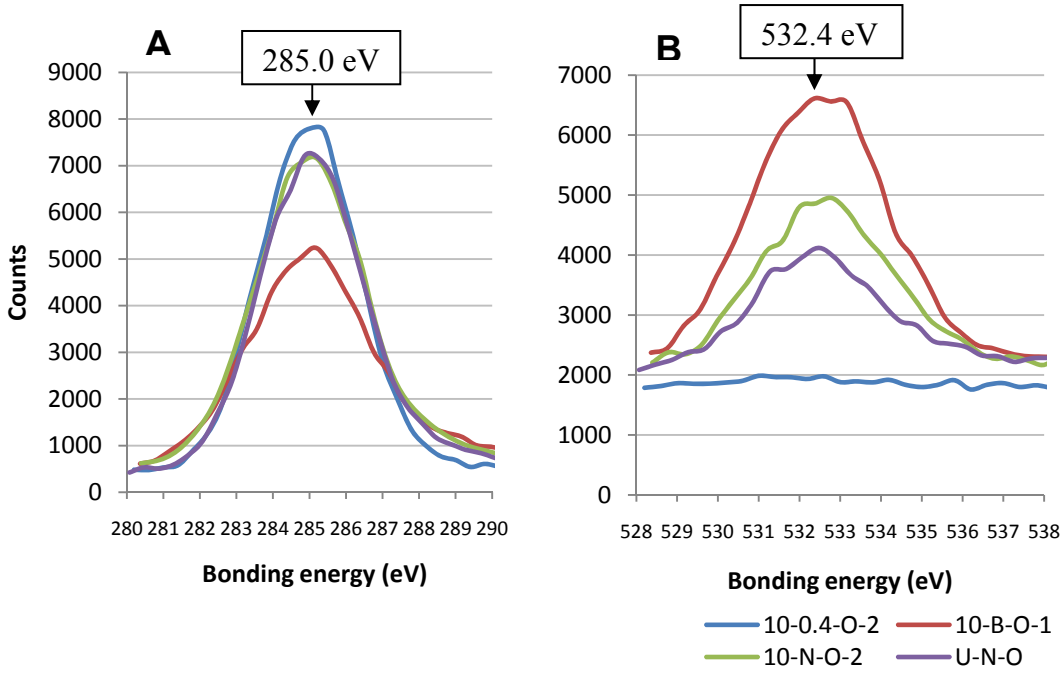

Figure 5-24 XPS spectra of A) C_{1s} and B) O_{1s} peaks

IR results showed that the 0.4mm skin PE core pipe outer surface is free from oxidation. In Table 5-5, only trace oxygen and nitrogen atoms are detected for sample 10-0.4-O-2 confirming the results from the IR spectra. The oxygen atom may come from ester groups of additives such as phenolic stabilizers and the nitrogen atom may come from the fatty acid amide adhesion reducer and hindered amine light stabilizers. However, no significant O_{1s} peak in Figure 5-24B, it is not possible to tell where the trace of oxygen came from by the XPS results.

The remaining three samples are all uncoated pipes. Compared with the coated pipe result in Table 5-5, an increase in Si can be found for all the three samples. This atom is probably come from contamination during the weathering process. As indicated previously in section 3.2, the weathering site is at a desert area near Phoenix city and sand storm can occur at the site. The uncoated pipe surface may be contaminated by the sand dust which contains silicon dioxide and other oxidized mineral compounds.

The results also shows that the pigmented pipe (sample 10-B-O-2) has a higher composition of metal atom Si, Al and Mg and atom oxygen, indicated that this sample contaminated more seriously than the unpigmented pipes. Although an O_{1s} peak was found for the uncoated pipes, because the O_{1s} peak of SiO_2 is similar to the O_{1s} peak of oxidized products such as carbonyl, acid and alcohol (532.5 eV for SiO_2 and 532.2 eV for both C=O, O-C=O and 532.8eV for C-O-H), it is difficult to attribute the peaks in these spectra, especially when the compositions of the contaminants are unknown.

Alternatively, comparing the intensity of the C_{1s} peak at different bonding energy positions can indirectly distinguish whether the sample is seriously oxidized or not. The carbon atom in oxidized functional groups such as carbonyl (C=O), alcohol (C-O-H), and acid (O-C=O) group has higher bonding energy of C_{1s} electrons (288.0, 286.5 and 289.0 eV) than the C1s bonding energy of the PE chain backbone C-C. Figure 5-24A shows that the C1s peak maximum for skin pipe and uncoated pipe are all located at 285.0 eV, indicating that no chemical shift of the C_{1s} peak due to oxidation occurred, confirming lack of obvious oxidation in these samples the same as the IR findings.

From the discussion above, contamination is observed on uncoated pipe outer surfaces. Although XPS is a more sensitive technique than the ATR-FTIR technique to detect chemical change on the sample surface, because of the contamination on the samples by the oxygen containing contaminants, the analysis of O_{1s} peak where indicates oxidation is restricted and no further conclusions can be made from the XPS results.

The chemical changes on the PE pipe outer surfaces were characterized by ATR-FTIR and XPS techniques and the similar conclusions were drawn. The following section will focus on molecule structure changes on the PE outer surface.

5.1.4 GPC

Molecular weight changes at both uncoated and coated pipe outer surfaces to a depth of 0.2~ 0.3mm during natural weathering were characterized by GPC. Pipe samples including blue pigmented uncoated pipe, uncoated ProFuse pipe and 1.5mm skin

ProFuse pipe under various weathering conditions were examined. The virgin PE pellets that used to produce ProFuse pipe were also characterized as a control. Most samples were measured at least twice to see the reproducibility, except one of the results for U-1.5-O-1 was questionable due to impurities and only a single run of the sample is shown here. The result report from RAPRA shown all the samples are dissolved in the 1, 2, 4-trichlorobenzene, therefore crosslinking during weathering is less likely to occur.

The chromatograms of the samples are classified into four groups in the following figures. The first group includes virgin materials and unaged samples. The second, third and fourth groups include pigmented uncoated pipe samples, uncoated ProFuse pipe samples and 1.5mm skin Profuse pipe samples under different levels of solar irradiation. These chromatograms are all plotted to the same area (the integrated area for all curves is the same).

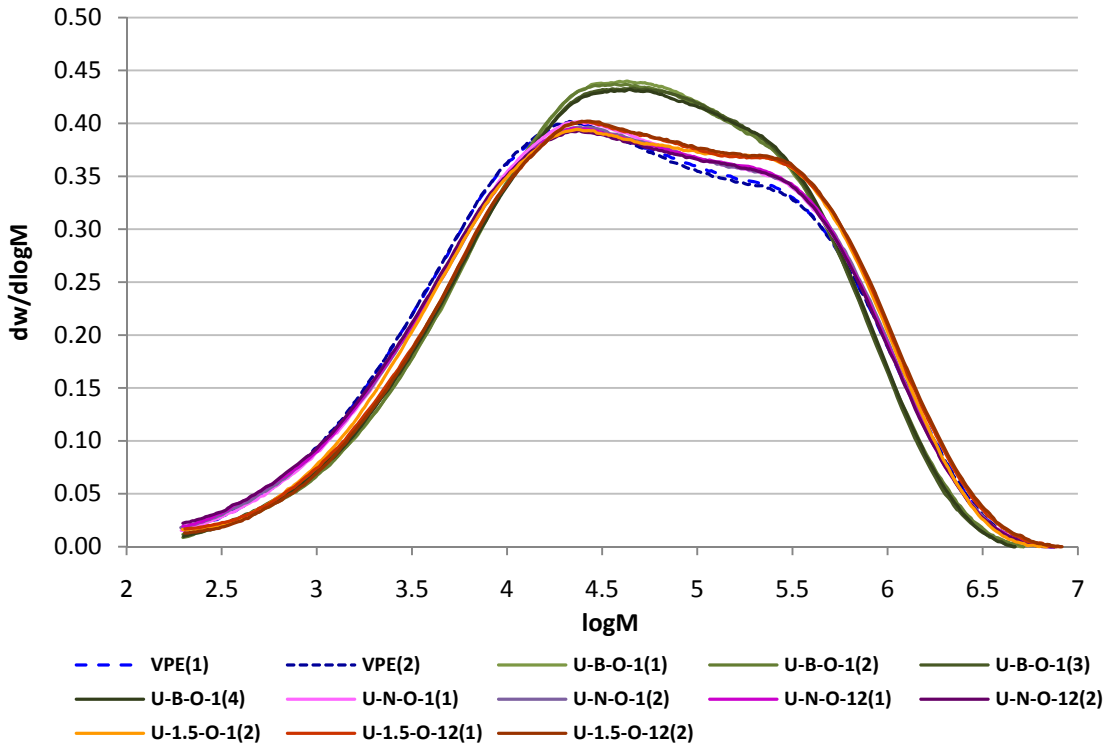

Figure 5-25 GPC curves of virgin PE and samples taken from unaged pipe outer surfaces

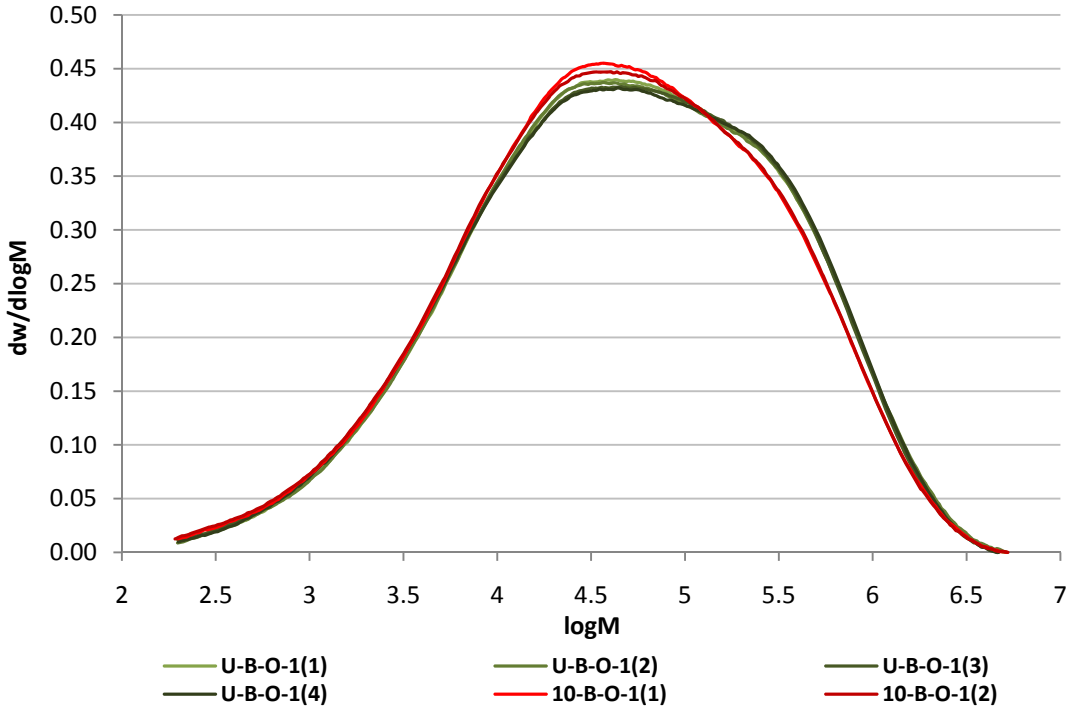

Figure 5-26 GPC curves of sample taken from the unaged and 10GJ/m^2 aged uncoated blue pigmented pipe outer surface

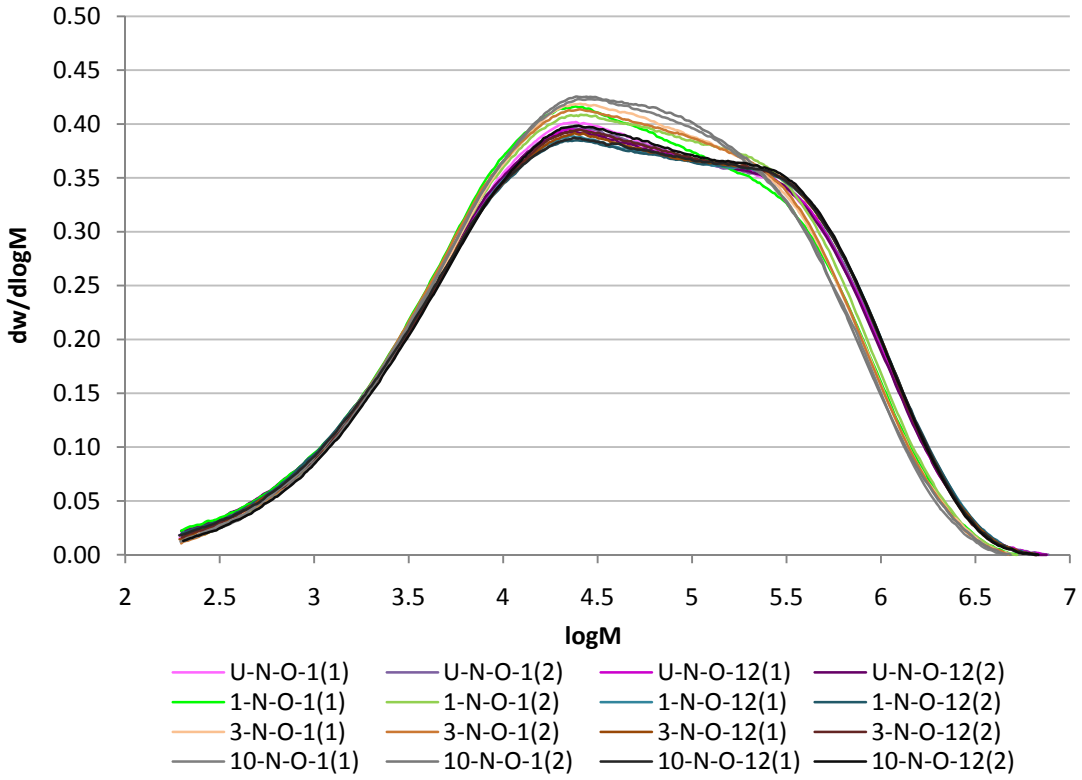

Figure 5-27 GPC curves of sample taken from uncoated ProFuse pipe outer surfaces

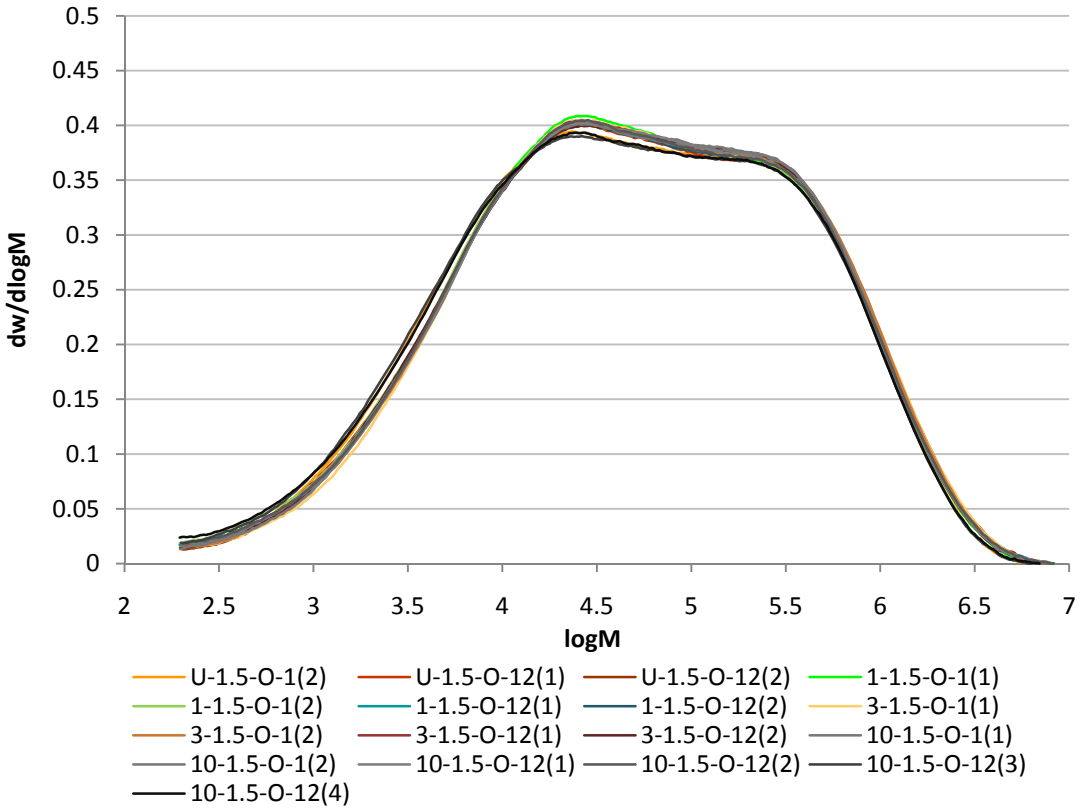

Figure 5-28 GPC curves of sample taken from 1.5mm skin ProFuse pipe outer surfaces

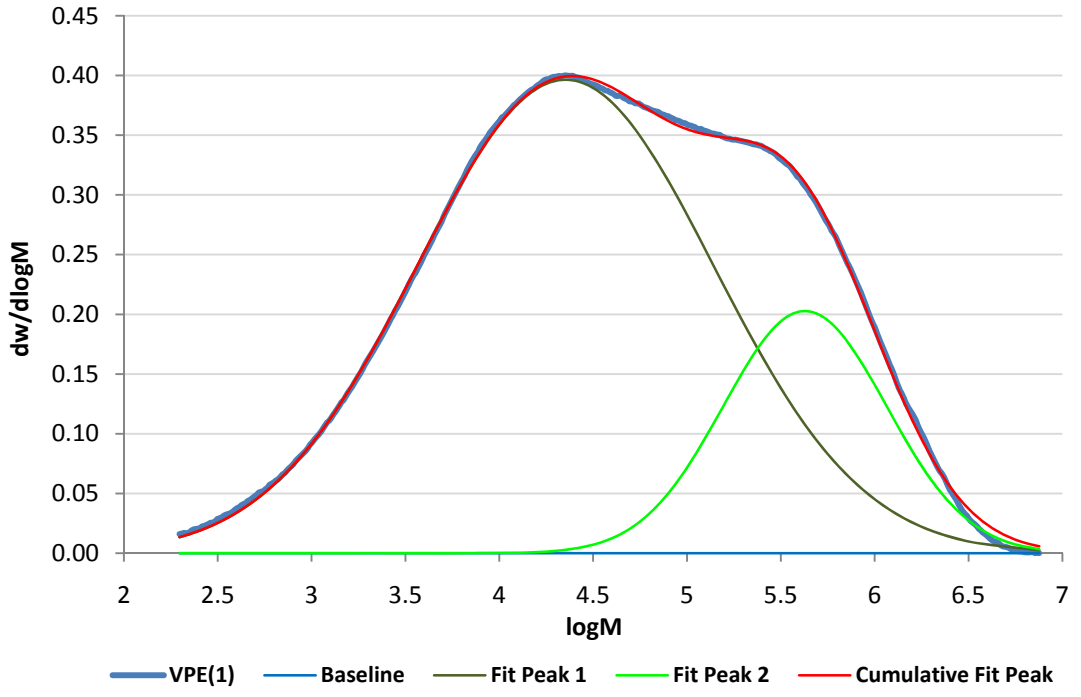

Figure 5-29 Demonstration of peak fitting for GPC curve

Two distinctive peaks can be identified in each GPC curve, confirming that all the PE materials are bimodal. The curves from a duplicated runs overlay, suggesting good repeatability of the technique. A peak fitting method was applied to deconvolute the compositional peaks using software OriginLab in order to quantify the change of the amount of low molecular weight (LMW) and high molecular weight (HMW) and their change of peak location.

All the GPC curves in Figure 5-25 to Figure 5-28 were fitted with two Gaussian type distribution functions as shown in Figure 5-29, which have been proved to be accurate for polymer GPC curve fitting [161]. The coefficients of determination (COD) of all the fittings are greater than 0.998 showing they are satisfying fittings. The peak center is detected by the second derivative curve. The area of the peak is proportional to the weight fraction of the corresponding MW portion.

Figure 5-25 shows that the blue pigmented pipe has a narrower molecular weight distribution (MWD) than those of the unpigmented Profuse pipes and their corresponding virgin materials. It can be inferred that the blue pigmented pipe is from a different type of bimodal PE than the PE used to produce skin pipe.

Figure 5-25 also shows that after processing, the uncoated Profuse pipe (pipe 'N') and the 1.5mm skin pipe (pipe '1.5') sample have a higher portion of high molecular weight (HMW) polymer than the corresponding virgin PE material, with the skinned pipe having the highest HMW portion. As no crosslinking residual was observed during sample dissolution, the higher portion of high molecular weight may because of materials itself rather than post production chemical reactions. The proportion of low molecular weight (LMW) remains the same for these pipes as the virgin PE material, it could be concluded that no obvious degradation occurred after processing which can be identify by molecular weight shifting to a lower values.

Figure 5-26 shows that after solar irradiation, there are increase in the LMW polymer and a decrease of HMW polymer for uncoated pigmented blue pipe. Figure 5-27 shows similar trend for the uncoated ProFuse pipe at the irradiated side. It also showed that the increase of LMW portion and decrease of HMW portion follow the increment of radiation level, indicating some relationship between photo-degradation

and radiation. The observation was confirmed in Figure 5-27 in that at the shaded part of the pipe, there is no obvious change of MWD even after 10 GJ/m^2 weathering compared to the side facing the sun.

Table 5-6 Summary of molecular weights and PDI during weathering

Radiation energy(GJ/m^2)	Samples					
	VPE	B-O-1	N-O-1	N-O-12	1.5-O-1	1.5-O-12
			Mn*			
0	7140	8940	7210	6940	7880	8850
1			7150	7110	8430	8590
3			7410	7290	9200	8720
10		8330	7480	7460	8810	8010
			Mw*			
0	222000	195000	222000	220000	239000	246000
1			191000	233000	238000	245000
3			188000	229000	248000	238000
10		180000	180000	229000	240000	234000
			PDI**			
0	**31**	**22**	**31**	**32**	**30**	**28**
1			**27**	**33**	**28**	**29**
3			**25**	**31**	**27**	**27**
10		**22**	**24**	**31**	**27**	**29**

*Averaged from duplicated runs; **Calculated from averaged Mn and Mw.

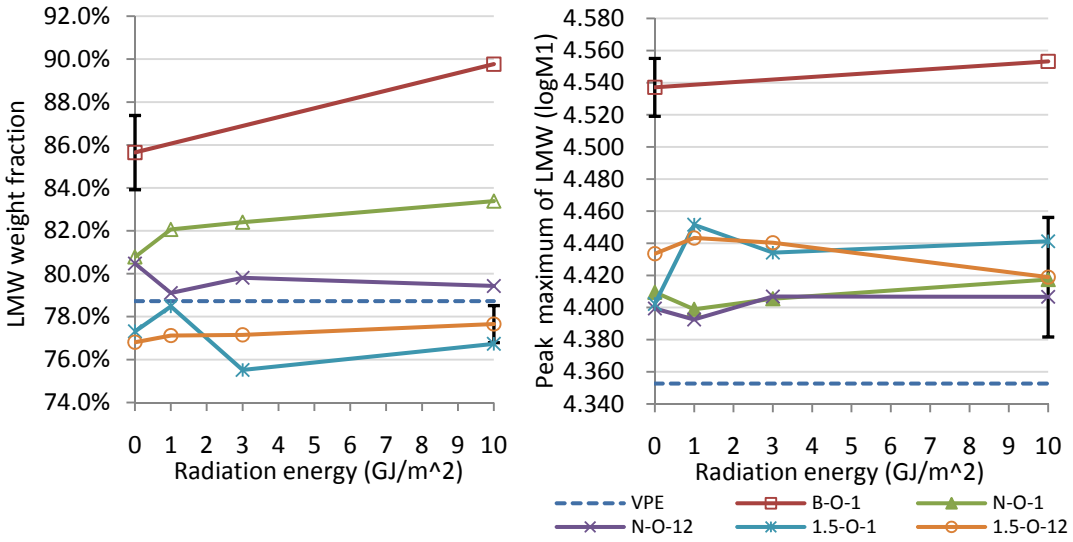

Figure 5-30 summary of LMW weight fraction and its peak location

In order to investigate the relationship between the amount of LMW and HMW and the radiation level, the molecular weights (MW) and polydispersity index (PDI= Mw/Mn) are summarized in Table 5-6 to quantify the change of MWD during

weathering. The area and peak maximum of the fitted curves are also summarized in Figure 5-30 and Figure 5-31 as a function of radiation energy.

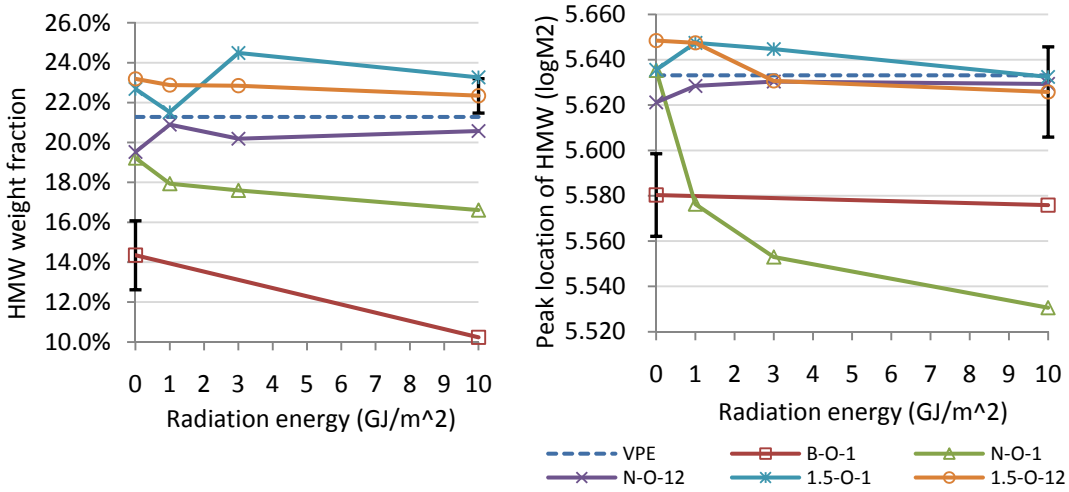

Figure 5-31 summary of HMW weight fraction and its peak location

Figure 5-30 and Figure 5-31 left plots confirmed that after natural aging, both uncoated pigmented (pipe 'B') and unpigmented (pipe 'N') pipes at the location facing the sun (location '1') have a increase in the amount of LMW and a decrease in HMW. Meanwhile, Figure 5-30 right plot shows that the positions of the LMW peak location did not change (within the standard deviation range), Figure 5-31 right plot also shows that most HMW peak did not change in position except pipe 'N'. There is a shift of HMW peak to a lower value for this unpigmented bare pipe. These findings suggest that for unpigmented bare pipe, chain scission is preferred at the HMW portion during natural weathering but no obvious chain scission is observed for the LMW portion. The shift of HMW polymer also causes a decrease in PDI for pipe 'N' showed in Table 5-6. Natural weathering seemed to be a procedure of HMW portion transforming to LMW portion in a radiation range up to 10 GJ/m^2.

Assuming that the tertiary carbon atom along PE copolymer chain is randomly distributed and has the same probability of chain scission, the overall chain scission probability for HMW chain is higher than the LMW chain. This assumption may explain the phenomenon observed above. For pigmented bare pipe, there is no such obvious change of peak location. This may because it has a narrower MWD and the peak shifting is more difficult to detect.

Figure 5-28 and Table 5-6 shows that for skin pipe which is made from the same type of PE as pipe 'N', the MWD before and after weathering did not change much. The portion of LMW and HMW polymer and their position are also unchanged compared with pipe 'N'. It can be concluded that the skin protects the pipe from outdoor photo-degradation.

The GPC results indicate that although no obvious oxidation was observed after 3 GJ/m^2 and only slight oxidation was observed after 10 GJ/m^2 on the unpigmented bare PE pipe outer surface which has been discussed in previous sessions on ATR-FTIR (5.1.2.2) and XPS (5.1.3), there is a shift of HMW portion to LMW portion and decrease of MW and PDI. Such decrease may due to the higher probability of longer chain. Due to the protection of the PP skin, the molecular weight of skinned PE core pipe is not affected even after 10GJ/m^2 irradiation.

5.1.5 Electro-fusion performance

The ATR-FTIR, XPS and GPC results showed that the skin protects the PE core pipe outer surface from contamination, oxidation and change of molecular weight. Surface free energy results showed that due to the additive on the skin, the PE core pipe has migrated secondary amide on its outer surface. In order to assess the effect of skin protection and effect of the migrated secondary amide on the electro-fusion quality, electro-fusion (EF) peel testing was carried out.

The peel test procedure was described in section 3.3.1.3. Unaged, 3 and 10 GJ/m^2 aged uncoated pipe 'N' and 0.4mm skin pipe '0.4' were examined. The peel energy of each peel test was integrated from the plot of force against extension peel curve. The integrated peel energy was then divided by average width of the fusion zone to produce a peel strength value.

The peel strength value is plotted as a function of its location along pipe circumferential direction in Figure 5-32. It should be noted that the numbering along

circumference is different from the previous results due to the larger sample size for the peel test.

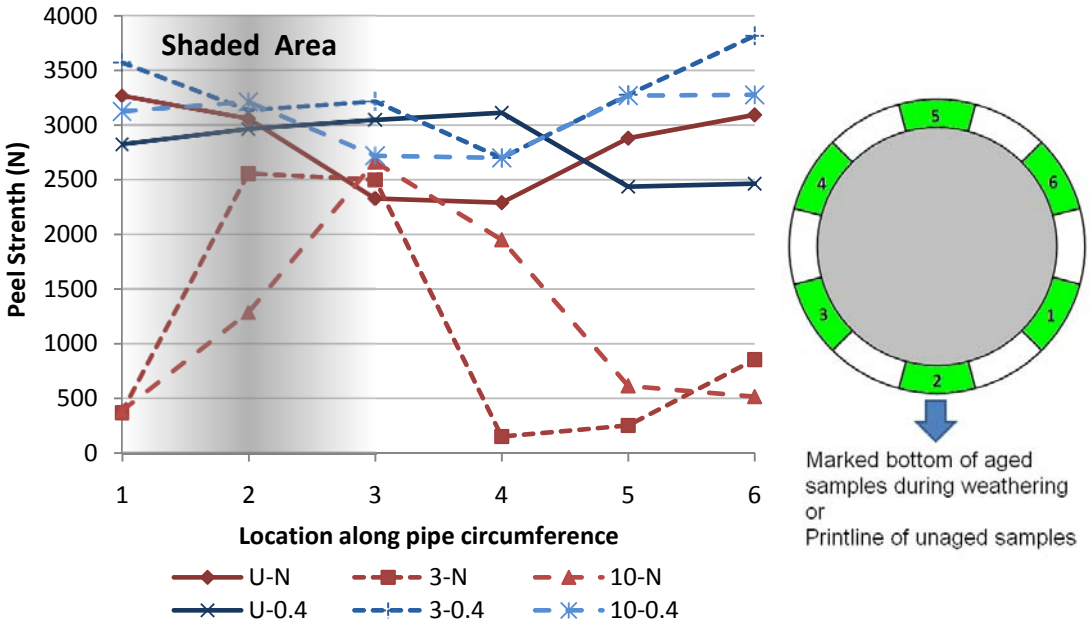

Figure 5-32 Peel strength along pipe circumference

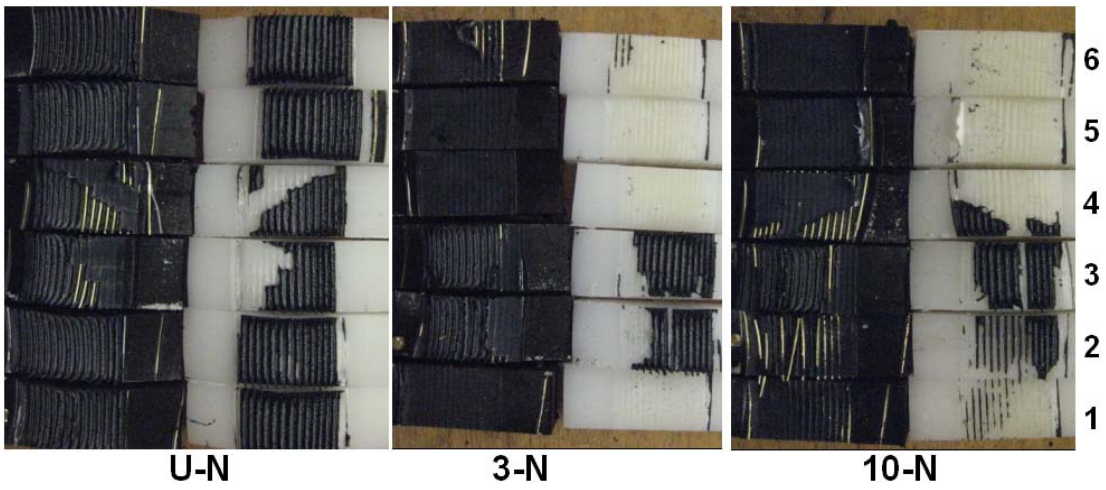

Figure 5-33 Peeled surface of uncoated Profuse pipe before and after aging

For skin pipe, the peel strength is retained after 10 GJ/m^2 aging along the whole pipe circumference. This is because the skin protects the PE core pipe from contamination as well as oxidation. But for uncoated pipe, although the outer surface was cleaned with alcohol wipes, peel strength was weakened after outdoor weathering at the side facing the sun (number 4, 5 and 6). The failure surfaces after peel testing are shown in Figure 5-33. At the uncoated pipe outer surface, the material of the black coupler

was not fused on the white pipe and failure happened at the pipe side. Yellowing can also be identified at the pipe surface indicating oxidation happened under the high temperature of electron-fusion process. It is believed that a brittle layer is formed at the pipe surface during electrofusion and the failure happened at this brittle layer, therefore, the failure surface is smooth. No material of the black coupler is adhered on the pipe surface because the force that causes failure at the brittle layer is reached before the force that can cause yielding of the material of the black coupler. The aged uncoated pipe peel samples that were facing the sun in weathering failed in a brittle mode as shown in the figure.

At the shaded side of the aged uncoated pipe, electro-fusion joints still showed residual material from the black coupler. The shifting of these locations with adhered black residual material around location 2 and 3 may be due to deviations in the marking and sample cutting process. The metal heating wire was pulled out during the peel test for the shaded samples. This indicates that the failure was initiated at the metal-PE interface in the coupler rather than at the pipe outer surface. After the metal heating wire and PE are separated, the stresses are concentrated in the PE material between the metal heating wires and then lead to fatal failure. PE fibrils can be identified at these stress concentrated sites indicating ductile failure as shown in Figure 5-34.

Figure 5-34 EF peeling test followed by ductile failure

The formation of the brittle layer may due to the oxidation products as well as the higher amount of LMW polymer that formed at the side facing the sun during weathering as shown by the GPC results. The depletion of antioxidant is also a main

reason. As antioxidants were consumed during weathering, the antioxidant is no longer able to protect the pipe surface from thermal oxidation during electro-fusion. Hence the weathered surface is oxidized and the oxidized brittle layer is formed after electro-fusion. The antioxidant level will be assessed by the OIT technique in the following section.

Section 5.1 discussed the effect of PP skin on the PE core pipe before and after weathering by analyzing the change of surface free energy, the oxidation groups formed on the PP and PE surfaces, the molecular weight (MW) and electrofusion assessment. These results showed that for uncoated PE pipe and PP skin, locations along the pipe circumference receive different level of solar radiation. The shaded side has a slower photo-oxidation process than the side facing the sun. The PP skin protects the PE core pipe outer surface so that it remains as intact as unaged pipes. The following sections will discuss the PP skin effect on the pipe properties across the pipe wall to give a complete view of pipe property changes after aging.

5.2 PP skin effect across pipe wall

5.2.1 OIT

The ATR-FTIR results showed that the PE has better oxidation resistance than the PP during weathering and only slight oxidation was identified at the 10 GJ/m^2 aged uncoated sample outer surfaces. However, from the EF peel test assessment, the uncoated pipe at the irradiated pipe side showed brittle failure indicating possible depletion of antioxidant while the aged skin pipe showed EF peel strength as good as unaged pipes suggesting that the skin provided protection to avoid loss of antioxidants on the pipe outer surfaces. In this section, OIT tests are carried out to investigate the effectiveness of antioxidant in both the uncoated pipe and skin pipe after weathering.

5.2.1.1 OIT profile of uncoated pipe

The unaged pipe outer surfaces and the aged pipe along its pipe circumference as well as across its thickness were examined by OIT testing. The OIT profile along pipe circumference is summarized in Figure 5-35.

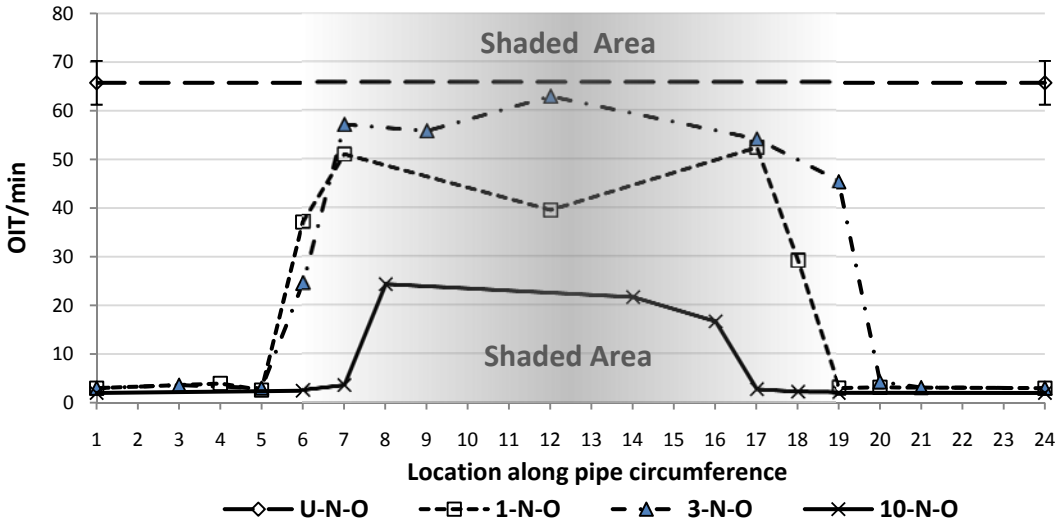

Figure 5-35 OIT value along pipe circumference of uncoated pipe

Figure 5-35 showed that all the OIT profiles along pipe circumference are symmetrical about location 12 which is the bottom during natural weathering. The following results with regard to OIT profile along pipe circumference are shown from location 1 to 12 and the other half of the OIT profile can be inferred.

For the unaged uncoated pipe outer surface 'U-N-O' (long dashed line), the OIT value that is shown in Figure 5-35 is an averaged value from samples taken quarterly along pipe circumference. Standard deviation is also shown in the figure as error bar, indicating the variation in the OIT values. It can be seen that the averaged values of the unaged uncoated pipe outer surface are all above those of the weathered pipes. Actually, no single OIT value was found to be lower than the values of the weathered samples, indicating that sufficient antioxidants are retained after processing meeting the industrial OIT requirement which is normally 10 to 20 minutes at 200 ^{o}C in a pure oxygen atmosphere.

However, after 1 GJ/m^2 solar irradiation, the curves (short dashed line) showed a sudden drop of OIT value to near zero at the irradiated side indicating depletion of

antioxidants, while the shaded side retained most of its original antioxidant concentration.

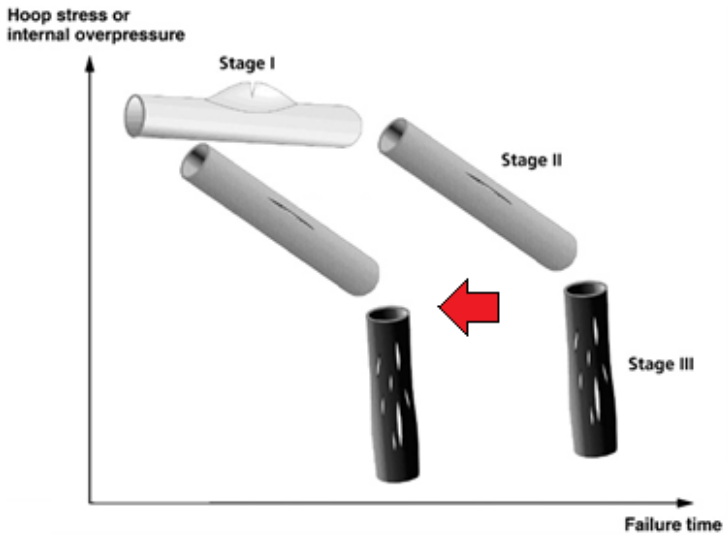

Figure 5-36 Pipe life shortening due to decease of antioxidant [152]

The rapid loss of antioxidants after 1GJ/m^2 equals to 45 days outdoor weathering in the Arizona desert from August to September. The loss of antioxidants from the irradiated surface in such a short period of time is surprising and is far out of the practical requirements in the UK which needs pipes to retain their antioxidant to above the industrial standard after at least 1 year outdoor storage. The loss of antioxidant will lead to formation of weak joints using the electro-fusion process and resulted in pipe system failure. It may also lead to early appearance of stage II that is caused by oxidative brittling in a pipe lifetime as shown in Figure 5-36, shortening the expected useful life of the pipe. The ATR-FTIR results also showed that the diffracted solar irradiation also will induce photo-oxidation. Therefore attention should be paid to pipe stored outdoor under strong solar radiation even for such short period of time in practice.

The loss of antioxidants from the irradiated surface is possibly due to their consumption against photo-oxidation. It has been proved that photo-oxidation occurred at the irradiated side of stabilized PP skin outer surfaces after 1 GJ/m^2 weathering and a build up of carbonyl products was observed (section 5.1.2.1). The weathering condition for the uncoated PE outer surface is the same as the PP skin outer surface. The irradiated PE outer surface was heated up during the day time. The

measured temperature along with the solar radiation and oxygen in the atmosphere constituted favorable photo-oxidation conditions on the irradiated PE outer surface. Once the photo-oxidation is initiated (normally identified by peroxide radical and hydroperoxide formation) the antioxidant at the outer surface would become active to protect the material from photo-oxidation. The antioxidants would be consumed when they are no longer able to stabilize the polymer and the auto-oxidation process begins. The details of photo-oxidation and its stabilization are discussed in section 2.2.2.5 and section 2.3.2. Unfortunately, the details of the antioxidant package used in this project remains confidential to the author and no further analysis of the antioxidant reactions during the photo-oxidation could be made.

The loss of antioxidant for the irradiated surface may also be due to migration. There are many researches reporting on the topic of antioxidant migration in thermoplastics including PE [106, 163]. The raised temperature at the irradiated side makes the migration process faster than at the shaded side. For low molecular weight antioxidant, the antioxidant may migrate to the atmosphere and other media such as rain. For high molecular weight antioxidants, the migration to the atmosphere is much slower but they can still be leached out by rain. Although Arizona is a desert area, it is well known that there is monsoon rain season in Phoenix City from July to September. Hence, it is possible that the antioxidants be leached out by the rain fall.

Although the antioxidant concentration decreased to near zero after 1 and 3 GJ/m^2 weathering, there was no obvious carbonyl build up on the uncoated PE pipe outer surface which was investigated by ATR-FTIR techniques in section 5.1.2.2. The buildup of carbonyl products and chain scission began after 10 GJ/m^2 aging on the PE outer surface were identified by the ATR-FTIR and GPC measurements in section 5.1.2.2 and 5.1.4. Such difference indicates that the degradation is not immediately followed by depletion of antioxidant on the PE pipe outer surface. This may due to the inherent inert chemical properties of PE that leads to slow oxidation rate.

As opposed to the irradiated side, the shaded side retained ~70% of its original antioxidant concentration after $1GJ/m^2$ weathering. The processes of antioxidant consumption and migration to the surrounding environment seems less likely to happen at the shaded side because the shaded outer surface is without direct solar

radiation and has a lower temperature than the irradiated side. However, previous results indicate that photo-oxidation and consumption of antioxidant are still possible at the shaded side. A rapid increase of carbonyl index on the shaded PP outer surface indicates auto-oxidation happened on the shaded side which was possibly caused by the scattered UV light after depletion of antioxidant. The weathering condition of the shaded PP skin outer surface is the same for the shaded PE pipe outer surface and there will be consumption of antioxidants lowering their concentration. The 10 GJ/m^2 weathered shaded pipe side also showed a decrease in antioxidant concentration to ~30% of the unaged level and shrinkage of its protected area.

As the antioxidant concentration is lowered at the outer surface, the antioxidant at the inner pipe wall tends to diffuse to the outer surface by the driving force of concentration difference. But the diffusion process is not simultaneously with the loss of antioxidant due to its low diffusivity in the polymer. Normally, low diffusivity of antioxidants in a polymer is intentionally designed by the additive manufacturer to avoid fast loss in long term application in the case of plastic pressure pipe. Possibly due to the hysteresis of the antioxidant diffusion, there is antioxidant replenishment at the 3GJ/m^2 aged samples indicated by increased OIT value and expanded antioxidant protected area (expanded from location 19 to 20 in Figure 5-35). Also because the loss of antioxidant at the pipe outer surface is faster than the antioxidant diffusion process within the pipe thickness, especially at the irradiated side where the rate of antioxidant loss is much faster than the diffusion rate from the inner pipe wall to the outer surface, the weathered outer surface showed a near zero antioxidant level.

As far as diffusion across thickness is concerned, the OIT values across the pipe thickness were also investigated to give a general view of antioxidant distribution through the pipe thickness.

The OIT values of 10 GJ/m^2 weathered samples located at the outer surface, middle part and inner surface along the pipe circumference were compared with the unaged pipe also at these three locations and the results are summarized in Figure 5-37.

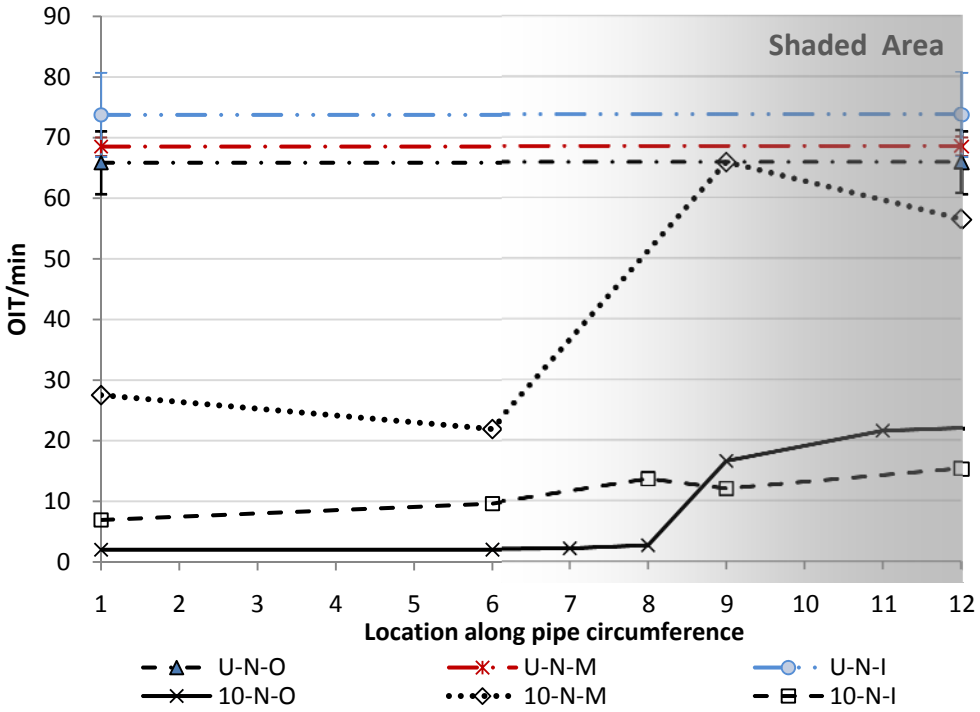

Figure 5-37 OIT values of unaged and 10 GJ/m^2 weathered uncoated pipe samples located at outer surface, middle part and inner surface along the pipe circumference

The OIT values of unaged pipe across pipe thickness were discussed in section 4.2.1. Most of the OIT values of unaged pipes are similar at around 60~80 minutes and higher than the 10 GJ/m^2 samples, except the shaded middle part of the 10 GJ/m^2 samples has a value close to the unaged pipes. The figure also showed that after 10 GJ/m^2 weathering, there are different distributions along pipe circumference at these three locations across the pipe wall.

The OIT profile of the outer surface along pipe circumference has just been discussed showing a sudden drop of antioxidant at the irradiated side. Oxidation and degradation also started at these locations.

The sample from the middle pipe wall shows the antioxidant concentration at this location is the highest of all the three locations. Due to absence of oxygen at the middle part, oxidation is unlikely to happen. The loss of antioxidant at this location is only due to diffusion. The OIT values at the irradiated side (number 1~6) and shaded side (number 7~12) are averaged and are summarized in Figure 5-38. The higher antioxidant concentration in the middle of the pipe wall drives the antioxidant diffusion to the two pipe surfaces, acting as a reservoir for the two surfaces. Because

the faster loss of antioxidants at the irradiated side and higher temperature, the antioxidant concentration of the irradiated side (the solid line) shows a lower level and flatter profile across pipe thickness than the shaded side (the dashed line) where the temperature is lower and the loss of antioxidant is slower.

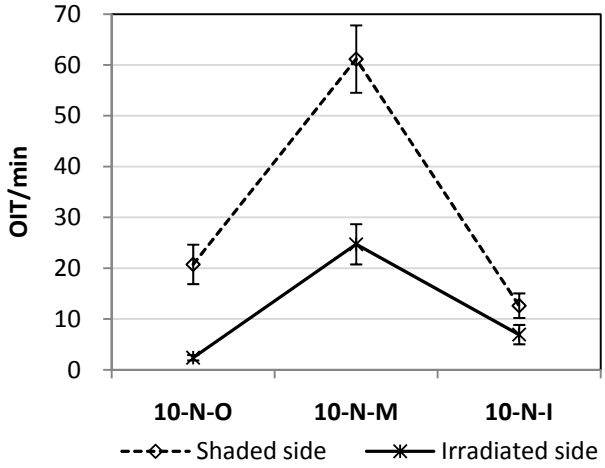

Figure 5-38 Averaged OIT value at irradiated and shaded sides of uncoated pipe across pipe thickness

The inner surface shows that although there is no sudden drop of antioxidant at the irradiated side, loss of antioxidant is still obvious. From Figure 5-37, it can also be seen that the irradiated side has a lower concentration than the shaded pipe side. Compared to the OIT values of other locations across the pipe wall, the inner surface at the shaded side has a lower antioxidant concentration than the other two positions. This indicates that photo-oxidation occurred at the inner surface. Because the pipe rings were taken from the middle of a 1.2mm pipe, solar radiation is unlikely to irradiate this surface. Alternatively, solar radiation may penetrate through the unpigmented pipe wall into the inner surface. It is possible that the solar radiation is scattered by the pipe wall, and the radiation irradiates the inner surface more evenly than the outer surface with lower intensity as shown in Figure 5-39. Furthermore, the inner surface is exposed to oxygen, making photo-oxidation possible. Therefore, the inner surface will consume antioxidant and it is reasonable that the shaded inner surface has a lower antioxidant level than its corresponding outer surface across the pipe wall that is at the bottom, shaded by the whole pipe.

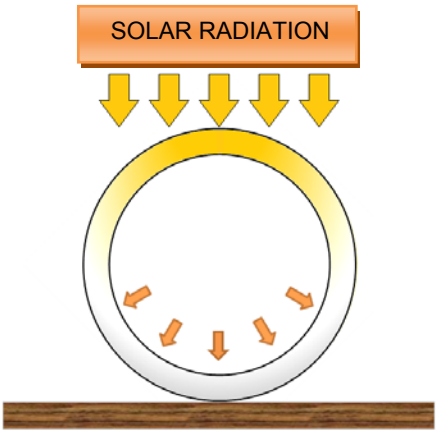

Figure 5-39 Schematic of solar radiation on the inner surface of uncoated ProFuse pipe

Section 2.4.2.2 showed that the failure of the PE gas pipe is initiated at the inner surface of the pipe [104]. The loss of antioxidant at the inner surface may affect the pipe service life more than the loss at other parts of the pipe in the pipe wall and the consequence would be a fatal one. Taking water pipe as an example, the antioxidant at the inner surface would be extracted by water [152, 164] and accelerate the loss of antioxidant and shorten the pipe life as illustrated in Figure 5-36. If the aqueous medium contains oxidative molecules (such as dissolved oxygen and chlorine dioxide used as a disinfectant) the extraction will be even faster [164, 165]. For pipes transporting gas, the concentration of antioxidant at the inner surface is less affected because it is reported that antioxidant extraction effect did not happen in the gas phase [164]. In practice, some pigmented pipes sealed with caps at their two ends so that the inner surface is protected from irradiation. However, caution still needs to be paid to thin or light colored pipes, as they may still allow solar radiation to penetrate into the pipe inner surface.

The effects of location along the pipe circumference direction and across pipe thickness on the antioxidant distribution are discussed above for uncoated pipe. Such effects stem from the differences in radiation intensity at these locations and the presence of oxygen. The next section will discuss the OIT value of the skinned pipe to see the protective effect of the skin on the PE core against photo-oxidation.

5.2.1.2 OIT profile of skin pipe

The OIT values of 0.4 and 1.5 mm skin PE core pipe outer surface are summarized in Figure 5-40A. These values are averaged along the pipe circumference and plotted as a function of radiation energy in Figure 5-40B.

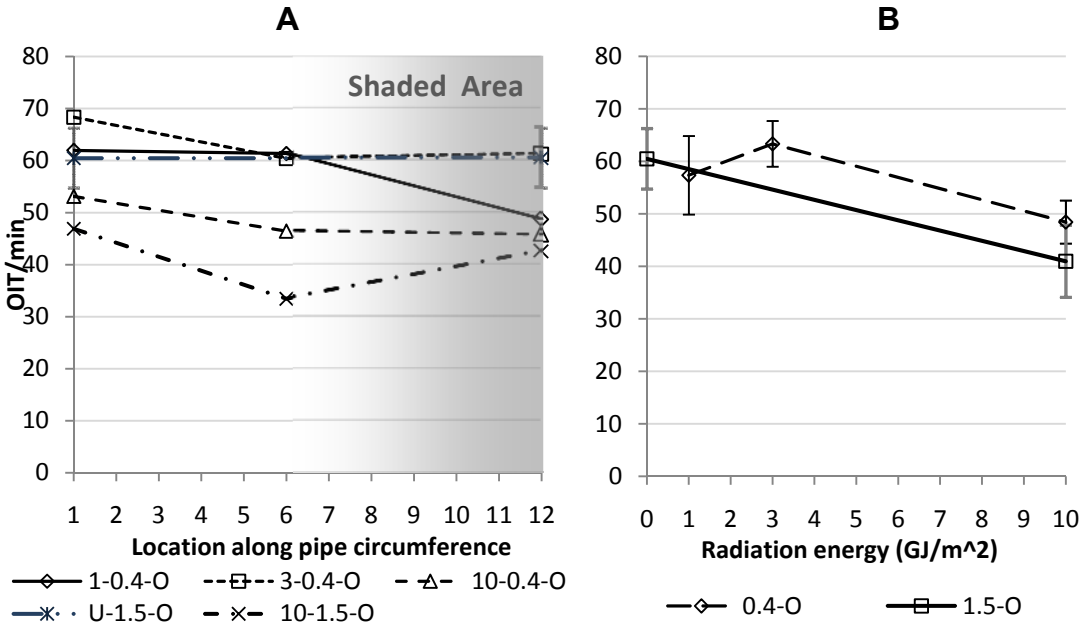

Figure 5-40 A) OIT values of PE core pipe outer surface along pipe circumference with 0.4 and 1.5 mm skin; B) Averaged OIT values of PE core pipe outer surface as a function of radiation energy

The averaged OIT value of unaged 1.5mm skinned pipe PE outer surface (U-1.5-O) is also incorporated in Figure 5-40A with standard deviation error bars. The OIT values of 0.4mm skinned pipe PE outer surface ('0.4-O' samples) are within or close to the variation range of the averaged U-1.5-O values. No sudden drop of OIT values to zero is found. These OIT values meets the industrial OIT requirement which is 10 ~20 minutes at 200 ^{o}C in pure oxygen atmosphere. The 10GJ/m^2 radiation equal to outdoor exposure in Arizona desert for more than 1 year also satisfies the industrial pipe storage time requirement in the UK where radiation intensity is lower than Arizona. The electrofusion assessment in section 5.1.5 showed that the 3 and 10 GJ/m^2 aged 0.4 mm skin pipe all failed in a ductile mode, indicating the antioxidants on the PE core pipe outer surface are sufficient for electrofusion even after 10 GJ/m^2 aging.

From Figure 5-40A, it can also be seen that most of the antioxidant concentration at the irradiated side shows a higher concentration than the shaded side, indicating

antioxidant accumulation. The antioxidant accumulation is possibly because of its migration which mostly depends on temperature. The temperature at the irradiated side is higher than the shaded side due to the heat effect of radiation. Therefore, the antioxidant migration from the middle pipe wall to the PE core pipe outer surface at the irradiated side is faster than the migration at the shaded side. As the blue pigmented PP skin is intimately adhered to the PE core pipe outer surface, the radiation and oxygen are less likely to penetrate into the PE pipe and the antioxidant is less likely to be consumed or lost. Hence, the antioxidants accumulate at the PE core pipe outer surface.

The skin pipe after weathering still shows a high level of antioxidant and even accumulation of antioxidants. However, fluctuation of antioxidant concentration can still be evident for both 0.4mm and 1.5mm samples when weathering proceeded as shown in Figure 5-40B. After 10 GJ/m^2 weathering, the OIT profiles of these two samples along pipe circumference shifted to a lower value as a whole. It seems that the thicker skin has a faster antioxidant loss rate than the thin skin pipe at the PE core pipe outer surface and the 1.5mm skin pipe samples shift to lower values than the 0.4mm skin. The 10 GJ/m^2 weathered 0.8 mm skinned pipe PE outer surface ('0.8-O') would has an OIT profile that is between the OIT profile of the samples with 0.4 and 1.5 mm skin. As the accumulation of antioxidant can still be evidented, the antioxidant loss is less likely due to irradiation and its consequent temperature differences. Rather, it may because of the skin thickness and other factors that are independent of the variation along pipe circumference. A possible explanation is that the antioxidant migrats to the PP skin. But due to the limited runs, the standard deviation range is still unknown for samples under different aging conditions and no further analysis and conclusions could be drawn at this point.

The OIT values across the skinned PE pipe wall at different locations around the pipe circumference are shown for 0.4mm and 1.5mm skin pipes in Figure 5-41.

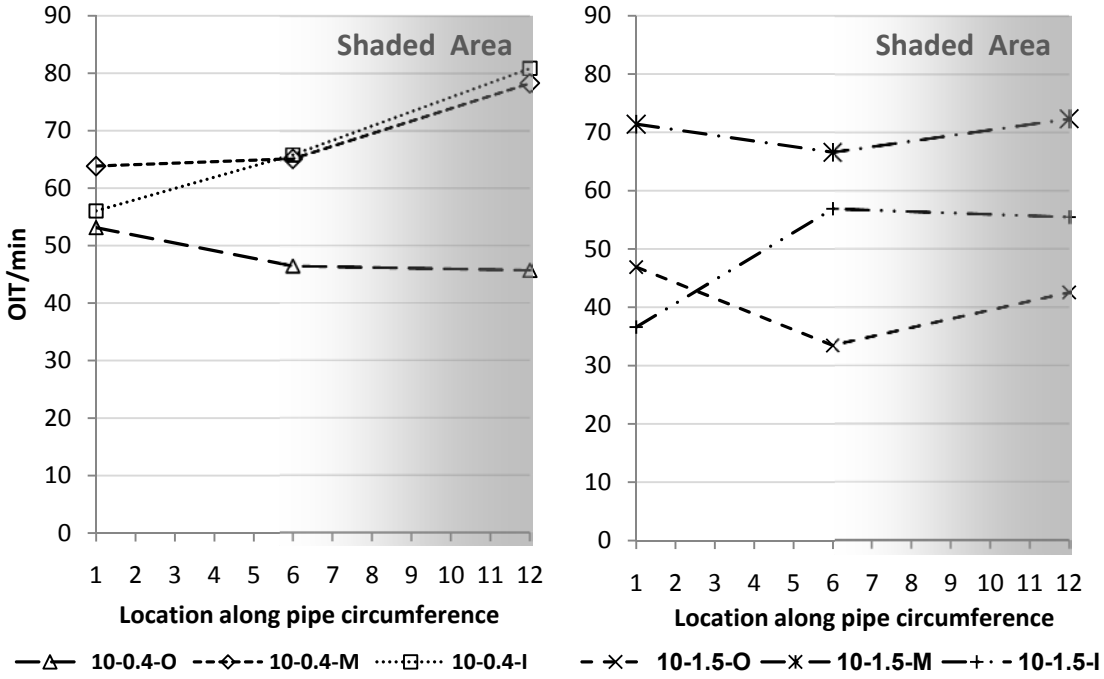

Figure 5-41 OIT values of 0.4 and 1.5 mm skin pipe across PE core pipe thickness

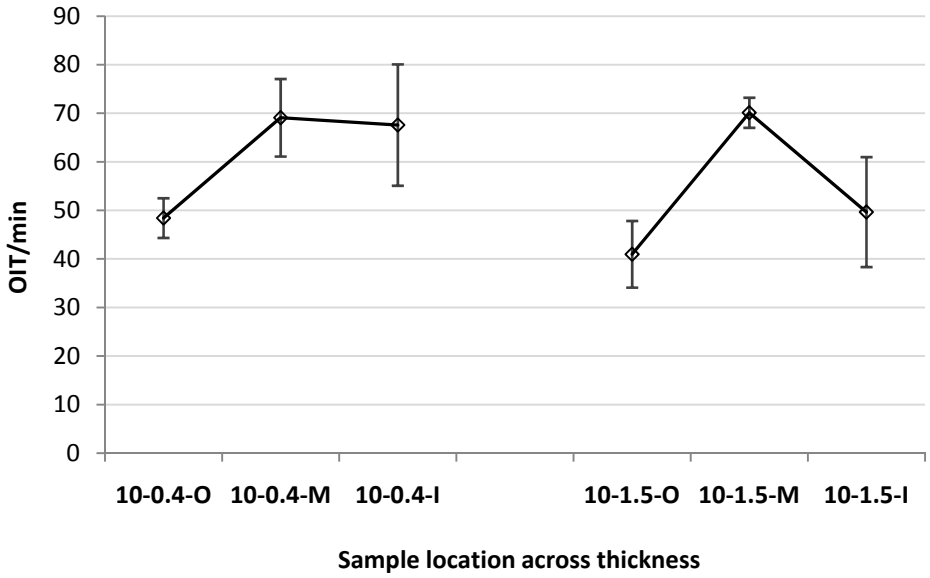

Figure 5-42 Averaged OIT values of 0.4 and 1.5mm skin pipe across PE core pipe thickness

In Figure 5-41, both skin pipes have the highest OIT value in the middle at around 60~80 minutes, indicating the antioxidant at the middle of pipe wall will still act as reservoir for the PE core pipe inner and outer surfaces.

The OIT values at the same location across the pipe thickness regardless of their location along the pipe circumference are further averaged and shown in Figure 5-42.

Compared with the averaged OIT profile in Figure 5-38 at the shaded side, the profile of the skin pipe across the pipe wall is flatter. The averaged OIT value of the inner surface is close to the OIT value in the middle part, this is probably because this surface was protected from solar irradiation as it is also shaded by the blue pigmented PP skin. Due to the protection of the blue PP skin against solar radiation, the loss of antioxidant at the inner surface may only due to migration into the air rather than consumption against photo-oxidation.

This section discussed the consequence of outdoor weathering on the antioxidant distribution along pipe circumference and across pipe wall for both uncoated pipe and skinned pipe. As the phenolic antioxidant concentration is proportional to OIT value. The results showed that the uncoated pipe outer surface facing the sun lost most of its antioxidants after only 1 GJ/m^2 weathering while the shaded part of the pipe retained ~70 % of its antioxidant after 1 and 3 GJ/m^2 weathering but still decreased to ~30 % after 10GJ/m^2 weathering compared to the unaged samples. The differences of irradiation conditions along pipe circumference also led to variation of antioxidant distribution on the middle pipe wall and inner surface where a more gradual decrease was found. Although the middle of the pipe wall acted as antioxidant reservoir to both pipe surfaces and replenishment of antioxidant was observed, caution still should be paid to the outdoor storage of unpigmented pipe because a rapid drop of antioxidant level after a short outdoor exposure time for about 45 days will occur at the irradiated pipe side and lead to weak EF joints and reduced pipe life time. The skinned pipe showed better resistance to antioxidant loss than the uncoated pipe. The antioxidant level in the whole pipe thickness is above 50% of its original value even after 10 GJ/m^2, and still meets the industrial standard. The results in this and previous sections are mainly concerned with the weathering effect on chemical changes. The following section will discuss the effect of weathering on physical changes such as density, crystallite distribution and residual stress.

5.2.2 Density

The density profiles of uncoated Profuse pipe 'N' and 1.5mm skin Profuse pipe '1.5' across pipe thickness after aging are showed in Figure 5-43 and Figure 5-44 using the same scale.

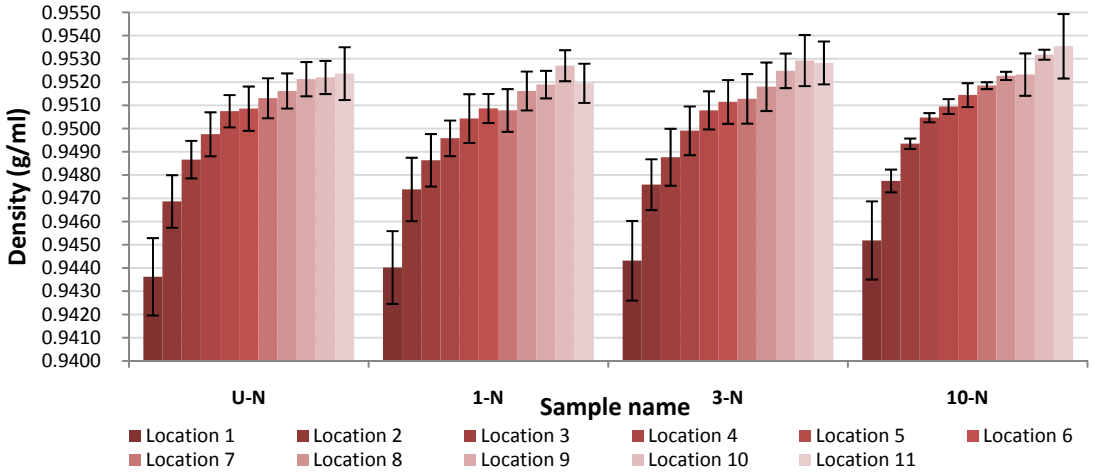

Figure 5-43 Density profiles of uncoated Profuse before and after weathering

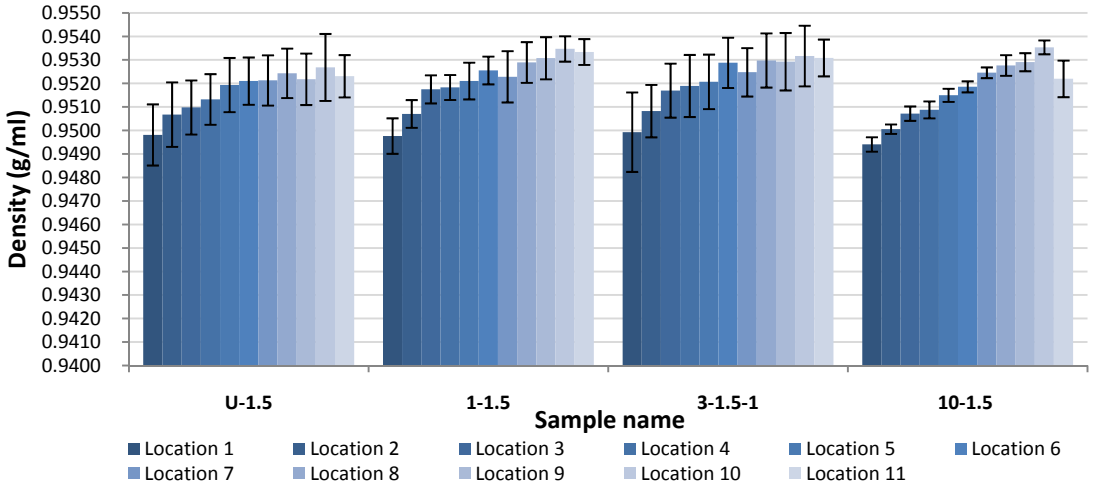

Figure 5-44 Density profiles of 1.5mm skin Profuse before and after weathering

The location numbers indicated in the figures are depth from the outer surface and their values are roughly equal to millimetre steps. Samples are taken randomly irrespective their location along the pipe circumference. The density values shown in these two figures are averaged values of at least three duplicated measurements. Standard deviation values are showed on each bar. Despite the deviations shown by

the error bar, the quenching effect of the uncoated pipe that arise from water cooling procedure still exists even after 10 GJ/m^2.

The density values are further averaged across the thickness and summarized in Figure 5-45, showing that the overall density did not change much after aging. The 1.5mm skin pipe still retained the highest overall density while the overall density of the uncoated Profuse is still the lowest. It can also be inferred that the 0.4 and 0.8 mm skin pipes overall density values are between these two pipes. The increased density of the skin pipe is mainly due to the skin preventing PE core pipe being quenched as discussed in section 4.2.2.

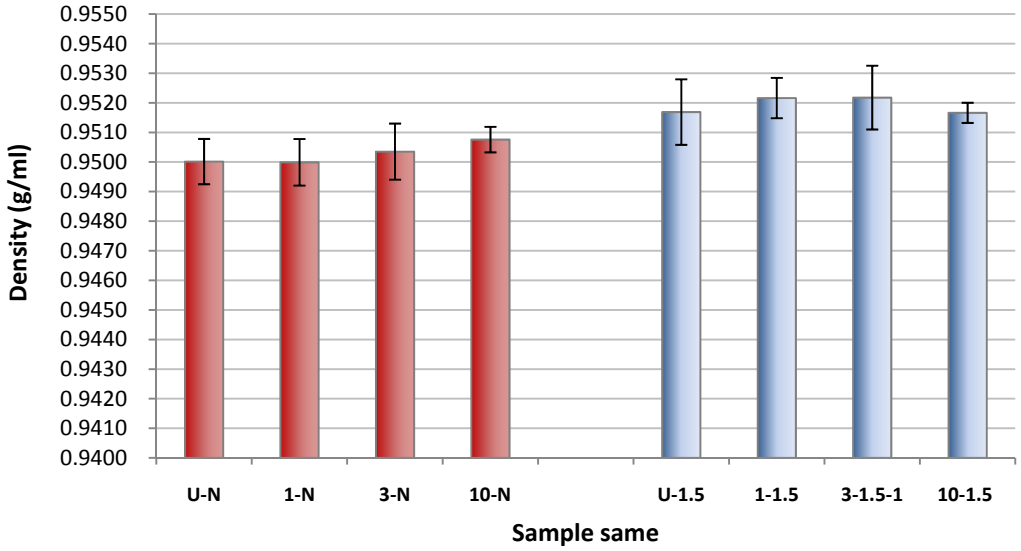

Figure 5-45 Averaged density across pipe thickness for uncoated and 1.5mm skin pipes

It seems no obvious that secondary crystallization happened which would cause an increase in density. For the 1.5mm skin pipe, the error bar is shortened after 10 GJ/m^{2}but no obvious increase of density was found either.

For the skin pipe, because the properties on the shaded side and the side facing the sun are the same as in the previous study, it is believed that weathering did not affect the density of the skin pipe, especially in the case when it was annealed during processing. Annealing during weathering is less likely to happen for the skin pipe than the uncoated pipe.

Property differences for the uncoated pipe outer surface at the shaded side and the side facing the sun were found in previous sections. The density of the samples at these two sides is also investigated in order to correlate the relationship between density and the previous investigated properties. 10 GJ/m^2 aged uncoated pipe density profiles across pipe wall at these two locations are shown in Figure 5-46 along with the unaged density profiles. The increase of density occurred to a depth of 2~3mm from the uncoated pipe outer surface. Interestingly, there is also a density increase at the inner surface of pipe (location 11).

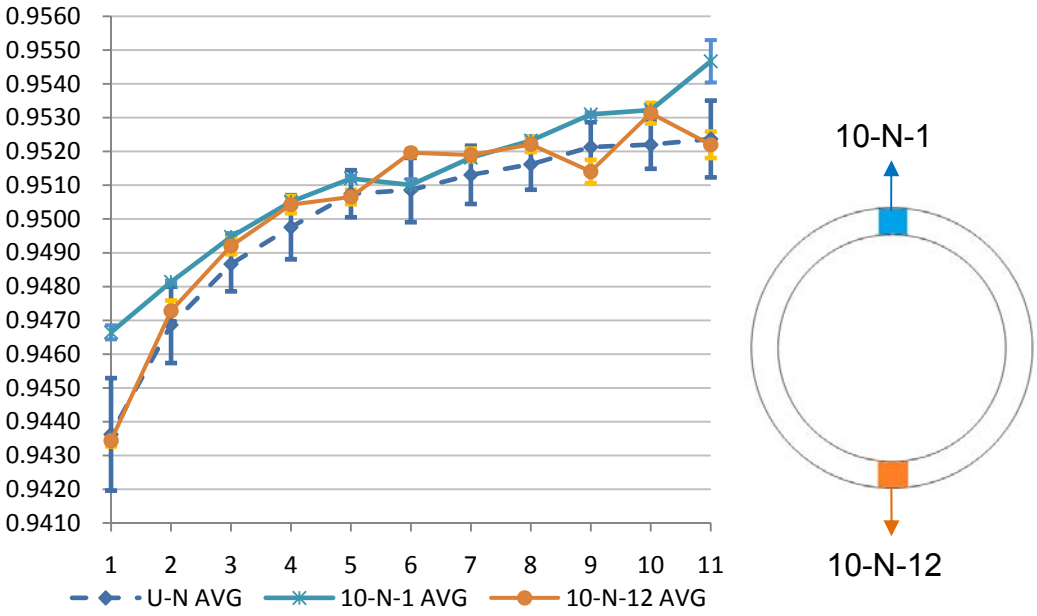

Figure 5-46 Density profile of 10 GJ/m^2 aged sample located at the top and bottom during aging

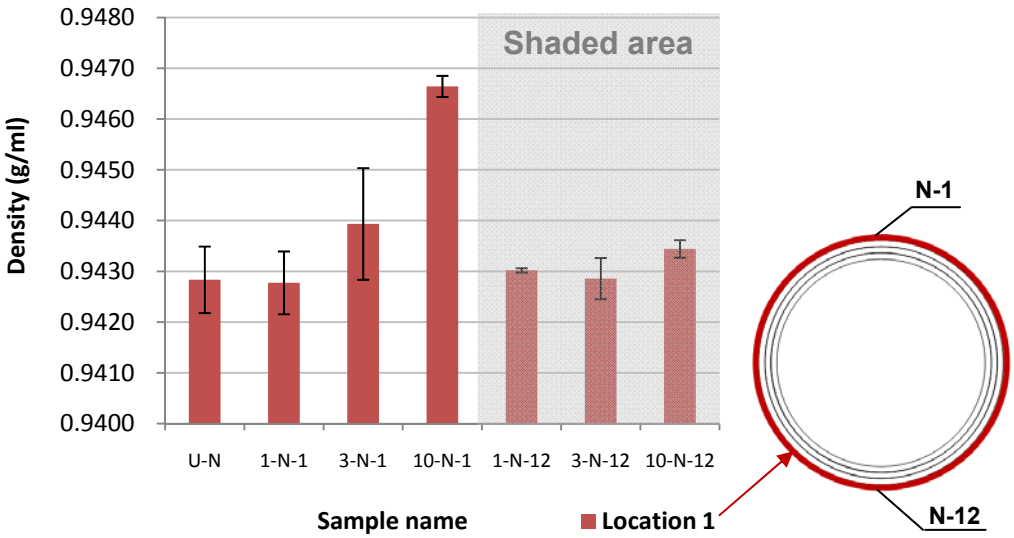

Figure 5-47 Density of uncoated pipe outer surface to a depth of ~1mm before and after aging

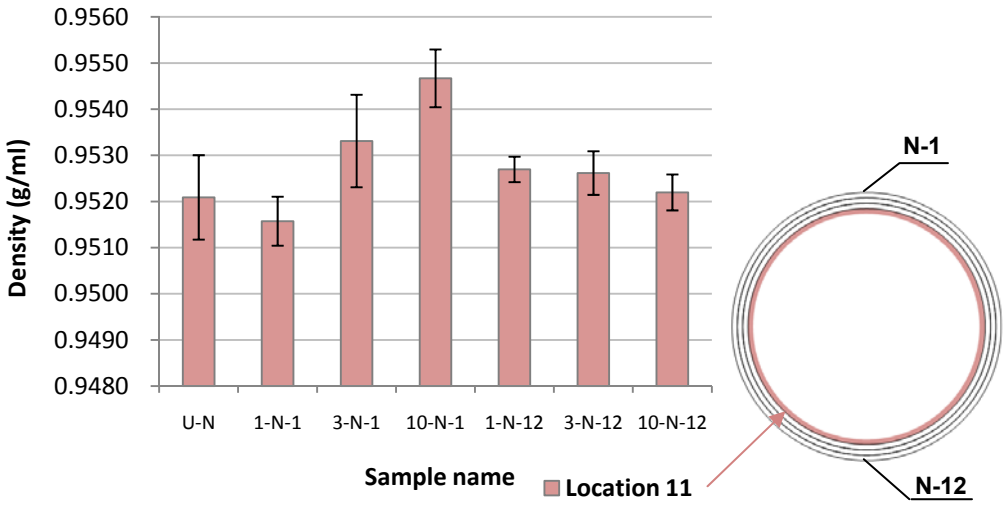

Figure 5-48 Density of uncoated pipe inner surface to a depth of ~1mm before and after aging

To focus on the density change at these two surfaces, the density of the outermost sample ('Location 1', roughly equal to a depth of 1mm) located at the top and bottom during weathering (number 1 and 12 along circumference) are summarized in Figure 5-47. The density of uncoated inner surface is shown in Figure 5-48.

The outer surface to a depth of ~1 mm shows that at the side facing the sun (sample position number 1) there is increase of density as the sun radiation dosage increases after 3GJ/m^2 aging. Such trend is especially obvious for the 10 GJ/m^2 aged sample, while at the bottom (sample name with number 12), the density remained as low as the unaged samples.

The inner surface to a depth of ~1 mm at the top also shows increase of density with sun radiation dosage after 3GJ/m^2 weathering, but the increment is less obvious than the outer surface at the pipe top. For the inner surface at the pipe bottom, the density is also remained as low as the unaged samples.

The density increments of both outer and inner surfaces at the pipe top are possibly caused by annealing during weathering. As heat originates from the pipe outer surface at the top by radiation during weathering, it is probable that the temperature of the shaded pipe inner surface at the top was heated up by heat transfer from the irradiated

pipe outer surface. The heated materials at the pipe top including both the outer and inner surface allowed the molecules in the amorphous regions to rearrange more quickly and form a more regular alignment (i.e. annealing). Because of the poor heat conductivity of PE, the temperature of the inner surface at the top is lower than the outer surface at the top. Hence the former shows a less obvious annealing effect and has less density increment. The large distance between the top and the bottom inhibited the heat transfer hence the bottom part including both inner and outer surfaces remained at a lower temperature. Therefore, the density at the top facing the sun is increased but the bottom part is not. The results also confirm that the reflected or scattered solar irradiation is less likely to cause secondary irradiation for samples located at the bottom during weathering.

Thermal analysis was carried out to further investigate the crystallinity changes after weathering of the material as described in the following section.

5.2.3 Thermal analysis

The density measurement showed that uncoated pipe outer surface facing the sun undergoes a more obvious annealing than the shaded side. Such annealing is akin to the annealing effect that was introduced by the skin on the PE core pipe outer surface during processing. For the annealing on the uncoated pipe during aging, there was degradation in the amorphous region. Thermal analysis in this section will focus on the distribution of the crystallites and melting temperature to investigate the annealing effect of weathering on the uncoated pipe with the consideration of polymer degradation.

It was showed in Figure 5-47 and Figure 5-48 that the increment of density caused by weathering become obvious in 3 GJ/m^2 aged samples, hence the 3 and 10 GJ/m^2 aged uncoated pipe outer surface sample melting curves are shown along with two unaged uncoated pipe outer surfaces (one is a duplicated run) in Figure 5-49. The corresponding melting temperature (Tm) and crystallinity by weight that was calculated from enthalpy of fusion through equation (4-5) is summarized in Table 5-7.

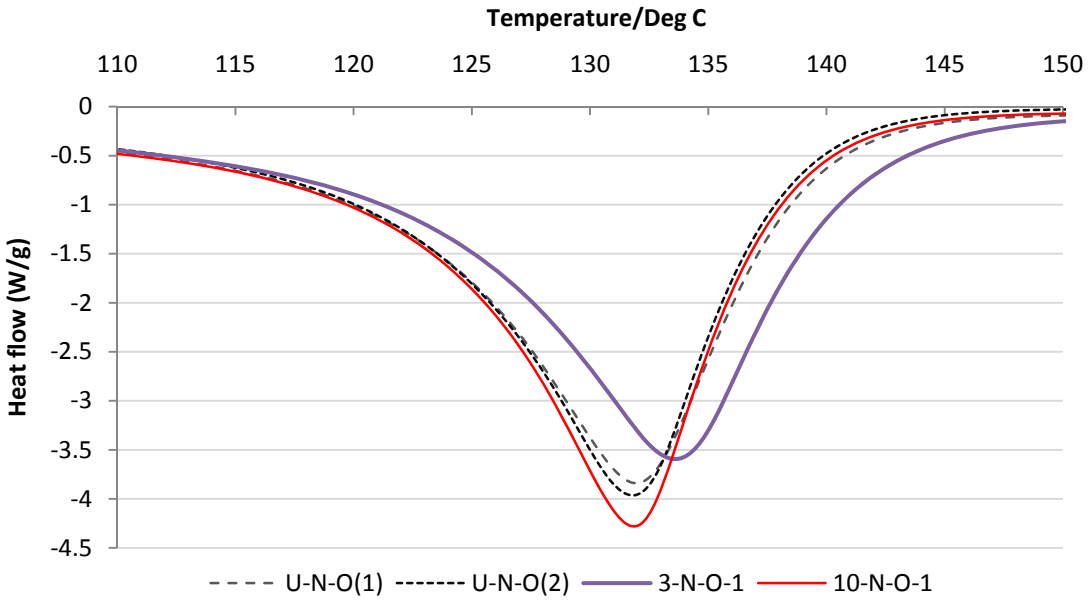

Figure 5-49 melting curves of aged uncoated pipe outer surface at the top and at the bottom during weathering

Table 5-7 Tm and crystallinity summary of aged uncoated pipe outer surfaces

Sample	Crystallinity by weight (%)*	Tm(°C)
U-N-O(1)	62.6	132.0
U-N-O(2)	60.4	131.8
3-N-O-1	61.7	133.6
10-N-O-1	64.1	131.9

*By using enthalpy of fusion of PE crystal value 293J/g [135]

Table 5-7 shows that there is increase of enthalpy of fusion with radiation dosage following the order of radiation level in the sample N-O-1 which is at the top during aging. Such a trend is identical with the density values showed in Figure 5-47. The increase of enthalpy of fusion is also due to annealing that occurred after 3 GJ/m^2 to 10 GJ/m^2 weathering.

For the 3GJ/m^2 aged sample, the melting curve in Figure 5-49 is similar to the unaged skinned pipe outer surface that caused by annealing as shown in Figure 4-17. The increase of crystallinity is accompanied by increase of Tm, indicating the increase of crystallinity is mainly due to lamellae thickening.

For the 10 GJ/m^2 aged sample, GPC results showed that chain scission occurred. Chain scission releases chains in the amorphous region from entanglements, and

therefore increasing the number of lamellae growth sites. Secondary crystallization may occur at the newly degraded chain. Lamellae growth may also happen at the existing crystallites that were not reacted with oxygen. Overall, the crystallinity of 10 GJ/m^2 aged samples still increases.

The melting curves in Figure 5-49 also show that there is an increase of melting temperature in the sample after 3 GJ/m^2 aging. However, after 10 GJ/m^2, the melting temperature shifted back to the value of unaged samples with increased enthalpy of fusion.

The decrease of melting temperature of the 10 GJ/m^2 aged sample indicates that the thickest lamellae that formed in the 3GJ/m^2 aged samples may be destroyed. This is probably due to oxidation and chain scission which decreased the perfection of the existing crystallites when degradation occurred. Lamellae thickening occurred at the new sites rather than existing crystallites. Therefore the melting temperature is decreased. Because oxidation level is still low for 3GJ/m^2 aged samples, the decrease of Tm is not obvious and lamellae thickening are still predominant.

Because the crystallinity values in Table 5-7 are identical with the density values shown in Figure 5-47, no more duplicated runs were carried out for the sample located at the top during aging. It is also considered that the DSC results gave indirect information of lamellae thickness distribution which is mostly based on the Gibbs-Thomson equation. Research showed that there are differences of directly measured lamellae thickness from DSC curves calculated from Gibbs-Thomson equation for linear PE and ethylene random copolymers [162] and caution should be paid using the equation. Therefore, the melting temperature and the curves from the DSC measurement only give preliminary information of the annealing effect on the pipe outer surface after aging. In order to investigate the morphology change in depth, direct lamellae measurements which includes transmission electron microscopy (TEM), longitudinal acoustic mode (LAM) in Raman spectroscopy and small angle X-ray scattering (SAXS) are suggested for future work.

The thermal analysis results are identical to the density results with increase of crystallinity after aging observed at the pipe outer surface located at the top. DSC

curves shows shifting of Tm to lower temperatures which may be caused by photo-oxidation and chain scission. Overall, the annealing during aging is confirmed by the thermal analysis results. The following section will discuss the residual stress change during weathering, which is also believed to be affected by annealing.

5.2.4 Residual stress assessment

It has been shown in section 4.2.4 and 4.3.1 that annealing reduces residual stress which increases the pipes' hydrostatic strength. Annealing was also observed after outdoor weathering in previous sections and it is necessary to assess its effect on the residual stress and its consequences for the pipe hydrostatic strength. The pipes NSPF, 0.8SPF and 1.5SPF were tested in the same way as the unaged samples. The creep curves are summarized as following figures.

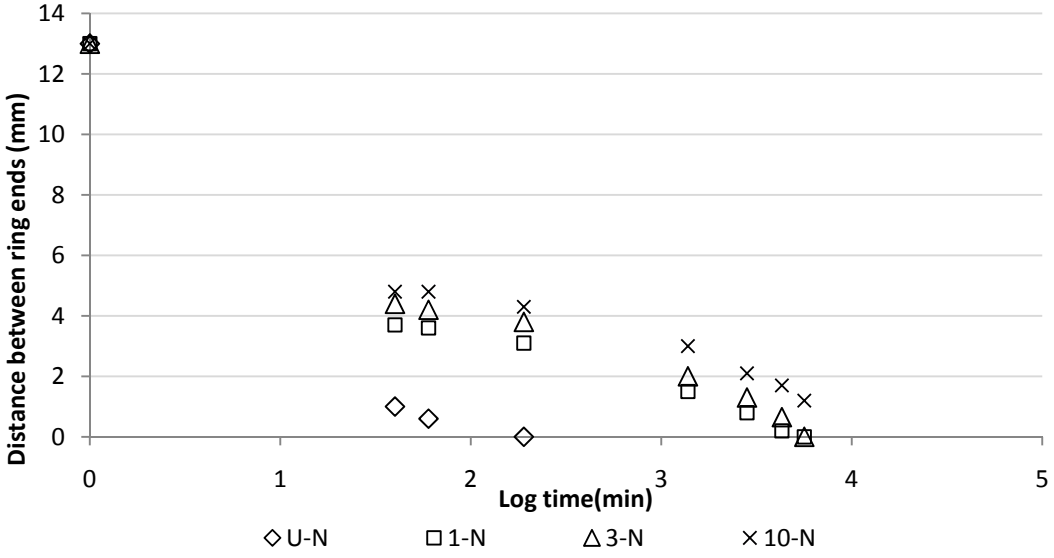

Figure 5-50 Creep rupture curve for pipe NSPF before and after weathering

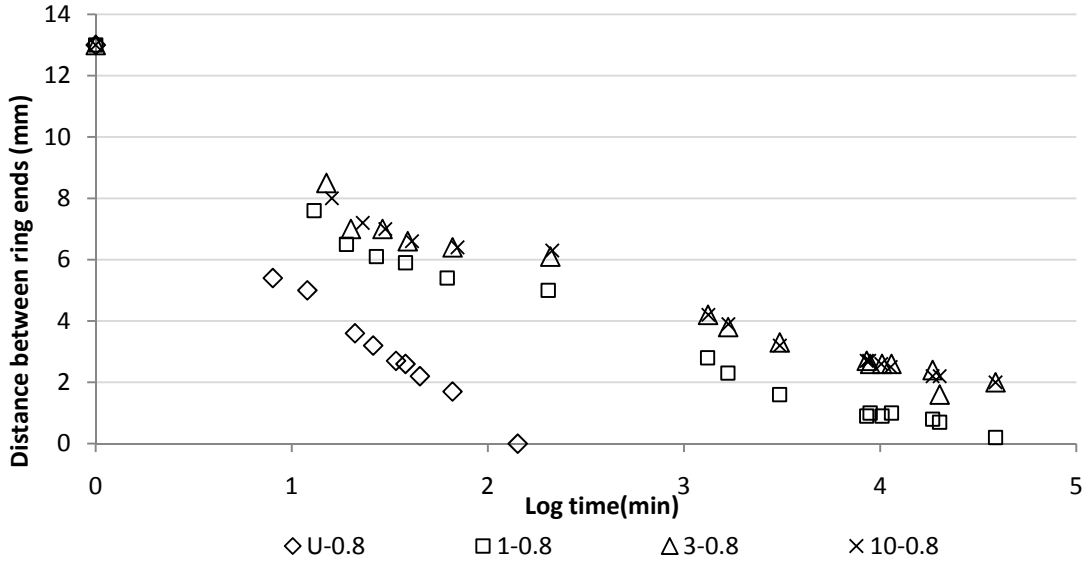

Figure 5-51 Creep rupture curve for pipe 0.8SPF before and after weathering

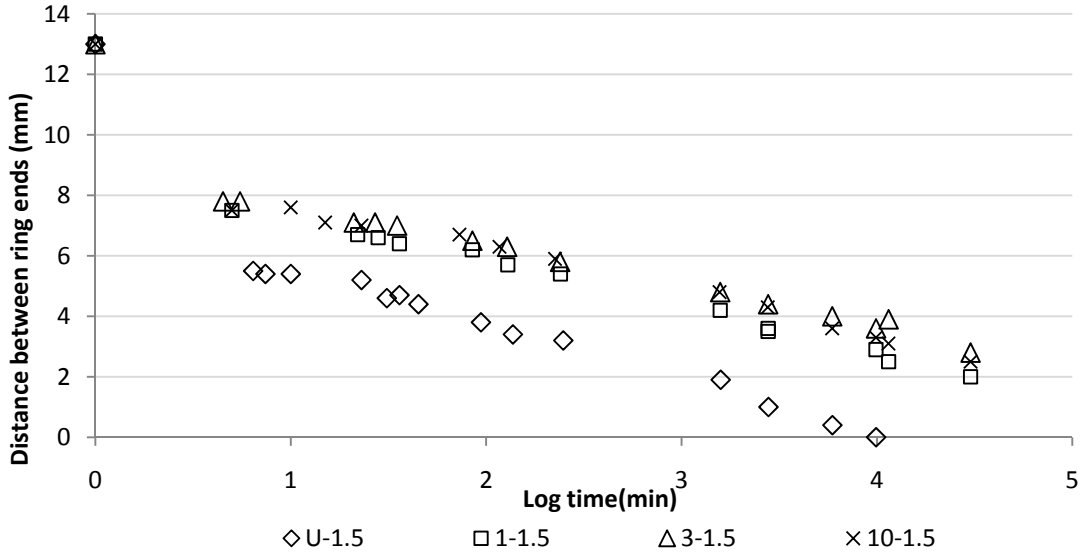

Figure 5-52 Creep rupture curve for pipe 1.5SPF before and after weathering

These curves show that regardless of whether the pipe has a skin or not, as the radiation energy increases, the general slope of the residual stress curve decreases, suggesting a lower level of residual stress. It can also be found that most of the residual stress was released after 1GJ/m^2 weathering for both the uncoated pipe and skin pipes. After 1GJ/m^2 weathering, the decrease of residual stress is small even after 10 GJ/m^2 aging.

To quantify the residual stress level, the same curve fitting method was applied to the data of the aged samples as for the unaged samples in section 4.2.4. Due to limited data, the fitting for unaged NSPF samples was not applicable. The model below was applied in the curve fitting procedure, the same as equation (4-10) in section 4.2.4.

$$Y = a(1 - exp(-bx)) + c\,(1 - exp(-dx))$$

The parameters of the fitted curve are summarized in the following tables.

Table 5-8 Fitted parameters for unaged and aged pipes NSPF, 0.8SPF and 1.5SPF

	Radiation Energy (GJ/m^2)			
	0	1	3	10
Fitting Parameters	**NSPF**			
a		0.0113	0.0140	0.0272
b		0.0005	0.0004	0.0678
c		0.0310	0.0290	0.0118
d		0.0670	0.0646	0.0004
R^2		0.9941	0.9937	0.9938
ε_0^*		**0.0423**	**0.0430**	**0.0391**
	0.8SPF			
a	0.0226	0.0177	0.0129	0.0150
b	0.0057	0.0008	0.0006	0.0007
c	0.0292	0.0214	0.0209	0.0190
d	0.1607	3.3391	6.9411	3.1367
R^2	0.9870	0.9796	0.9945	0.9838
ε_0^*	**0.0518**	**0.0391**	**0.0338**	**0.0339**
	1.5SPF			
a	0.0148	0.0107	0.0088	0.0117
b	0.0039	0.0004	0.0003	0.0004
c	0.0241	0.0234	0.0222	0.0206
d	5.0792	0.8970	1.4416	3.7205
R^2	0.9780	0.9933	0.9836	0.9868
ε_0^*	**0.0390**	**0.0340**	**0.0310**	**0.0323**

*** ε_0=a+c**

As the overall residual stress is released, the time between ring slitting until the two ends met was greatly increased and more data points could be collected at longer creep times. The 1, 3 and 10 GJ/m^2 weathered sample have creep time spans from

1250 to 10,000 minutes which was suggested time range for good fittings [144], therefore more reliable curve fit results were obtained. The coefficient of determination R^2 value for weathered NSPF was higher than 0.99. Although some fitted data for the skin pipe are between 0.97~0.99, they are still good enough to yield informative results.

From the approximated equation (4-9), it is known that the residual stress at the very beginning of pipe ring closing procedure σ_0 is proportional to its corresponding strain ε_0. Taking the maximum strain in Table 5-8 (the strain value of unaged 0.8SPF) as 100% residual stress, the percentage of retained residual stress of the remaining samples compared to this 100% residual stress can be obtained by dividing their strain value by the maximum strain value then multiplying by 100. The percentage of retained residual stress is plotted as a function of radiation dosage in Figure 5-53.

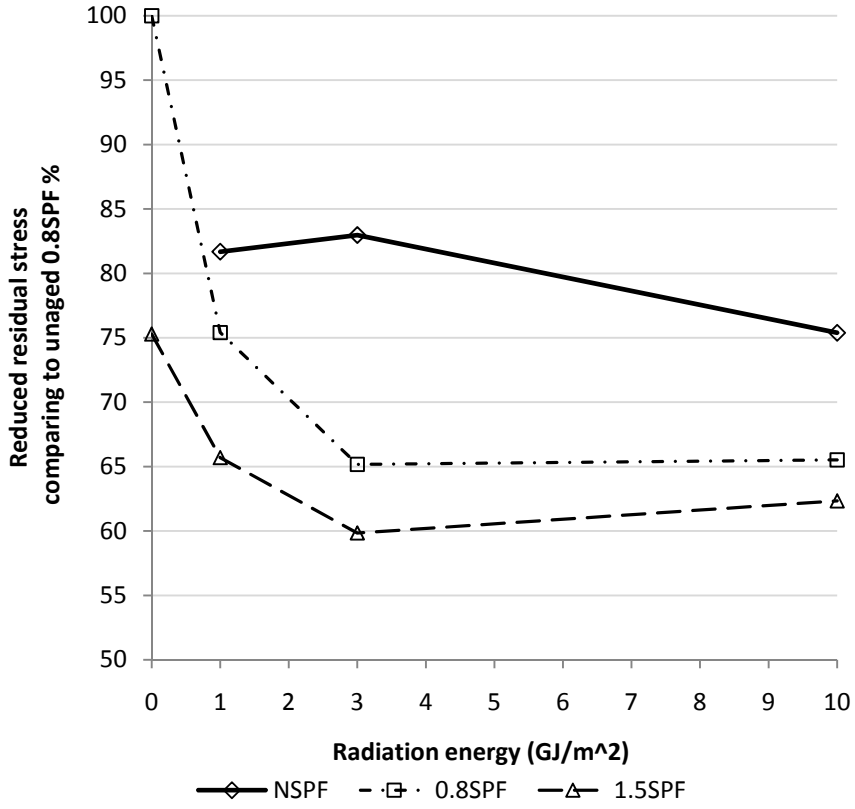

Figure 5-53 Percentage of retained residual stress is plotted as a function of radiation dosage

For the skinned pipe 0.8SPF and 1.5SPF, rapid release of residual stress occurred after 1GJ/m^2. The residual stress release rate decreased as the radiation energy increased.

After 3 GJ/m^2 the residual stress release rate became so low that the residual stress level for 3 and 10 GJ/m^2 aged sample are close to each other.

For the unaged uncoated pipe, due to fast pipe ring closure, only limited data were obtained and curve fitting is not applicable to this sample. However, from the creep curve in the Figure 4-21, it can be seen that the residual stress of the unaged uncoated pipe NSPF is higher than the unaged 0.8SPF which is taken as 100 % residual stress. Therefore, the retained residual stress level of unaged NSPF is higher than 100% if it could be drawn in Figure 5-53. Hence, there is also a rapid release of residual stress for uncoated pipe after 1GJ/m^2 weathering.

Figure 5-53 also shows that the residual stress of uncoated pipe is always higher than the skin pipe under the same weathering conditions, indicating that although annealing occurred during weathering, the quenching effect of the uncoated pipe still affected the residual stress and resulted in such a residual stress ranking. The PP skin did not seem to affect the stress relaxation of the skin pipe during weathering compared to the uncoated pipe.

The manner of the rapid decrease of residual stress followed by a low stress decrease rate near zero as a function of radiation energy for both uncoated pipe and skin pipes can be explained by the viscoelasticity of PE at different temperatures.

As the sample receives solar radiation, it will have a higher temperature than the sample stored in the lab at room temperature. According to the principle of time-temperature equivalence for viscoelastic materials, the higher temperature in the desert area equates to a longer time of stress relaxation at room temperature. Therefore, the sample that received more radiation energy at higher temperature during outdoor weathering equates to longer relaxation time than the relaxation time at room temperature and has a lower relaxed residual stress than the sample stored at room temperature.

Interestingly, the residual stress relaxation curve resembled a conventional stress relaxation curve. But due to the limited data, it is difficult to describe the stress relaxation behavior of uncoated and skin pipe during weathering.

For the unaged pipes, the skin pipe has a lower residual stress than the uncoated pipe. It is generally believed [141, 142 and 166] that pipe with less residual stress has higher long term hydrostatic strength as discussed in section 4.2.4. Because the skin pipe always has a lower residual stress than the uncoated pipe when they experience the same weathering conditions, it is also believed that the skin pipe will have higher long term hydrostatic strength after weathering because the ranking of stress level did not change. The skin strengthening effect on the PE core pipe still exists compared to its corresponding uncoated PE pipe. As the time for long term hydrostatic strength (LTHS) test for weathered pipe are so long and expensive that it has not been carried out at this stage, but could be investigated later.

The density and thermal analysis results of skin pipes showed a low level of annealing during weathering because the skin pipes are already annealed during processing as the skin prevents quenching. However, the residual stress results of the skin pipe showed an obvious annealing effect for skin pipes during weathering. It is believed that further crystallization may occurred in the amorphous region, and further investigations are needed to correlate the morphology and mechanical properties of both uncoated pipe and skin pipes.

Section 5.2 discussed the effect of the PP skin on the PE core pipe properties across the pipe thickness. OIT results indicated that the skin prevented the PE core pipe from antioxidant loss and after 10 GJ/m^2 outdoor weathering, the antioxidant level throughout the whole pipe still met the industrial standards while the uncoated pipe showed rapid antioxidant drop to close to zero at the solar irradiated outer surface just after 1 GJ/m^2 weathering. The density and thermal analysis results indicate that annealing occurred during weathering for the uncoated pipe but for the skin pipe the density and thermal property do not change significantly. The residual stress assessment confirmed the effect of annealing during weathering in a more obvious manner. The PP skin did not seem to affect the residual stress relaxation behavior during weathering. According to previous research, pipe with lower residual stress will have higher LTHS values. Hence, the skin pipe should still have a higher LTHS value compared with the uncoated pipe after the same weathering conditions.

Chapter 6 CONCLUSIONS

This project investigated the production of PP/PE dual layer pipe and its properties as produce and after outdoor weathering under various radiation dosages by comparing them with the uncoated PE pipe.

6.1 Conclusions for unaged samples

The properties of the unaged pipe surfaces were characterized by contact angle measurement and ATR-FTIR. Using these techniques, it was found that a fatty acid amide type adhesion reducer was present in the PP skin. This additive migrated to the PP/PE interface and led to reduction in dispersive component of the surface free energy at these surfaces. ATR-FTIR results also proved that the concentration of migrated adhesion reducer increases with the skin thickness which is believed to be due to the thicker skin have a lower cooling rate and longer migration time for the adhesion reducer. Although the adhesion reducer migrated to the PE outer surface, the EF peel testing results of unaged samples showed that the additive has little effect on EF peel strength.

The antioxidant concentration in the PE pipe was evaluated by using OIT measurement. The results showed that the OIT value of the as produced PE pipe is lower than the virgin PE pellets. This may because during processing, part of the antioxidant package (probably the secondary antioxidant) was consumed. The OIT values across the pipe wall show that the uncoated pipe has a flatter OIT profile than the skinned pipe, indicating that the skin affects the antioxidant distribution across the pipe thickness. The OIT values of the uncoated pipe outer surface along the pipe circumference showed that antioxidant is evenly distributed at this surface. This result was used as a control to show the effect of solar radiation on the PE pipe outer surface.

Density results showed that due to the PP skin reducing the quenching of the PE core pipe outer surface by the cooling water, the pipe with the thicker skin has a flatter density profile across the pipe wall and a higher overall density than those with

thinner skins or bare pipes. This is because the thermal conductivity of PP is around half that of the PE. The pipe with the thicker skin has a lower cooling rate and a longer time for chain rearrangement.

The Tm and melting range obtained by thermal analysis support the density results. Thermal analysis also showed that the increase of density may not only be due to the thickening of lamellae, but may also be due to better-defined stacking of the lamellae and larger spherulites.

The prevention by the skin of the PE core pipe from quenching also reduces residual stress. The residual stress in the hoop direction was evaluated by a slit ring closure method and it was found that the 1.5mm skin reduced the residual stress of the uncoated pipe by more than 25%.

The LTHS test results showed that due to the increase of density and decrease of residual stress, the skinned pipe has a higher LTHS than the corresponding uncoated pipe. If the same pressure were applied, there would be an approximately 10.9% increase in LTHS of the 1.5mm skin pipe compared with the bare pipe at the 50-year extrapolation and the safety factor of the skin pipe would be raised by 7.2%.

6.2 Conclusions for aged samples

The properties of the weathered pipe surfaces both uncoated and skinned were characterized by contact angle, ATR-FTIR, XPS and GPC techniques, and the EF peel test was carried out to assess the quality of EF joints that largely depend on the EF surface properties.

The contact angle results showed that generally, after weathering, there is increase of surface free energy (SFE) in both uncoated and skinned PE pipe inner and outer surfaces (for skinned pipe, it is the PP outer surface). The SFE increment at these surfaces is a result of increase in the polar component (which is the main factor) and decrease of the dispersive component. The increase of the polar component may be because of possible oxidation as well as antioxidant migration, while the decrease of

the dispersive component may possibly be due to possible increase of $–CH_3$ groups at these surfaces. The surface free energy of the PP/PE interface decreased as the weathering process proceeded. This decrease was assumed to be due to more adhesion reducer migrating onto the PP/PE interface.

Infrared results (IR) give further information about the PP and PE surfaces. The IR results for the PP inner surface confirmed that it was free from oxidation. However the IR spectra of the PP outer surfaces showed photo-oxidation products in the C=O and O-H absorption regions at the solar irradiated side and concentrations of these groups and oxidized areas increased with radiation dosage. A peak fitting technique showed the relative concentration of five possible oxidation products containing C=O groups during weathering, among which carboxylic acids had the highest concentration. During the solar irradiation procedure, it was found that there is a slowdown of oxidation between 1 and 3 GJ/m^2 weathering and then an auto-accleration of oxidation afterwards.

The IR results of the skinned pipe PE outer surface showed that the PP skin protects the PE outer surface from oxidation even after 10 GJ/m^2 weathering. Meanwhile, the antioxidants on the uncoated PE pipe outer surface remain effective at a lower concentration after $3GJ/m^2$, however, slight oxidation was observed after 10 GJ/m^2 aging. During the whole weathering process, the PE inner surface was still protected by the antioxidants.

Although XPS results did not provide further oxidation information on the 10 GJ/m^2 aged uncoated PE pipe outer surfaces, contamination was observed. The results also showed that the PP skin protects the PE core pipe from contamination after $10GJ/m^2$ weathering.

The GPC results indicate that no obvious degradation was observed after 3 GJ/m^2 and only slight degradation was observed after 10 GJ/m^2 on the bare PE pipe outer surface, but there is a shift from higher molecular weight polymer to lower molecular weight polymer, and decrease of Mw and PDI. Such decrease may due to the higher probability of chain scission in longer chains assuming that branches are evenly distributed along each molecule main chain. Due to the protection of the PP skin, the

molecular weight of skinned PE core pipe is not affected even after 10 GJ/m^2 irradiation. Because the samples dissolved fully in the GPC solvent, the possibility of crosslinking during weathering can be excluded.

EF peel test results indicate that due to consumption of antioxidants, the irradiated side of uncoated PE pipe will form a brittle layer and weaken the EF joint. Due to the protection of PP skin on the PE core pipe from oxidation, the EF joint quality of skin pipe is as good as unaged samples.

The properties such as OIT values, crystallinity, crystalline structure and residual stress across the PE pipe wall and along the pipe circumference were also investigated as a function of irradiation energy.

The OIT results gave an indication of the antioxidant distribution along pipe circumference and across the pipe wall for both uncoated pipe and skin pipe. As the primary antioxidant concentration is proportional to the OIT value [128], it can inferred from the results that the uncoated pipe outer surface facing the sun lost most of its antioxidants after only 1 GJ/m^2 weathering while the shaded part of the pipe retained ~70 % of its antioxidant after 1 and 3 GJ/m^2 weathering but the decreased to ~30 % after 10GJ/m^2 weathering compared to the unaged samples. The differences in irradiation conditions along pipe circumference also led to variation of antioxidant distribution in the middle of the pipe wall and inner surface where a more gradual decrease was found. Although the middle of the pipe wall acted as antioxidant reservoir for both pipe surfaces, and replenishment of antioxidant to the two surfaces was observed for both uncoated and skinned pipes, the skinned pipe showed better resistance to antioxidant loss than the uncoated pipe. The OIT results showed that the antioxidant level of the skinned pipe through the PE pipe wall is above 50% of its original value even after 10 GJ/m^2, and still meets the industrial standard.

The density results showed that irrespective of sample location along the pipe circumference, the average density values showed no obvious change after weathering. The quenching effect caused by water spray cooling during processing still existed for uncoated pipe at the shaded side after 10 GJ/m^2 weathering. However, an annealing effect was found at the irradiated pipe outer and inner surfaces after weathering. The

difference in density along the pipe circumference is possibly due to the thermal effect of the infrared portion in the solar radiation. The solar irradiated side heated up during irradiation and secondary crystallization occurred.

Thermal analysis results further investigate the change of crystallinity and crystalline structure after natural weathering. It was found that for the uncoated pipe outer surface at the top facing the sun (location 1), the crystallinity increase with radiation energy, but the melting temperature (Tm) increased until 3GJ/m^2 radiation and a decrease was observed for 10GJ/m^2 radiation. For sample irradiated up to 3GJ/m^2 radiation, the increase of crystallinity is possibly due crystal growth in existing crystallites. For sample irradiated up to 10 GJ/m^2, the crystal growth may be interrupted by oxidation which was evident by ATR-FTIR and it was showed by the decreased of Tm. However, due to chain scission which was evident by GPC, the newly degraded chain that was released from the long chain entanglement may crystallize increase the crystallinity.

Residual stress showed that for both uncoated pipe and skinned pipe, the residual stress was rapidly released after 1GJ/m^2 weathering then the release rate slowed down. After 3 GJ/m^2 weathering, the residual stress release rate decreased to nearly zero. During the whole weathering process, the pipe with the thicker skin had a lower residual stress than the pipe with the thinner skin. From the residual stress and LTHS results of the unaged samples, it can be inferred that under the same irradiation conditions, the skinned pipe may have a higher LTHS than the uncoated pipe because the former has a lower residual stress.

This project investigated the chemical composition, crystalline structure and performance of uncoated pipe and skinned pipe as well as the additives such as the adhesion reducer within the skin and especially antioxidants under different outdoor weathering conditions. Some mechanisms are proposed to explain the results. It can be concluded that the skinned pipe has a better weathering resistance than the corresponding uncoated pipe. As some mechanisms are based on assumptions or hypothesises, some future work is suggested for further investigations.

Chapter 7 FUTURE WORK

- Using FTIR imaging technique to study the distribution of $–CH_3$, $–CH_2$, amide and C=O groups on pipe surfaces and explain the change of polar and dispersive components of the surface energy during weathering.
- Extract the antioxidants in the PE and PP and analyze their chemical properties before and after weathering.
- With the knowledge of the antioxidants, distinguish the oxygen element that is attributed to antioxidant or is introduced by oxidation or even contamination.
- Study the behaviour of the antioxidant in the PE pipe with and without skin, along the pipe circumference and across the pipe thickness, and propose a possible reaction scheme of the antioxidants in the two pipes.
- Study the antioxidant behaviour of the PP skin and evaluate its protection limit (for example, maximum outdoor weathering time) to the PE core pipe against outdoor weathering.
- Investigate the migration behavior of the antioxidant before and after weathering in both the PE pipe and the PP skin, and study the effect of antioxidant consumption, evaporation and extraction by rain on antioxidant migration.
- Investigate the weathering resistance of the blue pigmented solid pipes which were weathered along with the unpigmented solid pipes and the skin pipes. Compare the protection of the PE materials against photo-oxidation by pigments and by the PP skin.
- Carry out direct lamellae measurements including transmission electron microscopy (TEM), longitudinal acoustic mode (LAM) in Raman spectroscopy and small angle X-ray scattering (SAXS) to investigate the effect of degradation on the morphology change of the 10 GJ/m^2 aged samples.
- Measure the long term modulus of the PP and PE to produce a more accurate pipe life prediction for the skinned pipe through the LTHS extrapolation method.
- Perform LTHS tests on the aged samples, especially the 10 GJ/m^2 aged uncoated pipes to evaluate the outdoor weathering effect on the pipe performance during its service life.

REFERENCES

1 J. Bowman, D. Harget, Uponor Ltd., *Pipeline & Gas Journal*, Dec 2001.

2 Patent: US 6,968,762 B1.

3 Radius Systems Ltd, *2007 Polyethylene pipes and fittings price list and product selector*.

4 J. Bowman, *Polymer Engineering and Science*, 37, 4 (1997) 674-691.

5 Patent: WO2006/092567.

6 E.W. Fawcett, R. O. Gibson, M. W. Perrin, J. G. Patton, E. G. Williams, *British Patent 471590*, Sept 6, 1937 (1937).

7 A. J. Peacock, Handbook of Polyethylene Structures, Properties, and Applications, Marcel Dekker, New York, 2000, pp. 51, pp. 58, pp. 462.

8 K. Ziegler, *Germany Patent 878560*, (1953).

9 P. J. DesLauriers, M. P. McDaniel, D. C. Rohlfing, R. K. Krishnaswamy and S. J. Secora, *Polymer Engineering and Science*, 45 (2005) 1203-1213.

10 Standard: BS EN ISO 9080:2003.

11 L. Hubert, L. David, R. Seguela, G. Vigier, C. Degoulet and Y. Germain, *Polymer*, 42 (2001) 8425-8434.

12 T. Späth and M. Stranz, *High-pressure pipes made from polyethylene only--a new generation of plastic pipes*, Plastic Pressure Pipes 2009, Cologne, Germany.

13 M. P. Kruijer, L.L. Warnet and R. Akkerman *Composites Part A: Applied Science and Manufacturing*, 36 (2005) 291–300.

14 T. Pekmen, *Innovations to Overcome Challenges in Demanding Pressure Piping Applications: Thick-Long-Reinforced HDPE Pipes*, Plastic Pressure Pipes 2009, Cologne, Germany.

15 D. Stani, *Complete system for energy-efficient large diameter pressure pipe production*, Plastic Pressure Pipes 2009, Cologne, Germany.

16 J. H. Schut, *Plastics Technology*, Dec 2008, pp. 36.

17 L. C. E. Struik, *Physical Aging in Amorphous Polymers and Other Materials*, Elsevier, Amsterdam, 1978.

18 J. R. White, *Comptes Rendus Chimie*, 9 (2006) 1396-1408.

19 J. R. White, in: 4th Int. Conf. on deformation, yield and fracture of polymer, Publ. PRI, London, Cambridge, 1979, Paper 8.

20 D. C. Mellor, A. B. Moir and G. Scott, *European Polymer Journal*, 9 (1973) 219.

21 C. N. Kartalis, C. D. Papaspyrides, R. Pfaendner, K. Hoffmann, H. Herbst, *Journal of Applied Polymer Science*, 73 (1999) 1775.

22 F. Gugumus, *Polymer Degradation and Stability* 27 (1990) 19-20

23 J. Billiani and E. Fleischmann, *Polymer Degradation and Stability*, 28 (1990) 67.

24 J. B. Adeniyi and G. Scott, *Journal of Polymer Materials*, 5 (1988) 57.

25 E. M. Hoàng, N. S. Allen, C. M. Liauw, E. Fontán and P. Lafuente, *Polymer Degradation and Stability*, 91 (2006) 1363-1372.

26 M. U. Amin, G. Scott and L. M. K. Tillekeratne, *European Polymer Journal*, 11 (1975) 85.

27 M. Philip and J. Attwood, A. Hulme, G. Williams and P. Shipton, *Evaluation of weathering in mixed polyethylene and polypropylene products, The Waste & Resources Action Programme R&D Report: Plastics*, 2004.

28 S. Moss and H. Zweifel, *Polymer Degradation and Stability*, 25 (1989) 217.

29 E. M. Hoàng, N. S. Allen, C. M. Liauw, E. Fontán and P. Lafuente, *Polymer Degradation and Stability*, 91 (2006) 1356-1362.

30 F. Gugumus, *Polymer Degradation and Stability*, 74 (2001) 327–339

31 T. Kelen, *Polymer Degradation*, Van Nostrand Reinhold, New York, 1983, pp.132.

32 J. A. Kerr, *Chemical Reviews*, 66 (1966) 465-500.

33 A. Tidjani, *Journal of Applied Polymer Science*, 64 (1997) 2497.

34 T. Kelen, *Polymer Degradation*, Van Nostrand Reinhold Company, New York, 1983, pp. 131-135.

35 F. Gugumus, *Polymer Degradation and Stability*, 76 (2002) 329–340.

36 B. van Beusichem, M. A. Ruberto, Ciba Expert Services, Ciba Specialty Chemicals, Poster "*Introduction to polymer additives and stabilization*".

37 N. Grassie and G. Scott, *Polymer Degradation and Stabilization*, Cambridge University Press, New York, 1988, pp. 69-70.

38 S. J. Blanksby and G. B. Ellison, *Accounts of Chemical Research*, 36 (2003) 255-263.

39 B. Rånby, J. F. Rabek, *Photodegradation, photo-oxidation and photostabilization of polymers*, Wiley-Interscience, New York, 1975, pp. 573.

40 J. F. Rabek, *Photodegradation of polymers: physical characteristics and applications*, Springer-Verlag, Berlin Heidelberg, 1996, pp. 212.

41 J. F. Rabek, *Mechanism of Photophysical Processes and Photochemical Reactions in Polymers: Theory and Applications*, John Wiley & Sons, Chichester, 1987.

42 J. F. McKellar and N. S. Allen, *Photochemistry of Man-Made Polymers*, Applied Science Publ., London, 1979.

43 A. V. Shyichuka, J.R. White, I. H. Craigb and I. D. Syrotynskac, *Polymer Degradation and Stability*, 88 (2005) 415-419.

44 R. Magnus, *Kunststoffe -German Plastics*, 81,12 (1991) 19 (translation of *Kunststoffe*, 81 (1991) 1113).

45 B. Rånby, *Journal of Analytical and Applied Pyrolysis*, 15 (1989) 237-247.

46 M. U. Amin, G. Scott and L. M. K. Tillekeratne, *European Polymer Journal*, 11 (1975) 85-89.

47 C. H. Chew, L. M. Gan and G. Scott, *European Polymer Journal*, 13 (1977) 361-364.

48 A. Tidjani, *Polymer Degradation and Stability*, 68 (2000) 465-469.

49 G. Scott, *Coatings and plastics reprints*, American Chemical Society Meeting, Philadelphia, 35, 1 (1975) 163.

50 A. Factor, C. A. Russel and T. G. Traylor, *Journal of American Chemical Society*, 87 (1965) 3692.

51 T. G. Traylor and C. A. Russel, *Journal of American Chemical Society*, 87 (1965) 3698.

52 F. Severini, R. Gallo, S. Ipsale, *Polymer Degradation and Stability*, 22 (1988) 185-194.

53 J. R. White and A. V. Shyichuk, *Polymer Degradation and Stability*, 92 (2007) 1161-1168.

54 J. R. White, A. V. Shyichuk, *Polymer Degradation and Stability*, 92 (2007) 2095-2101.

55 J. R. White, A. V. Shyichuk, T. J. Turton, I.D. Syrotynska, *Polymer Degradation and Stability*, 91 (2006) 1755-1760.

56 A. V. Shyichuk, D. Y. Stavychna and J. R. White, *Polymer Degradation and Stability*, 72 (2001) 279-285.

57 S. N. Zhurkov, V. A. Zakrevskyi, V. E. Korsukov and V. S. Kuksenko, *Journal of Polymer Science Part A-2: Polymer Physics*, 10 (1972) 1509.

58 F. Bueche, *Journal of Applied Physics*, 26 (1955) 1133.

59 F. Bueche, *Journal of Applied Physics*, 28 (1957) 784.

60 F. Bueche, *Journal of Applied Physics*, 29 (1958) 1231.

61 K. L. DeVries and L. E. Hornberger, *Polymer Degradation and Stability*, 24 (1989) 213.

62 A. A. Popov, N. N. Blinovm, B.E. Krisyuk and G. E. Zaikov, *Polymer Degradation and Stability*, 7 (1984) 33.

63 G. Scott, *Polymer Engineering and Science*, 24 (1984) 1007.

64 N.C. Billingham, P. D. Calvert and G. Scott, *Development in Polymer Stabilisation-5th Ed*. Applied Science Publisher Ltd, Oxford, 1982, Chapter 5.

65 J. Lamire, J. L. Gardette, J. Lacoste, P. Delprat, D. Vaillant, *Polymer Durability*, Eds. R. L. Clough, N. C. Billingham K. T. Gillen, ACS Adv. Chem. Ser., 1996, pp. 577.

66 K. Jacobson et al, *Aging Studies & Lifetime Extension of Materials*, Ed. L. G. Mallinson, Kluwer Academic/Plenum Publisher, New York, 2001, pp. 253-259.

67 M. Dexter, R. W. Thomas and R. E. King III, *Encyclopedia of Polymer Science and Technology Vol.5 Antioxidant*, John Wiley & Sons, New York, 2002, pp. 164-179.

68 J. R. White and A. Turnbull, *Journal of Materials Science*, 29 (1994) 584-613.

69 R. Shelton, *Polymer Stabilization*, Ed. W. L. Hawkins, Wiley-Interscience, New York, 1972, pp. 97–98.

70 P. A. Smith and S. E. Gloyer, *Journal of Organic Chemistry*, 40 (1975) 2508–2512.

71 B. Ohtani, S. Adzuma, H. Miyadzu, S. Nishimoto and T. Kagiya, *Polymer Degradation and Stability*, 23 (1989) 271.

72 N. S. Allen, A. Chirinis-Padron and T. J. Henman, *Polymer Degradation and Stability*, 13 (1985) 31-76.

73 P. Gijsman, J. Hennekens and D. Tummers, *Polymer Degradation and Stability*, 39 (1993) 225-233.

74 O. Haillant, *Polymer Degradation and Stability*, 93 (2008) 1793–1798.

75 P. P. Klemchuk and M. E. Gande, *Polymer Degradation and Stability*, 22 (1988) 241.

76 T. Kurumada, H. Ohsawa and T. Yamazaki, *Polymer Degradation and Stability*, 19 (1987) 263.

77 D. Vyprachtický and J. Pospíšil, *Polymer Degradation and Stability*, 27 (1990) 227.

78 A. J. Chirinos-Padron, P. H. Hernandez, N. S. Allen, C. Vasilion, G. P. Marshall and M. de Poortere, *Polymer Degradation and Stability*, 19 (1987) 177.

79 A. J. Chirinos-Pardron, P.H. Hernandez, E. Chaves, N. S. Allen, C. Vasiliou and M. de Poortere, *European Polymer Journal*, 23 (1987) 935.

80 J. Pospíšil, *Polymer Degradation and Stability*, 20 (1988) 181.

81 K. B. Chakraborty and G. Scott, *Polymer Degradation and Stability*, 1 (1979) 37.

82 N. S. Allen, C. Vasiliou and G. P. Marshall, *Polymer Degradation and Stability*, 24 (1989) 17-31.

83 K. B. Chakraborty and G. Scott, *European Polymer Journal*, 13 (1977) 1007.

84 F. Gugumus, *Polymer Degradation and Stability*, 24 (1989) 289.

85 N. S. Allen, C. Vasilou, G. P. Marshall and W. Chen, *Polymer Degradation and Stability*, 24 (1989) 17.

86 Standard: BS 2782, Part 5, Method 550A (also as ISO 4607).

87 Standard: BS 3900, Part F6 (also as ISO 2810).

88 Standard: BS 2782, Part 5, Method 540A (also as ISO 877).

89 S. Suzuki, O. Nishimura, H. Kubota, K. Yoshikawa and T. Shiroya, in Proceedings of 23rd Japan Congress on Materials Research, Kyoto, pp. 293.

90 F. S. Qureshi, M. B. Amin, A. G. Maadah, and S. H. Hamid, *Journal of Polymer Engineering*, 9 (1990) 67.

91 A. Wojtala, *International Polymer Science and Technology*, 28 (2001) T/85.

92 R. Satoto, W. S. Subowo, R. Yusiasih, Y. Takane, Y. Watanabe and T. Hatakeyama, *Polymer Degradation and Stability*, 56 (1997) 275.

93 D. T. Clark and H. S. Munro, *Polymer Degradation and Stability*, 9 (1984) 63.

94 F. Gugumus, in Proceedings of Symposium on Polymer Stabilization and Degradation: Problems, Techniques and Applications, Manchester, September 1985 (Royal Chemical Society, London).

95 P. Gijsman and J. Sampers, *Polymer Degradation and Stability*, 58 (1997) 55.

96 P. Gijsman and J. Sampers, *Die Angewandte Makromolekulare Chemie*, 261/262 (1998) 77-82.

97 J. Sampers, *Polymer Degradation and Stability*, 76 (2002) 455.

98 Standard: BS 3900, Parts F3, F5.

99 D. K. Owens and R.C. Wendt, *Journal of Applied Polymer Science*, 13 (1969) 1741–1747.

100 D. H. Kaeble, *Journal of Adhesion*, 2 (1970) 66–819.

101 C. Rullison, "*So You Want to Measure Surface Energy?*" Krüss Laboratories technical memo.

102 R. J. Martinovitch and G. R. Hill, *Applied polymer symposia*, 4 (1967) 141.

103 L. Küpper, J. V. Gulmine, P. R. Janissek and H. M. Heise, *Vibrational Spectroscopy*, 34 (2004) 65.

104 H. B. H. Hamouda, *Polymer*, 42 (2001) 5425-5437.

105 J. V. Gulmine, P. R. Janissek, H. M. Heise and L. Akcelrud, *Polymer Degradation and Stability*, 79 (2003) 385–397.

106 G. Geertz, R. Brull, J. Wieser, R. Maria, M. Wenzel, K. Engelsing, J. Wust, M. Bastian and M. Rudschuck, *Polymer Degradation and Stability*, 94 (2009) 1092–1102.

107 Z. bigniew Dobkowski, *Polymer Degradation and Stability*, 91 (2006) 488-493.

108 Standard: BS ISO 11357.

109 Standard: ASTM D3895.

110 Standard: DIN EN 728.

111 G. Dörner and R. W. Lang, *Polymer Degradation and Stability*, 62 (1998) 421-430.

112 Z. Dobkowski, *Polimery*, 50 (2005) 213.

113 M. Schmid and S. Affolter, *Polymer Testing*, 22 (2003) 419-428.

114 R. K. Krishnaswamy, *Polymer Engineering and Science*, 47 (2007) 516-521.

115 F. M. Peres and C. G. Schön, *Journal of Polymer Research*, 14 (2007) 181-189.

116 G. Pinter, M. Haager, W. Balika and R.W. Lang, *Polymer Testing*, 26 (2007) 180-188.

117 J. Pospíšil, Z. Horák, J. Pila, N. C. Billingham, H. Zweifel and S. Neprek, *Polymer Degradation and Stability*, 82 (2003) 148.

118 M. Sardashti, B. A. Baldwin, D. J. O'Donnell, *Journal of Polymer Science: Part B: Polymer Physics*, 33 (1995) 571-576.

119 A. Adams and B. Blümich, *Non-destructive Testing of Polyethylene Pipes by Mobile NMR*, Plastic Pressure Pipes 2009, Cologne, Germany.

120 K. Kruczala, B. Varghese, J. G. Bokria, S. Schlick, *Macromolecules*, 36 (2003) 1899-1908.

121 Standards: ISO 12162: 1995.

122 Borealis material specification sheet.

123 Standards: BS 2782-6: Methods 620D: 1991.

124 D. K. Owens, *Journal of Applied Polymer Science*, 13 (1969) 1743.

125 D. K. Owens, *Journal of Applied Polymer Science*, 14 (1970) 1727.

126 J. V. Gulmine, P.R. Janissek, H. M. Heise and L. Akcelrud, *Polymer Degradation and Stability*, 79 (2003) 385–397.

127 Helmut Günzler and Hans-Ulrich Gremlich. *IR spectroscopy: An Introduction*. Translated by Mary-Joan Blümich. WILEY-VCH Verlag GmbH, Weinheim, Germany, 2002, pp. 223-226, pp. 82-83.

128 J. Viebke and U. W. Gedde, *Polymer Engineering and Science*, 37 (1997) 900.

129 N. S. Allen, S. J. Palmer, G. P. Marshall and J. Luc-Gardette, *Polymer Degradation and Stability*, 56 (1997) 271.

130 Michel Biron, *Thermoplastics and Thermoplastic Composites: Technical information for Plastics Users*, Elsevier, Burlington, 2007, pp. 238, pp. 258.

131 H.S. Bu, W. Aycock and B. Wunderlich, *Polymer*, 28 (1987) 1165.

132 R. Chiang, P. J. Flory. *Journal of American Chemical Society*, 83 (1961) 2857.

133 R. Kitamaru, L Mandelkern. *Journal of Polymer Science A-2*, 8 (1970) 2079.

134 G. Mendez and A. Muller, *Journal of Thermal Analysis*, 50 (1997) 593.

135 B. Wunderlich, *Macromolecular physics. Crystal melting, Vol. 3.* Academic Press, New York, 1980.

136 J. Suwanprateeb, *Polymer Testing*, 23 (2004) 160.

137 J. Hassinen, M. Lundbäckb, M. Ifwarson and U.W. Gedde, *Polymer Degradation and Stability*, 84 (2004) 266.

138 D. Trifonova, P. Drouillon, A. Ghanem and G. J. Vancso, *Journal of Polymer Science*, 66, 515-523 (1997).

139 D. R. Rueda, J. Martinez-Salazar and F. J. Baltá-Calleja, *Journal of Materials Science*, 20 (1985) 834.

140 J. Suwanprateeb, *Polymer Testing*, 23 (2004) 157.

141 R. K. Krishnaswamy M. J. Lamborn, *Advances in Polymer Technology*, 24 (2005) 230.

142 S. Choi and L. J. Broutman, *Polymer (Korea)*, 21 (1997) 93-102.

143 S. Choi and L. J. Broutman, *Polymer (Korea)*, 21 (1997) 73.

144 A. Kazakov, *Polymer Testing*, 17 (1998) 443–450.

145 K. Chaoui, A. Chudnovsky, A. Moet, J*ournal of Materials Science*, 22 (1987) 3873.

146 E. Q. Clutton and J. G. Williams, *Polymer Engineering and Science*, 35 (1995) 1381–1386.

147 N. W. Tschoegl, *The phenomenological Theory of Linear Viscoelastic behavior: An Introduction.* Springer-Verlag, Berlin, 1989, pp. 99.

148 J. Bowman, J. Huang, M. Gilbert, D. Muckle and R. Street, Strength Benifits Provided by Skinned Pipe, Plastic Pressure Pipes 2009, Cologne, Germany.

149 M. Farshad, *Polymer Testing*, 24 (2005) 1043.

150 UK Gas Industry Standard PL2 Part 2 (2008).

151 F. R. Larson and J. Miller, *Trans. ASME*, 74 (1952) 765−775.

152 E. M. Hoàng and D. Lowe, *Polymer Degradation and Stability*, 93 (2008) 1496–1503.

153 S. Wu, *Polymer Handbook Fourth Edition Vol. 2*, Wiley-Interscience, New Jersey, 1999, p. 524.

154 M. Salvalaggio, R. Bagatin, M. Fornaroli, S. Fanutti, S. Palmery and E. Battistel, *Polymer Degradation and Stability*, 91 (2006) 2775-2785.

155 A. Tidjani, *Journal of Applied Polymer Science*, 64 (1997) 2497-2503.

156 L. J. Bellamy, *The Infrared Spectra of Complex Molecules, Second Edition,* Methuen & Co Ltd, London, 1964, pp. 206.

157 A. V. Iogansen, G. A. Kurkchi and L. A. Dement'eva, *Journal of Structural Chemistry*, 18 (1977) 591.

158 F. Gugumus, *Polymer Degradation and Stability*, 46 (1994) 123-140.

159 J. H. Botkin, *Technical Approaches to Improving the Scratch Resistance of TPO's. Part I: Surface Lubrication*, 2007 SPE Automotive TPO Global Conference, Sterling Heights, Michigan, October 2007.

160 A. I. Brodskii, L. A. Kotorlenko, S. A. Samoilenko and V. D. Pokhodenko, *Translated from Zhurnal Prikladnoi Spektroskopii*, 14, 5 (1971) 867–873.

161 C. Aymes-Chodur, N. Betz, B. Legendre and N. Yagoubi, *Polymer Degradation and Stability*, 91 (2006) 657.

162 L. Lu, R. G. Alamo and L. Mandelkern, *Macromolecules*, 27 (1994) 6571.

163 N. E. Schlotter and P. Y. Furlan, *Polymer*, 33 (1992) 3323-3341.

164 M. Lundback, C. Strandberg, A. C. Albertsson, M. S. Hedenqvist and U. W. Gedde, *Polymer degradation and Stability*, 91 (2006) 1071-1078.

165 E. Gaudichet-Maurin, S. Oberti , S. Trottier , J. Carmier, L. Girardot, B. Brulé, T. Labour and A. Bonnet, *Ageing Study of a Novel Multilayer Plastic Pipe in Contact with Chlorine Dioxide Disinfected Cold Water*, Plastic Pressure Pipes 2009, Cologne, Germany.

166 R. K. Krishnaswamy, *Polymer*, 46 (2005) 11664–11672.

APPENDIX A

Pipe size specifications for LTHS test

Code	Min thickness/mm (incl skin)	Min thickness/mm (excl skin)	Skin thickness/mm	OD/mm	core OD/mm
2-NSPF	n/a	10.51	n/a	110.40	n/a
4-NSPF	n/a	10.52	n/a	110.43	n/a
5-NSPF	n/a	10.47	n/a	110.42	n/a
6-NSPF	n/a	10.48	n/a	110.44	n/a
9-NSPF	n/a	10.52	n/a	110.46	n/a
12-NSPF	n/a	10.53	n/a	110.47	n/a
8-NSPF	n/a	10.54	n/a	110.47	n/a
10-NSPF	n/a	10.41	n/a	110.48	n/a
1-NSPF	n/a	10.45	n/a	110.36	n/a
7-NSPF	n/a	10.56	n/a	110.47	n/a
4-1.5SPF	11.82	10.17	1.65	113.51	110.30
6-1.5SPF	11.42	10.17	1.25	113.50	110.30
8-1.5SPF	11.80	10.16	1.64	113.50	110.18
10-1.5SPF	11.77	10.19	1.58	113.50	110.30
11-1.5SPF	11.75	10.21	1.54	113.48	110.31
12-1.5SPF	11.90	10.20	1.70	113.48	110.27
1-1.5SPF	11.48	10.18	1.30	113.50	110.23
5-1.5SPF	11.77	10.16	1.61	113.53	110.27
3-NSPF	n/a	10.50	n/a	110.42	n/a
11-NSPF	n/a	10.50	n/a	110.48	n/a
2-1.5SPF	11.79	10.15	1.64	113.48	110.23
7-1.5SPF	11.75	10.07	1.68	113.44	110.19

APPENDIX B

LTHS report from Bodycote

PROGRESS REPORT FROM BODYCOTE POLYMER FOR

Radius Systems

Project no 10179 **Date of last report** 2008-09-12 **Date for this report** 2008-11-03

CODE	T [C]	Start	d m [mm]	e min [mm]	P [bar]	S [MPa]	Failure time [h]	Failure mode	Test time [h]	Changes	
2 NO SKIN -PROFUSE											
4079-1	20	07-11-13	110.00	10.00	27.85	13.93	141	Ductile			Welded
3 NO SKIN -PROFUSE											
4080-1	20	07-11-19	110.00	10.00	24.22	12.11	->		8 393		Welded
4 NO SKIN -PROFUSE											
4081-1	20	07-11-19	110.00	10.00	25.11	12.55	2 093	Ductile			Welded
5 NO SKIN -PROFUSE											
4082-1	20	07-11-15	110.00	10.00	26.09	13.04	885	Ductile			Welded
6 NO SKIN -PROFUSE											
4083-1	20	07-11-15	110.00	10.00	26.09	13.04	587	Ductile			Welded
9 NO SKIN -PROFUSE											
4084-1	20	07-11-13	110.00	10.00	27.85	13.93	137	Ductile			Welded
11 NO SKIN -PROFUSE											
4085-1	20	07-11-19	110.00	10.00	24.22	12.11	->		8 393		Welded
12 NO SKIN -PROFUSE											
4086-1	20	07-11-19	110.00	10.00	25.11	12.55	2 159	Ductile			Welded
2 1.5 mm SKIN -PROFUSE											
4087-1	20	07-11-15	110.00	10.00	26.48	13.24	->		8 493		Welded
4 1.5 mm SKIN -PROFUSE											
4088-1	20	07-11-15	110.00	10.00	27.07	13.54	7 747	Ductile		FAILED	Welded
6 1.5 mm SKIN -PROFUSE											
4089-1	20	07-11-13	110.00	10.00	27.85	13.93	2 707	Ductile			Welded
7 1.5 mm SKIN -PROFUSE											
4090-1	20	07-11-15	110.00	10.00	26.48	13.24	->		8 493		Welded
8 1.5 mm SKIN -PROFUSE											
4091-1	20	07-11-13	110.00	10.00	27.85	13.93	3 092	Ductile			Welded
10 1.5 mm SKIN -PROFUSE											
4092-1	20	07-11-13	110.00	10.00	29.91	14.96	391	Ductile			Welded
11 1.5 mm SKIN -PROFUSE											
4093-1	20	07-11-13	110.00	10.00	29.91	14.96	367	Ductile			Welded
12 1.5 mm SKIN -PROFUSE											
4094-1	20	07-11-15	110.00	10.00	27.07	13.54	7 883	Ductile		FAILED	Welded

Complementary LTHS report from Bodycote

PROGRESS REPORT FROM BODYCOTE POLYMER FOR
Radius Systems

Project no 10293 **Date of last report** 2009-01-12 **Date for this report** 2009-01-12

Material 1.5 mm SKIN (1)

CODE	T [C]	Start	d m [mm]	e min [mm]	P [bar]	S [MPa]	Failure time [h]	Failure mode	Test time [h]	Remark
20 C										
4469-1	20	08-11-11	110.00	10.00	33.31	16.66	55	Ductile		*Svetskoppl*
4470-1	20	08-11-11	110.00	10.00	33.31	16.66	63	Ductile		*Svetskoppl*
4473-1	20	08-11-11	110.00	10.00	29.12	14.56	61	Ductile		*Svetskoppl*
4474-1	20	08-11-18	110.00	10.00	29.12	14.56	61	Ductile		
4471-1	20	08-11-18	110.00	10.00	25.97	12.99	1 213	Ductile		*Svetskoppl*
4472-1	20	08-11-18	110.00	10.00	25.97	12.99	1 279	Ductile		FAILED

Bodycote Code	Radius marking	colour
4469	"…skin 1"	Blue
4470	"…skin5"	Blue
4471	"…No skin 1"	Natural
4472	"…No skin 7"	Natural
4473	"…No skin 8"	Natural
4474	"…No skin 10"	Natural